RECONSTRUCTING HISTORICAL EARTHQUAKES AND SEA-LEVEL CHANGE IN SOUTH-CENTRAL CHILE FROM TIDAL MARSHES AND UPLIFTED BEACHES

S SAHIN

PhD

2023

RECONSTRUCTING HISTORICAL EARTHQUAKES AND SEA-LEVEL CHANGE IN SOUTH-CENTRAL CHILE FROM TIDAL MARSHES AND UPLIFTED BEACHES

SEFA SAHIN

A thesis submitted in partial fulfilment of the requirements of the University of Northumbria at Newcastle for the degree of Doctor of Philosophy

Research undertaken in the Department of Geography and Environmental Sciences

May 2023

Abstract

The Chilean subduction zone is one of the most tectonically active regions in the world and the Mw 9.5 Valdivia earthquake of 1960 still remains the largest earthquake ever recorded. Key uncertainties remain in Chile, with knowledge of surface deformation in the 1960 earthquake being dominated by studies at the coast, and patterns of deformation inland are less well known. In contrast to 1960, far less is known about the 1737 earthquake, including precise constraints on the rupture length, vertical deformation, and rupture depth, which are critical for seismic hazard assessment. This thesis seeks to find sedimentological evidence for the historical 1737 earthquake at multiple coastal sites in the Valdivia region and to help constrain the eastward limit of coseismic deformation in the great subduction zone earthquakes from the San Antonio estuary.

Biostratigraphy and transfer function reconstructions from the San Antonio estuary do not provide clear evidence of coseismic deformation associated with the 1960 earthquake or its predecessors. The absence of such evidence, alongside observations from nearby sites, suggests that the estuary is located at the eastern limit of coseismic subsidence associated with the 1960 earthquake.

Coastal stratigraphy at Rosada, Loncoyén, Calfuco, and Chan-Chan in the Valdivia region is examined to identify evidence of coseismic land-level change associated with the 1737 rupture. While fossil diatom assemblages do not exhibit abrupt changes, the lithostratigraphy provides potential evidence for uplift caused by the 1737 CE earthquake, with organic peats overlying sands. Limitations with the abundances of diatoms, and with the chronology, mean further investigation is necessary to constrain the magnitude, depth, and amount of coseismic slip for this earthquake and highlight the along-strike variability in coseismic deformation pattern and seismic hazard in the region.

A further conclusion from this thesis is that elevation is not an important ecological determinant and reconstruction models should be treated with caution as many environmental variables influence the ecological response of the diatoms. Furthermore, given the significant importance of reconstruction models in further studies, it is crucial to engage in explicit discussions about the reliability of these reconstruction estimates and exercise caution in their interpretation. This is particularly important in the context of seismic hazard assessment, where the accuracy and validity of the reconstruction models play a critical role.

List of Contents

Chapter 1 :

List of Tables

List of Figures

Acknowledgements

The work presented in this thesis would not have been possible without full scholarship and travel grants from the University of Northumbria. This work also was supported by NEIF Radiocarbon NRCF010001 (allocation number 2137.1018) and ICM-MINECON, Nucleo Ciclo sismico (CYCLO) for radiocarbon dating.

Even though a PhD seems like a piece of work completed by a single person, it requires significant contribution and support from numerous people that we can rely on throughout this long and meandering road. First and foremost, I would like to thank my supervisors Emma Hocking and Ed Garrett. These types of laboratory-based studies require laborious effort and significant commitment especially for microfossils analysis, identification, and delicate treatment. As I am coming from a different background (engineering, geophysics, geology, and tectonic geomorphology) I did not have any experience in analysing microfossils, which is a vitally important step for rigorous data production stage for this study. They have always been next to me, over the last three and half years. Hence, I am extremely grateful for their splendid support, guidance, and immeasurable contribution as well as this marvellous opportunity. It has been a privilege to work with you. Future students are so lucky to work with you. Furthermore, I am thankful for them since they had to deal with my unique writing style over the last three years. I also would like to thank Matthew Pound for his help whenever I needed.

I would like to acknowledge the contribution of all the people. Conducting fieldwork with Daniel Melnick and Paulina Ditzel was an amazing experience and they made remarkable contributions. I am so grateful for Daniels's hospitality and spending time with his amazing family as well as Paulina's help over the course of my time in Chile and after that. I appreciate Fernanda, Diego, and Manuel for their help during the fieldwork in Chile. I am also thankful to Sabine Schmidt for offering help for radiometric dating. In addition, my thanks to our laboratory technician Dave Thomas and his support and guidance for laboratory analyses.

Newcastle upon Type has become a special place to me. I met many wonderful people, especially, my landlords Joyce and Derek White acknowledge me and my wife as their own children and they are our British parents now. There is no way that I can express my gratitude to them. Their kindness and support would undoubtedly be appreciated. Moreover, this city presented a great opportunity to meet Sanem who

became not only my friend but also my mentor encouraging, supporting, and guiding me during challenging times.

Moving from Istanbul to the UK demands a great deal of sacrifice in many perspectives. I am so grateful to my mother, father, elder brother, and my sister for their incredible support. My mother, father, elder brother, and sister have been my pillars of strength. I find myself so lucky to have such a great family. I also would like to thank my parents-in-law and sister-in-law for their support. Most importantly, my wife Ülfet, who abandoned her living standards, gave up her successful career, the job she loved where she was loved and adored by all students and colleagues to support me and my endeavours. Moreover, not only has she been working for the NHS to support people who terribly need help amidst COVID-19 pandemic but also supporting me even after we lost our baby angels after devastating miscarriages. There are no words that I can explain my love and my gratitude to her, I am extremely lucky to have her.

Declaration

I declare that the work contained in this thesis has not been submitted for any other award and that it is all my own work. I also confirm that this work fully acknowledges opinions, ideas, and contributions from the work of others.

Any ethical clearance for the research presented in this thesis has been approved. Approval has been sought and granted by the Faculty Ethics Committee on 08/10/2018 and 15/01/2019.

Dr Ed Garrett carried out field work in San Antonio tidal marsh, tidal modelling for study areas, identification of plant species and initial diatom analysis for the modern samples.

Paulina Ditzel carried out several Differential Global Positioning System (dGPS) measurements for height of the coastal exposures along with top and bottom of peat deposits during the joint fieldwork in January 2019.

I declare that the Word Count of this thesis is 74,835 words.

Name: Sefa Sahin

Date: 24/05/2023

Chapter 1 : Introduction

1.1 Background

Earthquakes and accompanying tsunamis are some of the most devastating natural disasters causing fatalities and destruction to properties, infrastructure, and heritage. The detrimental impacts on a state's economy, communication networks, electric transmission, water distribution, transportation systems, politics and social fabric often remain for years (Morell et al., 2020, Walton et al., 2021) (e.g., 1999 Izmit, Turkey; 2001 India; 2004 Sumatra; 2005 Kashmir, India; 2008 Wenchuan, China; 2010 Maule Chile; 2010 Haiti; 2011 Tōhoku, Japan; 2016 Muisne, Ecuador). Moreover, considering the majority of the world's population and most densely populated cities are located around coastal areas (Nicholls et al., 2007, Bryant, 2008, Neumann et al., 2015, Hauer et al., 2020) these circumstances, combined with often large aseismic intervals and inadequate anticipation, make seismically active regions extremely vulnerable to the consequences of these major tectonic events.

According to plate tectonic theory, subduction zones are formed by the ongoing movement of rigid plates at plate boundaries (Wilson, 1963, 1965a, 1965b, Vine and Matthews, 1963, McKenzie, 1966, 1969, Le Pichon, 1968). These zones are characterised by the occurrence of concentrated seismic activity, with most earthquakes taking place along plate boundaries. The instrumental records demonstrate that subduction zones produce, in particular, the most powerful earthquakes in the world (e.g., USGS Earthquake Catalogue). Subduction zone earthquakes, also known as megathrust earthquakes, result from continuous and persistent tectonic movements where two plates converge (e.g., Chile, Sumatra, Japan, and Alaska, Aleutian). Owing to different geological and thermal setting differences (e.g., Burridge and Knopoff, 1967, Blanpied et al., 1991; 1995, Thatcher and Rundle, 1984, Marone, 1998, Wang, 1995, Bürgmann and Dresen, 2008, Scholz, 2019), these plates are locked at some point and over time, this locking accumulates stress along the locked (seismogenic) zone. As stated in the elastic rebound theory, once the accumulation of stress at the boundary exceeds the frictional strength of the fault, an earthquake occurs (Reid, 1910), suddenly releasing the energy that accumulated over centuries between convergent plates during pre- and interseismic phases. Consequently, this seismic activity may result in coseismic deformation such as uplift and/or subsidence in land level (Yeats et al., 1997, Nelson et al., 1996, Leonard et al., 2010, Shennan et al., 2016). In addition, these megathrust earthquakes can also exhibit tsunami-producing behaviours resulting from coseismic

deformation between the subducting and overlying plates. Large earthquakes follow four distinct phases, each displaying different crustal response: the interseismic, preseismic, coseismic and postseismic stages are termed as the earthquake deformation cycle (Figure 1.1).

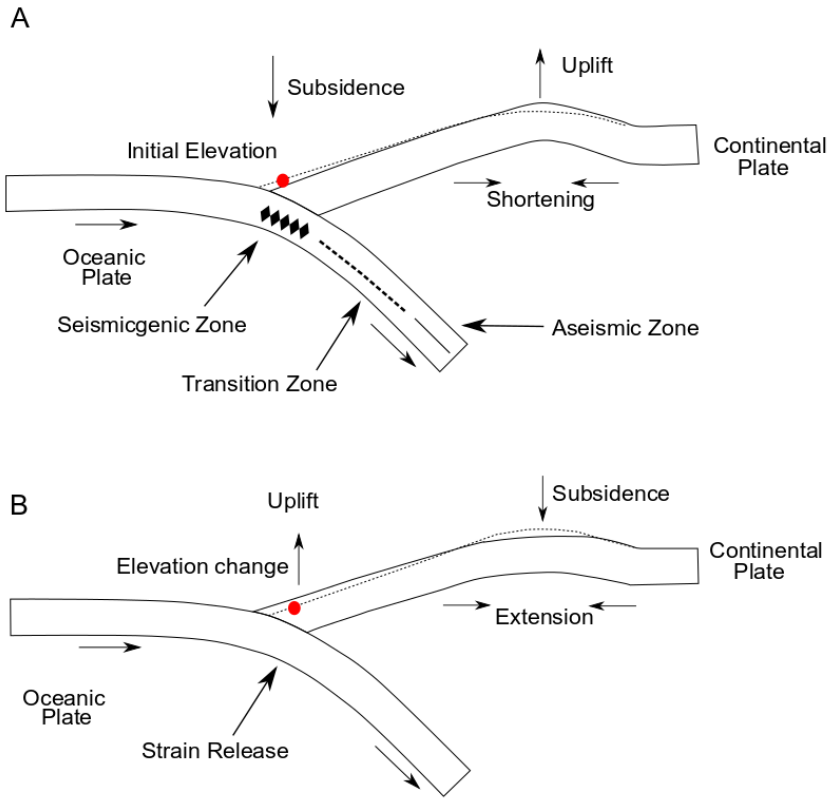

Figure 1.1 : An illustration of deformation associated with a subduction zone earthquake showing A) interseismic deformation and B) coseismic deformation (simplified after Hamilton and Shennan, 2005, Figure 2).

It is well known that the Chilean subduction zone is one of the most earthquake-prone regions on Earth (Figure 1.2; Table 1.1). The M_w 9.5 great Chilean earthquake in 1960 that struck south-central Chile is still the largest earthquake that has been recorded in instrumental history. Yet, as instrumental records are limited to the 20th and 21st centuries, our current knowledge about subduction zone earthquakes relies heavily on historical accounts. Chile has a nearly 500-year long historical record since the arrival of Spanish settlers presenting information such as timing, locations, shaking intensities and presence/absence of tsunami about subduction zone earthquakes (Lomnitz, 1970; 2004, Comte and Pardo, 1991, Cisternas et al., 2005; 2017a). Based on this information we may constrain certain properties such as frequency, estimated rupture length and intensity of subduction zone earthquakes (Kelleher, 1972).

However, as earthquake size, rupture depth and recurrence intervals vary between events, and the length of historical and instrumental records are too short to adequately assess recurrence intervals, seismic hazard assessment can be difficult. On account of incompleteness of historical records and the infrequent nature of subduction zone earthquakes, it leads us to focus on geological records registering tectonic events to extend historical records. Sedimentary records can also provide evidence for multiple earthquakes and tsunamis and allow us to estimate recurrence intervals of these events on millennial timescales in Chile (e.g., Cisternas et al., 2005, Garrett et al., 2015, Dura et al., 2015).

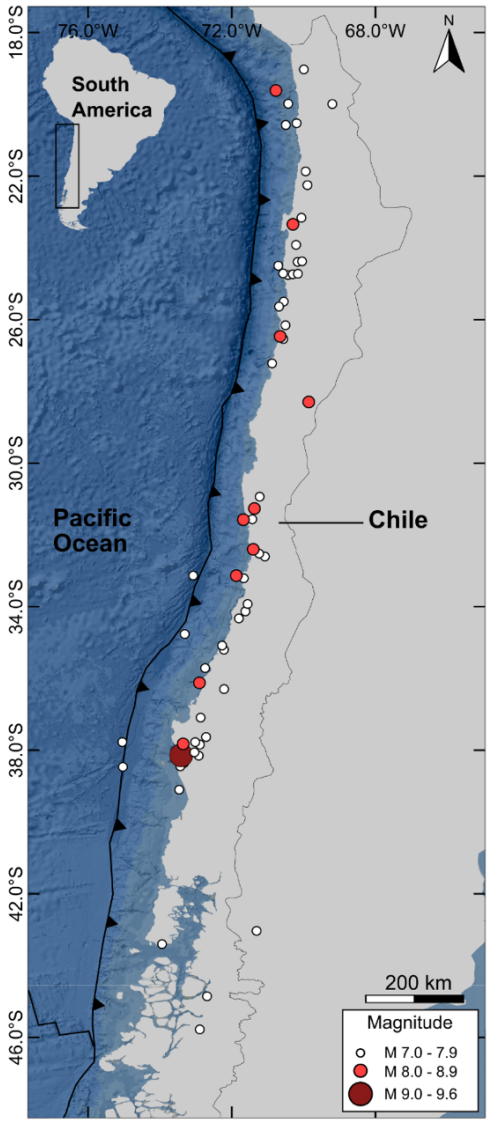

Figure 1.2 : Epicentres of great (Mw ≥ 8) and large (Mw ≥ 7) earthquakes from 1900 to present on the Chilean subduction zone megathrusts from the U.S. Geological Survey National Earthquake Information Center catalogue (USGS-NEIC, https://earthquake.usgs.gov).

Table 1.1 : Distribution of the tsunamigenic earthquakes with magnitude of 7 or more that occurred between 2005 and 2015 along the Chilean subduction zone (Hayes et al., 2017).

Date	Location	Magnitude
2005	Tarapaca	7.8
2007	Antofagasta	7.7
2010	Maule	8.8
2010	Bio-Bio	7.4
2011	Araucania	7.2
2012	Maule	7.1
2014	Iquique	7.7
2014	Iquique	8.2
2015	Illapel	8.3
2015	Illapel	7.0

Ultimately, in order to improve seismic hazard assessment we, as a research community, must better understand: 1) the timing of subduction zone earthquakes and evidence for accompanying tsunamis; 2) the location of ruptures and spatial distribution of deformation patterns, and 3) the magnitude of past earthquake events (Bilet 2010, Bilek and Lay, 2018). As the magnitude of earthquakes chiefly hinges upon the ruptured area and average slip on the fault (Kanamori, 1977, Hanks and Kanamori, 1979, 2008, Wells and Coppersmith, 1994), constraining rupture length and estimating vertical displacement is of utmost importance for characterising earthquakes (e.g., Moreno et al., 2009).

In order to contribute to advancement of understanding in these broad areas, we must supplement historical records with geological evidence preserved in sediments. Since coastal areas mainly reside next to subduction zones, coastal palaeoseismology has been shown to be a powerful approach to reconstructing earthquake history (Satake and Atwater, 2007, Stein and Okal, 2011, Philibosian and Meltzner, 2020). If we adopt this approach at multiple sites in coastal areas, it becomes possible to advance the understanding of such megathrust earthquakes. Consequently, this thesis aims to carry out palaeoseismic investigations to find evidence of subduction zone earthquakes in Chile by identifying and analysing sedimentological and biostratigraphic evidence from coastal environments in south-central Chile for seismic hazard assessment.

1.1 Rationale

Although historical records present evidence for subduction zone earthquakes and tsunami in Chile, they are inadequate for hazard assessment and limited to covering only the last ~500 years (Cisternas et al., 2005, Cisternas et al., 2017a). Furthermore, because of their nature, historical records can only provide limited information such as timing and shaking distribution of earthquakes. Also, it is suggested that due to the civil unrest, political and administrative reasons, as well as different types of reporting preferences, historical records can reflect bias about intensity of earthquakes (for details see Lomnitz (2004)) or events may simply be missing from the historical record. In this case, the earthquakes occurred in 1575 CE, 1737 CE, and 1837 CE could be considered comparable to that of the 1960 earthquake; however, geological investigations suggest that only the 1575 earthquake reflects similar features to the 1960 earthquake (Bartsch-Winkler and Schmoll, 1993, Cisternas et al., 2005, 2017b, Garrett et al., 2015). Furthermore, geological surveys introduce the occurrence of two more large subduction zone earthquakes displaying similarity to the 1960 earthquake and three more earthquakes of relatively moderate size events (Cisternas et al., 2017b). Hence, geological records can provide detailed and comparable sedimentary evidence, as well as longer records, for subduction earthquakes and accompanying tsunamis.

Coastal palaeoseismology is currently utilised to study sedimentary deposits in coastal regions, with the aim of providing valuable evidence for subduction zone earthquakes. This evidence can be used to better constrain the length of ruptures, vertical deformation patterns, and recurrence intervals associated with these events Furthermore, in addition to geological evidence, coastal biostratigraphy enables the implementation of a statistical approach for the estimation of land-level change and relative sea-level change. This method is known as the transfer function method, and its details are elaborated below. Accordingly, the ultimate rationale behind this research is to provide geological records for these events that occurred on the Chilean subduction zone in the late Holocene.

1.2 Sedimentary evidence for coseismic deformation

Understanding the behaviour of subduction zone earthquakes in terms of vertical deformation patterns requires both sedimentary and microfossil evidence. Hence, coastal paleoseismology provides sedimentary and microfossil evidence that can be evaluated through quantitative and qualitative methods, which may assist in obtaining

a reliable assessment of seismic hazards (e.g., Dura et al., 2016b and references therein).

Coastal palaeoseismology focusing on low-energy depositional environments (e.g., tidal marshes, estuaries) involves investigation of stratigraphic, sedimentological, and morphological features to provide information on relative land-level change resulting from subduction zone earthquakes (McCalpin and Carver, 2009). Previous palaeoseismic studies have found evidence of subduction zone earthquakes by analysing of sedimentary sequences in Chile (e.g., Atwater et al., 1992, Cisternas et al., 2005, 2017b, Dura et al., 2015, Garrett et al., 2015, Nelson et al., 2009); Cascadia (e.g., Long and Shennan, 1994, Atwater, 1987, 2005b, Nelson et al., 1996, 2008, Witter et al., 2003); Alaska (Combellick, 1991, Hamilton and Shennan, 2005, Hamilton et al., 2005, Briggs et al., 2014); Japan (Sawai et al., 2002, 2004b, Nanayama et al., 2003, 2007); and New Zealand (Hayward et al., 2004, 2006).

During the coseismic stage of the seismic cycle, coastlines next to subduction zones either uplift or subside or both (Nelson et al., 1996). This coseismic deformation (uplift or subsidence) is registered as a sharp contact in the sedimentary record that reflects an abrupt change in land level related to seismic activity (Yeats et al., 1997, Nelson et al., 1996, Shennan et al., 2016). The sedimentological indicators of coseismic uplift can be found as a minerogenic-organic couplet as organic rich materials overlie intertidal deposits whereas organic-minerogenic couplets represent coseismic subsidence at coastal sites (e.g., Leonard et al., 2010). However, it is suggested that similar sedimentary sequences can also be observed on seismic coasts resulting from non-seismic processes (Long and Shennan, 1994, Nelson et al., 1996, Witter et al., 2001). In order to infer deposition by seismic rather than non-seismic sources, six criteria were established by Nelson et al. (1996) and updated Shennan et al. (2016): 1) lateral extent of peat-mud or mud-peat couplets with sharp contacts; 2) suddenness of submergence or emergence, and replicated within each site; 3) amount of vertical motion, quantified with 95% error terms and replicated within each site; 4) synchroneity of submergence and emergence based on statistical age modelling; 5) spatial pattern of submergence and emergence; 6) possible additional evidence, such as evidence of a tsunami or liquefaction concurrent with submergence or emergence.

1.2.1 Microfossil evidence for coseismic deformation

In addition to lithostratigraphic evidence, microfossils preserved within tidal marsh sediments allow estimation of earthquake related relative sea-level change and

accompanying tsunami at subduction zones (e.g., Horton et al., 2013). Analysing microfossils (e.g., diatoms, foraminifera) is one of the most useful methods for reconstructing relative sea-level change (for review Pilarczyk et al., 2014) as these microorganisms inhabit specific zones in the tidal frame (Gehrels et al., 2001), and a change in elevation will be reflected by a change in associated microfossils.

Diatoms are unicellular algae which belong to the class Bacillariophyceae and occur and abound in freshwater, brackish, and marine environments (Round et al., 1990, 2007). Their siliceous cell wall provides resistance to various chemical and physical processes and makes them a dominant species in coastal wetland environments (Admiraal, 1984, Palmer and Abbott, 1986, Cooper, 2010). Their distribution depends on a range of environmental factors such as salinity, substrate, vegetation, pH, and tidal exposure (Whiting and McIntire, 1985, Gehrels et al., 2001, Patterson et al., 2005, Horton et al., 2006, Roe et al., 2009). The role of diatoms as sedimentological archives is well known because of the pattern of their zonation of species (Zong and Horton, 1999) showing a direct relationship with elevation in the tidal frame (Horton et al., 2006) and frequency of tidal inundation (e.g., Hemphill-Haley, 1996, Shennan et al., 1996, Zong and Horton, 1999, Sawai et al., 2002, 2004b, Hamilton and Shennan, 2005, Woodroffe and Long, 2010). Due to different salinity tolerances, zonation and widespread preservation, diatoms are a well-established important indicator across the intertidal zone for earthquake and tsunami studies (Nelson and Kashima, 1993, Hemphill-Haley, 1996, Sherrod, 1999, Horton et al., 2006, 2011, Sawai et al., 2008, Garrett et al., 2013, 2015, Dura et al., 2015) and thereby they provide important information on relative sea-level change at subduction zones (Horton et al., 2010).

Diatoms collected from coastal areas next to active plate margins have been used to reconstruct late Holocene relative sea-level history associated with earthquakes and accompanying tsunamis (for review see Dura et al., 2016b). Quantitative diatom analyses have been used to estimate vertical land-level change and relative sea-level change associated with subduction zone earthquakes successfully through the use of transfer functions (e.g., Kemp and Telford, 2015).

Transfer functions are a statistical approach that use regression analysis to present the relationship between an environment parameter (e.g., elevation, pH) and relative abundance of modern microfossils (i.e., diatom, foraminifera) (Birks, 1995; 1998, Juggins and Birks, 2012). Assemblages of diatoms can be a suitable sea-level indicator based on where they are found (Zong and Horton, 1998, Barlow et al., 2013, Zong and Sawai, 2015). By collecting samples across a transect of the intertidal zone,

which includes low marsh, mid marsh, high marsh, and freshwater upland, a wide range of biota can be obtained, reflecting the highly variable occurrence of diatoms that are indicative of both tidal frequency and duration. Subsequently, transfer function models may be able to estimate change in fossil data and test its relationship with environmental gradient to provide information about relative sea-level changes (Barlow et al., 2013, Kemp and Telford, 2015). The goal is to develop transfer function models as accurately as possible thereby they can be used to reconstruct relative sea-level in the past in accordance with the relationship between modern diatom assemblages and tidal elevation. Thus, it is aimed to provide robust and reliable quantitative information on vertical displacement resulting from subduction zone earthquakes in south-central Chile.

1.3 Research gaps, aims, questions and objectives

As stated earlier, the occurrence of great and large subduction zone earthquakes and accompanying tsunamis are not limited to only the last 500 years and geological evidence can be used to extend the historical record in south-central Chile (Cisternas et al., 2005; 2017b). However, our current knowledge of the rupture length and width of these events and the spatial distribution of coseismic deformation are limited and also inadequate to compare the magnitude and coseismic deformation patterns for historic and prehistoric earthquakes (Cisternas et al., 2017a, b).

Previous studies report the occurrence of earthquakes over the last 1000 years (Cisternas et al., 2005, 2017b, Atwater et al., 2013, Moernaut et al., 2014, Garrett et al., 2015), including magnitude 9+ earthquakes in 1960 (event A), 1575 (event B), c. 1270 – 1450 CE (event C) and c. 898 – 1220 CE (event D), alongside smaller (likely magnitude 7.5+) events in 898 – 1308 CE (event cd), 1304 – 1470 CE (event bc1), 1505 – 1548 CE (event bc2), 1837 CE (event ab) and 1737 CE (Figure 1.3). The length and width of both the larger and the smaller prehistoric ruptures are currently constrained by a very small number of sites, limiting understanding of how the size and distribution of earthquakes has varied over time. Therefore, it is crucially important to provide more geological evidence for past subduction zone earthquakes to decipher coseismic deformation patterns.

Constraining the spatial distribution of coseismic deformation patterns resulting from these subduction zone earthquakes using new sedimentological and diatom-based reconstruction models can enable us to compare behaviours of these ruptures. While larger earthquakes have the potential to cause greater damage (e.g., 1960 and 1575),

the smaller earthquakes (such as those in 1837 CE and 1737 CE) may occur more frequently and have been the focus of recent study (Hocking et al., 2021). As with the larger prehistoric earthquakes, understanding of their rupture length and vertical coseismic deformation at the coast is limited. Both the 1837 CE and 1737 CE earthquakes caused large shaking across south-central Chile (Lomnitz, 1970, 2004, Cisternas et al., 2017b). Our current knowledge of the 1737 rupture is derived from a single coastal site (Hocking et al., 2021) and turbidite records from inland lakes (Moernaut et al., 2014). Similarly, sedimentary evidence for the 1837 CE earthquake includes turbidite signatures from Reloncavi fjord (St-Onge et al., 2012), submerged trees in San Rafael fjord (Reed et al., 1988), and tsunami deposits at Cocotué (Cisternas et al., 2017a) and Lago Huelde (Kempf et al., 2017). Hence, it is critical to acquire additional geological records in order to differentiate these events and better constrain their rupture lengths as well as vertical coseismic deformation.

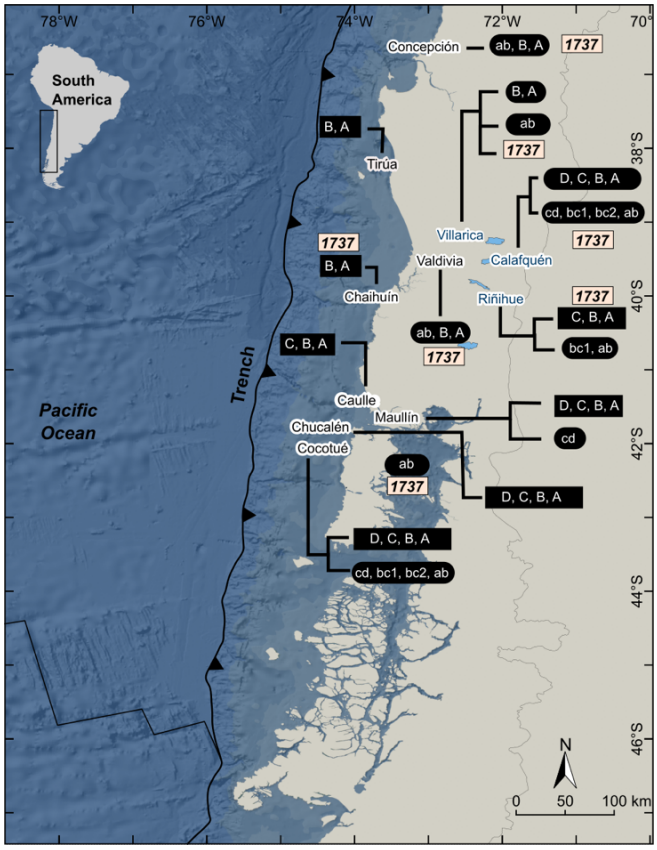

Figure 1.3 : Prehistoric great (D, C, B, A) and unreported large earthquakes (cd, bc1, bc2, ab) as described in text. The 1737 CE earthquake is not specifically named in the original publication. Historical records from Lomnitz (1970, 2004) and Cisternas et al., (2005, 2017a) and geological records from Ely et al., (2014); Cisternas et al., (2005, 2017a), Atwater et al., (2013), Moernaut et al., (2014), Garrett et al., (2015) and Hocking et al., (2021). Base Map: ESRI.

With the aim of obtaining new geological evidence to constrain the spatial pattern of deformation of historical and prehistoric subduction earthquakes of the past ~1000 years (both those similar to the 1960 M_w 9.5 Great Chilean earthquake and the more moderate ruptures such as those which occurred in 1837 CE and 1737 CE), the San Antonio estuary and six coastal sites in the Valdivia region have been investigated using lithostratigraphy, sedimentology and quantitative biostratigraphy. San Antonio estuary is located at a similar latitude to Maullín and Chucalén, where historical and prehistoric deformation and tsunami deposits are reported (Cisternas et al., 2005, Garrett et al., 2015). Thus, San Antonio offers the potential to provide further information about the pattern of coseismic deformation with increasing distance from the trench during the largest earthquakes (those analogous to the 1960 earthquake). The coastal sites in the Valdivia region, in contrast, present an opportunity to investigate possible rupture lengths and slip distributions of the smaller ruptures that occurred in 1737 CE and 1837 CE.

1.3.1 Spatial pattern of deformation during great and large earthquakes

Although existing geological evidence enables us to constrain apparent rupture length associated with great subduction zone earthquakes in south-central Chile, our current knowledge of the width of megathrust fault ruptures is still limited to model outputs, despite rupture width being an essential component in seismic hazard assessment (e.g., Dragert et al., 1994, Nelson et al., 2008, Herrendörfer et al., 2015). Therefore, the lack of qualitative and quantitative information about coseismic deformation emanating from the past great earthquakes especially the inland extent of ruptures that may have a similar magnitude to the 1960 Mw 9.5 earthquake remains uncertain. Providing new constraints for the possible width of these ruptures may constrain magnitude and slip distribution models as well as enable comparisons with the extent of seismic slip from these significant ruptures since it is suggested they have similarities regarding geological records (Cisternas et al., 2017b).

The intertidal marsh developed in the San Antonio estuary, situated in a semi-enclosed basin, provides a favourable location to register relative sea-level changes (Figure 1.4). Its positioning at the eastern boundary of the region affected by coseismic subsidence resulting from the 1960 earthquake in south-central Chile allows us to potentially constrain the width of megathrust fault ruptures, including those of previous events such as B, C, and D. This particular intertidal environment presents a suitable location to analyse the modern distribution of diatoms since it is sheltered from large waves. Moreover, the location of the study site is ~ 180 km away

from the part of south-central Chile across the Peru-Chile trench in the eastern Pacific Ocean; thus, any substantial change in sedimentary sequence may aid in constraining the landward limit of coseismic subsidence or the occurrence of uplift as well as assist in constraining the down-dip landward limit of great subduction zone earthquake (Hyndman, 2013, Wang and Tréhu, 2016, Ramos et al., 2021).

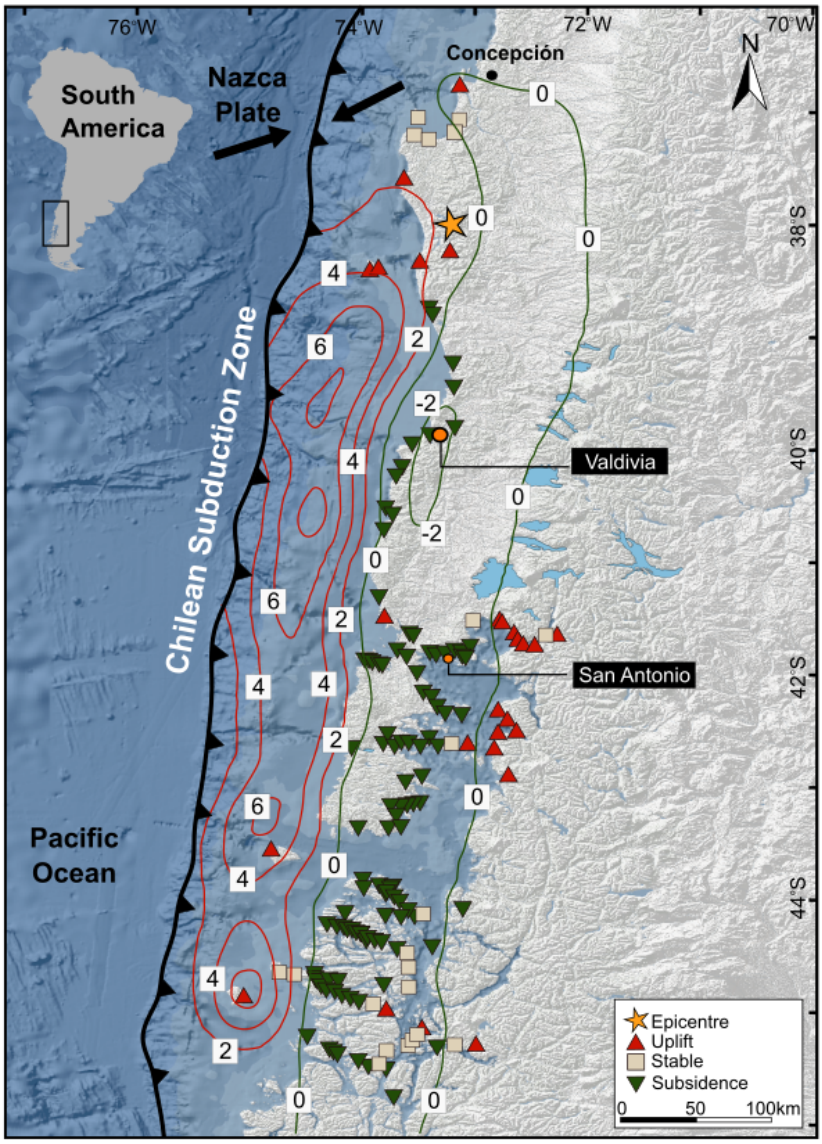

Figure 1.4: Coseismic vertical deformation and slip distribution caused by the Mw 9.5 1960 earthquake. The barbed line shows the subduction zone; red contours show uplift, green contours show subsidence from Moreno et al., (2009); red triangles, green triangles and white rectangles indicate sites recording emergence, submergence and no vertical displacement (m) relative land-level changes associated with the 1960 Mw 9.5 earthquake respectively (adapted and modified from Plafker and Savage (1970, Figure 2) and Moreno et al., (2009, Figure 3). DEM is based on ETOPO1 dataset from Amante and Eakins (2009). Basemap: ESRI.

Estimating the spatial distribution of coseismic deformation is an important factor for quantitatively modelling the geometry of the plate interface and constraining magnitudes of subduction zone earthquakes, as seismic moment is calculated by using average fault displacement (coseismic slip) and area of the fault plane (e.g., Moreno et al., 2009, Wang et al., 2013). Furthermore, the amount of energy released as a result of these earthquakes can be constrained (Kanamori, 1977). Therefore, we may model seismic deficits (the difference between accumulated and realised strain during an earthquake) and give ideas about possible future earthquakes in the region and contribute to seismic hazard assessment (Satake and Atwater, 2007, Bilek and Lay, 2018).

1.3.2 Evidence of smaller historical ruptures

Despite considerable advancements in our understanding of when megathrust earthquakes occurred in south-central Chile, there are still remarkable knowledge gaps regarding pre-1960 earthquakes (1737 CE and 1837 CE) in terms of their spatial distribution of coseismic deformation and rupture length and also evidence for tsunami. Only partial historical records are available for both of these events (Lomnitz, 1970, 2004, Cisternas et al., 2005, 2017b). Moreover, our current knowledge is limited when it comes to constraining rupture length and estimating the magnitude of these events from coastal sites. Direct records from tsunami deposits have only been obtained in a recent study, which suggests that the 1737 CE earthquake was responsible for such deposits (see Hocking et al., 2021).

The marine terraces located at coastal sites in the Valdivia region offer a valuable opportunity to investigate sedimentary evidence associated with the 1737 CE and 1837 CE earthquakes, which are characterized as moderate magnitude events (Moernaut et al., 2014, Cisternas et al., 2017b). These earthquakes, however, have limited available sedimentological information. Investigating the presence of any direct sedimentological evidence for coseismic deformation resulting from the 1837 CE and 1737 CE earthquakes at multiple coastal sites also permits constraint of rupture lengths. Furthermore, diatom analyses and further transfer function models may provide additional constraints on vertical coseismic deformation associated with these historical events.

1.3.3 Aims and research questions

The overall aim of this study is to find evidence for relative land-level (sea-level) changes associated with subduction zone earthquakes in south-central Chile. Seeking evidence for these earthquakes (the 1960 and its predecessors), investigations have been carried out on coastal sites in the Valdivia region and San Antonio estuary on Isla Quihua in the Los Lagos region. This includes assessing whether coseismic deformation (vertical land-level change) occurred in either the 1960 Mw 9.5 earthquake or earlier prehistoric earthquakes (event B, C and D); and constraining the rupture length of smaller historical (pre-1960) earthquakes from six sites in the Valdivia region. This will improve our understanding of palaeoseismic activity of the Chilean subduction during the late Holocene and may contribute towards seismic hazard assessment.

In order to achieve these aims the following questions will be answered:

- Is there geological evidence of relative land-level change at San Antonio estuary associated with the 1960 earthquake, which may corroborate the location of the eastern limit of coseismic subsidence?
- Is there any evidence in tidal marsh sediments at San Antonio for pre-1960 earthquakes (e.g., event B, C and D) that may help constrain the width and magnitude of these ruptures?
- Do peat deposits on beach terraces in the Valdivia region represent possible occurrence of uplift during a pre-1960 earthquake?

The primary objectives defined to address the aims are as follows:

1. Conduct litho- and bio-stratigraphic analyses of coastal sediments from tidal marshes and coastal exposures for evidence of past earthquakes in south-central Chile.
2. Constrain the timing of any earthquakes identified in the sedimentary record.
3. Improve understanding of modern intertidal diatom distributions and develop transfer function models for quantifying coseismic deformation.
4. Reconstruct vertical coseismic deformation associated with historic earthquakes in the Valdivia seismic segment.
5. Explore the potential and importance of using rigorous statistical methods to investigate limits and reliability of transfer function-derived reconstruction estimates.

1.4 Thesis structure

Including this introductory chapter, presenting research questions and objectives, this thesis consists of seven main chapters. Chapter 2 synthesises the seismic history of the study area and introduces the specific field sites for this study. Chapter 3 describes the methods employed throughout this study. Chapter 4 develops diatom-based transfer function models in order to reconstruct relative sea-level changes for study sites. Chapter 5 performs relative sea-level reconstruction for the San Antonio estuary. Chapter 6 presents findings from laboratory and fieldwork for the coastal sites in Valdivia region and reconstructs relative sea-level changes. Chapter 7 presents discussions. Finally, Chapter 8 presents conclusion and insights on findings and makes suggestion for future research.

1.5 Summary

Subduction zones generate the most powerful earthquakes and tsunamis in the world. Investigation of coastal sedimentology and palaeoecology and their association with megathrust earthquakes provide invaluable information for seismic hazard assessment. This study uses both quantitative biostratigraphic and lithostratigraphic approaches in order to develop quantitative reconstructions of relative land surface deformation caused by great earthquakes in south-central Chile and compares its findings with previous studies and historical records. Consequently, the findings of this study contribute towards seismic hazard assessment in the Chilean subduction zone.

Chapter 2 : Seismic history of south-central Chile

2.1 Introduction

This chapter presents the tectonic setting and seismic history of south-central Chile, as well as gives details about the study sites. It introduces the historical and sedimentary records of major subduction earthquakes and discusses relative sea-level change during the Holocene and the deglaciation history of the region since the last glacial maximum to provide context.

2.2 Structure and seismicity along the Chilean convergent margin

2.2.1 Tectonic setting

The Chilean convergent margin is divided into two main sections: 1) the arc spans ~6000 km from the Panama plate in the north at 7.15^{o}N and terminates at 46.50^{o}S at the Chilean margin triple junction (CTJ) offshore of southern Chile; 2) to the south the Antarctic plate collides with the South American plate (Figure 2.1). Along this arc, the convergent plate margin runs nearly parallel to the Pacific coast where the oceanic the Nazca and Antarctic plates are descending beneath the continental South American plate (Figure 2.1). The margin presents a broad range of tectonic conditions such as different geometry and seismic coupling (Tichelaar and Ruff, 1991, Gutscher et al., 2000, Lange et al., 2007, Moreno et al, 2010, Béjar-Pizarro et al., 2013, Kopp, 2013, Métois et al., 2016; Haberland et al., 2016). This tectonic setting forms the Chilean subduction zone that occurs between the Arica Bend (18.2°S) in the north and the CTJ (~46.5°S) in the south. The onset of subduction has been initiated in the Pennsylvanian approximately ~305 Ma based on isotopic dating in south-central Chile (Willner et al., 2004). The motion between plates has been oblique since ~48 Ma and showing dextral movement with the exception of orthogonal convergence from 26 Ma to 20 Ma (Cande and Leslie, 1986, Pardo-Casas and Molnar, 1987). As opposed to the rapid convergent rate of 120 mm/yr in the late Cenozoic (25 - 20 Ma) (Somoza, 1998), the present-day convergent rate is 66-74 mm/yr (Angermann et al., 1999, DeMets et al., 2010); the latter is based on both GPS and palaeomagnetic data. The angle of movement along the Nazca plate varies between 10^{o} - 15^{o} north-northeast with a slightly oblique component (Angermann et al., 1999, Wang et al., 2007, DeMets et al., 2010). Along the arc there are many aseismic ridges, fracture zones and seamounts associated with seismically active segments on the Nazca plate (e.g., Bilek, 2010, Sparkes et al., 2010, Contreras-Reyes, 2018).

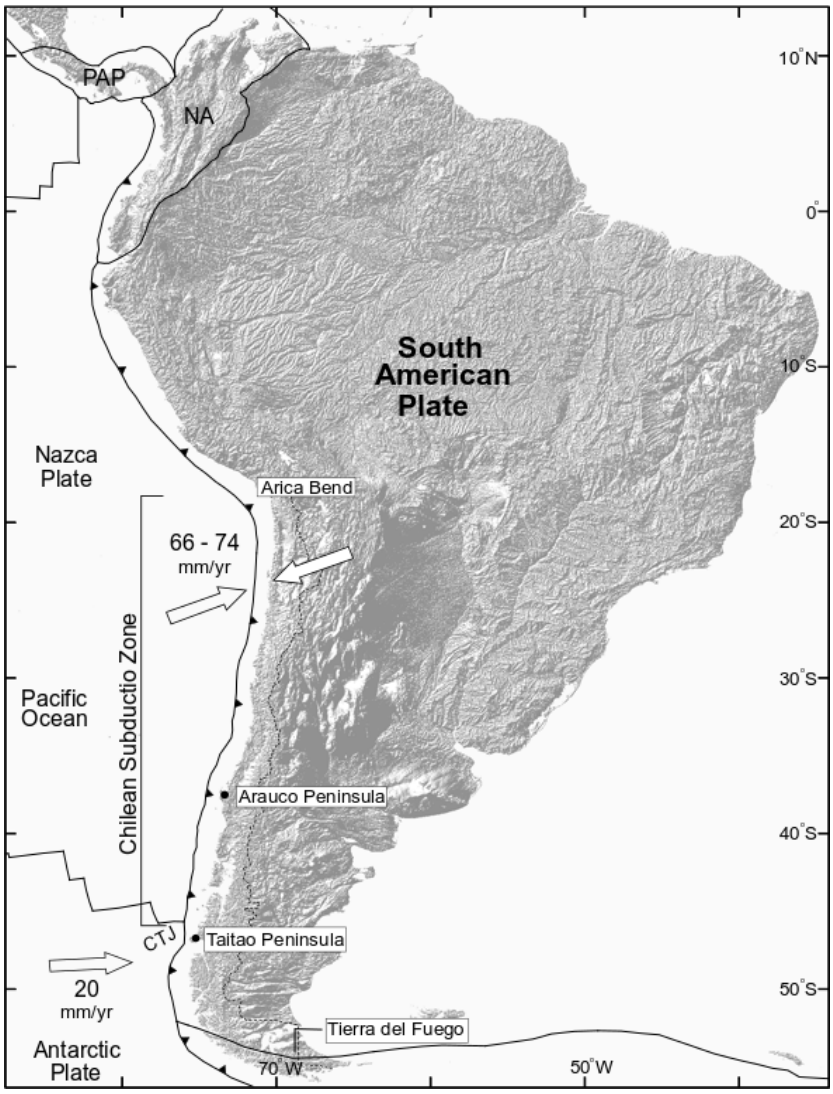

Figure 2.1 : Plate-tectonic setting of Chile in western South America. The Peru-Chile trench occurs where the Nazca plate is descending beneath the South American plate off the west coast of South America. Convergence rates for the Nazca Plate from Angermann et al., (1999); DeMets et al., (2010); for Antarctica Plates from DeMets et al., (2010). The black barbed line for the trench; white arrows for convergence direction and the rates; PAP: Panama Plate; NA: North Andeas Plate; CTJ: Chile Triple Junction. DEM is based on ETOPO1 dataset (Amante and Eakins, 2009).

2.2.1.1 Dipping angle of slabs and ridges

One of the key factors influencing the seismotectonic setting of convergent margins is the dipping angle of descending plates (flat or steep), as it shapes seismotectonic behaviour, thermal structure, and the depth of the seismically coupled zone of the margin (e.g., Dewey and Lamb, 1992, Tichelaar and Ruff, 1993, Oleskevich et al., 1999, Gutscher et al., 2000, Gutscher, 2002). The complex geometry of the

segmented convergent margin of the South American Plate shows significant along-strike variation in the dipping angle of subduction style that alternates between flat-slab and steep-slab mechanisms (Barazangi and Isacks, 1976, Cahill and Isacks, 1992, Tassara et al., 2006) because of buoyancy of the oceanic plate depending on the age and controlling thickness of the descending oceanic plate along the margin (Cahill and Isacks, 1992, Gutscher, 2002). The age of the oceanic plate decreases from 48 Ma (~20°S) in the north to 0 Ma at the Chile triple junction (46.5°S) in the south (Müller et al., 1997). The segments that descend beneath central Peru (5° – 15°S) and Argentina (28° – 33°S) exhibit flat slab geometry with low subducting angle at intermediate depth associated with the Nazca ridge at ~15°S and the Juan Fernández ridge at ~33°S; the other two Carnegei at ~1°S and Iquique at 20°S Ridges penetrate under Ecuador and central Chile (Gutscher et al., 2000, Yáñez et al., 2002). Moreover, flat-slab style subduction extends hundreds of kilometres inland until it reaches depths greater than 100 km before proceeding the subduction into mantle (Tichelaar and Ruff, 1993, Gutscher et al., 2000, Anderson et al., 2007). In contrast, the dip angle of the subducting plate in the north central, south central, and southern Chile varies between 25°– 30°S and displays steep-slab style with increasing depth of ~200 km along the convergent margin (Gutscher et al., 2000, Bohm et al., 2002, Tassara et al., 2006, Haberland et al., 2006, Lange et al., 2007).

2.2.1.2 Fracture zones

The Nazca plate displays numerous fracture zones and four prominent aseismic ridges (Carnegie, Iquique, Nazca, Juan Fernández ridges) that have a crucial impact on the tectonic setting of the subduction zone (Figure 2.2). All these fracture zones and aseismic ridges originate from the East Pacific Ridge (Wilson, 1965). Fracture zones are trails of transform faults originating at the ocean ridge system where thermal stress is relieved (Sandwell, 1986). The Valdivia Fracture Zone system (~40°S) is a major discontinuous constituent on the Nazca plate and has been active over the last 15 Ma, consisting of several fracture zones (Figure 2.2) (Herron et al., 1981, Tebbens et al., 1997). This system divides the oceanic crust that developed at the East Pacific Rise from the oceanic crust formed at the Chile Rise (Tebbens and Cande, 1997).

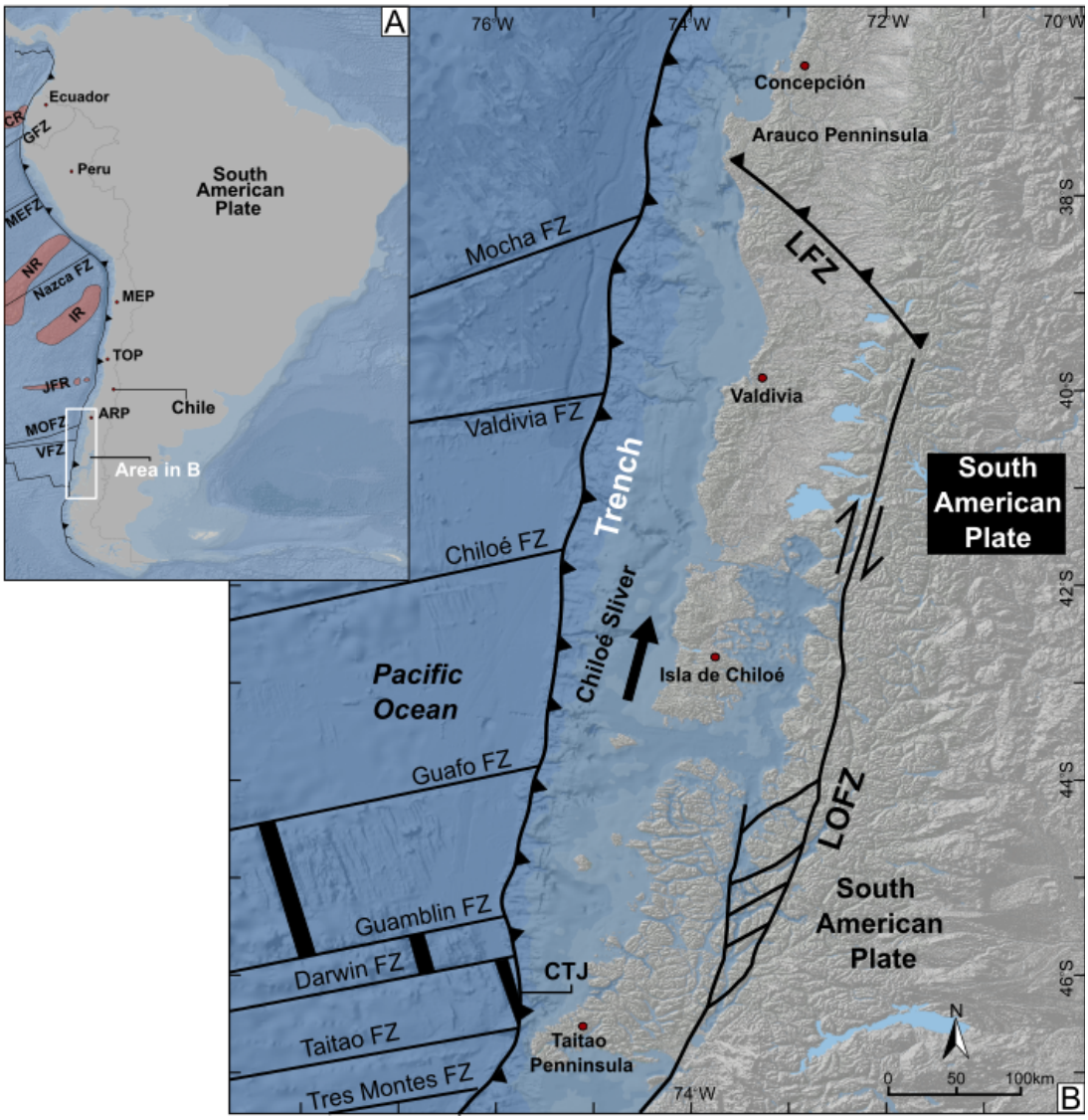

Figure 2.2 : A) Fracture zones and aseismic ridges affecting seismotectonic behaviours of the South American plate margin. Grijalva Fracture Zone (GFZ); Mendana Fracture Zone (MEFZ); Nazca Fracture Zone (NFZ); Mocha Fracture Zone (MFZ); Valdivia Fracture Zone (VFZ); Carnegei Ridges (CR); Nazca Ridge (NR); Iquique Ridge (IR); Juan Fernandez Ridge (JFZR). B) Main tectonic features of the Valdivia seismotectonic segment. Fracture zones (FZ) from Cande and Leslie (1986); Tebbens and Cande (1997). The Liquiñe-Ofqui Fault Zone (LOFZ) from Cembrano et al. (2000) and Chiloé block along the Valdivia segment in south-central Chile. DEM is based on ETOPO1 dataset (Amante and Eakins, 2009). World Ocean Basemap: ESRI.

It is suggested that peninsulas and bays are one of the important coastal features associated with barriers of major rupture propagation of earthquakes since they are correlated with complex tectonic structures such as fracture zones and ridges (e.g.,

Armijo and Thiele, 1990; Barrientos and Ward, 1990; Moreno et al., 2008; 2010; Audin et al., 2008; Melnick and Bookhagen, 2009). For instance, the nucleation of the 1960 (M_w 9.5) earthquake (Plafker and Savage, 1970; Cifuentes, 1989) and termination of the 2010 (M_w 8.8) rupture (Moreno et al., 2010) are observed at the Arauco Peninsula, adjacent to the Mocha fracture zone. Also, the northern boundary of rupture the 2010 (M_w 8.8) earthquake is located where the Juan Fernández Ridge subducts (Sparkes et al 2012).

2.2.1.3 Main fault zones and Chiloe block in south-central Chile

The upper plate fault zones have a strong impact on the tectonics of the Valdivia segment of the subduction zone. The Lanalhue Fault Zone (LFZ) is northwest-southeast oriented, with crustal-scale strike-slip fault in the Arauco-Nahuelbuta region showing sinistral movement since the early Permian (~275 Ma). It is also an apparent boundary for distinct metamorphic units which are called the Eastern and Western Series (Glodny et al., 2006). Furthermore, it acts as a natural barrier that controls earthquake initiation and propagation in the northern part (37.5ºS) of the Valdivia segment (Melnick et al., 2009). The Liquiñe-Ofqui Fault Zone (LOFZ) is a nearly ~1100-km-long strike-slip fault zone and one of the striking tectonic features in the region accommodating the south-central and southern cordillera. It has been active since the Eocene and shapes the architecture of the intra-arc region between 38ºS – 46.5ºS. Its geometry is characterised as dextral strike-slip movement because of oblique subduction of the oceanic plate and high uplift rates in the Holocene (Hervé, 1994, Cembrano et al., 1996, 2000, Rosenau et al., 2006). Although dextral movement of the fault zone increased in the Middle Miocene (Cembrano et al., 2000) and average estimates of velocity decreases northwards from 36 mm/yr to 13 mm/yr since the Pliocene ~6 Ma (Rosenau et al., 2006). The LOFZ is responsible for the 1965 M_w 6.2 Hodson earthquake (45.8°S), the 1989 M_s 5.3 Lonquimay earthquake (38.5°S) and the 2007 M_w 6.2 Aysén (45.2°S) earthquake. Present deformation is controlled by both postseismic deformation and interseismic strain accumulation after the 1960 earthquake (Klotz et al., 2001, Khazaradze and Klotz, 2003, Wang et al., 2007). The fore-arc sector, which is next to the LOFZ, described as the Chiloé block, decoupled from the South American Plate owing to the dextral character of this intra-arc strike-slip fault and pushes it northward as far as the Arauco peninsula (Hervé, 1994, Cembrano et al., 2000, Rosenau et al., 2006, Wang et al., 2007). Yet, the movement of the fore-arc sliver in that region is inhibited because of the buttressing

effect and collides with Arauco-Nahuelbuta block (Beck et al., 1993, Rojas et al., 1994) and promotes uplift since the Pliocene (Melnick et al., 2009).

2.2.1.4 Segmentation

The Chilean megathrust displays along-strike segmentation with different segments showing differing seismic characteristics such as recurrence intervals, rupture lengths, and magnitude of earthquakes (Lomnitz, 1970, 2004, Cisternas et al., 2005). The main factors that govern segmentation are the presence of the upper plate's discontinuities (McCaffrey, 1992, Song and Simons, 2003), bathymetric irregularities, fracture zones, seamounts, aseismic ridges in the incoming oceanic plate (Kelleher and McCann, 1976, Taylor et al., 1987, Barrientos and Ward, 1990, Robinson et al., 2006, Bassett and Watts, 2015) and the thickness of sediments in the trench (Ruff, 1989, Thornburg et al., 1990, Völker et al., 2013). The two southerly segments of the Chilean megathrust from ~35°S to 46°S are defined by recent earthquakes in 1960 (Valdivia segment) and 2010 (Concepcion segment). The Valdivia seismic segment extends from the Arauco Peninsula in the north to Taitao Peninsula in the south, terminating at the Chilean triple junction (Merron and Hayes, 1969) where younger oceanic lithosphere presents, and high heat flow is observed to the south (e.g., Cande et al., 1987, Tichelaar and Ruff, 1991, Oleskevich et al., 1999). The northern limit of the Valdivia and southern limit of the Maule segments overlap in the Arauco-Nahuelbuta region at 37–38°S (Figure 2.3). It is suggested that this overlap may stem from the occurrence of continental basement discontinuities (Melnick et al., 2009); relief of the underthrusting Nazca plate (Sparkes et al., 2010; Moreno et al., 2011) and splay fault that bring about permanent shortening in upper plate (Moreno et al., 2012). Furthermore, seismotectonic behaviour of the subduction interface of the megathrust is thermally controlled within these segments (Völker et al., 2011). Multi-disciplinary datasets that explored coastal deformation at Arauco Peninsula (37.1–38.5°S) at various timescales suggests that the Valdivia segment has been active since the early Pleistocene (Melnick et al., 2009). Also, postseismic deformation is still occurring after the 1960 Mw 9.5 earthquake (Hu et al., 2004, Wang et al., 2007).

2.2.1.5 Coupling related to subduction zone earthquake occurrence

Seismic coupled zones (seismogenic zones) occur between subduction oceanic lithosphere and overriding convergent plates which is contingent upon a multiplicity of factors at subduction zones. This coupling is associated with age of the slabs, asperities, seamounts, fracture zones, slab geometry and thermal settings and

hydrated mantle wedge that cause locking between plates and trigger and promote seismic events (e.g Vlaar and Wortel, 1976, Ruff and Kanamori, 1983, Van Den Beukel and Wortel, 1988, Taylor et al., 1987, Tichelaar and Ruff, 1993, Oleskevich et al., 1999, Gutscher et al., 2000, Robinson et al., 2006, Melnick et al., 2009, Contreras-Reyes and Carrizo, 2011). Earlier models indicate that the Chilean subduction zone is strongly coupled and capable of generating megathrust earthquakes along its entire length (e.g., Plafker, 1972, Barrientos and Ward, 1990, Tichelaar and Ruff, 1991). Moreover, kinematic models using GPS measurements suggest the megathrust interface shows heterogeneity and highly coupled segmentation at various rates. (Moreno et al., 2011, Métois et al., 2012). The spatial distribution of earthquakes occurring on this sector of the megathrust extends from Arauco Peninsula to the triple junction in south-central Chile. Therefore, seismic coupling is one of the most significant reasons for the numerous significant large subduction zone earthquakes that have taken place along the Valdivia seismic segment in the past.

2.3 Major subduction zone earthquakes and tsunamis in south-central Chile

Historical accounts of the shaking, deformation and tsunami occurrence along the Chilean subduction zone go back to the mid-1500s, and document the existence of destructive earthquakes and accompanying tsunamis (Lomnitz, 1970, Lomnitz, 2004, Cisternas et al., 2005) (Figure 2.3). This section focuses on the Valdivia segment of the Chilean megathrust, in which written records document four major ruptures in 1960, 1837, 1737 and 1575. Together with historical records and considering the 1960 event, the recurrence interval is suggested as 128 ± 62 years (Nishenko, 1985). However, many studies demonstrate variability in rupture mode (Cifuentes, 1989, Stein et al., 1986, Barrientos and Ward, 1990, Cisternas et al., 2005), and the average recurrence interval for full 1960 style ruptures calculated from longer sedimentary records is 270-280 years (Moernaut et al., 2014, Garrett et al., 2015). This highlights the importance of analysing historical and sedimentary records in tandem for seismic hazard assessment.

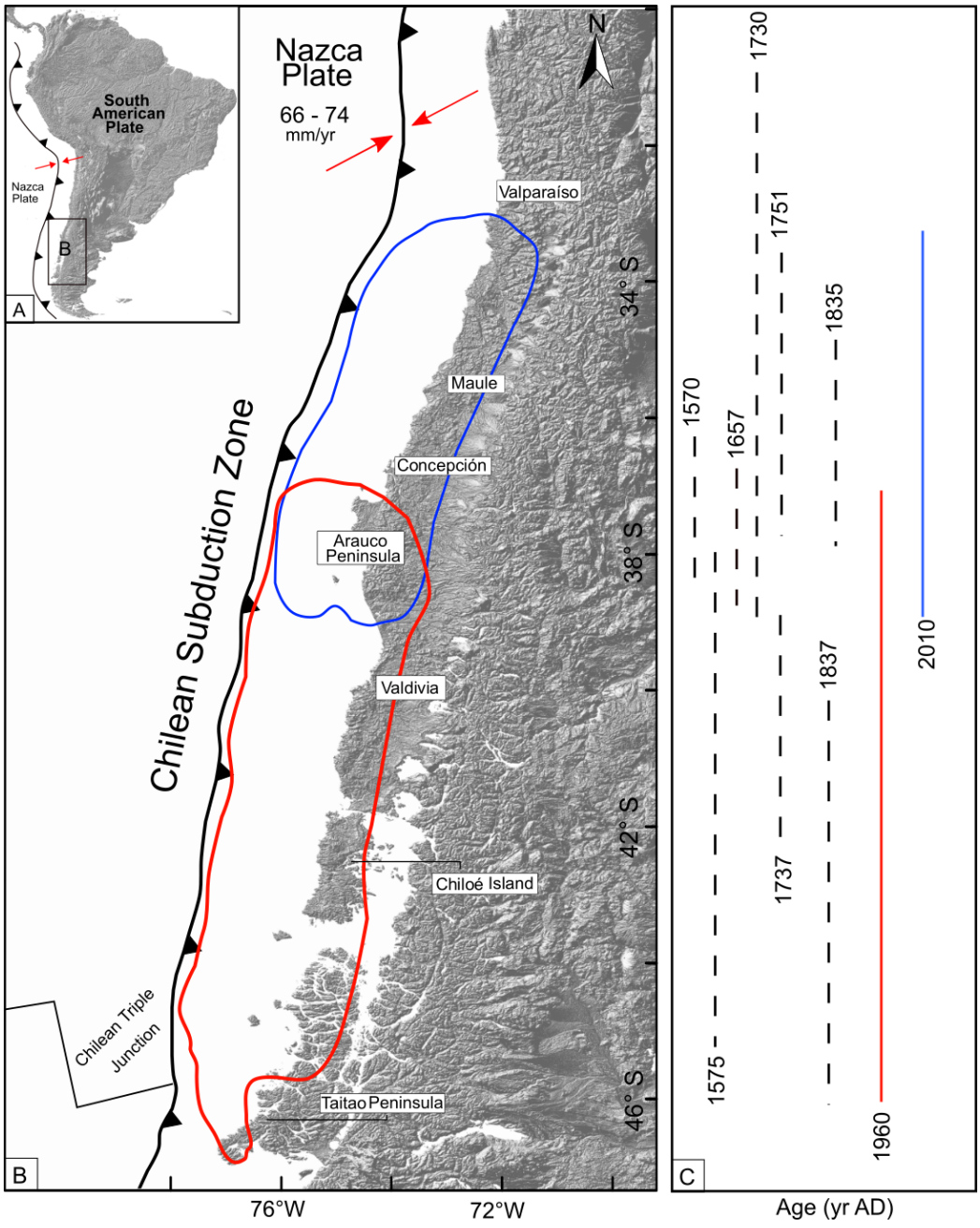

Figure 2.3 : Index Maps. A) Inset map shows the location of subduction zone (rectangle with bold lines) and convergence margin. B) Presents the area of the rupture zones for both the 1960 M_w 9.5 and the 2010 M_w 8.8 earthquakes compiled after Plafker and Savage, (1970) and Moreno et al., (2012). C) Historical and instrumental records of the rupture extents for megathrust earthquakes of the past 500 years in south-central Chile. The barbed line for the subduction zone; dashed lines show rupture extents estimated from historical records and solid lines show instrumentally recorded earthquakes (compiled from Lomnitz, 2004; Cisternas et al., 2005; Ely et al., 2014). DEM data is from Amante and Eakins (2009).

2.3.1 The 1960 great Chilean earthquake

The great 1960 earthquake ruptured a ~1000 km length of the Chilean megathrust between 37.5°S and 46°S (Benioff et al., 1961, Plafker and Savage, 1970, Cifuentes, 1989, Barrientos and Ward, 1990, Moreno et al., 2009) (Figure 1.4). Four foreshocks exceeding M_w 8.0 (Cifuentes, 1989) occurred on 21-22 May 1960, before the M_w 9.5 main shock on 22 May 1960 (Kanamori, 1977) that initiated where the Mocha Fracture Zone subducts beneath the South American Plate, followed by a M_w 7.9 aftershock (Engdahl and Villasenor, 2002). The energy released by the main shock of this earthquake is still the largest seismic event ever recorded in instrumental history. Estimates for the width of the rupture range between 125 and 150 km (Cifuentes, 1989, Völker et al., 2011). Nucleation of the earthquake initiated at the Arauco peninsula where the Mocha fracture zone occurs (Cifuentes, 1989). There, the age of the incoming oceanic plate is older (~30 Ma) and denser than southward of the rupture zone (Tebbens et al., 1997, Völker et al., 2011). It was a shallow-intermediate depth rupture at 30 - 55 km (Cifuentes, 1989; Barrientos and Ward, 1990; Engdahl and Villasenor, 2002; Lange et al., 2007; Moreno et al., 2009), with slip on the fault averaging 20-30 m (Plafker, 1972, Plafker and Savage, 1970, Cifuentes, 1989) and reaching a local maximum of 40 m at Valdivia (Barrientos and Ward, 1990, Moreno et al., 2009).

Extensive observations of coseismic land-level change in 1960 suggest the great earthquake caused sudden subsidence of up to 2 m, with maximum subsidence of 2.7 m near the city of Valdivia and maximum uplift of 5.7 ± 0.2 m offshore from Isla Guamblín (Figure 1.4). An area of at least 130,000 km^2 was affected by vertical coseismic deformation (Plafker and Savage, 1970). The uplifted sea floor created a large and destructive tsunami, with a crest up to 10-15 m high in Chile (Sievers et al., 1963, Davis and Karzulovíc, 1963, Plafker and Savage, 1970), 10 m in Hawaii (Eaton et al., 1961) and 6 m in Japan (Watanabe, 1998). It resulted in the deaths of over 1,000 people in Chile, 61 people in Hawaii and 142 people in Japan (Cisternas et al., 2005, Atwater et al., 2005a, Satake and Atwater, 2007). In addition, the earthquake also produced a large mass-wasting event that blocked the outflow of Lago Riñihue, resulting in the water level of the lake rising 26.5 m and jeopardising vicinities (Davis and Karzulovíc, 1963).

Geological evidence for the 1960 earthquake and accompanying tsunami comes from tidal marsh sediments at Tirúa river estuary (Ely et al., 2014, Dura et al., 2017) and Quidico (Hong et al., 2017) in the north, turbidite records from three inland lakes

Calafquén, Riñihue and Villarica in the Valdivia region (Moernaut et al., 2014), tidal marsh sediments at Maullín (Cisternas et al., 2005) and Caulle (Atwater et al., 2013) to the south; a coastal outcrop at Cocotué (Cisternas et al., 2017b); and from tidal marsh sediments at Chucalén (Garrett et al., 2015) in the northwest of Isla de Chiloé, and turbidite records of tsunami in coastal lakes Cucao and Huelde on the west coast of Isla de Chiloé (42.6°S) (Kempf et al., 2015).

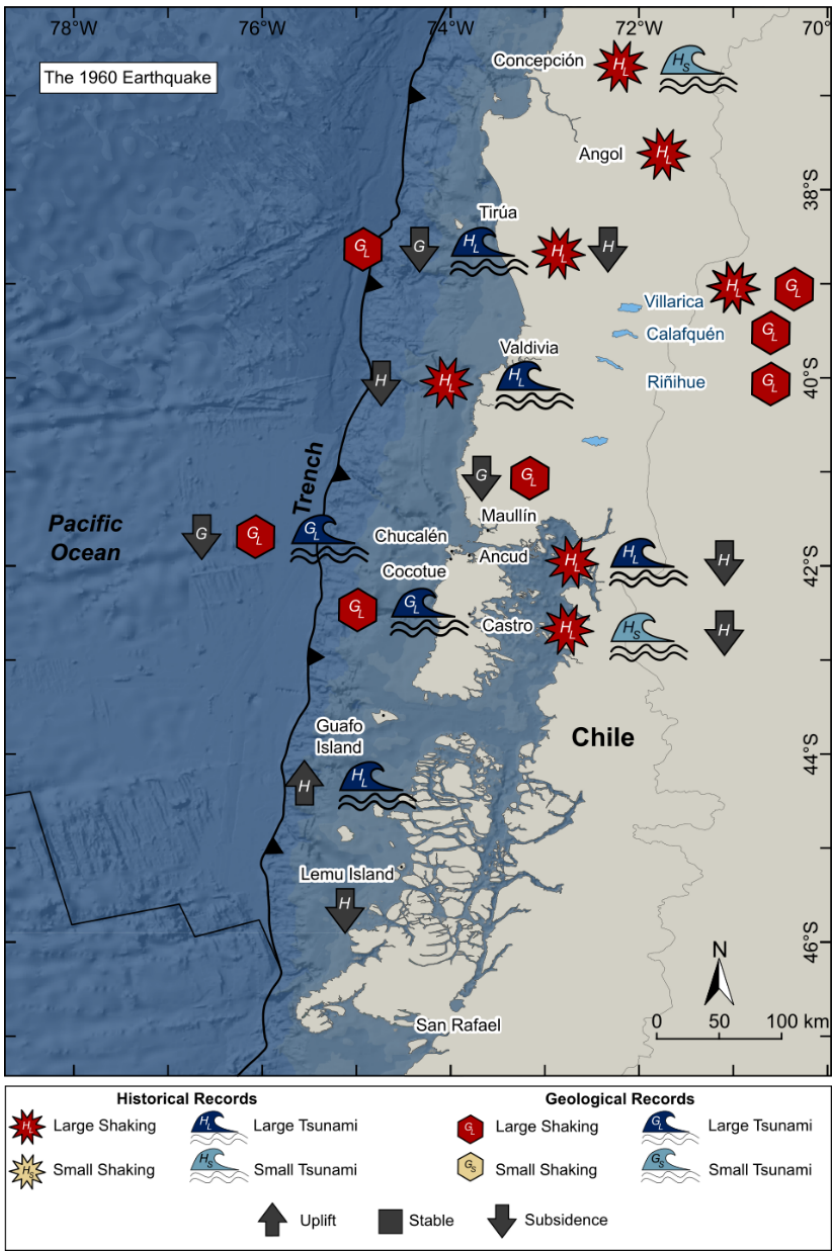

Figure 2.4: Historical (H) and geological (G) evidence for the M_w 9.5 1960 earthquake and accompanying tsunami along the Valdivia segment (Plafker and Savage, 1970, Cisternas et al., 2005, 2017b, Ely et al., 2014, Moernaut et al., 2014, Garrett et al., 2015, Kempf et al., 2017). World Ocean Basemap: ESRI.

Observational data originate from three different sources as addressed by Plafker and Savage (1970): 1) measured difference between pre- and post-earthquake position of extreme tides as indicated by local residents; 2) measured difference between lower growth limit of pre- and post-earthquake terrestrial vegetation; 3) measured difference between upper growth limit of pre- and post-earthquake mussels. In contrast, quantitative geological records arise from certain application by establishing statistically robust and a specific relationship between diatoms and tidal elevation to generate reconstruction models (e.g., Juggins and Birks, 2012).

2.3.2 The 1837 earthquake

The 1837 CE earthquake struck many coastal sites from Concepción in the north to Castro on Isla de Chiloé in the south (Figure 2.5). The occurrence of many landslides, as well as ~2.4 m uplift to the north on Lemu Island was documented (Darwin, 1851, Lomnitz, 2004). Also, this event was accompanied by a tsunami up to 6 m high in Hilo Hawaii, also reaching and damaging Samoa and Japan (Abe, 1979, Watanabe, 1998, Lomnitz, 2004). Based on observations of land-level change and extent of shaking, the area effected by the 1837 CE earthquake has been delimited to the southern part of the Valdivia segment (Cisternas et al., 2017b). There were no traces of a tsunami or coseismic deformation associated with the 1837 earthquake preserved in the Maullín estuary or Chucalén outcrop (Cisternas et al., 2005, Garrett et al., 2015). Even though there was not any evidence for this event in Lago Puyehue, turbidite records from glacigenic lakes Lago Villarrica, Calafquén, and Riñihue, ~120 km north of Lago Puyehue indicate seismic activity in 1837 CE (Moernaut et al., 2014). Moreover, sediments of Reloncavi Fjord shows anomalous thickness of turbidites, geochemistry such as Fe content, allowing the differentiation of terrestrial sources of sediments, and fining upward grading related to the 1837 CE earthquake (St-Onge et al., 2012) (Figure 2.5). The fact that the 1837 event, for which historical records exist, is not preserved in tidal marsh sediments, and only preserved in lacustrine and fjord sediments, requires further investigation.

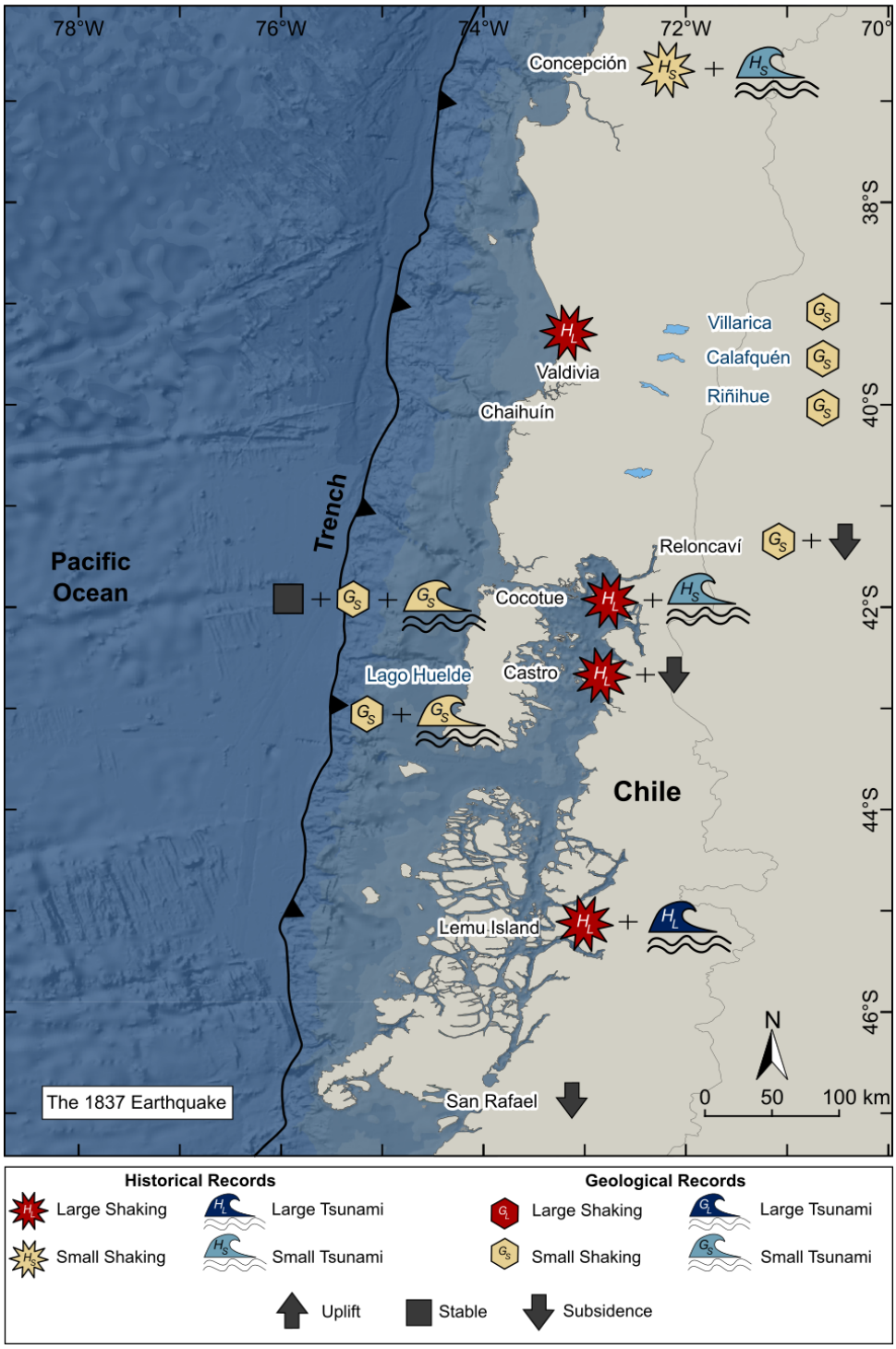

Figure 2.5 : Historical (H) and geological (G) evidence for the 1837 CE earthquake and accompanying tsunami along the Valdivia segment. Geological records are compiled from St-Onge et al., (2012), Moernaut et al., (2014), Kempf et al., (2017), Cisternas et al., (2017a) and historical records from Lomnitz (2004; 1970), Cisternas et al., (2005; 2017b). World Ocean Basemap: ESRI.

2.3.3 The 1737 earthquake

Historical records indicate that the 1737 CE earthquake caused shaking along a ~500 km section of the Valdivia segment, extending from Isla Chiloé to Valdivia (Figure 2.6). However, unlike the 1960 earthquake, previous studies based on historical and geological records have found no evidence to suggest the occurrence of a tsunami associated with this event (Lomnitz, 1970, 2004; Atwater et al., 2005b; Cisternas et al., 2005, 2017a)

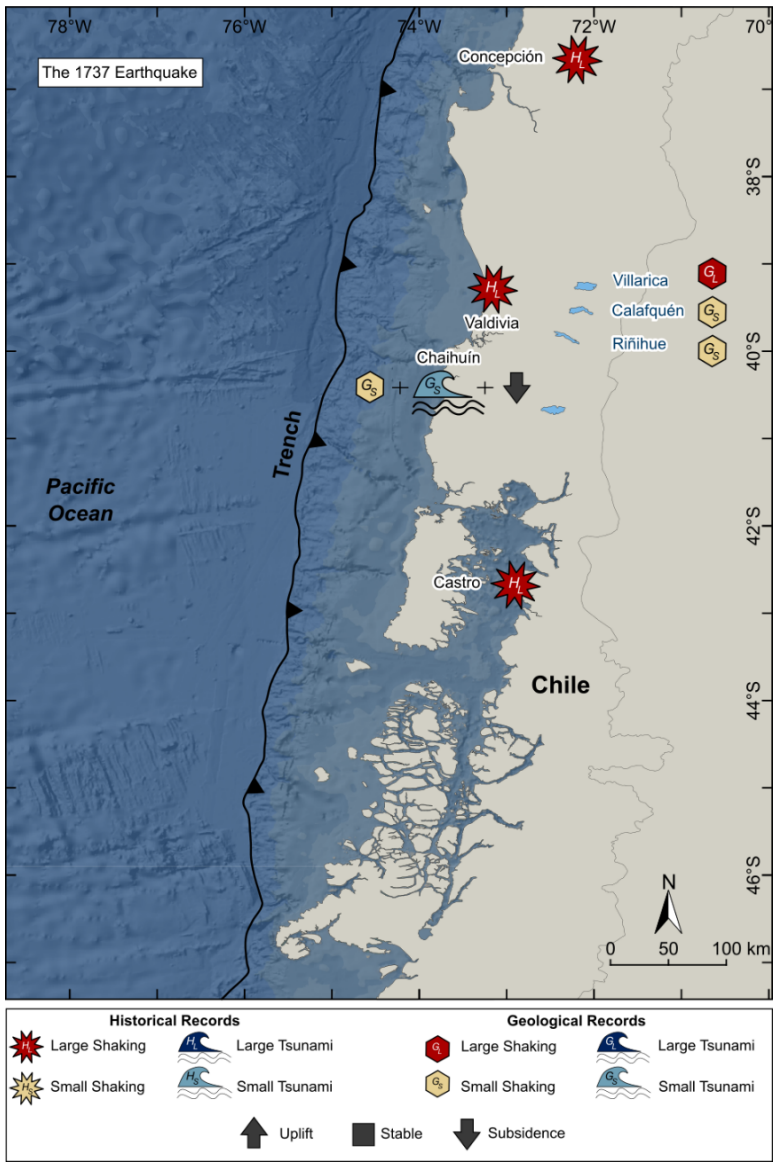

Figure 2.6 : Historical (H) and geological (G) evidence for the 1737 CE earthquake and accompanying tsunami along the Valdivia segment. Geological records are compiled from (Hocking et al., 2021; Moernaut et al., 2014) and historical records from (Lomnitz, 2004; 1970; Cisternas et al., 2005; 2017a). World Ocean Basemap: ESRI.

Turbidite deposits from Lago Villarrica, Calafquén, and Riñihue are inferred to have been induced by shaking during the 1737 CE earthquake (Moernaut et al., 2014). Yet any evidence for that earthquake and tsunami was not found in the sedimentary record at Maullín or Chucalén (41.38°S - 41.51°S) (Cisternas et al., 2005, Garrett et al., 2015); nor in mass-wasting deposits in Lago Puyehue (Moernaut et al., 2007) or turbidite records from Reloncavi Fjord (41.42°S) (St-Onge et al., 2012). On the basis of turbidite thickness and spatial extent of evidence, it has been suggested that the 1737 CE event was a modest event in terms of magnitude (Moernaut et al., 2014). However, the coastal sedimentary record from the Chaihuín estuary (39.56°S), 30 km southwest of Valdivia, presents evidence for tsunami inundation and coseismic deformation associated with the 1737 CE earthquake (Hocking et al., 2021). Although Cisternas et al., (2017b) propose a deeper rupture, recent geological evidence reported by Hocking et al. (2021) suggests the opposite, indicating a shallower rupture than previously proposed. However, due to the apparent disagreement between historical records, sedimentary records, and rupture models, further investigation of evidence for this earthquake is required.

2.3.4 The 1575 earthquake

On 16th December 1575, a great seismic event caused major shaking extending from Castro on Isla Chiloé in the south to Concepción in the north and destroyed the outposts of Imperial, Valdivia, Villarrica, Osorno and Castroas (Lomnitz, 1970). Furthermore, landslides occurred in Riñihue Lake next to the Andean foothills, these landslides blocking the lake outflow then four months later a flood occurred and took over a thousand lives. Moreover, the accompanying tsunami caused thousands of deaths in the north of Valdivia (Lomnitz, 1970, 2004, Cisternas et al., 2005).

Historical and geological evidence suggest the 1575 CE earthquake was of similar magnitude to 1960 and also characterised by shallow offshore slip (Lomnitz, 1970, 2004, Cisternas et al., 2005, Plafker and Savage, 1970). Tidal marsh sediments at Tirúa, Maullín (Cisternas et al., 2005) and Chucalén (Garrett et al., 2015), turbidites in Reloncavi Fjord (St-Onge et al., 2012), lake sediments from Villarica, Calafquén, Riñihue (Moernaut et al., 2014), Puyehue (Moernaut et al., 2007) and Huelde (Kempf et al., 2017) and coastal lowland sediments at Cocotué record coseismic subsidence, shaking and/or tsunami inundation occurred in 1575 CE. However, geological findings indicate that the recurrence interval of such a 1960 style rupture is 270-280 years (Cisternas et al., 2005, 2017b, Moernaut et al., 2014, Garrett et al., 2015). Geological

records suggest that the 1960 and 1575 earthquakes were quite different to the 1737 and 1837 events (e.g., Cisternas et al., 2017b).

2.3.5 Prehistoric and undocumented earthquakes

In addition to historical earthquakes, the Valdivia segment of the subduction zone has also experienced large prehistoric earthquakes and tsunamis. As written records only extend back to the 16th century, the record for the older seismic events has been extended from evidence obtained from sedimentological records.

Previous studies report the presence of greater and lesser magnitude earthquakes over the last 1000 years (Cisternas et al., 2005, 2017b, Atwater et al., 2013, Moernaut et al., 2014, Garrett et al., 2015), including magnitude 9 > earthquakes in 1960 (event A), 1575 (event B), c. 1270 – 1450 CE (event C) and c. 898 – 1220 CE (event D), alongside smaller (likely magnitude > 7.5) events in 898 – 1308 CE (event cd), 1304 – 1470 CE (event bc1), 1505 – 1548 CE (event bc2), 1837 CE (event ab) and the 1737 CE (Cisternas et al., 2017b) (Figure 1.3). Due to the fact that they represent similar sedimentological features to the 1960 and 1575 earthquakes, the ruptures in c. 1270 – 1450 CE and c. 898 – 1220 CE have been named as events C and D, and relatively smaller earthquakes between these larger events are named cd, bc1, bc2 and ab (Cisternas et al., 2017b). Evidence for events C and D comes from Chucalén (Garrett et al., 2015) and Cocotué (Cisternas et al., 2017b) and turbidite deposits from Calafquén Lake (Moernaut et al., 2014). Geological evidence for event C has also been reported from the beach-ridge plain at Caulle (Atwater et al., 2013) and evidence of shaking in Riñihue Lake (Moernaut et al., 2014). Evidence of smaller events was found at Cocotué, Maullín, Calafquén and Riñihue (Cisternas et al., 2017b).

Combining both historical and sedimentological records indicates that subduction zone earthquakes reflect variable rupture modes and recurrence intervals. It is suggested that the average recurrence interval for the smaller earthquakes is ~ 85 yr while this interval is ~ 300 yr for the large earthquakes (Cisternas et al., 2017b).

2.3.6 Knowledge gaps

Although recent studies have provided valuable insights into the extent of rupture and slip distribution during the 1960 earthquake, our knowledge regarding pre-1960 earthquakes remains relatively limited. In comparison to the well-documented 1960 event, our understanding of the 1737 CE and 1837 CE earthquakes is relatively sparse, and there are inconsistencies between historical records and sedimentary

evidence regarding the 1737 CE earthquake. Additionally, there is a spatial gap in the Valdivia segment from the Arauco Peninsula to Isla de Chiloé (37.2°S - 41.5°S) where limited evidence of pre-1960 earthquakes has been reported.

The available data suggests that the great Chilean 1960 earthquake of M_w 9.5 is relatively well known in terms of rupture length and coseismic deformation in comparison with its predecessors (Plafker and Savage, 1970, Plafker, 1972, Barrientos and Ward, 1990, Moreno et al., 2009). Furthermore, models suggest that the width of plate-boundary fault rupture for this event is about ~140 km (Cifuentes, 1989, Völker et al., 2011). However, the spatial distribution of coseismic deformation for its inland boundary from the 1960 earthquake has not been obtained by any geological finding. Thus, further research is required to accurately constrain the morphological response at the coastal sites located inland, which could provide valuable information for more precise reconstructions of the deformation patterns associated with the 1960 Mw 9.5 earthquake and its predecessors in south-central Chile.

2.4 Relative sea-level change and deglaciation since the last glacial maximum

Relative sea-level (RSL) is the position of the sea surface relative to the base level at a given location (Khan et al., 2015, Harff, 2016). Changes in relative sea level result from vertical movements of the ocean's surface (due to factors such as eustasy and stereodynamics i.e., ocean's circulation, temperature and saltiness) or changes in the land level (due to isostasy, tectonic vertical crustal movements and local effects) and local factors (e.g., tidal regime change and sediment consolidation) (Farrell and Clark, 1976, Clark et al., 1978, Pirazzoli, 1991, Shennan and Horton, 2002, Mitrovica and Milne, 2002, Peltier, 1998a; 1998b; 2004, Törnqvist et al., 2008, Peltier et al., 2015).

The equation below addresses change in relative sea-level (ΔRSL) at a given geographical location (φ) and time (t) (Shennan and Horton, 2002, Shennan et al., 2012).

$$\Delta RSL\ (\varphi, t) = \Delta EUS(\varphi, t) + \Delta ISO(\varphi, t) + \Delta TEC(\varphi, t) + \Delta LOCAL(\varphi, t) + \Delta UNSP(\varphi, t) \quad \text{Eq. (2.1)}$$

Where ΔEUS(φ, t) is the time and space-dependant eustatic function (originally expressed astime-dependent only), ΔISO(φ, t) is the total isostatic effect of the glacial rebound process including the ice load (glacio-isostatic), water load (hydro-isostatic) and rotational contributions to the redistribution of ocean mass; ΔTEC(φ, t) is the

tectonic effect; ΔLOCAL(φ, t) is the total effect of local processes, including tidal regime changes and post-deposition sediment consolidation; ΔUNSP(φ, t) is the sum of unspecified factors, either not quantified or not thought of (Shennan et al., 2012).

One of the most important drivers of global sea level is the growth and decay of land-based ice sheets (Fleming et al., 1998, Yokoyama et al., 2000, Lambeck et al., 2002a) inducing glacio-isostatic adjustment (GIA) which leads to changes in the coastline (Peltier and Andrews, 1976, Clark et al., 1978, Peltier, 1998a; 1998b; 1999). This important factor is a physical process describing the Earth-ocean response to changes in ice sheets during glacial cycles since RSL change emanates from mantle relaxation and rebound of plates associated with decay of glaciers following climate change (Peltier, 1998; 1998b; 2004). The magnitude of RSL change evidently varies due to GIA processes among near-, intermediate, and far-field regions (Fleming et al., 1998, Peltier, 1998, Khan et al., 2015). In near-field regions (those areas located beneath and occupying sites of former land-based ice sheets), the RSL signal is dominated by GIA, whilst in intermediate-field regions (at increased distance from the centre of former continental ice sheets), the contribution of GIA remains relatively traceable, but its magnitude is considerably reduced. As we move farther away to regions distant from major ice sheets, in far-field regions, the eustatic contribution dominates RSL change (Clark et al., 1978, Quinlan and Beaumont, 1981, Fleming et al., 1998, Peltier, 1998a, 1999; 2002, Peltier and Fairbanks, 2006, Milne et al., 2002, Milne et al., 2005, Yokoyama et al., 2000, Lambeck et al., 2002b, Shaw et al., 2002).

The weight of glaciers and ice sheets cause deformation of the Earth's crust through both adding and removing ice mass. The rate of deformation varies depending on the earth's rheology, thickness of the lithosphere and the glacial history providing the thickness and geometry of ice load (Peltier and Andrews, 1976, Peltier, 1998a; 1998b; 2004, Mitrovica and Peltier, 1991b). After reaching their maximum extent, due to both millennial and centennial climate oscillations, ice sheets globally have started waning (Clark et al., 2009 and references therein). As the distribution of ice sheets and their mass loads and properties the Earth's surface is not homogeneous, RSL change related to the global melting of ice sheets does not demonstrate uniform behaviour (e.g., Clark et al., 1978, Mitrovica and Peltier, 1991b, Lambeck et al., 1998). Accordingly, GIA exhibits a spatially variable response (Lambeck et al., 1998, Peltier and Fairbanks, 2006, Peltier et al., 2015). The response of removal of a mass of ice, which causes downwarping of the Earth's crust during glacial periods, is an adjustment of the crust by rebounding upward that sector covered by glaciers as well

as RSL change associated with the process (Peltier, 1998a, b, 1999, 2004; Peltier et al., 2015). One of the predominant effects of advancing and retreating glaciers is to bring about rise and fall of RSL following these events (Peltier, 1999).

2.4.1 Glacial history in Chile

Owing to its large longitudinal extent, Chile lies across several climatic zones (from subpolar to warm), the country displays one of the most variable glacial and climate change histories (McCulloch et al., 2000). Today, ice coverage in the Los Lagos region is characterised by Alpine type glaciation (glaciers confined to mountain valleys), while in southern Chile, ice fields in Patagonia reflects Piedmont style glaciation (glacier spread out in lowlands and flat plains at the base of mountains) (e.g., Caldenius, 1932, Hollin and Schilling, 1981, Porter, 1981, Hulton et al., 2002).

During the last glaciation, which is termed the Llanquihue Glaciation, it is suggested that the continuous Patagonian Ice Sheet formed and encompassed 38°S – 56°S (Caldenius, 1932, Porter, 1981, Denton et al., 1999, Rabassa and Clapperton, 1990, Hollin and Schilling, 1981, Hulton et al., 2002, Glasser et al., 2008). It is suggested that when the ice sheet reached its maximum extent it only covered the southern half of Isla de Chiloé based on well preserved moraine and outwash plains (Figure 2.7) (Heusser and Flint, 1977, Denton et al., 1999, Hulton et al., 2002, García, 2012). As we move to the south the Patagonian regions, both mainland and islands in the Pacific Ocean were mantled by the ice sheet. The estimated volume of this relatively large ice sheet was reported as corresponding to 1.2 m of global sea level contribution (Hulton et al., 2002). Between 17.5 and 17.15 ka BP, it is reported that Patagonian piedmont glaciers melted quickly due to warming temperatures (Denton et al., 1999, McCulloch et al., 2000) and models suggest that the ice sheet lost 20% of its Last Glacial Maximum (LGM) volume within 2000 years (Hulton et al., 2002). Remnants of LGM ice were reported in the north, with geomorphological and palaeoecological data collected from the Chilean Lake District at 41°S (Figure 2.7) presenting evidence for five stage ice advances between 36 ka and 18 ka BP (Mercer, 1970, Denton et al., 1999). The last three advances of the Lago Llanquihue glacier were identified by examining end moraines and associated outwash plains sometime before 20 ka, between 20-19 ka BP and 15-13 ka BP and a younger event respectively in the Lake District (Porter, 1981). This cold period was followed by a relatively warm period between 13.5 ka BP and 4 ka BP (Heusser and Streeter, 1980, Rabassa and Clapperton, 1990). However, this relative warmer period was followed by Neoglacial ice field expansion due to an increase in precipitation and cold climate regime in the

late Holocene (Glasser et al., 2004, Bertrand et al., 2012). Three or four periods of glacier advance occurred, in addition to the Little Ice Age (Mercer, 1970, Aniya, 1996, Araneda et al., 2007). Today, the Patagonian icefields only extend between 47°S and 51°S, with the smaller Cordillera Darwin icefields around 54°S (Rignot et al., 2003). According to models, the contribution to global sea-level rise of ice loss from the Patagonia icefields since 1870 has averaged 0.0052 ± 0.0008 mm/yr (Glasser et al., 2011); however, this estimate has been refined and shows increased contributions of 0.067 ± 0.004 mm/yr between 2000 and 2012 (Willis et al., 2012).

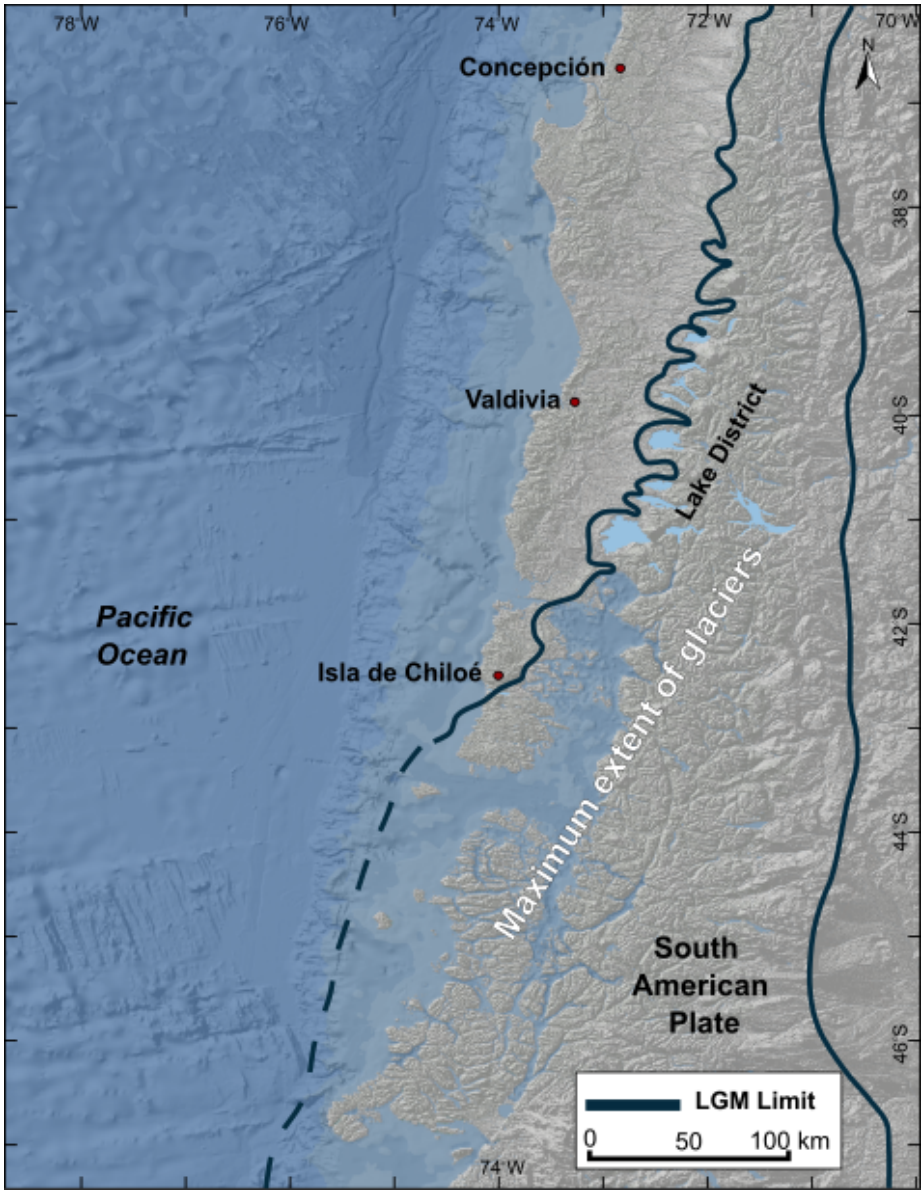

Figure 2.7 : Maximum ice extent during the LGM in south-central Chile (compiled from Porter, 1981, Hollin and Schilling, 1981, McCulloch et al., 2000, Hulton et al., 2002). DEM data is based on the ETOPO1 from Amante and Eakins (2009). World Ocean Basemap: ESRI.

2.4.2 Holocene relative sea-level change in south-central Chile since the Last Glacial Maximum

The Last Glacial Maximum occurred around 26,000 – 18,000 years ago and estimated eustatic sea-level was 120 – 125 m below present (Yokoyama et al., 2000, Peltier, 2002, 2006, Clark et al., 2009). Following the LGM, major land-based ice sheets located in the northern hemisphere have melted and led to a rise in global sea level (eustatic) (Khan et al., 2019 and references therein). The main causes of eustatic sea level rise are not only limited to decay of glaciers and ice sheets but also associated with thermal expansion of ocean water (Wigley and Raper, 1987, Khan et al., 2015, Widlansky et al., 2020) which is still ongoing today (e.g., Frederikse et al., 2020). However, there has been significant spatial variation in RSL change particularly during the Holocene (Pirazzoli, 1991, Mitrovica and Milne, 2002, Garrett et al., 2020, Khan et al., 2015). Investigation into RSL change along both Atlantic and Pacific coastal sites of South America highlight spatiotemporal variation (Milne et al., 2005, Garrett et al., 2020). It is suggested that relatively rapid and uniform sea-level rise has been occurring in the Caribbean since the early Holocene (rising at rates of 7-8 mm/yr and 5 mm/yr before and after 7 ka BP respectively) (Nakada and Lambeck, 1988, Fleming et al., 1998, Milne et al., 2005), whilst data from Suriname, Brazil and southernmost South America indicate falling RSL change from a mid-Holocene highstand (Milne et al., 2005 and references therein). The rise of RSL to the highstand and subsequent fall in these regions attributed to continuous GIA processes by both hydroisostatic (continental levering*)* and glacioisostatic loading of the Earth's surface also termed as equatorial ocean syphoning (Mitrovica and Peltier, 1991a, Mitrovica and Milne, 2002).

In addition to GIA models, former positions of relative sea level can be obtained by a variety of proxies. Sea-level index points (SLIP) provide estimates for former sea level based on the former position of RSL at specific space and time. These include terrestrial and marine limiting points, which constrain the upper and lower positions of relative sea level at a given point in space and time. Also, the term indicative meaning refers to the relationship between a sea level indicator and modern tidal levels (Van de Plassche, 1986, Shennan et al., 2015, Khan et al., 2019, Garrett et al., 2020).

Recently, Garrett et al. (2020) has compiled a history of RSL changes in Chile throughout the Holocene, using a range of different data sources from a variety of studies, encompassing 11 coastal regions from along the tectonically active coast of north, central and south-central Chile (18.5°S – 43.6°S). Most of the sea level data is

obtained from central and south-central Chile since data for northern Chile is limited. This database suggests a significant spatial variation in regional RSL histories during the Holocene along the Chilean coast. It also constrains RSL which was higher than present elevation and RSL fall since the mid-Holocene to between <5 m and 30 m (Garrett et al. 2020). Furthermore, the height of RSL for the mid-Holocene highstand and its timing are still imprecise since GIA and reconstructions from coastal proxies present varying ranges in the Valdivia region (6 m to 2 m) and the Chacao Channel (0.5 m to 0.7 m) (for further detail see Garrett et al., 2020). The sections below only discuss evidence for the RSL records based on accepted sea-level data by Garrett et al., (2020) along coastal sites in south-central Chile.

Accepted sea-level data from near the northern limit of the Valdivia seismic segment were produced from Isla Santa Maria (37°1.7'S, 73°31'W) and Tubul (37°13'S, 73°26'W) as four basal index points and one limiting point (Bookhagen et al., 2006, Garrett et al., 2020). Four index points constrain the RSL history between 3.11 m and 5.21 m with large vertical uncertainties of ±1.6 m between c. 2.4 and c. 1.8 ka BP and a marine limiting point from Tubul indicating sea level above 2.57 m at c. 5 ka BP (Figure 2.8) (Garrett et al., 2020, Region 5).

Ten index, nine marine limiting and eight terrestrial limiting points provide the RSL record for the Southern Bío Bío region (Stefer et al., 2010, Garrett et al., 2020, Region 6). The oldest index points that were generated from clastic sediments containing marine shells and foraminifera place RSL between -22 m and -47 m between 8 to 11 ka BP. Within the last 1.9 ka, the dated organic sediments from Quidico and Tirúa indicate RSL between - 0.6 m and 0.4 m from accepted 21 sea-level data (Ely et al., 2014, Dura et al., 2017, Hong et al., 2017, Garrett et al., 2020).

The RSL record for Isla Mocha was constrained by ten index points, which comprises basal samples, and a single marine limiting point at Punta Pájaros Niños (38°19'S, 73°57'W) (Nelson and Manley, 1992, Kaizuka et al., 1973, Garrett et al., 2020). The accepted sea-level data suggest that between c. 6 ka BP and 2.5 ka BP RSL was between ~30 m and ~23 m above present, followed by a decline to 5 m above present at c. 0.9 ka BP (Garrett et al., 2020, Region 7). This is based on two accepted marine limiting points which were collected at Bahía Hualaihué (42°1.5'S, 72°41'W) on the northeast of Chiloé that place RSL at1.90 – 2.90 m above present at 418 cal a BP (Hervé and Ota, 1993). The last accepted records for RSL change come marine deposit from Cucao, on the western coast of Chiloé which constrain RSL to 1.89 m above present at 325 cal a BP (Hervé and Ota, 1993). The subsequent sections (2.4.2

and 2.4.3) introduce the current evidence for RSL during the Holocene particularly the regions of interest where study sites are located in the Valdivia region and the Chacao Channel.

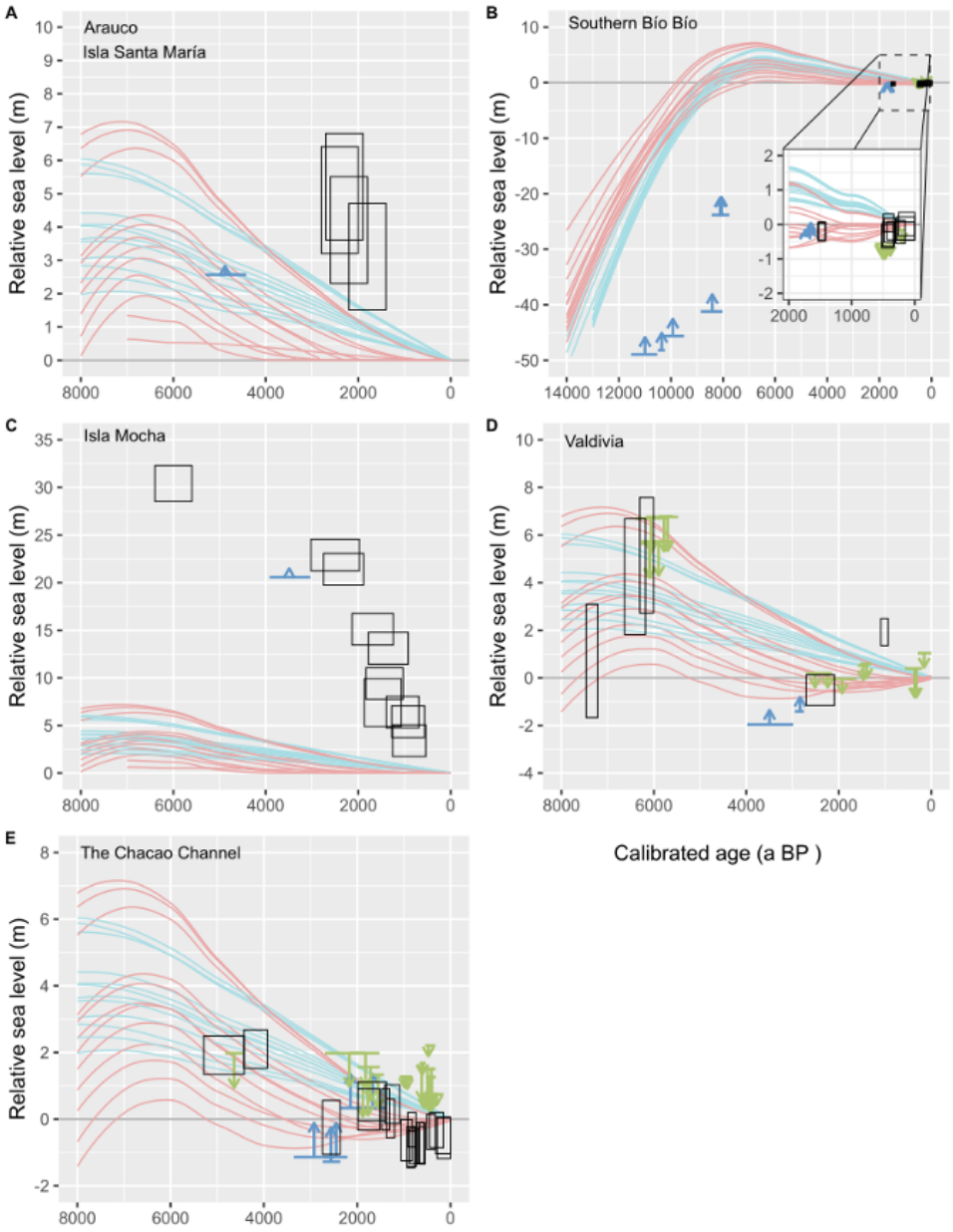

Figure 2.8 : Regional RSL change in south-central Chile, showing comparison of sea-level data points with glacial isostatic adjustment (GIA) model predictions based on Peltier, (2004) and Peltier et al., (2015). The sea-level index points are represented by black rectangles, while the green T-shaped and blue ⊥-shaped symbols indicate terrestrial and marine limiting points, respectively. The GIA prediction models are displayed as light blue and pink curves for ICE_5G and ICE_6G, respectively. The lithospheric thickness and upper mantle viscosity are varied between 71 and 120 km and 5 x 10^{19} Pa s and 2 x 10^{20} Pa s for both ice models (data from Garrett et al., 2020).

RSL data from the Valdivia region are relatively limited, consisting of five index, two marine limiting and fourteen terrestrial limiting points (Garrett et al., 2020, Region 8). The oldest record was collected from a sand deposit containing shell fragments which indicates a beach environment as an index point at Isla Mancera (Villalobos Silva, 2005). The age of this deposit corresponds to c. 7.3 ka BP where RSL ranges from -1.7 to 3.1 m and the indicative meaning covers between mean lower low water (MLLW) and highest astronomical tide (HAT) + 3 m (Garrett et al., 2020). Index and terrestrial points were also generated from beach sediments and dunes at Chan-Chan. Dates from these sediments constrain RSL to between 1.8 and 7.6 m at c. 6 ka BP (Pino and Navarro, 2005). Index and marine limiting points from sediment collected at Las Coloradas inlet and terrestrial limiting points from Isla Mancera indicate RSL was ~1-2 m above present at c. 3.5 ka BP (Villalobos Silva, 2005, Nelson et al., 2009). The most recent index point was reported from a landward edge of the modern beach exposure at Pilolcura beach, suggesting RSL was 1.92 ± 0.57 m around 1 ka BP (with depositional elevation ranges from mean tide level (MTL) to HAT) (Garrett et al., 2020).

The Chacao Channel is located between the northern coast of Isla de Chiloé and the vicinity of Rio Maullín (Garrett et al., 2020, Region 9). This region includes the study site of San Antonio. This region provides a relatively high number of sea-level index points comprised of 26 index, 5 marine limiting and 19 terrestrial limiting points obtained from paleoseismic studies of coastal sites at Chocoi, Dadi, Puente Cariquilda, Maullín, Chucalén, and Cocotué (Atwater et al., 1992, Cisternas et al., 2005, 2017b, Garrett et al., 2015). The oldest RSL record from a tidal marsh peat layer at Chocoi, c. 18 km southwest of Río Maullín, places the mid-Holocene highstand c. 2 m above present between c. 5 and 4 ka BP (Atwater et al., 1992). Six points which were generated from tidal marsh deposits from Dadi, Puente Cariquilda (Atwater et al., 1992) and Maullín (Cisternas et al., 2005) constrain RSL between -1 and 1 m between 3 and 1 ka BP, suggesting a fall in RSL after the mid-Holocene highstand. Marine limiting points constrain sea level above -1.5 m at c. 3 ka BP, while terrestrial limiting points indicate RSL stood 0.35 m below present at c. 2 ka BP. For the last 1 ka, terrestrial limiting points from Maullín and Cocotué suggest the elevation of sea level ranged from 2.3 m to 0.7 m (Cisternas et al., 2005, Cisternas et al., 2017b). Studies investigating palaeoseismic evidence from tidal marsh sediments from Maullín and Chucalén provide six and twelve index points respectively (Cisternas et al., 2005, Garrett et al., 2015). Findings from these studies place RSL ~1 m below present at 0.9 ka BP. Both sedimentary and microfossil findings, however, suggest

rises in RSL associated with great subduction zone earthquakes causing inter and coseismic subsidence (Garrett et al., 2015).

2.4.3 Relative Sea-Level Change in Holocene and Subduction Zone Earthquakes

The history of RSL changes that were observed from a range of coastal evidence between 18.5°S – 43.6°S in south-central Chile incorporates a range of different types of sea-level indicators and suggests a high degree of spatial variability in the Holocene along the Chilean coastline (for further detail see Garrett et al., 2020). RSL reached its maximum of c. < 5 - 30 m above present in the mid-Holocene (Garrett et al., 2020) and has fallen thereafter due to dominant local GIA processes (Peltier, 2004, Peltier et al., 2015). However, it is also pointed out that the majority of the sea-level data covers only the last 2 ka (Garrett et al., 2020). Therefore, this led to obtaining a discrete record of the history of RSL changes related to subduction zone earthquakes.

Palaeoseismological studies have reported that sedimentary evidence for RSL change is preserved only in periods where gradual rise in RSL occurred before the mid-Holocene highstand and/or within the last 3 - 1 ka where possible since Chile is a far-field region due to its large distance from major northern hemisphere ice sheets (see Dura et al., 2016a). Moreover, it is suggested that RSL fall since the mid-Holocene highstand has negative effects on preservation of sediments due to erosional processes (Nelson et al., 2009, Nelson, 2013, Dura et al., 2016a) making RSL reconstruction challenging and evidence for prehistoric large subduction zone earthquakes is roughly available for the only last millennium. The issue is illustrated in Figure 2.9, where Nelson, (2013) presents a comparison between the Pacific Northwest and south-central Chile. This occurrence is probably due to the notable recovery that took place after multiple earthquakes, coupled with the gradual decline in RSL over the past 6,000 years, leading to the erosion and retreat of shorelines. Consequently, the coastal stratigraphy presents relatively limited and/or sedimentological evidence of prehistoric subduction zone earthquakes (Nelson et al., 2009, Nelson 2013, Dura et al., 2016a) since fall in RSL precludes to provide the required accommodation space for sediment deposition.

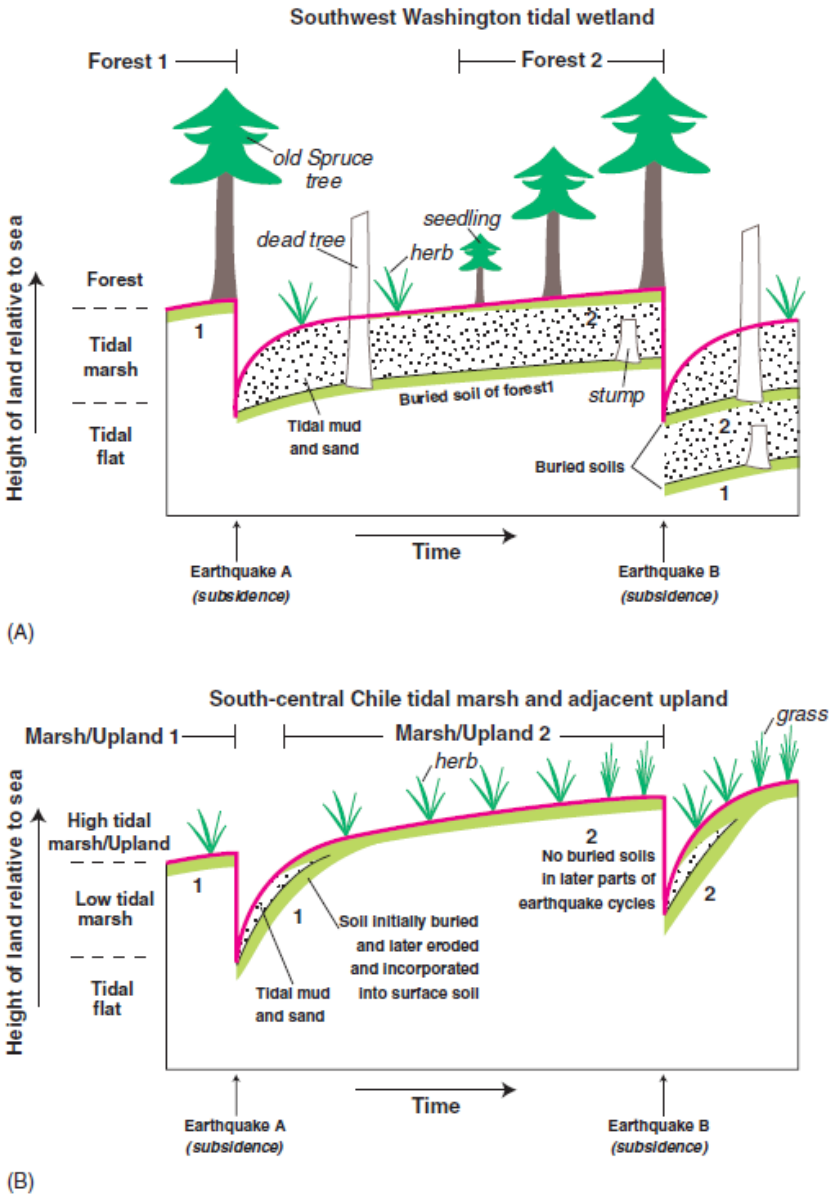

Figure 2.9 : Simplified models of land-level change in estuary tidal wetlands during two earthquake cycles above subduction zones of southwest Washington and south-central Chile. Heavy line shows inferred land-level change relative to sea level. A) Buried coastal forest and wetland soils (1 and 2) are quickly buried by many decimeters of tidal mud and sand following coseismic subsidence due to modest postseismic recovery and slowly rising sea level. B) similar subsidence, largely complete postseismic recovery, and slowly falling sea level result in minimal burial and later erosion of tidal marsh soils; buried soils are not preserved (same illustration from Nelson, 2013, Figure 15).

2.5 Field Sites

There are two main study areas, both situated within the Valdivia seismogenic segment of the Chilean subduction zone. Three main geological units occur within this sector of the subduction zone (36°S – 46°S) from the west to the east: the Coastal Cordillera, Central Valley, and Main Cordillera. The Coastal Cordillera consists of two metamorphic units recognised as a major discontinuity: the Eastern Series occurs to the north of 38ºS and the Western Series complex occurs to the south of 38ºS (e.g., Hervé et al., 1988). The Central Valley is a depression that presents young geologic features incorporating late Oligocene to Holocene deposits (Jordan et al. 2001, and references therein). The Main Cordillera comprises sedimentary, magmatic, metasedimentary, and volcanic rocks of Paleozoic to Holocene age (Glodny et al., 2006). The field sites are located in the Coastal Cordillera and Central Valley and are mantled by the late Holocene deposits.

The first field site San Antonio estuary (41.46°S) is located midway along the Valdivia seismic segment in the Central Valley; and the second focus is on six uplifted beaches (39.3°S – 39.5°S) situated in the northern sector of the Valdivia segment in the Coastal Cordillera. Field sites are sought to assess the litho- and bio- stratigraphic evidence for the 1960 earthquake at San Antonio estuary and pre-1960 earthquakes at multiple sites along the Valdivian coast.

2.5.1 San Antonio Estuary

The San Antonio estuary is situated 40 km southwest of the city of Puerto Montt, 8 km to the west of Calbuco on Isla Quihua, and approximately 180 km east of the trench (Figure 2.10). This site lies around the eastern limit of coseismic subsidence associated with the 1960 earthquake, with subsidence occurring to the west and uplift to the east (Plafker and Savage, 1970, Moreno et al., 2009). Nonetheless the current knowledge of coseismic deformation comes only from local observations of extreme tides made pre- and post-earthquake by local residents (Plafker and Savage, 1970). This site is also selected to extend the geological record of pre-1960 earthquakes in the region. As tidal marshes contain sedimentological evidence for coseismic deformation associated with subduction zone earthquakes, the aim is to collect samples from the San Antonio estuary and use a diatom-based transfer function to reconstruct RSL change in order to seek any association with subduction zone earthquakes.

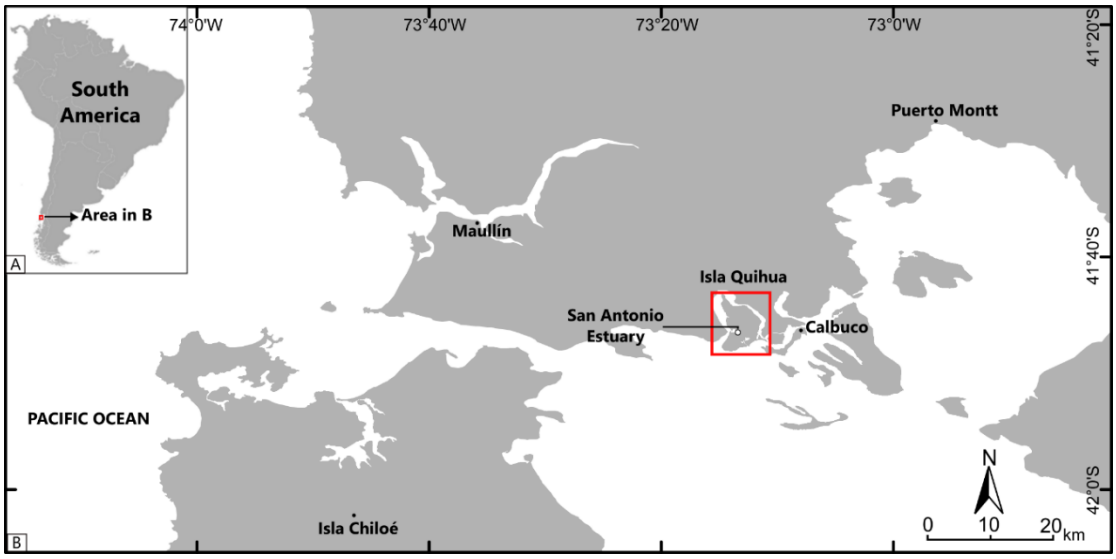

Figure 2.10 : Location map of the San Antonio estuary.

2.5.2 Valdivian Coast

The Valdivian coast has been affected by numerous megathrust earthquakes as it is located next to the subduction zone. The locations of study sites were chosen to correspond to areas affected by pre-1960 earthquakes according to historical records and fill the spatial gap in sedimentary records. Along the Valdivian coast, six field sites were targeted containing coastal exposures from the north to south (39.30°S - 39.53°S) at Chan-Chan, Calfuco, Loncoyén North and Loncoyén South, Rosada and Isla Mancera covering a ~45 km long stretch of the coastline in south-central Chile (Figure 2.11). Although these sites have not been studied for microfossil content in order to generate quantitative estimates for RSL change and vertical coseismic deformation, investigation of the coastal stratigraphy were carried out synchronously with Ditzel (2019). Therefore, they have a promising potential to provide sedimentological and microfossil evidence for pre-1960 earthquakes.

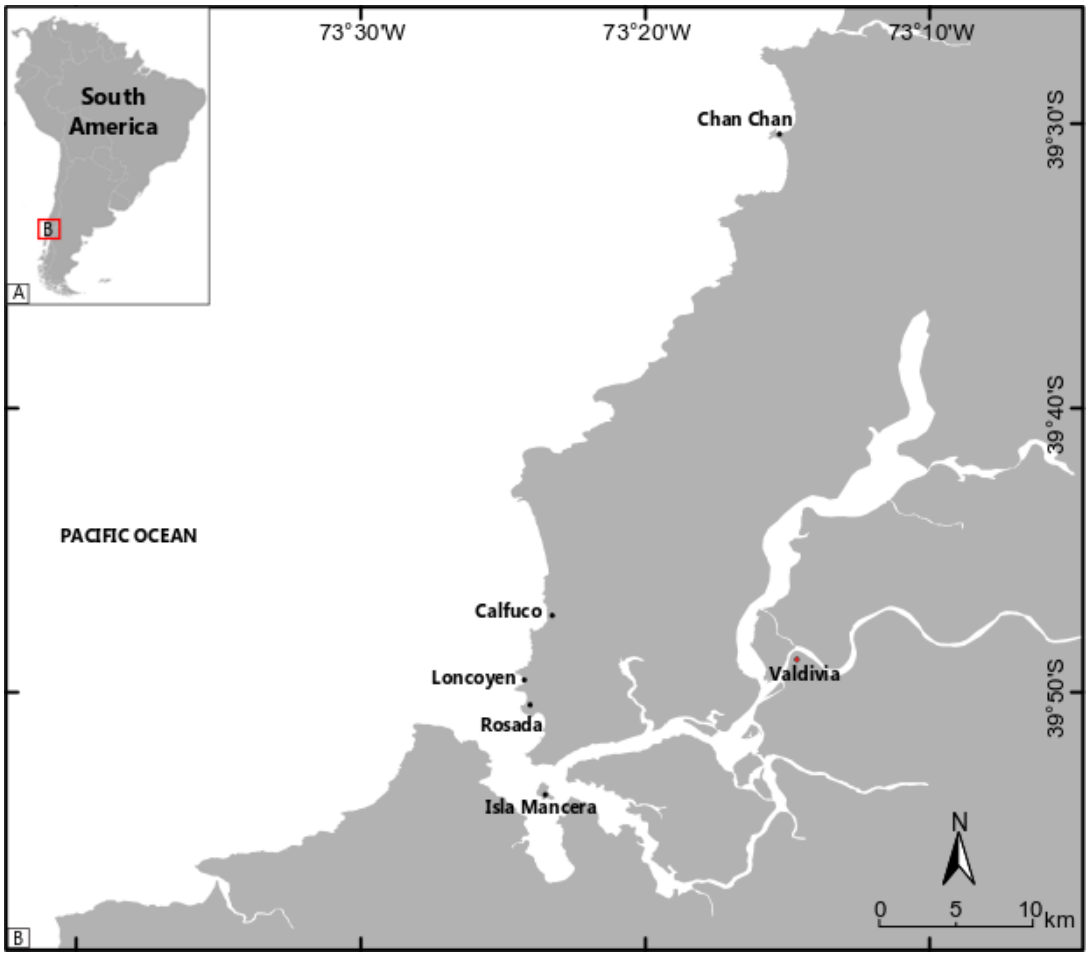

Figure 2.11 : Location map of field sites in south-central Chile. Black circles demonstrate samples that were collected from uplifted beaches at Isla Mancera, Rosada, Loncoyén, Calfuco, and Chan-Chan in south-central Chile; red circle shows Valdivia is the biggest city in the region.

2.6 Summary

This chapter presents the current understanding of the tectonic, palaeoseismological, post-LGM glacial and RSL history of south-central Chile. The Chilean subduction zone produces large to great megathrust earthquakes and accompanying tsunamis. Historical records provide the timing and shaking locations of the earthquakes along the Valdivia seismogenic segment, but they present limited information over only the last ~ 500 years. Geological evidence can extend the palaeoseismic record and can also be critical where historical records may be missing. Whilst Chilean palaeoseismology has advanced significantly in the last couple of decades, uncertainties remain particularly around rupture lengths, mechanisms, and characteristics of pre-1960 earthquakes. This study, therefore, focuses on finding evidence of such events by employing both biostratigraphic and lithostratigraphic

approaches within the Valdivia segment. Moreover, this study also aims to investigate RSL change at six coastal sites potentially affected by pre-1960 earthquakes and a tidal marsh site to find evidence of the 1960 earthquake by employing methods described in the Chapter 3.

Chapter 3 : Study area and methods

This chapter presents the methods that are employed to achieve the objectives set out in chapter one. The methods are divided into four categories: 1) field methods describing sampling and lithostratigraphy; 2) laboratory methods including particle size and diatom analysis; 3) statistical approaches employed for data analyses and diatom-based transfer function development; and 4) radiometric dating techniques.

3.1 Field sampling

3.1.1 San Antonio

The San Antonio estuary (41°46'30.68"S, 73°13'11.55"W) is situated on Isla Quihua, around 40 km southwest of the city of Puerto Montt and 8 km to the west of Calbuco on the northern margin of the Gulf of Ancud (Figure 3.1). The coastal lowland, tidal flat and marshes fringe the western margin of the San Antonio estuary. The lowland receives some fluvial input, and the large tidal range allows the growth of salt marsh vegetation. The estuary has a highly enclosed nature; the connection to the sea is constrained by bedrock headlands, with gravel barriers further reducing the inlet width to ~100 m. The mouth of the estuary faces north-north-east and is therefore highly sheltered from tsunami or storm waves (Figure 3.1).

Modern samples were taken for diatom analysis (section 3.4) along a transect across the tidal marsh (Chapter 4), and fossil cores were taken along two transects that were positioned both perpendicular and parallel to the coast with the intention of characterising the distribution of sediments (Chapter 5). Cores were taken with a one-metre-long gouge corer with a 25 mm diameter gouge. Fossil samples were taken for subsequent particle size (section 3.3) and diatom analysis (section 3.4), and radiocarbon and radionuclide dating (section 3.6).

3.1.2 Valdivia coast

Field investigations were carried out at six coastal sites within the northern part of Valdivia segment (39°53'S - 39°30'S) in January 2019 (Figure 3.2): Rosada (39.50°S, 73.24°W), Loncoyén North (39.49°S, 73.24°W) and South (39.50°S, 73.24°W), Calfuco (39.47°S, 73.23°W), Chan-Chan (39.30°S, 73.16°W) and Isla Mancera (39.53°S, 73.24°W). The coastal geomorphology is shaped by upper marine terraces (also named as Cancagua) of late Pleistocene age, dating to Marine Isotope Stage 5e (MIS 5e) with elevation ranging from 5 to 67 m (e.g., Astorga and Pino, 2011, Vega

et al., 2018, Ditzel, 2019). The lower terraces at the back of the beach are much younger, dating to the late Holocene, and are the focus of this thesis (chapter 6).

Figure 3.1 : A) Map of South America highlighting south-central Chile. B) Location of study area on Isla Quiha. C) Intermediate-scale map of the estuary. D) Location of the San Antonio estuary showing location of the sediments collected as modern analogues for diatom analysis.

During the joint fieldwork in January 2019, Paulina Ditzel carried out several measurements using the Differential Global Positioning System (dGPS) to determine the height of coastal exposures, including the top and bottom of peat deposits. The error ranges of these measurements were determined by considering the instrumental error of the dGPS, the standard deviation of multiple measurements taken at a specific elevation, and the differences between the measured and modelled tidal values using TPXO 9.1 (Ditzel, 2019). At each site, the lithostratigraphy of the exposures was described in the field (section 3.2), and then exposed sections were sampled using 25 cm monolith tins for subsequent diatom analysis (section 3.4) and radiocarbon dating (section 3.6).

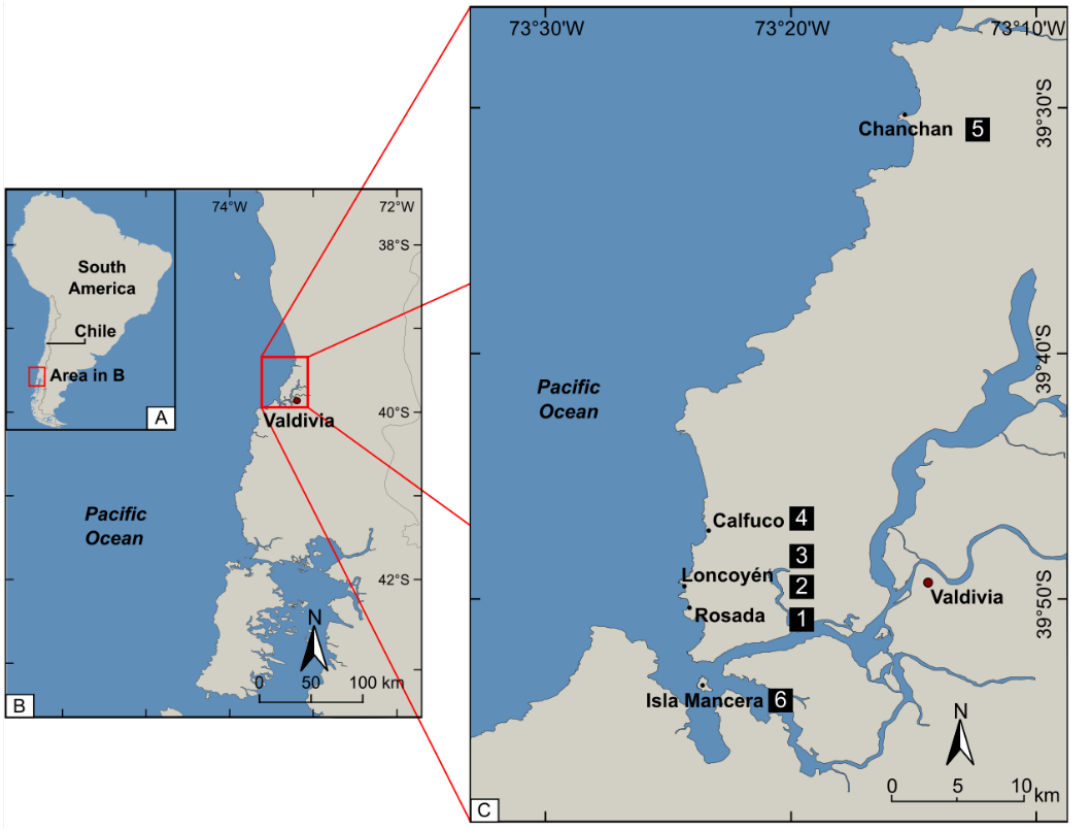

Figure 3.2 : Location of study sites within the Valdivia region, in the context of Chile (A) and south-central Chile (B). The six sites examined in chapter 6 are shown in (C): Rosada (1), Loncoyén South (2) and North (3), Calfuco (4), Chan-Chan (5) and Isla Mancera (6).

3.1.3 Surveying tidal level and converting sample elevation

Tidal levels were measured in order to constrain Mean Sea Level (MSL) and Mean Higher High Water Level (MHHW). These measurements are employed as a reference level for the relative elevation of surface samples, and sediments below the

marsh or exposure surface. All measurements were linked to local benchmark and tidal datum documented as elevation in metres relative to mean tide level from each site.

Surveying of coastal exposures in Valdivia was carried out using a differential GPS system and tide level values were referenced to the mean level of the TPXO 9.1 tidal model (Egbert and Erofeeva, 2002). Measurements and subsequent modelling were carried out by Ditzel (2019) after the joint fieldwork that was carried out me and the fieldwork team in 2019. Surface samples and the cores at San Antonio were levelled using a standard staff and level, while tidal measurements were carried out using an ultrasound tide gauge (Wesson et al., 2014) by Dr Ed Garrett in April 2018. To estimate tidal datums, the TPXO8-ATLAS global model of ocean tides was employed (Egbert and Erofeeva, 2010). Tidal modelling was carried out by Dr Ed Garrett.

The elevation of all samples required conversion into Standardised Water Level Index (SWLI) to account for differences in tidal range between sites. SWLI is calculated following (Hamilton and Shennan, 2005) using the equation:

$$SWLI_n = \frac{100\,(h_n - h_{MSL})}{h_{MHHW} - h_{MSL}} + 100 \qquad \text{Eq. (3.1)}$$

$SWLI_n$ = Standardised Water Level Index for sample n, h_n = elevation of sample n, h_{MSL} = mean sea level elevation, h_{MHHW} = mean higher high water elevation in metres.

3.2 Lithostratigraphy analysis

It is essential to characterise the lithostratigraphy of the field sites in order to provide a first order assessment of depositional environments and identify transitions between potentially different sedimentary environments, in particular looking for abrupt contacts which require further investigation as to whether they are of seismic origin.

During fieldwork, coastal sediments were recorded and described using the Tröels-Smith classification scheme (Tröels-Smith, 1955). This is a widely used scheme which classifies sediment into a coded system that includes composition of units, organic content, and stratigraphic position of the layer as upper and lower depths relative to the modern surface through visual observation. The faces of exposures (Valdivia coastal sites) were cleaned horizontally over many metres in order to trace the lateral extent of sedimentary units, and then sediments were logged and photographed before sampling. Likewise, where core transects were employed (San Antonio), sediments were described and logged in all cores to trace the spatial distribution of

sediment units before representative cores were collected to be taken for subsequent analyses.

3.3 Particle size analysis

Particle size analysis measures the percentage of different sized sediment grains and was used since it is not possible to distinguish some sediments by observation alone. The laser diffraction grain-size analyser was used for particle size analysis.

The subsamples from the monolith collected at San Antonio estuary were taken at 1 cm intervals in order to differentiate sediments that were described during the fieldwork. Thereupon, in the laboratory at Northumbria University, samples were treated with 20% hydrogen peroxide (H_2O_2) to digest and remove organic matter and 10% hydrochloric acid (HCl) was added to remove carbonates and sodium hexametaphosphate as a dispersant. Processed samples were analysed with a Malvern Mastersizer 2000 Particle Size Analyser (laser diffraction grain-size analyser) (Sperazza et al., 2004). Interpretations of particle-size distribution results are based on both percentages presented as differential volume and classification of size distribution (Wentworth, 1922). Clay, silt, and sand contents of sediments are reported as the percentage of volume: clay ≤ 2 μm, silt 2 μm to 63 μm, and sand > 63 μm based on the Wentworth scale.

3.4 Diatom analysis

As stated in Chapter 1, diatom analysis was carried out in order to generate diatom-based reconstructions of palaeosurface/palaeoterrace elevation and relative sea-level change. Diatoms incorporated into coastal sediments are an important proxy as species assemblages show distinct zonation and have a direct relationship to elevation within the tidal frame (Zong and Horton, 1999, Hamilton and Shennan, 2005).

Samples for diatom analysis come from three sources: modern samples from San Antonio estuary, fossil core samples from San Antonio and fossil samples from monoliths from coastal exposures around Valdivia. At each site, the number of subsamples taken was determined based on lithology. At San Antonio, fossil samples were taken at 0.5 cm intervals for diatom analysis (Chapter 5). At each of the Valdivian coastal sites, a total of 8 samples were taken at 1 cm intervals where sharp contacts were present, or at 2 cm intervals where contacts were gradational (Chapter 6).

For sample preparation at Northumbria University, standard laboratory procedures were followed (Palmer and Abbott, 1986). Around 1 g of sediment from monoliths and surface samples, together with 30 ml of 20% hydrogen peroxide (H_2O_2) were added to a 50 ml centrifuge tube then put into a hot water bath and heated to 80°C. The samples were kept at this temperature until all organic matter oxidised; determined by the absence of reaction to the H_2O_2. This step varied depending on the concentration of organic matter from 12 to 24 hours. Digested samples were then diluted with distilled water and centrifuged for 3.5 minutes at 3300 rpm. After decanting the supernatant liquid, 20 ml distilled water was added to conserve the processed sample. Slides for microscope analysis were prepared by pipetting a small volume of the processed sample onto coverslips. Coverslips were placed onto a 40°C warm hotplate until they were completely dry. Naphrax was used as a mounting medium and a small amount was placed onto each glass slide and heated on a hotplate to 100°C. Subsequently, coverslips were flipped and mounted onto glass slides. Once the Naphrax had boiled and resettled the slides were ready for microscope analysis. A minimum count of 250 diatom valves were counted per sample under oil immersion at 1000x magnification using a Leica DM500 microscope with an ICC50HD camera. Diatoms were identified to species level where possible, using available literature (Rivera et al., 1989, Vos and de Wolf, 1985, Denys, 1991, Hemphill-Haley, 1993, 1993, Van Dam et al., 1994, Hassan et al., 2009, Rebolledo et al., 2005, 2011).

3.5 Statistical approach

3.5.1 Zonation of datasets

In order to investigate zonation of diatom assemblages in the modern environment, unconstrained cluster analysis was performed. The number of zones was determined by applying a hierarchical agglomeration technique, that is stratigraphically unconstrained, constrained cluster analysis CONISS (Constrained Incremental Sum of Squares) (Grimm, 1987). The function was applied by using the vegan package (Oksanen et al., 2020) in R 3.6.3 (R Core Team, 2021). Through utilising the relative abundance of species, the generated dendrogram reflects a hierarchical relationship between clusters of similar composition of species and their zonation.

3.5.2 Ordination

Ordination is the simplest way to represent the relationship between multiple variables (species composition) and the environment (Gauch, 1982, ter Braak, 1995b). Species

presence is governed by many environmental factors, and it is generally thought that diatom species display a unimodal response (distribution) along environmental gradients (Gauch, 1982, ter Braak and Prentice, 1988, Legendre and Legendre, 1998, 2012). The main purpose of ordination is to generate and frame hypotheses upon the relationship between abundance of taxa (species) of the study site and the associated environmental gradients (Gauch, 1982, Digby and Kempton, 1987). In general, species display a unimodal response (single peak or one mode) with respect to environmental variables (Whittaker, 1956, 1967, ter Braak and Prentice, 1988, Legendre and Legendre, 1998). Ordination is a dimension-reduction technique applied to multivariate data. Here, ordination techniques are employed to seek the major patterns of change in diatom distribution. Unconstrained ordination (indirect gradient analysis) also allows identification of clustering within the contemporary dataset; and constrained ordination (direct gradient analysis) by an environment gradient (elevation), aids in assessing the proportion of variability in the modern diatom dataset by measuring the rate of species turnover along a gradient (ter Braak and Prentice, 1988, Birks, 1995). Here, it was preferred to employ both indirect and direct gradient analysis rather than conventional ordinations because these methods scale sample scores as standard deviation units (SD) of compositional change (Hill and Gauch, 1980, ter Braak and Prentice, 1988; Gauch, 1982) and provide easy interpretations for further modelling.

Detrended Correspondence Analysis (DCA) is an indirect analysis method that presents the major pattern of variation in species composition without a priori hypotheses and thus supports subsequent modelling of anticipated environmental variables (Hill and Gauch, 1980). As a rule of thumb, if the length of the first axis in DCA is greater than 4 SD, it indicates a unimodal response model for species (Hill and Gauch, 1980, Gauch, 1982). This criterion is commonly used in subsequent direct gradient analysis to determine the appropriate response curve (ter Braak and Prentice, 1988, ter Braak, 1995b, Lepš and Šmilauer, 2003). Following that, the Detrended form of Canonical Correspondence Analysis (DCCA) (ter Braak, 1986) is carried out to further explore species-environment relationships, which facilitates ordering of samples and species composition, provided that there is a unimodal distribution, based on a linear relationship with the environmental gradient (ter Braak, 1986). DCCA can be employed to explore whether elevation plays an important role as an environmental gradient in determining species distributions and whether species display unimodal distributions where the environmental gradient is larger than 2 SD units (Birks, 1995). DCCA is performed using CANOCO 4.5 (ter Braak and

Šmilauer, 2002). Finally, Canonical Correspondence Analysis (CCA) (ter Braak, 1986) is also performed in order to calculate the relative explanatory power of the environmental variable of interest (ter Braak, 1988, Juggins, 2013). The eigenvalue is a measure, which lies between 0 and 1, reflecting the importance of the ordination axis (ter Braak, 1986; 1988). When the dissimilarities between samples, which are based on species scores, are large, the eigenvalue increases (ter Braak, 1988). Moreover, it is suggested that an eigenvalue larger than 0.5 indicates significant dissimilarities between species scores along ordination axes, providing important information about the environmental gradient (ter Braak, 1995b). The ratio between the eigenvalue of the first axis of constrained ordination and the eigenvalue of unconstrained ordination λ_1/λ_2 in CCA ordinations was calculated to assess the explanatory power of the environmental variable of interest, since it is suggested that where this value is greater than 1.0, it is considered as an important environmental variable as a rule of thumb (ter Braak, 1988, Juggins, 2013). CCA allows us to estimate percentage of variance accounted for by the environmental variable in the diatom dataset. Therefore, the relationships between diatom assemblage composition and measured sample elevation were examined by employing CCA (ter Braak, 1986, ter Braak and Verdonschot, 1995). Both indirect and direct gradient analyses methods were employed using “vegan” package version 2.5-7 (Oksanen et al., 2020) in R (R Core Team, 2021).

3.5.3 Transfer function development

Transfer functions (Imbrie and Kipp, 1971) are a statistical approach that use regression analysis to present the relationship between an environmental parameter (e.g., elevation, salinity, pH) and the relative abundance of modern biological data (e.g., diatoms, foraminifera) (Birks, 1995, Juggins and Birks, 2012, 1998, Kemp and Telford, 2015). Following this, an empirical relationship model uses fossil assemblage data to predict the environmental gradient of interest.

Employing transfer functions has enabled reconstruction of relative sea-level (RSL) change since diatom assemblages are highly zoned with elevation gradient in the tidal frame (Nelson and Kashima, 1993, Sherrod, 1999, Zong and Horton, 1999). Subsequently, transfer functions have become a widely applied means to reconstruct RSL around the world including in seismically active regions, such as in Cascadia (Nelson et al., 1996, 2008, Shennan et al., 1996), Alaska (Zong et al., 2003, Hamilton and Shennan, 2005, Hamilton et al., 2005, Shennan and Hamilton, 2006, Watcham et al., 2013, Shennan et al., 2014a, 2014b), Japan (Sawai et al., 2004a), New Zealand

(Hayward et al., 2006), and Chile (Nelson et al., 2009, Garrett et al., 2013, 2015, Hocking et al., 2017; Hocking et al., 2021) (for review see Kemp and Telford (2015)). In addition, microfossil transfer functions have also been applied to reconstruct aseismic RSL change from the UK (Juggins, 1992, Horton, 1999, Zong and Horton, 1999, Horton et al., 2000; Barlow et al., 2013), Spain (Leorri et al., 2008), Greenland (Woodroffe and Long, 2010) and the Atlantic Coast of North America (Kemp et al., 2011; Barlow et al., 2014), where they have similarly showed their usefulness in providing quantitative estimates for RSL.

3.5.3.1 Basic assumptions

Transfer functions are a statistical technique that are applied to establish the relationships between relative abundance of taxa and the environmental variables governing their distribution in the intertidal zone. However, this statistical approach requires basic assumptions. The basic assumptions in quantitative palaeoenvironmental reconstructions are based on the following criteria, which were first established by Imbrie and Kipp (1971) and Imbrie and Webb (1981), and subsequently by Birks et al. (1990), Telford and Birks (2005; 2009), Birks, (2010), Juggins and Birks (2012) and Juggins (2013).

1. The biological assemblages in the modern training-set are systematically related to the environment in which they live.
2. The environmental variable(s) to be reconstructed is, or is linearly related to, an ecologically important determinant in the system of interest.
3. The biological assemblages in the training set are the same biological entities as in the fossil taxa and their ecological responses to the environmental variable(s) of interest have not changed over the time represented by the fossil assemblage.
4. The mathematical methods adequately model the biological responses to the environmental variable(s) of interest and yield numerical models that allow accurate and unbiased reconstructions.
5. Environmental variables other than the one of interest have negligible influence, or their joint distribution with the environmental variable does not change with time.
6. In model evaluation by cross-validation, the test data are statistically independent of the training set.

The first and second assumptions work in tandem. The third assumption is basically the doctrine of uniformitarianism. The fourth assumption benefits from varying robust statistical methods that were developed. The fifth assumption is the most difficult one since consideration of the constant effects of other environmental variables in the past may not seem possible. The sixth and the last assumption points to independence of the modern training set yet due to the limited size of modern sample training sets and lack of external cross-validations method it may not reflect independency.

3.5.3.2 Transfer function methods

In order to develop different transfer function models, three regression and calibration methods are employed. The first Weighted averaging (WA) (ter Braak and van Dame, 1989, Birks et al., 1990), second Weighted Averaging-Partial Least Squares (WA-PLS) (ter Braak and Juggins, 1993, ter Braak et al., 1993), and third Locally Weighted Weighted-Averaging (LWWA) (Birks, 1998, Hübener et al., 2008, Juggins and Birks, 2012) are used, respectively.

The WA method comprises three consecutive stages: regression (estimating species optima by using environmental variables), calibration (estimating environmental variables by using species optima) and deshrinking which is explained below (ter Braak and van Dame, 1989, ter Braak and Barendregt, 1986, ter Braak and Looman, 1986). WA regression follows the equations 3.2, 3.3 and 3.4 to estimate species optima and tolerance:

$$\hat{u}_k = \frac{\sum_{i=1}^{n} y_{ik} x_i}{\sum_{i=1}^{n} y_{ik}} \qquad \text{Eq. (3.2)}$$

Where $i = 1, \ldots, n$ samples and $k = 1, \ldots, m$ taxa; $\hat{u}_k$is the WA optimum of taxon k; y_{ik} is percentage of taxon k in sample i; x_i observed environmental variable of interest in sample i; t is tolerance of taxon k:

$$\hat{t}_k = \sqrt{\frac{\sum_{i=1}^{n} y_{ik}(x_i - \hat{u}_k)^2}{\sum_{i=1}^{n} y_{ik}}} \qquad \text{Eq. (3.3)}$$

WA calibration estimates environmental variable of interest from species optima which calculated from the regression step above:

$$\hat{x_i} = \frac{\sum_{k=1}^{m} y_{ik} \hat{u}_k}{\sum_{k=1}^{m} y_{ik}} \qquad \text{Eq. (3.4)}$$

$\hat{x_i}$ refers to estimated environmental variable of interest for fossil sample i ; y_{ik} refers to abundance of species k in fossil sample i and $\hat{u}_k$ = optima of species k.

Moreover, as the averages are taken twice during the regression and the calibration stages, which shrinks the range of values towards the mean, the results are vulnerable to nonlinear distortions and creating edge effects (ter Braak and Prentice, 1988, Birks, 1995). Therefore, depending upon species position along the environmental gradient, these values can be affected by the overestimation of species optima at the low end and underestimation at the high end (Birks et al., 1990, ter Braak and Juggins, 1993). Subsequently, the deshrinking part follows as it is an essential part to remove under- and over-estimated taxa optima depending upon species position along the environmental gradient (ter Braak and van Dame, 1989, ter Braak and Juggins, 1993, Birks et al., 1990, Birks, 1995). Furthermore, there are two cases of deshrinking: classical and inverse, with the former deshrinking more than latter one as expected (see Birks et al., 1990, Birks, 1995). However, WA is vulnerable to nonlinear distortions; hence, both types of deshrinking are compared to see which results in better linear distribution.

Furthermore, as opposed to these two linear procedures, other methods known as monotonic smoothing deshrinking (ter Braak and Juggins, 1993, Marchetto, 1994), which is a non-linear approach (spline regression) can also be utilised to rescale species optima and restore variance as well as compare the statistical performance. This approach may avoid the nonlinear distortions that can occur at the edges of the gradient, a characteristic known as edge effects in correspondence analysis (Hill and Gauch, 1980; ter Braak, 1985; ter Braak and Prentice, 1988; ter Braak and Juggins, 1993).

Table 3.1: List of deshrinking types is employed in WA method (Juggins, 2020, Simpson, 2021). The variables β_0 and β_1 refer to regression coefficient; x_i and $\hat{x}_i$ are observed and estimated environmental variable, respectively.

Type	Model
Classical	$x_i = \beta_0 + \beta_1 \hat{x}_i$
Inverse	$\hat{x}_i = \beta_0 + \beta_1 x_i$

A solution for solving the problem of edge effects is employing the WA-PLS method (ter Braak and Juggins, 1993, ter Braak et al., 1993). When the WA method is combined with partial least square (PLS) regression, each additional component is used to maximise covariance between other possible unknown factors assumed to

have a linear function of species distribution (ter Braak and Juggins, 1993, ter Braak et al., 1993). This method uses additional orthogonal components to explore the relationship between latent (unknown) variables. Subsequently, the relationship of these latent variables is modelled using residuals of sample data. Hence, extra competent updates the species optima (beta coefficient) and may provide better estimates. However, this method is prone to overfitting thereby Birks (1998) suggests that where the RMSEP does not reduce by at least 5%, extra components should not be used to avoid overfitting. Nonetheless, it is important to note that a 5% reduction in RMSEP is a subjective threshold and may not always shield against overfitting; therefore, application of a simple randomization test (van der Voet, 1994) is suggested to compare the accuracy of the cross-validated components and to be considered useful (Juggins and Birks, 2012).

Species optima are updated by using additional components and they are referred to as the regression beta coefficients or parameters (ter Braak and Juggins, 1993, ter Braak et al., 1993). The main difference between WA-PLS and WA is that WA-PLS maximizes the covariance between taxa assemblages and environmental variables. (ter Braak and Juggins, 1993). Notwithstanding, this process causes reconstructed values at the lower end to be higher than actual values, and values at the higher end to be lower, as the method artificially compresses reconstructed values towards the mean of the range (ter Braak et al., 1993). Consequently, there will be bias for those predicted values at both the high and low ends along environmental gradients of interest and care must be taken when using extra components in order to avoid overfitting even if additional components provide better statistical performance.

Another WA method is also employed – Locally Weighted-Weighted Averaging (LW-WA), which is also known as the Moving-Window, as it aims to combine the best properties of weighted averaging and the modern analogue technique (Birks, 1998, Hübener et al., 2008, Juggins and Birks, 2012). Notwithstanding, this method is prone to overfitting. Consequently, several models can be employed based on varying sample size from the modern training set such as 10% to 50% to generate different reconstruction estimates and reach both statistically and ecologically reasonable explanations for the model.

The Bayesian framework may provide a more realistic species response curve because of its ability to generate multinomial response functions and employ many environmental variables at the same time. For instance, Holden et al. (2017) defined species response curves by using five parameters (tolerance scaling, probability of

presence at environment optimum, and expected abundance (given presence) at environmental optimum) in addition to the conventional unimodal Gaussian approach (ter Braak and Looman, 1986, ter Braak and van Dame, 1989), which only utilises two parameters, namely taxon optimum and tolerance. Moreover, one of the most important advantages of this approach is to use many sources of data (e.g., foraminifera, testate amoebae, pollen) and their associated uncertainties and combine them in a single framework (Cahill et al., 2016, Holden et al., 2017). Thus, calibration can then proceed by joint estimation of the variables and/or prior assumptions (constraints) such as constraining sample elevation which allows limiting species optima, using the Bayesian principle. This modern approach, however, is subject to complex mathematics and it is computationally demanding; therefore, the intensive computing power that is required, especially with the regional modern dataset composed of 289 samples and 235 species. Consequently, this study is not able to employ the Bayesian transfer function method because of this essential requirement.

Assessment of performance of the transfer functions is considered based on root-mean square error of prediction (RMSEP) and squared correlation of observed versus estimated values (r^2) based on bootstrap cross validation (1000 permutation cycles). The bootstrap cross validation method is particularly preferred so as to attain sample-specific error for each reconstructed fossil sample. The bootstrap standard estimated error is the standard deviation of the bootstrap samples. Sample-specific error is calculated using $s_{1\text{fossil}}$ and is the standard error of the bootstrap estimates of the environment for an individual fossil sample; $s_{2\text{model}}$ is the average bias (mean of residuals) from the transfer function model under bootstrapped cross-validation. When used in tandem, bootstrap cross-validation introduces ~ 68% uncertainty and this value is multiplied by 1.96 to obtain ~ 95% confidence interval for reconstructed estimates (Birks et al., 1990, Juggins and Birks, 2012).

$$RMSEP = \sqrt{s_{1fossil}^2 + s_{2model}^2} \qquad \text{Eq. (3.5)}$$

Sample-specific error contributors for the reconstruction of palaeomarsh surface elevation of the fossil samples are calculated using the bootstrap method. As a consequence of the multiple bootstrap cross-validation procedures employing randomly selected values in the dataset more than once (known as sampling with replacement), the training set is replicated in the same size during each cycle (1000

cycles) (Birks et al., 1990). Therefore, each reconstructed value comes with the standard error of prediction that consists of two components: 1) RMSEP for individual SWLI reconstruction and 2) overall RMSEP for the training set which is a constant value. By following Birks et al. (1990) and Juggins and Birks (2012), the standard error of the bootstrap estimates for each fossil samples (s_1) and the root mean squared error for the training set samples, across all bootstrap samples (s_2), which is same for all samples, is used to calculate the standard error of prediction (sample specific error). The standard error of prediction for each reconstructed sample is calculated as the square root of s_1 and s_2 by using equation 3.5.

It is suggested that the prediction error is mainly influenced by s_2, while s_1 reflects only 10 – 20% of the overall error in practice (Juggins and Birks, 2012). Here, this difference between these values were explored to seek out their individual contribution. Finally, these reconstructed values are in SWLI units, and they are kept in this unit not back-transformed to the metre scales and each output of error values is multiplied by 1.96 in order to obtain ~95% confidence interval.

When models are applied to fossil sequences to generate reconstructions of palaeomarsh/palaeoterrace surface elevation and relative sea-level change, models are also assessed based on similarity between modern analogues and fossil samples using the Modern Analogues Technique (MAT) (Prell, 1985, Overpeck et al., 1985, ter Braak, 1995a, Jackson and Williams, 2004, Simpson, 2007) with the squared chord distance dissimilarity method (Birks, 1995, Simpson, 2007, 2012). All transfer function models are performed using the "rioja 0.9-26" package in R (Juggins, 2020). Finally, when transfer function models are applied to fossil diatom assemblages, further approaches including goodness-of-fit (Birks et al., 1990, Birks, 1995) and significant tests (Telford and Birks, 2011) are also carried out to test the significance of reconstructions and to evaluate the reliability of transfer function models. Further information and detailed discussions of transfer function development and application are presented in Chapters 4 and 5.

3.5.4 Quantifying relative sea-level change

Relative sea-level change estimates are calculated using Eq 3.6:

$$RSL_n = FE_n - PMSE_n \quad \text{Eq. (3.6)}$$

For a sample n, RSL_n refers to the relative sea level estimate; FE_n is the elevation of the sample in the field above mean sea level; $PMSE_n$ is palaeomarsh surface elevation above mean sea level in metres.

Quantifying RSL change requires knowledge of the field elevation of samples and surface, both of which have an associated error term. Therefore, the RSL error must combine both and can be defined by the following formula:

$$RSL\ error = \sqrt{(PMSE\ error)^2 + (FE\ error)^2} \quad \text{Eq. (3.7)}$$

RSL error refers to the error associated with the relative sea-level estimate; PMSE error is the sample specific standard error provided by the transfer function; FE error is the error associated with measurement of the field elevation of the sample.

3.6 Dating techniques

In order to relate the sedimentary record from the San Antonio estuary and coastal sites in the Valdivia region to coseismic and/or post-seismic events associated with regional earthquakes, a chronology is required. The chronology for these sites was constructed from radiocarbon dating (^{14}C) of plant macrofossils and the youngest sediments from San Antonio were dated using Caeisum-137 (^{137}Cs) and Lead-210 (^{210}Pb) isotopes. Furthermore, a combined dating approach was undertaken in order to provide a more robust chronology. Age-depth models were carried out by using the "rplum" (Blaauw et al., 2020) and "serac" (Bruel and Sabatier, 2020) packages in R (R Core Team, 2021).

3.6.1 Radiocarbon dating

Radiocarbon dating (^{14}C) is the most widely employed approach for establishing chronology and relating events in the data to the known timing of historic large earthquakes and establishing recurrence intervals of seismic hazards (Atwater et al., 1992, Nelson et al., 1995, Cisternas et al., 2005). The principles of radiometric dating were documented in the seminal paper of Libby (1952). Accordingly, during photosynthesis plants use the ^{14}C isotope which is produced in the Earth's

atmosphere from the interaction of secondary cosmic rays and nitrogen-14 (Anderson et al., 1947). When plants die, uptake of the ^{14}C isotope stops, and then decomposition and decaying processes commence. The amount of decay can be measured based on the half-life (5570 ± 30 years) of the radioactive isotope; hence, it provides a time constraint for the plant or fossil used for dating and constrains the timing of deposition of sampled material. Accordingly, in order to establish a chronology of these events, plant material can be employed for radiocarbon dating.

Plant macrofossils (e.g., seeds and stems) were sampled from organic deposits for Accelerator mass spectrometry (AMS) radiocarbon dating. A total of seven plant macrofossils sampled from Valdivian coastal sites were submitted to DirectAMS Radiocarbon Dating Services in the United States of America (USA) and a single plant macrofossil (multiple seeds) was taken from the San Antonio core and analysed at the Keck Carbon Cycle AMS Facility, University of California, Irvine, USA for ^{14}C isotope analysis. Radiocarbon ages were calibrated using OxCal 4.3 software (Bronk Ramsey, 2009) with the southern hemisphere calibration curve SHCal20 (Hogg et al., 2020), or the post-bomb atmospheric southern hemisphere curve (SH1-2) for samples exceeding 100 percent modern carbon (pMC) (Hua et al., 2013, Hogg et al., 2020). The results are presented as calibrated age ranges at two standard deviations in Common Era (CE) or Before Present (BP) indicating years before 1950.

3.6.2 Caesium – 137 dating

Widespread nuclear weapon tests began early in the 1950s, with radioactive fallout reaching a peak in 1963 (Arnaud et al., 2006). The occurrence of the short-lived radionuclide Caesium-137 (^{137}Cs) originates from the atmospheric testing of nuclear weapons between 1952 and 1963 in the northern hemisphere (Schuller et al., 1993, Schuller et al., 2002, Arnaud et al., 2006). As a result, ^{137}Cs (half-life $t_{1/2}$ = 30 years) can be found in high levels in recent sediments deposited in the last 70 years, and produces an independent marker for short-term chronology (Walker, 2005). Caesium-137 dating was applied to the core from San Antonio, with subsampling carried out at Northumbria University and sample preparation and measurements carried out by Sabine Schmidt at the University of Bordeaux, France.

3.6.3 Lead – 210 dating

The occurrence of the short-lived radionuclide Lead-2010 (^{210}Pb) originates from the emission of radioactive radon gas (^{222}Rn) from the earth into the atmosphere. Due to precipitation, ^{210}Pb isotopes embed and deposit into sediments and then start

decaying. The half-life of this unstable isotope is 22.26 ± 0.22 yr; therefore, lead-210 dating can be used for dating recent sediment sequences deposited in the last 150 years (Robbins, 1978, Appleby and Oldfield, 1978, Appleby and Oldfieldz, 1983, Arnaud et al., 2006, Walker, 2005). When used in tandem with Caesium-137, this dating can be used to support data produced by radiocarbon dating. In this case, ^{210}Pb dating was employed at San Antonio to reveal the trace of the 1960 earthquake. Sample preparation and measurements were carried out at University of Bordeaux in France by Sabine Schmidt.

3.7 Summary

This chapter explains field, laboratory and analysis methods used to achieve the objectives stated in chapter one. Field sampling of tidal marsh sediments at San Antonio and coastal exposures at Valdivia involved lithostratigraphic surveys and was followed by particle size analysis (San Antonio fossil samples), diatom analysis (San Antonio modern and fossil samples and Valdivia fossil samples) and radiocarbon (San Antonio and Valdivia) and radionuclide (San Antonio) dating. This multi-proxy approach was followed in order to assess the sedimentary signature of any potential historical and prehistoric subduction zone earthquakes. Ordination techniques were adopted to explore the nature of modern diatom assemblage datasets and decide the subsequent transfer function development. Diatom-based transfer function models using weighted averaging approach were develop since they may enable the quantification of relative sea-level changes for the study sites in this work.

Chapter 4 : Results – Modern diatom distributions from the San Antonio estuary and transfer function development

4.1 Introduction

This chapter presents the characteristics of the modern tidal marsh at San Antonio including diatom assemblages, and development of transfer function models. In order to reconstruct past environmental change, analysing the properties of modern analogues is essential to interpret the fossil taxa in sediment following the principle of uniformitarianism. In this chapter, the relationship between diatoms and elevation is explored and transfer function models developed from the new modern training set. A new local training set from San Antonio is combined with a previously published south-central Chile training set to provide an enlarged and improved regional modern training set. The new training set is then used to develop various transfer function models, the performance of which are assessed and compared in order to utilise them to generate robust reconstructions of palaeomarsh surface elevation for sampling sites in the following chapters. In this way, enabling the third and fourth objectives of the thesis to be met and produce reconstructions of relative sea-level change at San Antonio and sites along the Valdivian coast in chapters 5 and 6.

4.2 Study area

The San Antonio estuary is situated 40 km southwest of the city of Puerto Montt, 8 km to the west of Calbuco on Isla Quihua (Figure 4.1). The coastal lowland, tidal flat and marshes fringe the western margin of the San Antonio estuary. The lowland receives some fluvial input, and the large tidal range allows the growth of salt marsh vegetation. The San Antonio estuary presents a suitable opportunity to explore modern diatom distributions and develop transfer function models. Thus, tidal flat and marshes at the eastern end of the estuary were targeted to collect modern analogues for the purpose of analysing diatom content across a transect perpendicular to the coast (Figure 4.1).

4.3 Vegetation

Marshes develop as a result of the accretion of differing saline tolerant plants. In coastal wetlands, tidal inundations might be demarcated by distinct vegetation (e.g., Wehrmann, 2013). The salt marsh plants show evident zonation relative to elevation, as different plants occupying the habitat are mostly controlled by inundation frequency. The salt marsh vegetation at San Antonio estuary is divided into a low

marsh dominated by *Carex sp*. and *Selliera radicans* and a high marsh of *Spartina densiflora*, *Juncus balticus, Rumex cuneifolius*, and *Schoenoplectus californicus*. Freshwater scrub above the highest tides includes *Myrtacea sp.*, *Ulex europaeus* and *Luma apiculata* (Figure 4.2). The identification of plant species was carried out by Dr Ed Garrett.

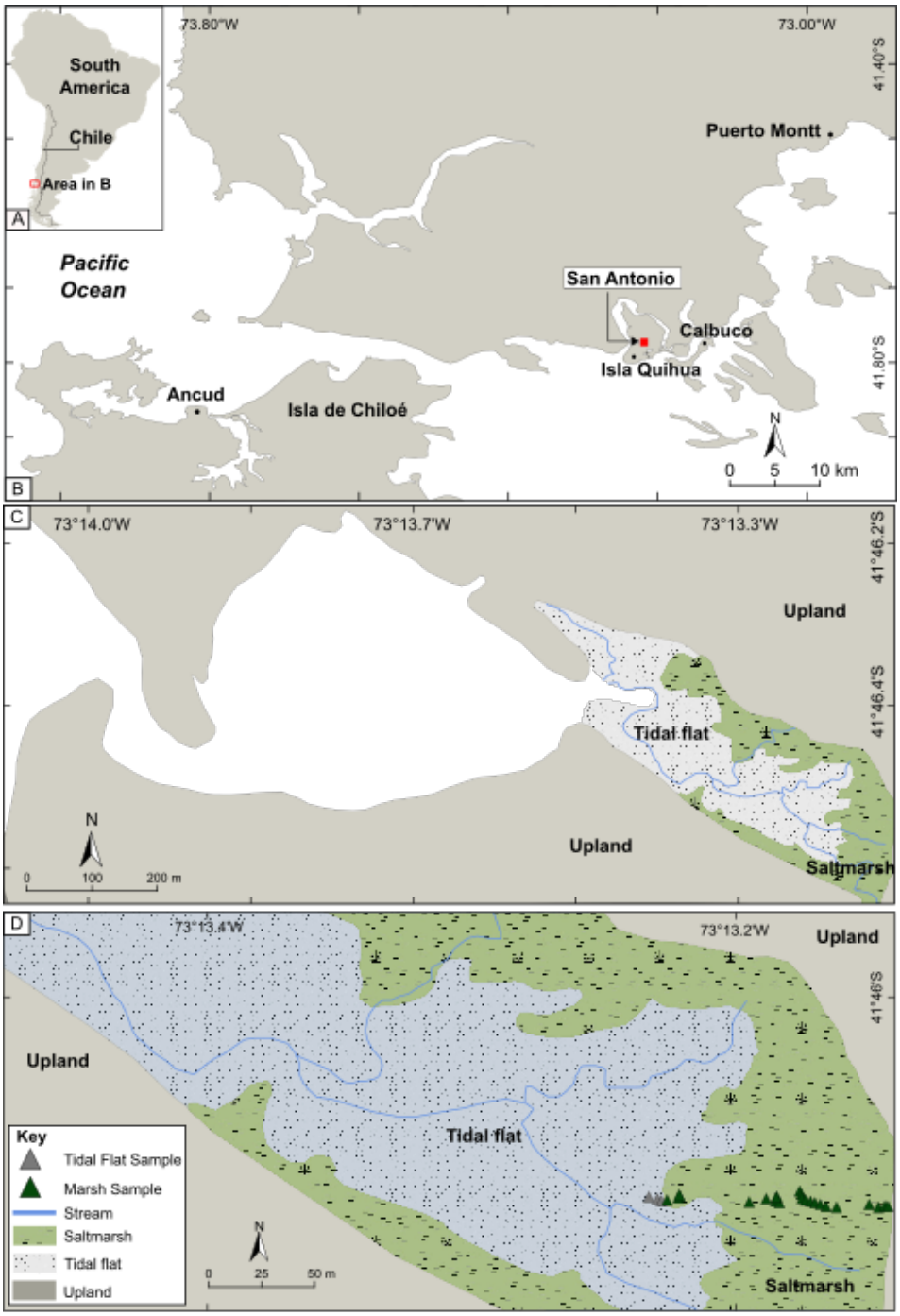

Figure 4.1 : Location of the San Antonio study area, (A) within south-central Chile and (B) on Isla Quihua. The location of the San Antonio estuary and of modern diatom sampling locations are shown on C and D.

4.4 Tides

The elevations of surface samples at San Antonio were levelled using a standard staff and level, while tidal measurements were carried out using ultrasound tide gauge (Wesson et al., 2014). To estimate tidal datums, the tide gauge measurements were compared to the TPXO8-ATLAS global model of ocean tides (Egbert and Erofeeva, 2010) which was carried out by Dr Ed Garrett. The model amplitude was adjusted to match the observations and the resulting scaled model provides a MSL – MHHW range at San Antonio of 2.98 m (Figure 4.3). The elevation of each modern sample was converted to standardized water level index (SWLI) to account for inter-site differences in tidal range when combined with the regional dataset (see chapter 3).

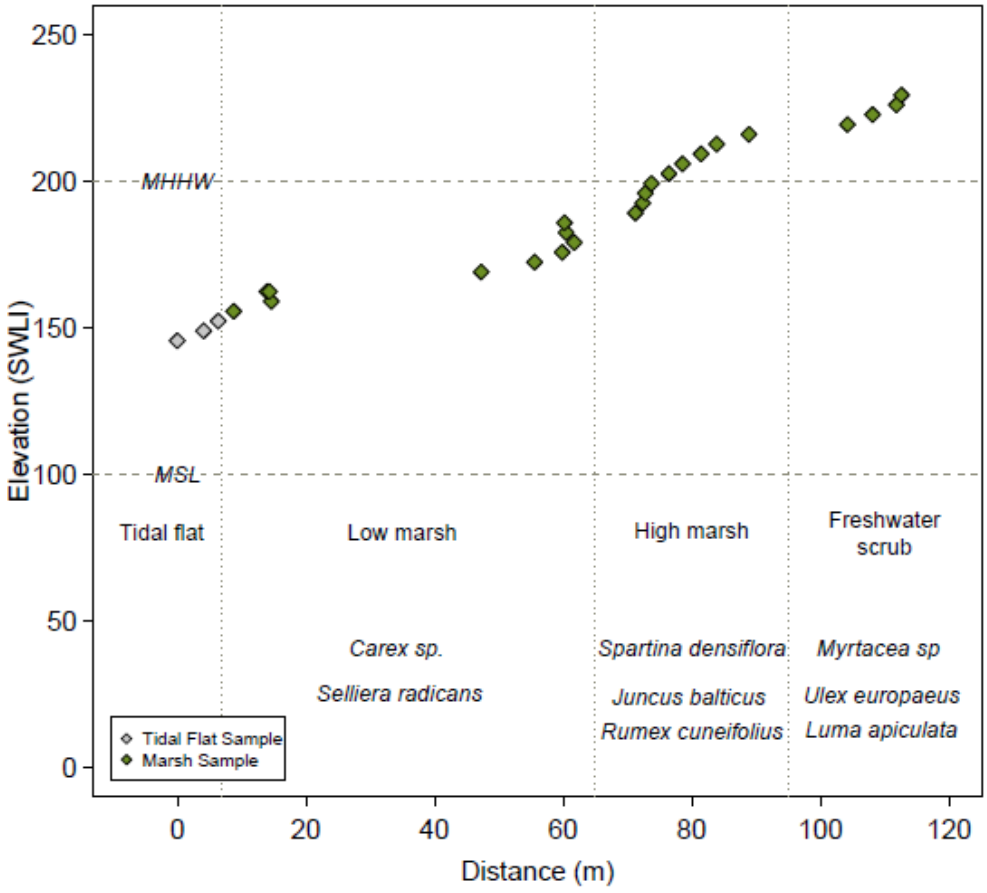

Figure 4.2 : Surface samples collected from San Antonio estuary and change in vegetation across the sampling transect from tidal flat to freshwater scrub.

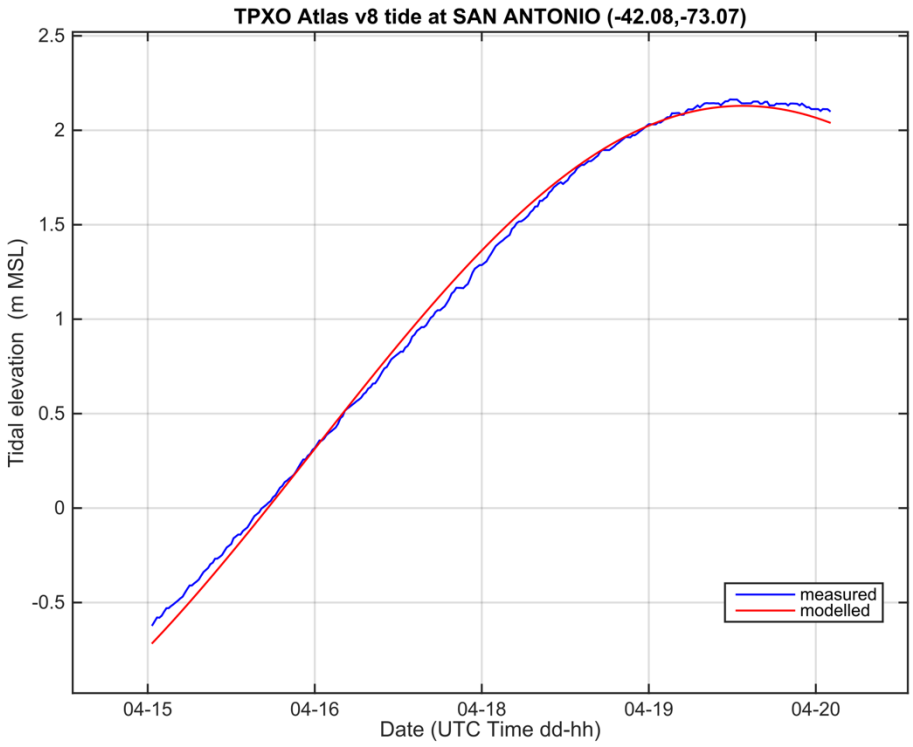

Figure 4.3 : Comparison of water levels measured at San Antonio estuary on 4th May 2018 with tides modelled using the TPXO8-ATLAS global model of ocean tides (Egbert and Erofeeva, 2010).

4.5 Diatom assemblages

In order to establish a relationship between diatom assemblages and tidal elevation, modern sediments were collected from the estuary. A total of twenty-six samples of the top 0.5 cm of modern sediment were taken along a perpendicular transect within the estuary (Figure 4.4), including three samples from the tidal flat and twenty-three modern samples collected from the low marsh, high marsh, and freshwater scrub (Figure 4.2).

Microscope examination shows that twenty-six modern intertidal samples from the San Antonio estuary incorporate 65 identified diatom species from 37 genera. Amongst these species, only 19 out of 65 species have an abundance of at least 10% in one or more sample (Figure 4.5). The distribution of diatoms in contemporary samples shows vertical zonation across the tidal marsh, and constrained cluster analysis reveals there are three distinct cluster zones (Figure 4.5).

Figure 4.4 : Field photo of the San Antonio tidal marsh looking towards the mouth of the San Antonio estuary and showing the modern sampling transect. Due to the perspective, please note that no scale is provided in the photo (Ed Garrett, 2018).

Stratigraphically constrained incremental sum-of-squares (CONISS) (Grimm, 1987) cluster analysis seeks to group samples together based on similar species composition of diatoms. CONISS was implemented by the *chclust* function in the "rioja 0.9-26" package in R using squared Euclidean distance (Juggins, 2020). Based on constrained cluster analysis CONISS (Figure 4.5) and following the broken stick-model (Bennett, 1996), three assemblage zones are revealed across the sampling site with elevation ranges of 1.34 – 2.53 m above MSL (SWLI 145-185, Zone 1), 2.53 – 3.13 m above MSL (185 – 205 SWLI, Zone 2) and 2.53 – 3.87 m above MSL (2.53 –3.87 SWLI, Zone 3).

Zone 1 is dominated by *Pseudostaurosira perminuta, Planothidium* sp. 1*, Opephora pacifica* small form and *Navicula cryptocephala.* In Zone 2, species with elevation optima above MHHW in the regional south-central Chile dataset (Hocking et al., 2017) appear, including *Navicula cincta, Nitzschia vitrea, Diploneis smithii,* whilst percentages of marine/brackish species such as *Navicula phyllepta, Diploneis litoralis, Planothidium delicatulum* and *Pseudostaurosira perminuta* remain high. Finally, there is a distinct transition in the assemblage at 205 SWLI (~MHHW), with

Zone 3 dominated by freshwater species such as *Nitzschia fonticola, Nitzschia frustulum, Denticula subtilis, Nitzschia vitrea* and *Eunotia perpusilla.*

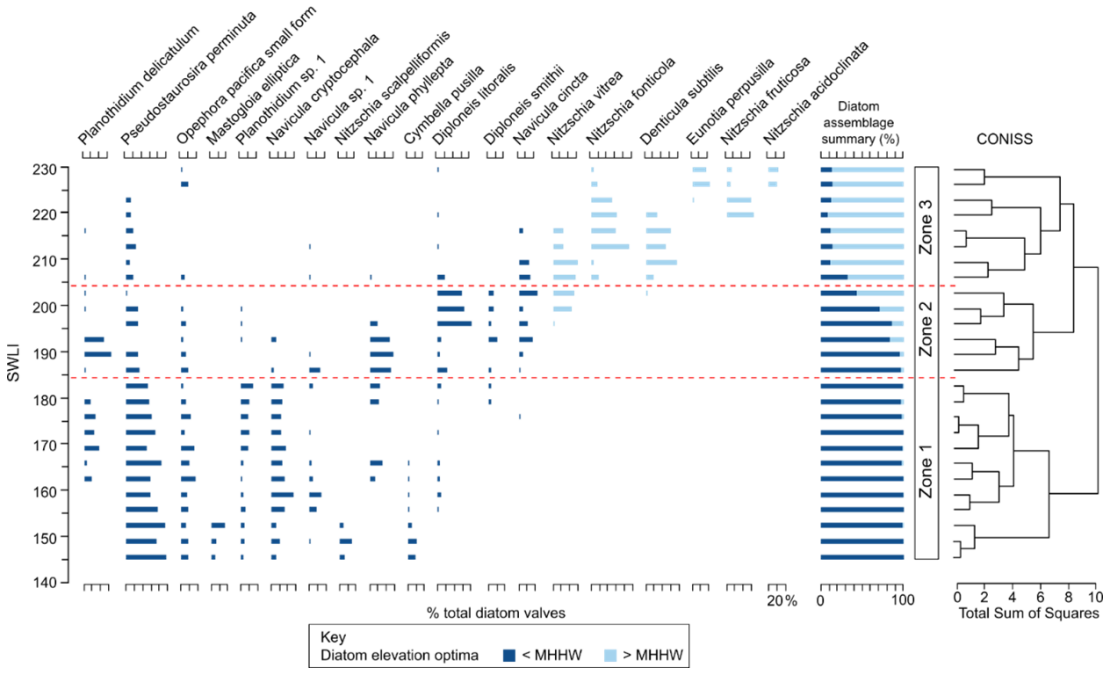

Figure 4.5 : Summary diagram of the modern diatom assemblage from the San Antonio estuary. Relative abundance of diatoms is expressed as a percent of the total count. Bar plot shows taxa exceeding 10% of total diatom valves in at least one modern sample. Species are ordered by elevation optima as calculated by the weighted averaging method. To the right side of the figure, the dendrogram shows the result of CONISS, which clusters samples based on the similarity of their assemblages. Data were not transformed in CONISS, and total sum of squares reported as Euclidean distance (MHHW: Mean Higher High Water = 200 SWLI; MSL: Mean Sea Level = 100 SWLI).

Diatom assemblages from San Antonio estuary are then compared to previously published data from six tidal marshes across south-central Chile (see Hocking et al., 2017) by plotting principal diatoms exceeding 20% of total diatom valves in at least one sample (Figure 4.6). The unique contribution of San Antonio to the regional dataset is the substantial occurrence of *Navicula cryptocephala* found between 140 - 190 SWLI. Another feature of the local San Antonio training set is that there are a smaller number of key species which dominate (e.g., *Diploneis litoralis, Nitzschia vitrea, Eunotia paladosa).* Moreover, as in the regional dataset the dominance of *Planothidium delicatulum* is akin to the local training set. Notwithstanding that the rest

of taxa show similar patterns along the elevation gradient as in the local training set. There is not any significant difference between the local and regional dataset in terms of species distributions and elevation optima display similar ranges.

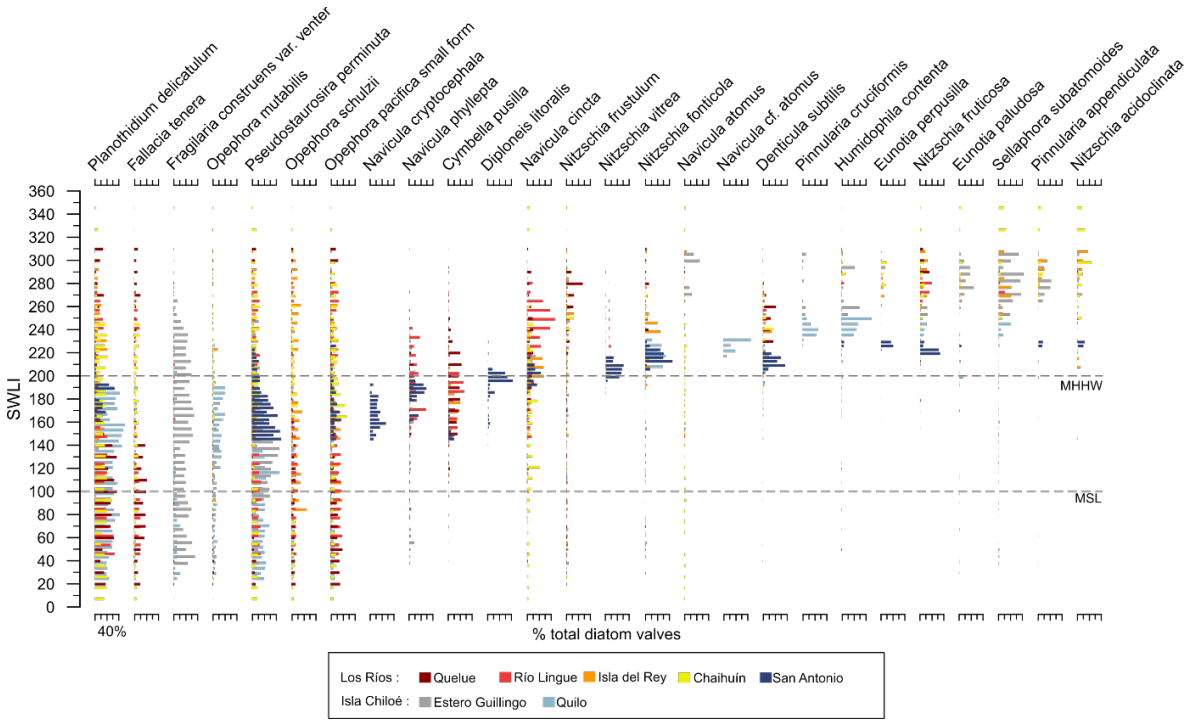

Figure 4.6 : Comparison of San Antonio modern diatom distributions with modern diatom assemblages from across south-central Chile (Hocking et al., 2017), showing taxa exceeding 20% of total diatom valves in at least one sample. Samples are ordered by elevation using SWLI values, and species are ordered by elevation optima as calculated by weighted averaging.

4.6 Ordination

4.6.1 Indirect gradient analysis

Indirect gradient (also known as unconstrained ordination) analysis uses only species samples without prior knowledge of external environmental variables; thus, analysis permits us to explore dissimilarity between samples based on taxa composition. The result of the ordination method suggests a close arrangement of samples and species display better commonality in connection with elevation than those samples and species that are distant from each other (Gauch, 1982, ter Braak, 1995b).

Here, this approach was employed to assess the relationship between modern diatoms in surface samples and elevation, as it is the only environmental variable of interest. The relative importance of species can be inferred by examining the length

of ordination axes since a longer axis explains more variation in the amount of species turnover compared to shorter axes (ter Braak, 1986, ter Braak and Prentice, 1988). The assemblage composition, therefore, was inspected in the unconstrained ordination method DCA in order to determine the explanatory dependent environmental variable, in this case elevation, and axis lengths are reported in Figure 4.7 since such ordination plots provide excellent outputs for visually assessing the major patterns of taxa variation within the data (Legendre and Birks, 2012). This method is based on a technique used to estimate unimodal response curves along the environmental gradient. No data transformations were applied in order to dampen the effects of the dominant species before running DCA.

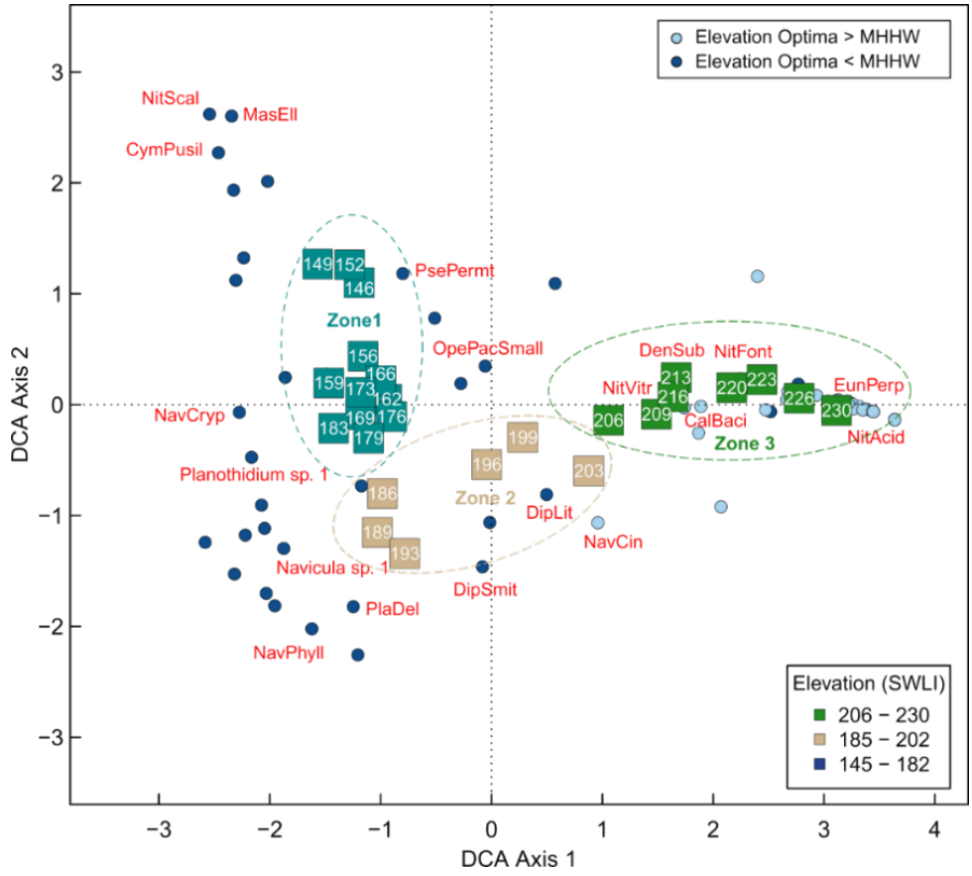

Figure 4.7 : Sample and species score of results from detrended correspondence analysis (DCA) for modern diatom samples from San Antonio. White texts in the boxes show measured elevation values in SWLI units. Red text shows names of diatoms exceeding 10% relative abundance in at least one sample. As a result of the multivariable statistical analysis, samples with similar species compositions are grouped together while samples that have different species compositions plot apart. Ellipses show three different elevation zones which are identified based on CONISS and the broken-stick model.

Moreover, unconstrained ordination methods have been successfully employed to describe relationship between species composition and environmental gradient for diatoms (Garrett et al., 2013, Hocking et al., 2017). However, as this ordination rescaled and is limited by the certain number of segments, the axis scores have no more meaning to explain species composition response (ter Braak and Prentice, 1988). This is a crucial point as DCA divides them into different segments; therefore, the main focus here is the axis lengths rather than species or sample scores (ter Braak and Verdonschot, 1995). Fundamentally, similar species plot close together on the DCA diagram, whilst those species with quite different environmental preferences plot far from one another at opposing ends along a primary axis.

The ordination diagram presents the summary of data showing (dis)similarity of samples or sites and species (Figure 4.7). There is apparent zonation of diatom assemblages based on elevation optima, with elevation appearing to be the primary control on DCA axis 1. Moreover, the DCA axis 1 has a length of 4.63 SD units suggesting there is a unimodal species-environment relationship, and unimodal methods are appropriate for further modelling (Lepš and Šmilauer, 2003).

In addition, DCA was also carried out with the regional dataset from the seven sites in order to explore the pattern of species abundance varying along the underlying compositional gradients (Figure 4.8). The first-axis sample ordination has a length of 4.03 SD indicating unimodal distribution (Lepš and Šmilauer, 2003). Again, elevation explains most of the variation along DCA axis 1, with tidal flat samples clustering towards the negative side of axis 1. It appears that the distribution of modern samples from San Antonio is more aligned with the south-central Chile sites (Queule, Rio Lingue, Isla del Rey, Chaihuín) than two sites on Isla Chiloé (Estero Guillino, Puente Quilo). However, it is also noticeably different to the south-central Chile samples especially for those samples collected at marsh surface. Furthermore, there is greater variation along axis 2 in samples from San Antonio, Rio Lingue and Isla del Rey compared to the other sites. In the regional dataset, the relative importance of the ordination axis can be inferred from the eigenvalues resulting from DCA of modern diatom assemblages. The first axis, with the largest eigenvalue of 0.421, suggests an evident influence while, the second axis, with an eigenvalue of 0.400, also represents an important environmental variable. Moreover, the modern samples do not form a straight or quasistraight line along the first axis, which implies that other environmental variables are also important. This suggests that elevation alone is not a strong

determinant and that other environmental gradients play a role in shaping the changes in diatom distribution across contemporary samples.

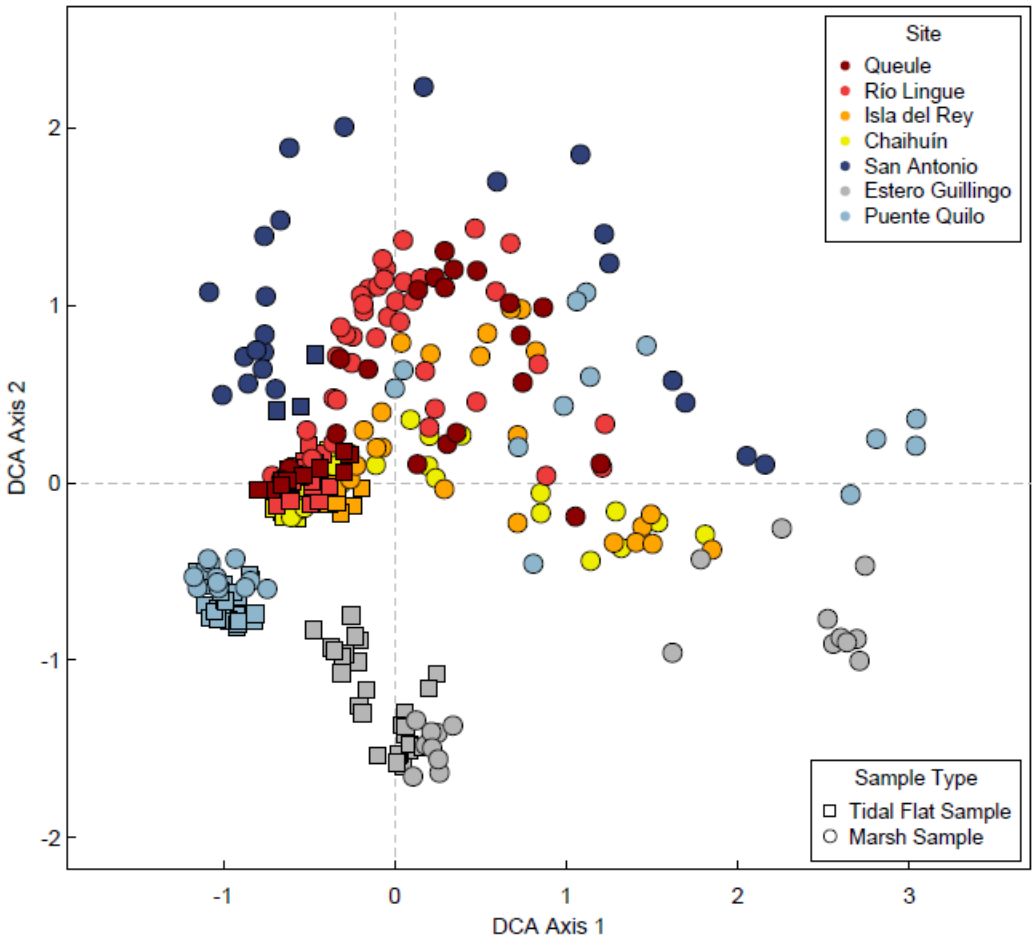

Figure 4.8 : Detrended correspondence analyses plot for the modern samples from seven sites in south-central Chile using all modern samples. Colours reflect sites and symbols reflect sample type from modern environments.

4.6.2 Direct gradient analysis

The relationship between species composition and the known environmental variable of interest (sample elevation) can be measured by employing constrained ordination methods, also known as direct gradient analysis (ter Braak, 1986, ter Braak and Prentice, 1988, Lepš and Šmilauer, 2003). Direct gradient analysis is applied and constrained by using SWLI values as elevation to ascertain the gradient length. The DCCA results show that the gradient length of axis 1 for the San Antonio dataset is 4.44 SD units and 2.69 SD units for the regional dataset, both of which exceeding 2 standard deviation (SD) units (Birks, 1995) and thereby show adequate rate of species compositional change along the elevation (SWLI) gradient to be able to

assume a unimodal species response and adoption of unimodal methods in subsequent transfer function development. Hence, the result from the DCCA supports the hypothesis that diatom assemblages are associated with elevation. These estimates provide a guide to which type of regression to be followed for developing of calibration functions from modern samples for quantitative environmental reconstructions (ter Braak et al., 1993, Birks, 1995, 2010).

CCA is a multivariate analysis to establish the relationship between a dependent variable (biological assemblages) and independent variable (environmental gradient) (ter Braak, 1986). The ratio between the eigenvalue of the first axis of the constrained ordination and the eigenvalue of the unconstrained ordination (λ1/λ2) in CCA ordinations was calculated to assess the explanatory power of the environmental variable of interest. It has been suggested that when this value is greater than 1.0, it can be considered as an important environmental variable for calibration (ter Braak, 1988, Juggins, 2013). Moreover, CCA allows us to estimate how much variance is explained by the environmental variable in the diatom dataset. Therefore, the relationship between diatom assemblage composition and measured sample elevation was examined by employing CCA (ter Braak and Verdonschot, 1995).

4.7 Transfer function development

There are various approaches available for developing transfer function models, including WA, WA-PLS, and LW-WA, which are discussed in detail in Section 3.5.3.2 (Birks, 1995, Juggins and Birks, 2012, Kemp and Telford, 2015). This section explores and assesses these approaches based on their accuracy and statistical robustness and ensures modern taxa-environmental relationships make ecological sense (Birks, 1995, Juggins and Birks, 2012).

Ordination methods confirm a unimodal species response to elevation. It is, therefore, appropriate to use weighted averaging methods for transfer function development (ter Braak and Prentice, 1988, Lepš and Šmilauer, 2003, Birks, 2010). The weighted averaging method estimates species optima and tolerance based on measured relative abundance species and environmental variables; thus, species characterised by their occupation upon these niches in environmental space (ter Braak and Barendregt, 1986, ter Braak and Prentice, 1988, ter Braak and van Dame, 1989).

As there is no certain consensus and also various suggestions on how to select the training set to use to develop the transfer function depending on the taxa-

environmental relationship (Birks, 1995, Juggins and Birks, 2012), different methods are employed to establish transfer function models.

The entire modern diatom dataset comprises 289 samples and 235 taxa from seven sites across south-central Chile (San Antonio from this study and six other sites from Hocking et al., 2017). For the purpose of the sample selection, datasets are considered as twofold: a) the local training set covering 26 modern samples from San Antonio and b) the regional training set comprising all 289 surface samples. Different models are developed using these modern training sets from different spatial scales and using different regression and calibration outputs (WA, WA-PLS and LW-WA).

The model choice hinges upon statistically significant performance and inspection of elevation optima of species. Performance was evaluated based on the statistical summaries of root mean squared error of prediction (RMSEP), maximum bias and coefficient of determination (r^2) values, as is common practice (Birks, 1995, 1998, Juggins and Birks, 2012) and species coefficients (Wright et al., 2011, Hocking et al., 2017). Moreover, when residuals were considered as outliers if they were present and lie outside of range larger than 2.5 SD units, these samples were excluded from the regional training set in order to improve the performance of transfer function models (Juggins and Birks, 2012). In all cases, bootstrapping cross-validation was applied to obtain sample-specific errors (Birks et al., 1990, Birks, 1995). Therefore, these steps are followed to generate the best transfer function models so as to apply to fossil samples for reconstructing palaeosurface elevation change, and hence RSL, at San Antonio and coastal sites along the Valdivian coast.

4.7.1 Transfer function model development with local dataset

The local training set contains 26 modern samples from the San Antonio tidal marsh. Only three samples come from the tidal flat and the rest are from vegetated parts of the marsh. As the number of samples is limited, for the purpose of developing the transfer function with the local training set, all samples are included in the analysis. CCA indicates that SWLI (elevation) accounts for a total of 22% of the total variance in diatom data from San Antonio; λ_1/λ_2 is 1.11 which is greater than 1.0; thus, it suggests that the variable of interest represents an important ecological determinant in the local training set and meets criterion for a useful calibration (ter Braak, 1988). The modern diatom surface distributions of the sampled tidal zone in the San Antonio estuary exhibit a well-established relationship with elevation and hence are suitable for reconstructing RSL change.

The local WA-PLS model does well at predicting elevation (Figure 4.9), residuals are non-structured, and the performance statistics show that the three-component model performs best with the highest r^2 and lowest RMSEP providing at least 5% reduction with addition of extra components (Birks, 1995, 1998) (Table 4.1). The four and five component models are not considered as RMSEP values increase and the models are influenced by overfitting (ter Braak and Juggins, 1993).

Table 4.1 : Summary statistics of WA-PLS regression for the local training set.

Model	**Samples Included**	**No. of samples**	**WA-PLS Component**	**Av bias** $_{boots}$	**Max bias** $_{boot}$	r^2_{boot}	**RMSEP** $_{boot}$	**ΔRMSEP (%)**
Local Model	All	26	1	0.90	12.77	0.91	9.01	-
			2	0.98	9.59	0.94	7.37	18.20
			3	1.35	8.29	0.96	6.92	8.80

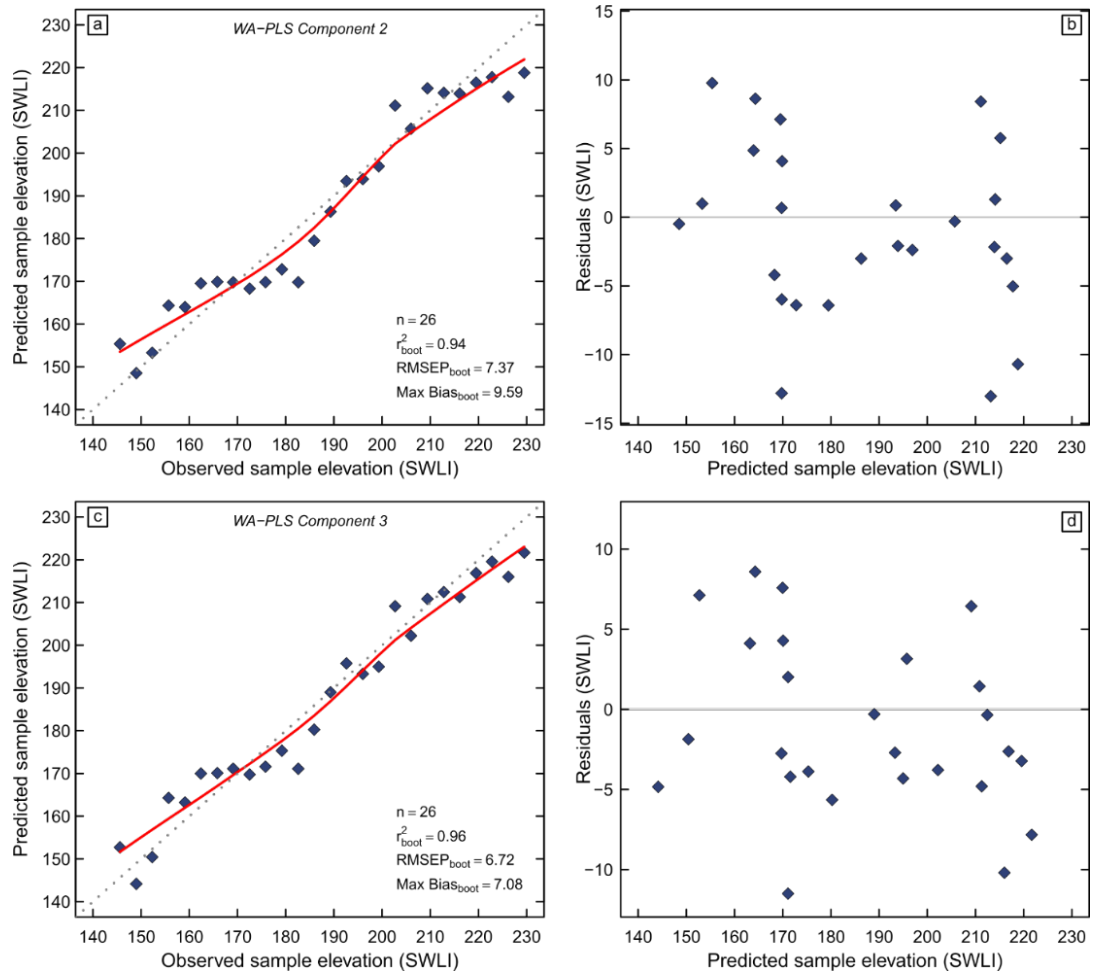

Figure 4.9 : Predictive ability and bias for WA-PLS two and three component transfer function models developed using the local diatom training set from San Antonio. WA-PLS component 2 and 3 models are shown in (a) and (c) with solid lines representing a locally weighted regression and smoothing scatterplot (LOWESS); the grey dotted is a 1:1 line; (b) and (d) show residuals. With the purpose of avoiding apparent prediction bias in the model, estimates for residual and predicted values are used for the axes (following Racca and Prairie, 2004).

However, instead of relying solely on performance statistics, any distortion of elevation optima of the major species (> 5%) by addition of model components is investigated. It is suggested that when applying unimodal based methods, many species ought to their reach optima within the sampled gradient (ter Braak and Barendregt, 1986, ter Braak and Looman, 1986). Therefore, the species optima and beta coefficients are investigated for all components on the basis of their effects on model performance (see Wright et al., 2011). Species optima with WA and species coefficients with WA-PLS methods were plotted against SWLI units (Figure 4.10). The first component of the WA-PLS model uses an adjusted form of inverse deshrinking

of WA model (ter Braak and Juggins, 1993, ter Braak et al., 1993), and as a result, they show very similar performance. By adding more components, in theory WA-PLS regression adjusts species' coefficients with the optima at the low end and high end of the elevation gradient (ter Braak and Juggins, 1993). As in the theory, here it is observed that the WA-PLS component 1 and WA display rather similar species pattern along the sampling elevation. The only distortion of species coefficients occurs at the lower end of the elevation gradient, with only *Nitzschia scalpelliformis*, *Cymbella pusilla* and *Mastogloia elliptica* sensitive to component selection. There is no considerable or systematic difference between the two or three component model in terms of species coefficients. Therefore, on the basis of performance statistics and consideration of species components, the WA-PLS component 3 model is confirmed to be the preferable model for reconstruction using the local modern training set.

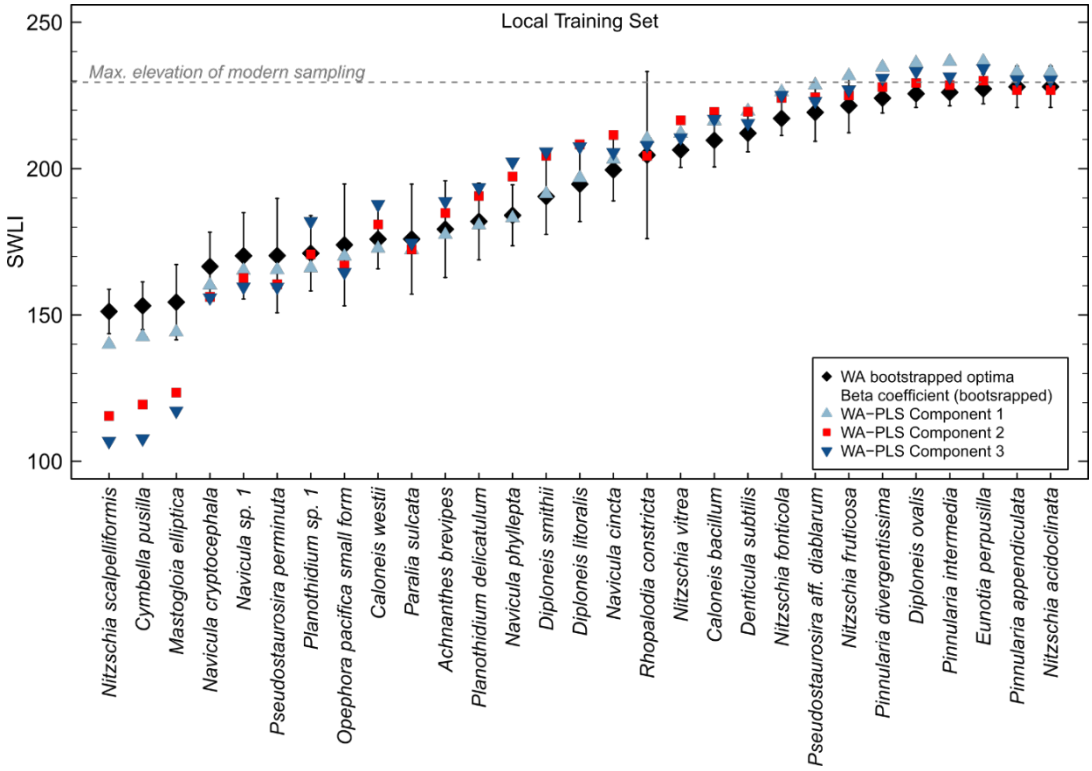

Figure 4.10 : Comparison of species coefficients for WA and WA-PLS first, second and third components with vertical errors bars for species. Only diatoms exceeding 5% in a single sample are shown.

4.7.2 Transfer function model development with regional dataset

4.7.2.1 Weighted Averaging Partial Least Squares Model (WA-PLS)

WA-PLS is first performed using the entire regional training set. Relative to the first and second components, the three-component model statistically performs best (Table 4.2), but unfortunately when the full regional dataset is used, the transfer function does not do well at predicting elevation particularly for tidal flat samples (generally below ~125 SWLI), and the residuals are also highly structured, with the well-known edge effects in weighted averaging and correspondence analysis methods being apparent (Hill and Gauch, 1980, ter Braak and Prentice, 1988) (Figure 4.11). CCA indicates that SWLI accounts for a total of 5% of the total variance in diatom data from San Antonio; λ_1/λ_2 is 0.51 which is lower than 1; thus, it suggests that the variable of interest does not represent an important ecological gradient in the regional training set and does not meet criterion for a useful calibration (ter Braak, 1988).

Table 4.2 : Summary statistics for model A: WA-PLS regression with full training set. Model A contains 289 modern analogues.

Model	Samples Included	WA-PLS Component	Av bias boots	Max bias boot	r^2 boot	RMSEP boot	ΔRMSEP (%)
Model A	All (289)	1	0.17	120.62	0.56	50.53	-
		2	-0.49	106.70	0.65	45.85	9.26
		3	**-0.85**	**99.85**	**0.72**	**42.00**	**8.41**

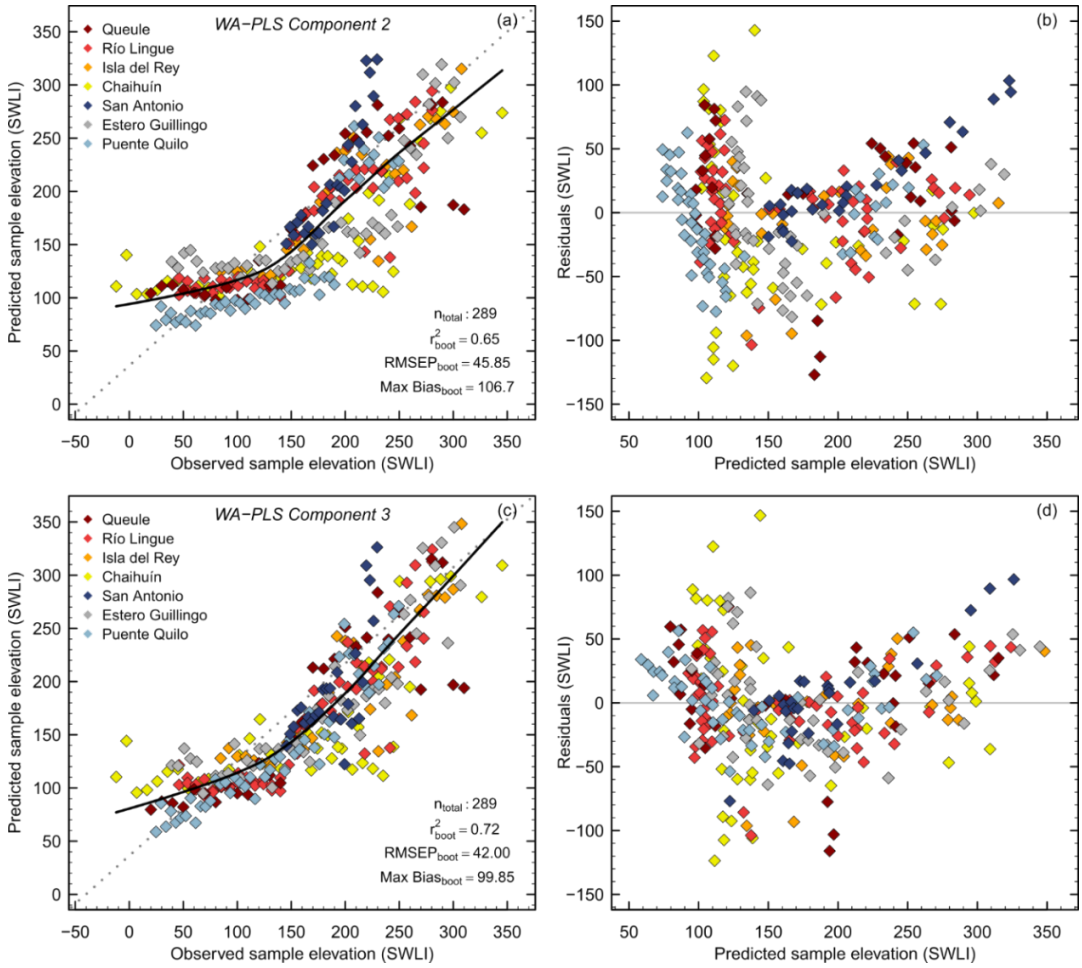

Figure 4.11 : Predictive ability and bias for WA-PLS two (a, b) and three (c, d) component transfer function models developed using the full regional diatom training set. Predicted marsh surface elevation values are plotted against observed (a, c) and residuals (b, d). Solid lines on (a) and (c) represent LOWESS; the grey dotted is a 1:1 line.

With additional components, species optima are significantly distorted (Figure 4.12). Both WA-PLS components 2 and 3 produce unrealistic species coefficients that do not make ecological sense and predict elevations outside the range of sampling. Therefore, Model A with the full regional set including all samples should not be used going forwards in reconstructions.

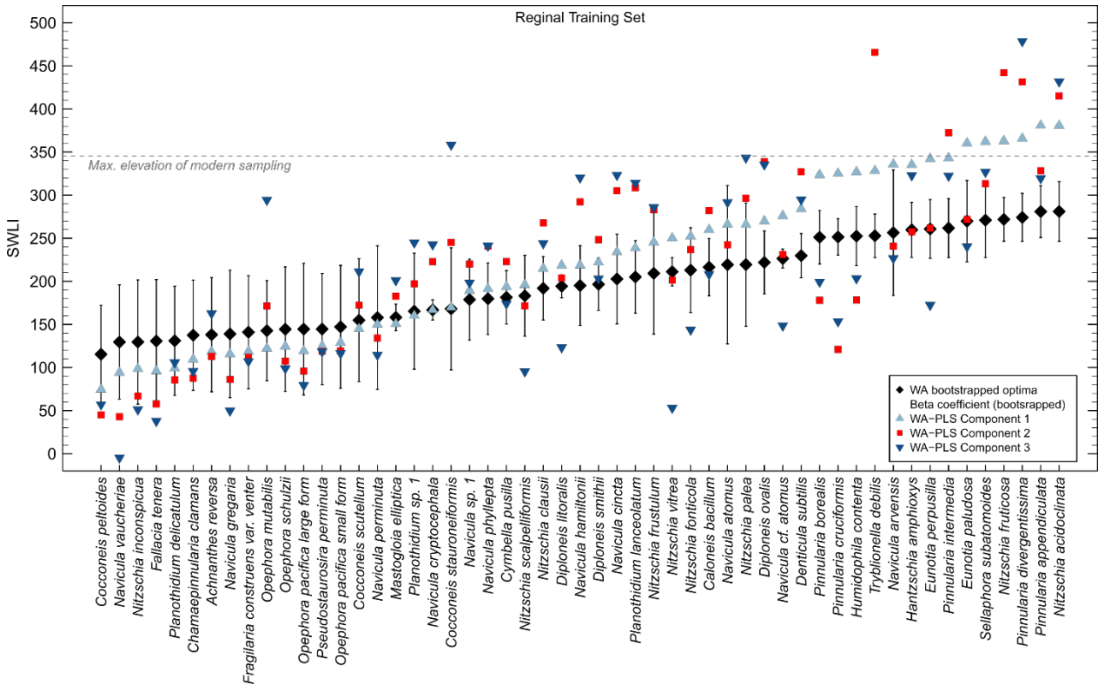

Figure 4.12 : Comparison of species beta coefficients values for Model A (full regional modern training set) based on WA and WA-PLS first, second and third component models under bootstrapped cross-validation for the regional training set. Vertical bars show error values for WA beta coefficients for the Model A.

Due to the poor performance of the transfer function at lower elevations, the regional transfer function (Model A) was re-run removing tidal flat samples (Model B) (Figure 4.13). This improves model performance (3% and 39% improvements in r^2 and RMSEP respectively) (Table 4.3). Moreover, it is suggested that where residuals of samples are out of the range standard deviation (SD)*2.5, these are identified as outliers (see Juggins and Birks, 2012) and excluded from the training set (Model C).

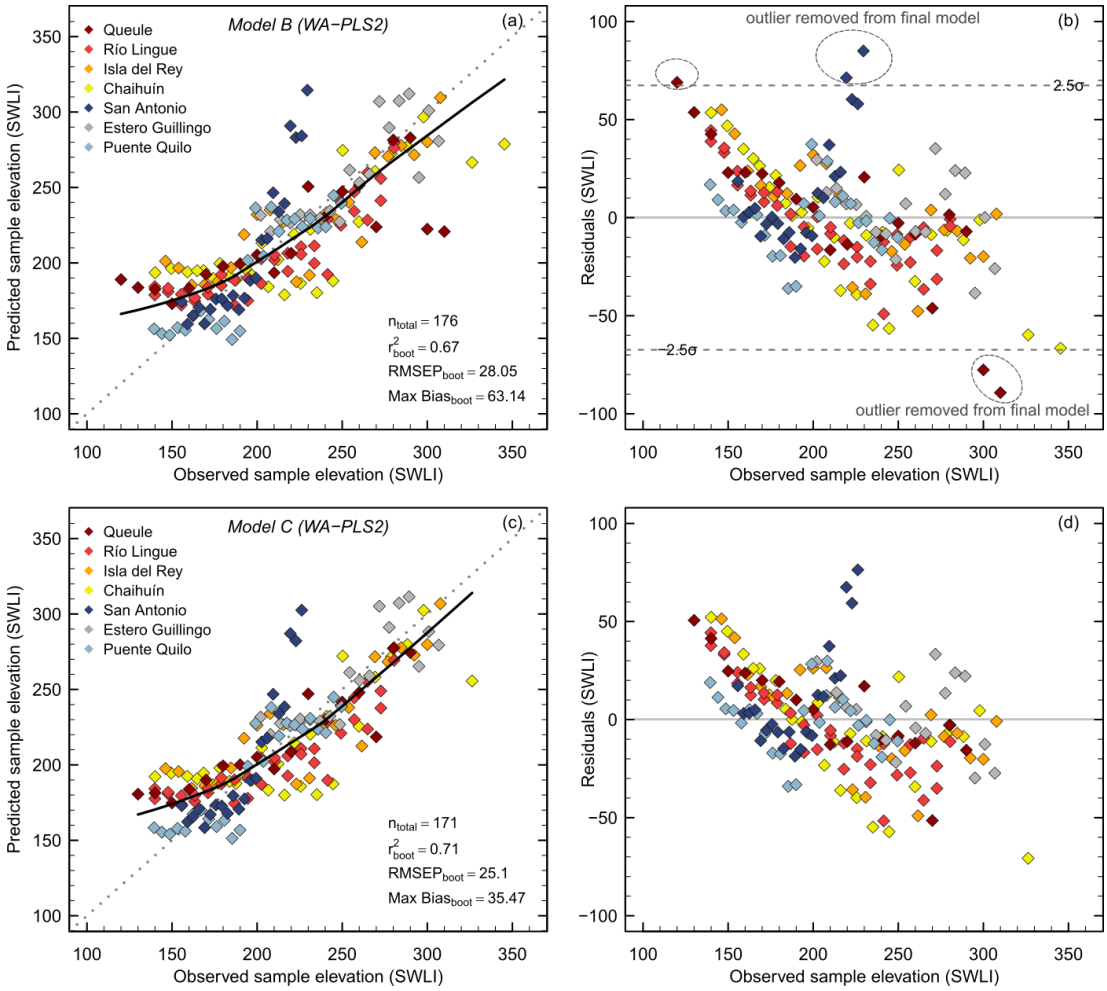

Figure 4.13 : Predictive ability and bias for WA-PLS two component models using the regional training set after removal of tidal marsh samples (Model B – a, b) and with excluding tidal flat samples and residual outliers >2.5 SD (Model C – c, d). Predicted marsh surface elevation values are plotted against observed (a, c) and residuals (b, d). Solid lines on (a) and (c) represent LOWESS; the grey dotted is a 1:1 line.

When tidal flat samples and residual outliers are removed (Model C), this further improved performance, particularly at the higher end of the elevation gradient. Based on performance statistics, the two-component model performs best, with the addition of a third component not producing the required 5% reduction in RMSEP (Birks, 1995). However, CCA indicates that SWLI accounts for a total of 5.94% of the total variance in diatom data from San Antonio; λ_1/λ_2 is 0.66 which is lower than 1.0; thus, it suggests that the variable of interest does not represent an important ecological gradient in this dataset and does not meet criterion for a useful calibration (ter Braak, 1988).

Table 4.3 : Summary statistics of models B and C: WA-PLS regression with regional dataset excluding tidal flat samples (B) and excluding tidal flat samples and residual outliers (>2.5SD) (C). Models in bold are preferred number of components. Model B contains 176 modern analogues, Model C contains 171 modern analogues after removal of tidal flat samples.

Model	Samples Excluded	WA-PLS Component	Av bias boots	Max bias boot	r^2 boot	RMSEP boot	ΔRMSEP (%)
Model B	Tidal flat samples (176)	1	-0.21	79.61	0.57	30.97	...
		2	**-0.56**	**63.14**	**0.67**	**28.05**	**9.41**
		3	-0.55	53.45	0.70	27.13	3.31
Model C	Tidal flat + outliers (>2.5SD of residuals) (171)	1	-0.07	43.25	0.61	28.21	...
		2	**-0.32**	**35.47**	**0.71**	**25.10**	**11.03**
		3	-0.46	35.85	0.74	24.08	4.07

Further investigation of species coefficients was carried out to confirm the appropriate number of components in WA-PLS regression. Figure 4.14 confirms that removing tidal flat samples and outliers significantly reduces the distortion of species coefficients compared to when all regional samples are included. Notwithstanding, *Nitzschia frustulu*m and *Nitzschia acidoclinata* still present distortion for the 2 and 3 component models and species coefficients exceed the maximum elevation of modern sampling range (Figure 4.14). However, significant distortions do not occur for other species and therefore the WA-PLS component 2 model can be employed in fossil reconstructions.

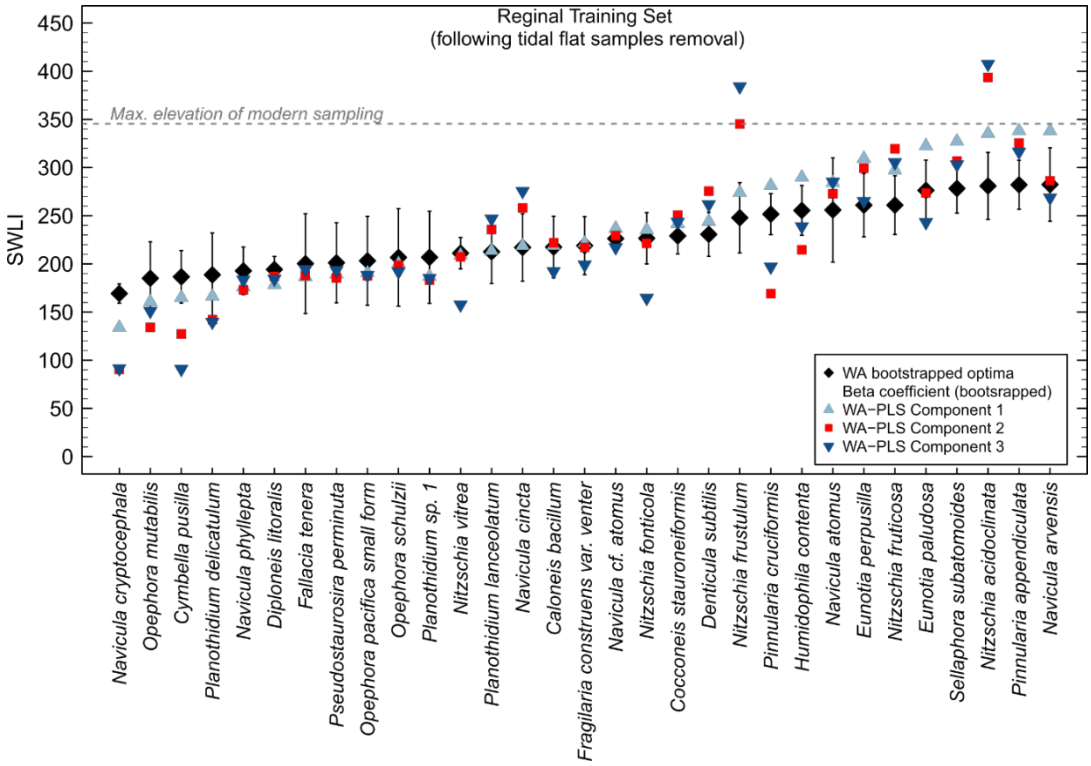

Figure 4.14 : Comparison of species beta coefficients values based on WA and WA-PLS for Model C using the regional modern training set excluding tidal flat samples and outliers >2.5 SD. Vertical bars shows error values for WA beta coefficients for the No Tidal Flat Models.

4.7.2.2 Locally Weighted Weighted-Averaging (LW-WA)

In addition to WA-PLS, Locally Weighted-Weighted Averaging (LW-WA) is also employed using the regional dataset, as LW-WA aims to combine the best properties of weighted averaging and the modern analogue technique (Birks, 1998, Hübener et al., 2008, Juggins and Birks, 2012). This method is also known as moving-windows which utilise k-nearest-neighbour (k-NN) approach where an algorithm classifies the number of close samples in the modern dataset (Hübener et al., 2008). There are no definitive criteria on the choice of sample size, instead the number of samples is decided as a proportion of the total number of samples. The regional dataset consists of 289 samples and here the number of samples to be used in the local training set is selected from 10% to 50% of the total sample number. Both classical and inverse deshrinking methods are also compared for each model (Table 4.4; Figure 4.15).

Table 4.4 : Summary statistics of cross-validated LW-WA regressions using the regional dataset.

Model	Samples Included	No. of Samples in local training set	Deshrinking	Av bias boots	Max bias boot	r^2 boot	RMSEP boot
Model D	Outliers excluded*	29	Inverse	3.25	72.01	0.86	29.60
			Classical	1.41	64.56	0.88	28.31
Model E	All	29	Inverse	3.13	82.35	0.84	32.64
			Classical	0.93	72.24	0.85	31.85
Model F	All	58	Inverse	1.46	100.31	0.76	39.08
			Classical	-6.04	90.99	0.78	39.38
Model G	All	87	Inverse	-0.96	109.43	0.72	41.44
			Classical	-11.21	103.89	0.74	44.51
Model H	All	116	Inverse	-2.24	113.27	0.69	43.16
			Classical	-13.75	109.31	0.70	49.12
Model I	All	146	Inverse	-2.78	113.06	0.66	44.95
			Classical	-14.56	105.00	0.67	53.32

*Outlier samples standard deviation (SD*2.5) excluded

Model performance improves as the number of samples included in the local training set decreases. In all cases, as the local sample size used in the model increases, the inverse deshrinking method performs slightly better than classical deshrinking in terms of reducing RMSEP. However, when the number of local samples is smaller (29), the LW-WA model performs slightly better with classical deshrinking in terms of RMSEP and r^2. Together with the local sample size increase, LW-WA overestimates sample elevation at the higher end and overestimates at the lower end of the elevation gradient. However, the benefits of classical deshrinking decrease in parallel with additional sample numbers in the local training set (Figure 4.15).

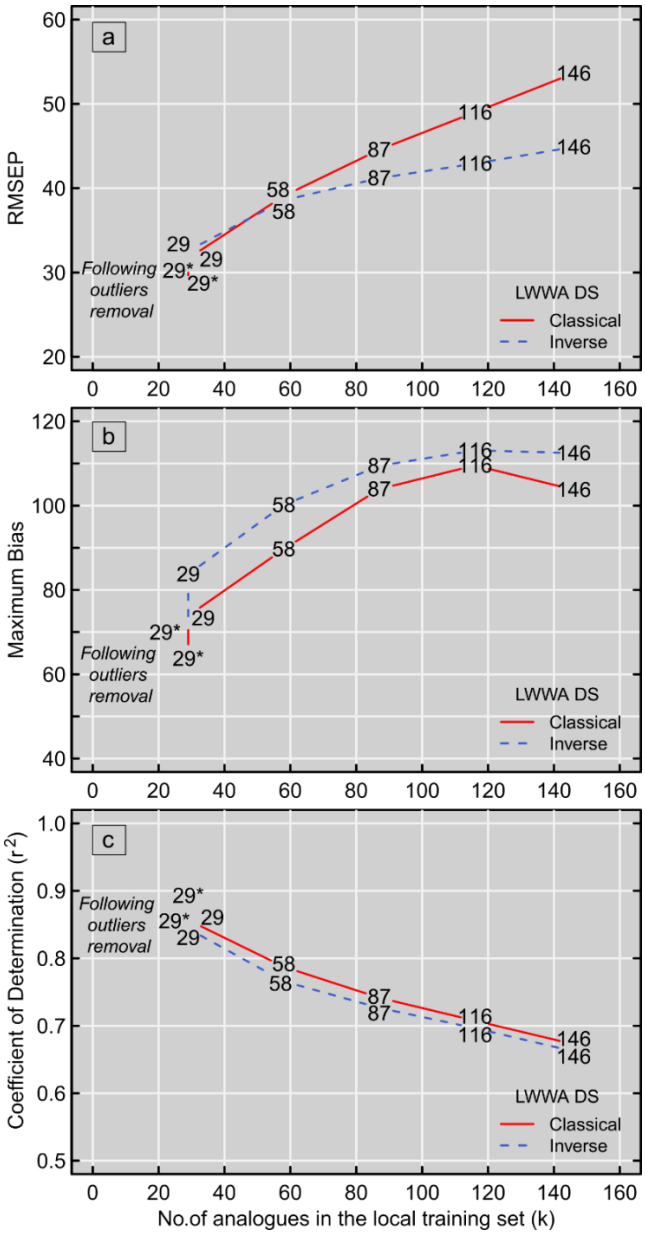

Figure 4.15 : Summary statistics – RMSEP (a), maximum bias (b), r^2 (c) – of cross-validated LW-WA regressions using the regional dataset. Numbers on both red and blue lines indicate the number of samples used in the local training set. Asterisk indicates the model results after removal of the outlier samples from the training set.

Even though both deshrinking methods display quite comparable results in terms of statistical performance, there is a minor difference that needs to be highlighted. Since the classical model deshrinks more than the inverse model method and it is preferable when reconstructing at the upper and lower ends of the environmental gradient (Birks et al., 1990, Birks, 1998), LW-WA with classical deshrinking presents slightly better statistical results than the inverse deshrinking model when the local sample size in the training set equals 10% and 20% of the total number of samples (Table 4.4). After

excluding the outlier samples from the regional dataset, RMSEP improved by ~12% for classical deshrinking and ~15% for inverse deshrinking which both exceed the 5% reduction threshold (Birks, 1995; 1998). As a result, LW-WA shows promising results, and therefore becomes the third favoured method to employ in the transfer function to calibrate fossil assemblages. Specifically Model D with 10% of samples in the local training set and classical deshrinking (Figure 4.16) is the favoured model over inverse deshrinking (Figure 4.17); thus, this model will be applied in the following chapters to generate reconstructions of palaeosurface elevation.

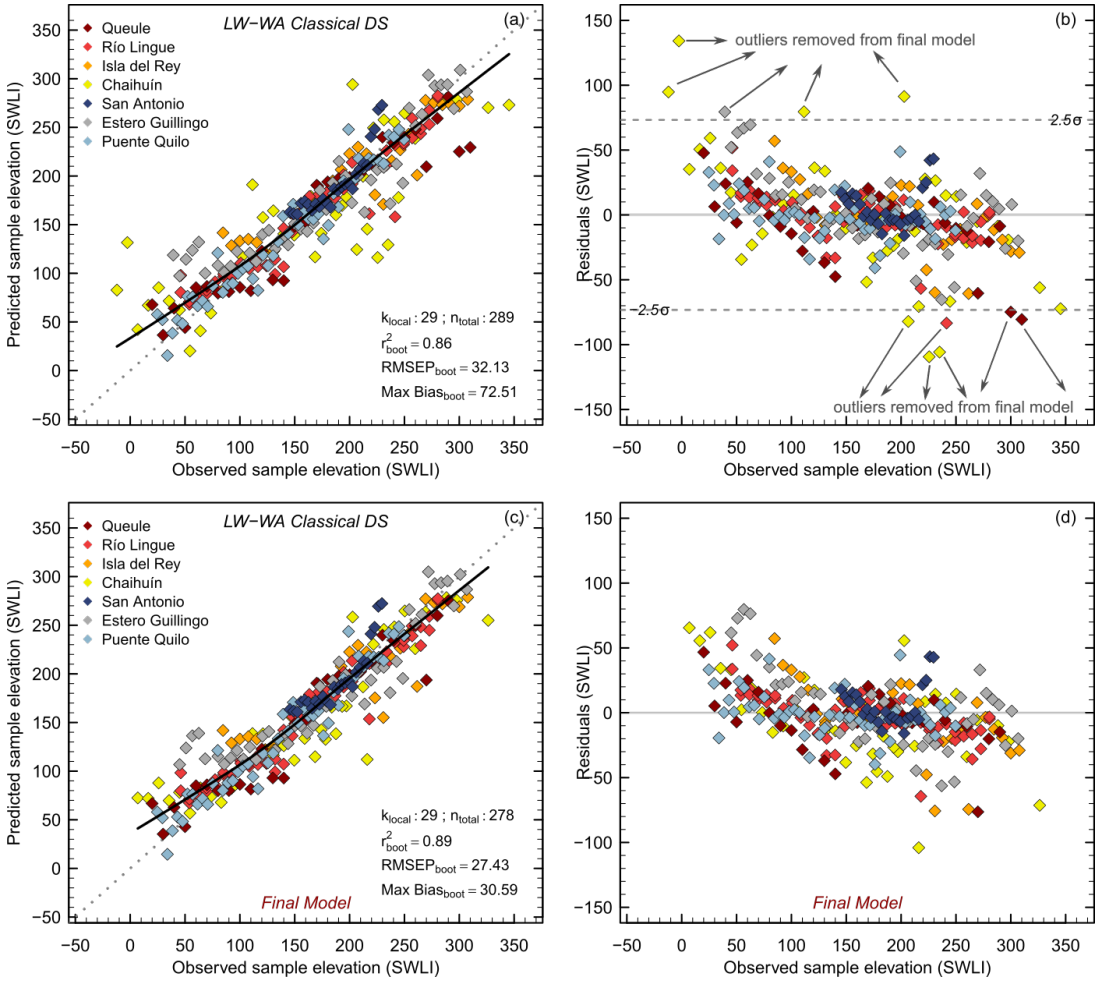

Figure 4.16 : Predictive ability and bias for LW-WA with classical deshrinking containing 10% of samples in the local training set (n=29) and classical deshrinking. Predicted marsh surface elevation values are plotted against observed (a, c) and residuals (b, d). Solid lines on (a) and (c) represent LOWESS; the grey dotted is a 1:1 line.

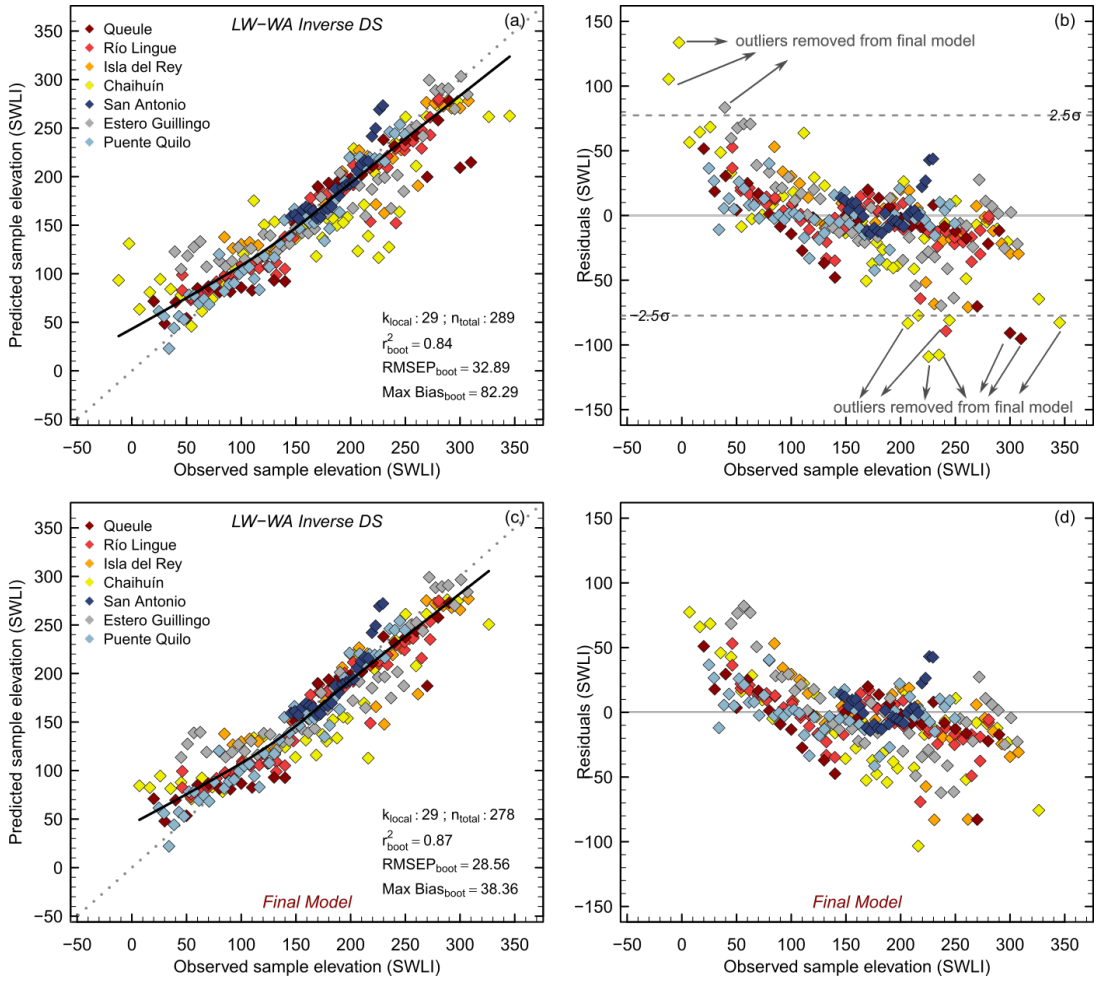

Figure 4.17 : Predictive ability and bias for LW-WA with inverse deshrinking containing 10% of samples in the local training set (n=29) and classical deshrinking. Predicted marsh surface elevation values are plotted against observed (a, c) and residuals (b, d). Solid lines on (a) and (c) represent LOWESS; the grey dotted is a 1:1 line.

4.8 Assessing transfer function models

Through employing different regression techniques and exploring different sample sizes to include and exclude from the modern training set based on spatial scale and sampling environment, numerous transfer function models have been generated and compared (Figure 4.18). The most critical point is to develop models which produce both ecologically and statistically meaningful results.

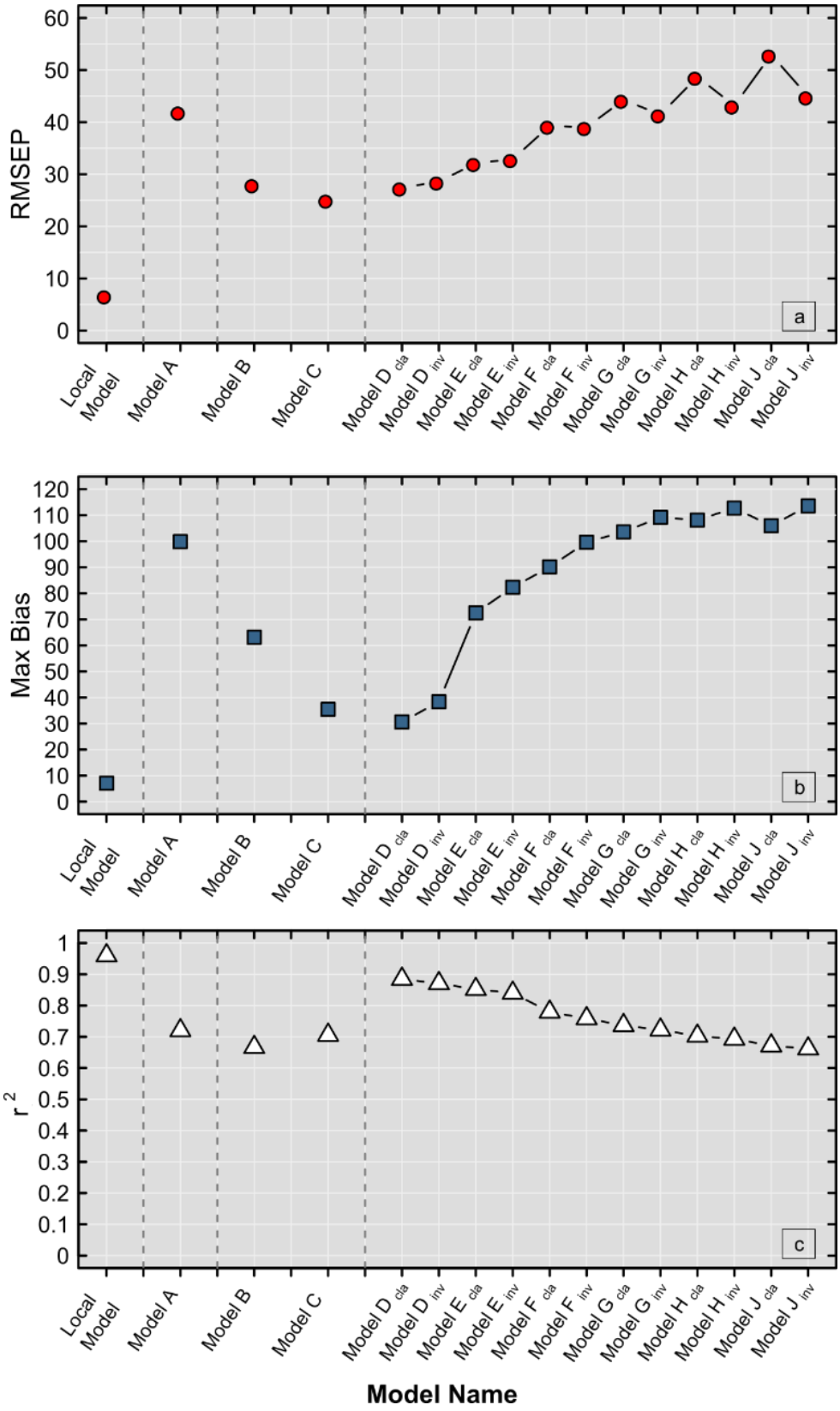

Figure 4.18 : Comparison of statistical performance of all transfer function models: a) RMSEP, b) Maximum bias and c) r^2 coefficient of determination. Cla: Classical deshrinking; Inv: Inverse deshrinking.

Firstly, RMSEP, maximum bias and r^2 values are evaluated for their statistical significance. Secondly, species showing ecologically unrealistic distribution along the sampling transect are inspected by exploring elevation optima from the WA model and species coefficients from the WA-PLS model components, and any models producing unrealistic distortion of species optima were disregarded. Thirdly, the regression method is assessed, and LW-WA models are carried out with varying numbers of local samples included. In summary, for WA-PLS regression, the statistically best model is provided with the local training set, which is followed by WA-PLS regression using the regional training set, but the best models result after removal of tidal flat samples and residual outliers, with the WA-PLS two component model preferred (Model C). The best LW-WA model employs 29 local training set samples (10% of the full training set) and excludes residual outliers (Model D) (Figure 4.18). Therefore, these three models will be applied to fossil data in order to reconstruct palaeosurface elevations in the subsequent chapters. However, SWLI as a variable of interest in both regional and data screen training sets does not represent an important ecological gradient and also the λ_1/λ_2 ratio is lower than 1.0, which does not meet ter Braak (1988)'s criterion for a "useful calibration" (Juggins, 2013). SWLI only accounts for 5% and 6% variance in these datasets, respectively. In contrast, the local dataset SWLI accounts for a total of 22% of the total variance in the diatom data and presents λ_1/λ_2 ratio greater than 1.0; consequently; it presents better and statistically robust estimates. Therefore, when the regional and data screen training sets are applied to the fossil assemblages for reconstructing past SWLI values; caution must be taken to interpret those outputs.

4.9 Summary

This chapter has explored modern diatom assemblages both locally from San Antonio and more broadly across south-central Chile, by using multivariate analysis and developed multiple transfer functions to fulfil the objective to "improve understanding of modern intertidal diatom distributions and develop transfer function models for reconstructing relative sea-change and seek out possible correlation with coseismic deformation" as set out in chapter one. The DCA indicated vertical zonation of species along an elevation gradient in the local training set. Moreover, both DCA and DCCA confirmed a unimodal relationship between diatom taxa and the environment in the regional training set. Subsequent transfer function development used methods appropriate for unimodal data: WA-PLS and LW-WA. The performance of different transfer function models was considered at both local and regional spatial scales. The

local training set demonstrated the best statistical performance while data screened regional training set was also considered, as removing outliers was shown to improve the statistical performance of transfer functions. After careful consideration of different models and elimination of poorer performing models, it was decided to employ the Local Model (WA-PLS component 3), Model C (WA-PLS component 2 with tidal flat samples and residual outliers excluded) and Model D (LW-WA using 10% of samples and classical deshrinking). However, CCA demonstrates that SWLI explains 21.58% of the variance in the local training set, 5.94% in the data screened regional training set and 5.05% in the regional training set. Furthermore, the relative explanatory power ($\lambda 1/\lambda 2$) of each training set also decreases with increasing scale of the training set, emphasising that elevation is not a significant ecological determinant when data are screened, and the regional training sets should be used for model reconstructions. However, elevation remains an important ecological determinant in local training sets.

In the following chapters, the transfer function models developed here will be applied to fossil sequences from San Antonio and six coastal sites across the Valdivia coast, and further assessed using the modern analogue technique to decide how reliable they are to infer palaeosurface change in the past.

Chapter 5 : Results – Reconstructions of relative sea-level change at San Antonio estuary

5.1 Introduction

This chapter presents the results of field and laboratory analyses of the tidal marsh sediments from San Antonio, including diatom assemblages, lithostratigraphy, particle size analysis and dating (radionuclide and radiocarbon). The purpose of this chapter is to analyse these data to reconstruct late Holocene relative sea-level change and determine if there is any evidence of seismic events, at a site located in the Valdivia segment of the subduction zone that ruptured in the 1960 earthquake. It will therefore address the first objective of the thesis, which is to quantify relative land-level (sea-level) change associated with past earthquakes. In order to estimate palaeomarsh surface elevation (PMSE) and consequently relative sea-level change, transfer function models developed in chapter 4 are applied to the fossil diatom record.

5.2 Study area

The setting of the site at San Antonio (41°46'30.68"S, 73°13'11.55"W) is described in chapter 3. Stratigraphic investigations focussed on the salt marsh found at its western end (Figure 5.1). (Figure 4.3).

5.3 Lithostratigraphy

The lithostratigraphy of the estuary was described using multiple cores. A total of 16 gouge cores were sampled across the tidal marsh, taken along two transects, the first one is ~200 m long in a north-south direction (Y-Y') parallel to the marsh front and the second one is ~100 m long and perpendicular to the sea in the east-west direction (X-X') (Figure 5.2).

The stratigraphy of multiple cores was described in the field. With the aim of differentiating the origins of sedimentological change, which may be associated with seismic or non-seismic factors, the presence of abrupt changes was investigated using the established criteria of Nelson et al. (1996) and Shennan et al. (2016). In general, the cores comprise five main sedimentary units (Figure 5.2).

Figure 5.1 : Location of the San Antonio study area, (A) within south-central Chile and (B) on Isla Quihua. The location of the San Antonio estuary and of modern diatom sampling locations are shown on C and D. The red box shows the location of cores that are shown in Figures 5.2. and 5.3.

Across both transects (X-X' and Y-Y'), all cores contain a basal sand unit (L1) which decreases in thickness with distance from the tidal flat, and a top layer of herbaceous peat (L5), which is sometimes silt-rich and of varying thickness. The lowest elevation that the herbaceous peat unit is seen in Y-Y' transect (N-S direction) is at 2.52 m MSL

and X-X' transect (W-E direction) is at 2.90 m MSL. A silt unit containing occasional plant fragments (L2) is observed only in 9 cores across both transects. An organic-rich silt containing abundant plant fragments (L3) found in 15 cores. The silty-rich herbaceous peat unit (L2) occurs every core across the transect. There are no abrupt transitions from organic to minerogenic deposition or vice versa except for a thin sandy-silt layer found at approximately 11 cm depth. This unit is found in six cores (SA18/2, SA18/12, SA18/20, SA18/14, and SA18/13) in X-X' transect and is a thin dark-yellow sandy-silt interbedded in the herbaceous peat at core depths of ~11-11.5 cm. The elevation of these cores ranges from 2.90 to 3.45 m above Mean Sea Level (MSL). The clearest stratigraphic sequence was observed along the X-X' transect; therefore, a pit from this area (SA18/20) was dug and sampled using a monolith tin to carry out further laboratory analyses (grain-size distribution, diatom examination and radiometric dating).

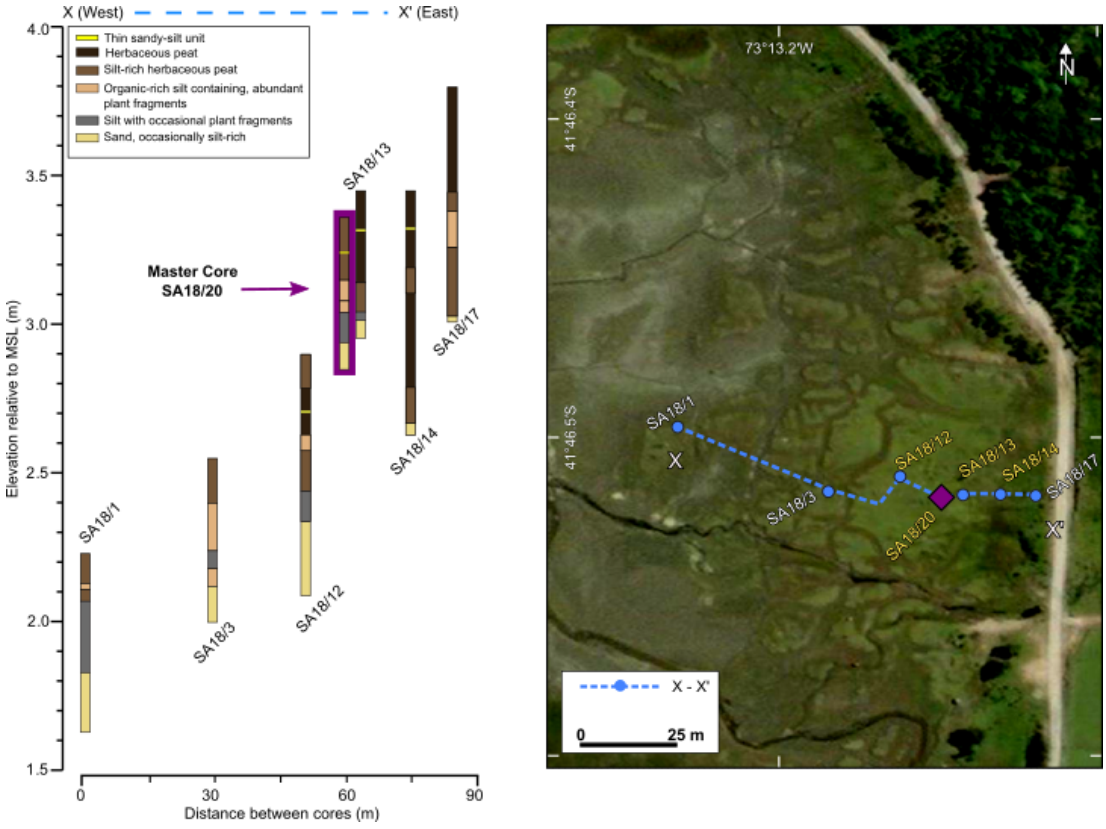

Figure 5.2 : Stratigraphy and location of cores described across an east-west transect at San Antonio tidal marsh. A monolith from pit SA18/20 was taken for further laboratory analyses.

The monolith (SA18/20) is 50 cm long and consists of six main lithostratigraphic units and also includes one thin sandy-silt bed which was considered and named as a main layer (Figure 5.4). The basal unit (U1) consists of a mid-grey sandy silt (43-50 cm). The overlying sedimentary unit U2 is predominantly composed of light-grey silt (32-43 cm). Following that, mid grey-brown (U3, 32-28 cm) and light-brown grey (U4, 28-21 cm) organic silt units occur consecutively. These are overlain by a dark-brown well-humified silty herbaceous peat (U5, 18-21 cm). The uppermost unit (U6) is an 18 cm-thick mid-brown herbaceous peat. This peat layer at the top of the core contains an interbedded thin sandy silt unit found around 11-11.5 cm.

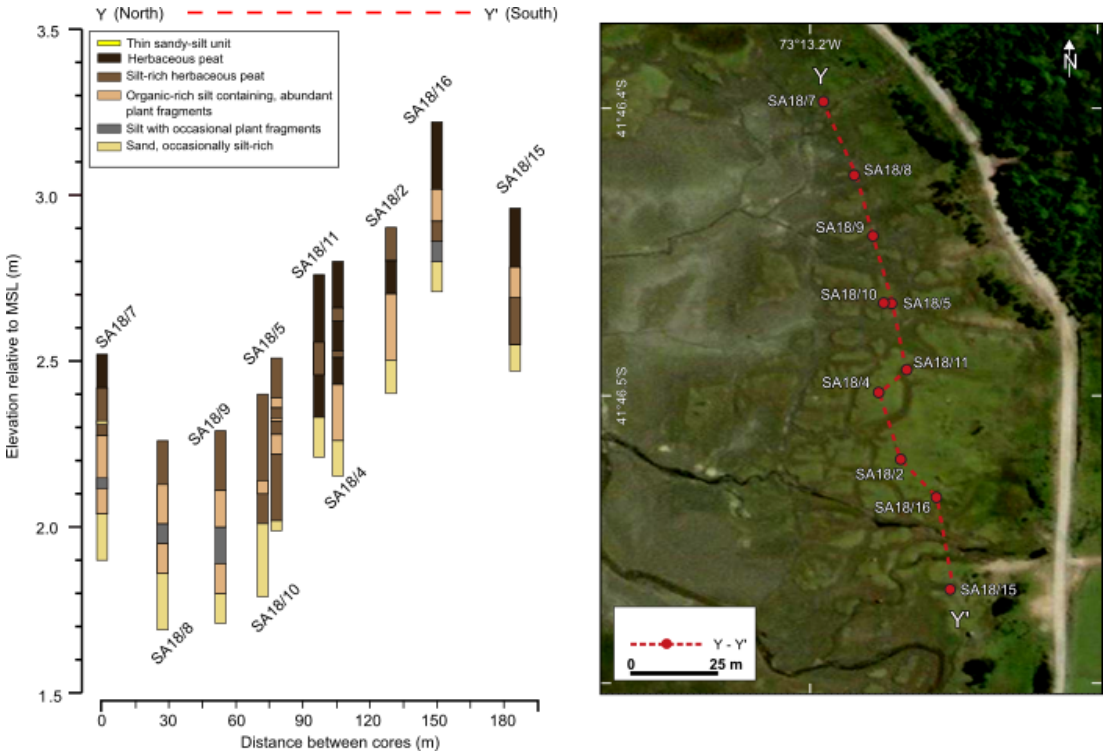

Figure 5.3 : Lithostratigraphy of cores across north-south transect at San Antonio.

Particle size analysis confirms silt dominates the minerogenic fraction of the entire core, with the exception of the bottom sandy layer and a discrete sample at 9 cm (Figure 5.4). The basal unit (U1) contains between 50 and 85% sand, and the minerogenic fraction of the peat layer (U4) also contains between 40-60% sand. The presence of clay is relatively low and never exceeds more than ~ 3% of the grain size distribution. The results of the particle size analysis did not provide a distinct classification for the dark yellow sandy-silt unit located between 11.5-11 cm in the core. From the stratigraphy and particle size analysis, there are two transitions in the core which warrant further investigation: 1) Unit 4 (silt) to 5 (peat) at 21 cm; and 3)

Unit 5 (dark brown silty herbaceous peat) to 6 (mid brown herbaceous peat) at 18-19 cm.

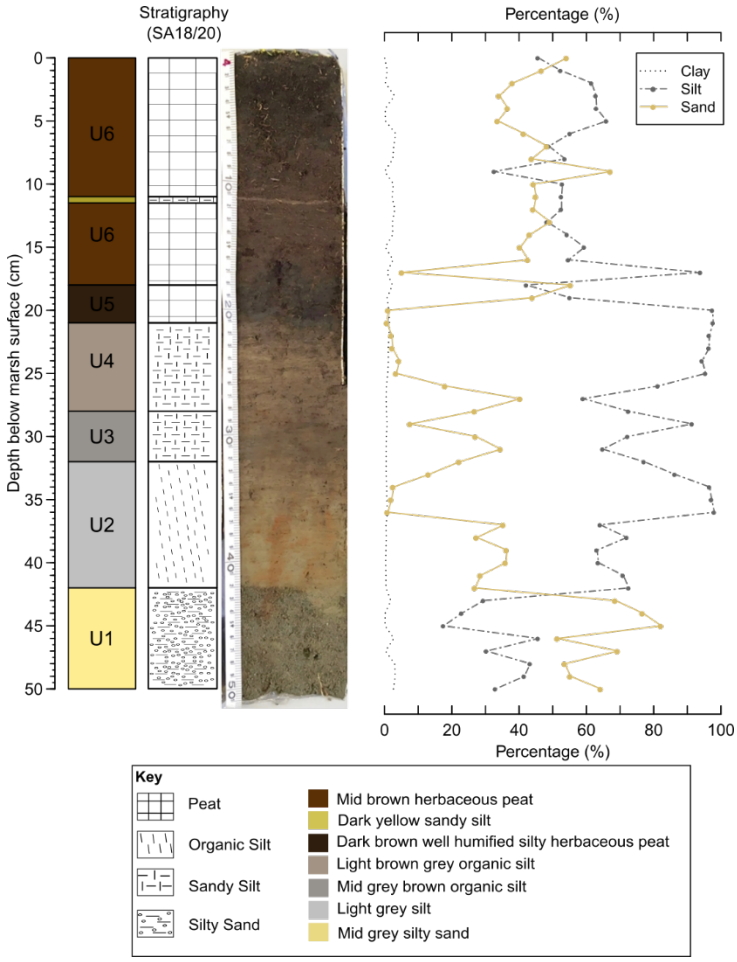

Figure 5.4 : Results of particle size analysis of SA18/20. A total of 50 subsamples were analysed for grain size measurement for the core.

Lastly, it should be noted that when samples were digested using hydrogen peroxide, amount of organic content in sediment can be removed completely and/or as much as acid works. In the case of the peat samples (U5 and U6), this chemical process resulted in the removal of organic material, leaving behind silt, clay, and sand-sized particles. As a result, the particle size analysis of these samples primarily reflects the composition of these particles and may not accurately represent the organic layers present in sediments with a high percentage of organic matter, such as peat. Therefore, particle size analysis may not be a suitable metric for characterising sediments with a significant amount of organic material.

5.4 Biostratigraphy

Preliminary diatom analysis through core SA18/20 was carried out by Dr Ed Garrett and confirmed there is apparent zonation of diatom assemblages (from 0 to 42 cm at 2 cm interval). Following this, sampling at higher resolution was undertaken in order to further examine changes in diatom assemblages around key transitions. This increased the sampling resolution to every 0.5 cm for 5-13 cm and 16-25 cm of the monolith and every 2 cm for other sections.

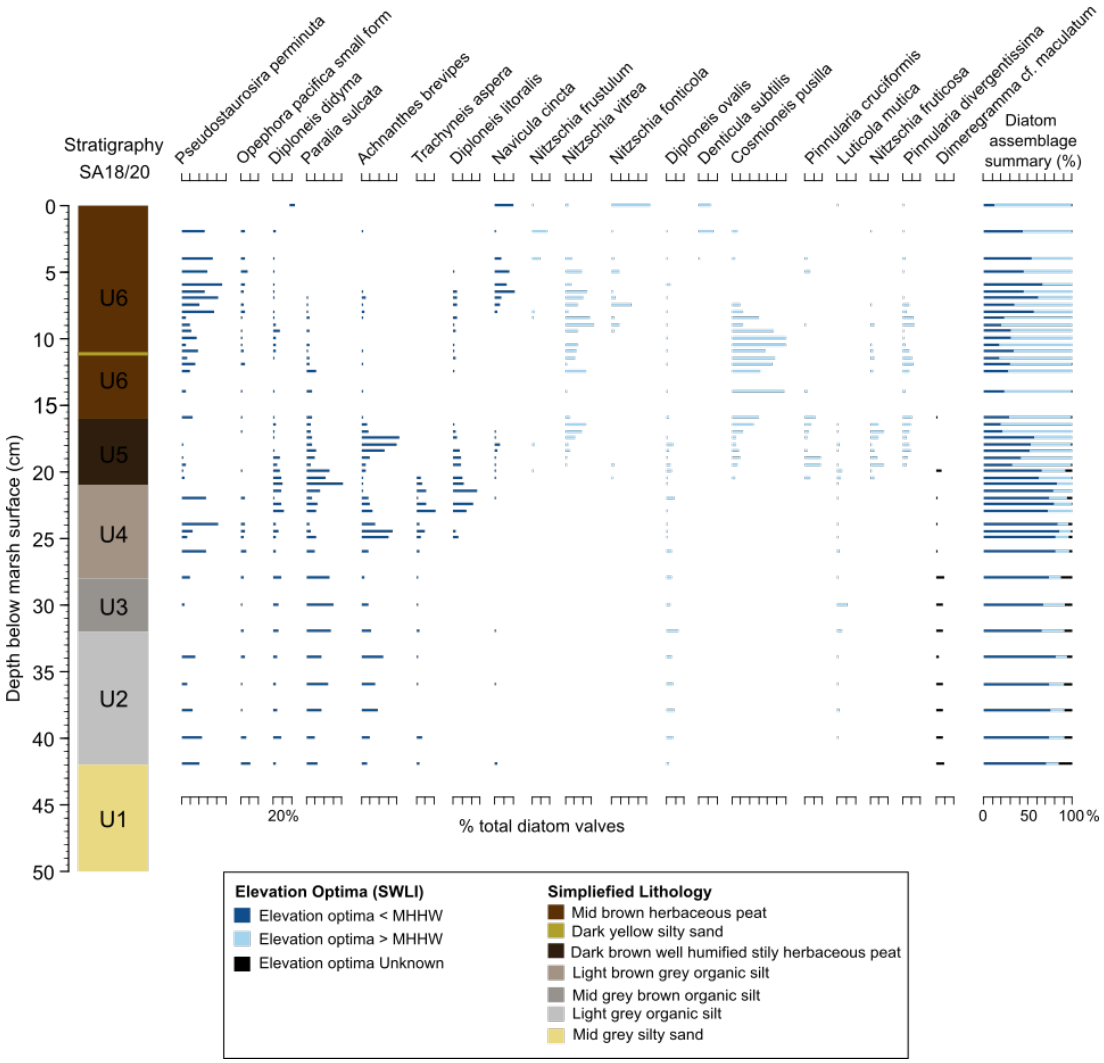

Figure 5.5: Summary of diatom assemblages from core SA18/20 at San Antonio estuary. Relative abundance of diatoms is expressed as the percentage of the total count. Only taxa exceeding 10% of total diatom valves in at least one sample are shown. Species are classified as below MHHW or above MHHW based on modern species elevation optima derived from the WA method.

Diatom analysis revealed 105 taxa, of which 100 also occur in the modern dataset (chapter 4), and only 19 exceed 10% in one or more fossil sample (Figure 5.5). Between 20 and 42 cm, the assemblages are chiefly dominated (~70-85%) by species with elevation optima below MHHW, particularly *Achnanthes brevipes*, *Paralia sulcata* and *Pseudostaurosira perminuta.* Across the silt-peat transition (unit 4 to 5) there is gradual decline in species with elevation optima below MHHW (e.g., *Pseudostaurosira perminuta*, *Paralia sulcata, Trachyneis aspera* and *Diploneis litoralis*) and appearance of species with higher elevation optima (e.g., *Cosmioneis pusilla, Pinnularia cruciformis, Nitzschia fruticosa, Pinnularia divergentissima*). At 17 cm, 1 cm below the transition between units 5 and 6, there is a sharp decrease in relative abundance of *Achnanthes brevipes* (from 40 to ~5%) and increase in abundance of *Nitzschia vitrea* and *Cosmioneis pusilla*. The sandy layer at 11-11.5 cm is not associated with a change in diatom assemblage. Above this, there appears to be a transition in diatom assemblages around 7-8 cm, with increase in the relative abundance of species with sub-MHHW elevation optima including *Pseudostaurosira perminuta* and *Navicula cincta*, and a decline in the abundance of species with supra-MHHW elevation optima including *Nitzschia vitrea* and disappearance of *Cosmioneis pusilla* and *Pinnularia divergentissima*.

5.5 Chronology

The chronology of the monolith (SA18/20) was established through radiocarbon (^{14}C) and radionuclide (Lead-210, ^{210}Pb, and Caesium-137, ^{137}Cs) dating (Table 5.1, Figure 5.6, Figure 5.7, Figure 5.8). Sub-sampling for ^{210}Pb and ^{137}Cs measurement was conducted using 1-cm thick samples at intervals of 1 cm, starting from 0.5 cm down to a depth of 9.5 cm. The last subsample was collected at a depth of 13.5 cm, providing the necessary number of samples for measuring ^{210}Pb, ^{226}Ra, and ^{137}Cs isotopes. However, only samples that yielded adequate measurements were at 1.5, 3.5, 5.5, 7.5, 8.5, 9.5 and 13.5 cm. A single plant macrofossil was used for radiocarbon dating at 37.5 cm depth to constrain the maximum age for the core. The radiocarbon age is calibrated to calendar years using the Southern Hemisphere atmospheric calibration curve SHCal20 (Hogg et al., 2020) in OxCal 4.3 (Bronk Ramsey, 2009). The age-depth model was generated using the serac package in R based on constant flux constant sedimentation (CFCS), constant initial concentration (CIC) and Constant Rate Sedimentation (CRS) models (for details see Bruel and Sabatier, 2020).

The age model generated based on measurement of ^{210}Pb provides a shorter record of ~140 years (Figure 5.6). The activity of ^{210}Pb excess decreases monotonically with

depth and suggests a sedimentation accumulation rate (SAR) of 0.099 cm/yr using the CFCS model. The three models suggest slightly different depths for the 1960 earthquake, with depths of 5.5, 7.5 and 8-9 cm suggested by the CFCS, CRS, and CIC models, respectively. For sediments below 9.5 cm depth, the CIC model presents large uncertainties and indicates the age of the sample at 13.5 cm as ~1880 CE. The presence of the ^{137}Cs peak between 5.5 and 8.5 cm depth points out that the atmospheric testing of nuclear weapons between 1952 and 1963 (Schuller et al., 1993, 2002, Arnaud et al., 2006). Although the error range in each model varies slightly, nearly all age-depth models seem to fit well with where ^{137}Cs reaches its peak (Figure 5.6).

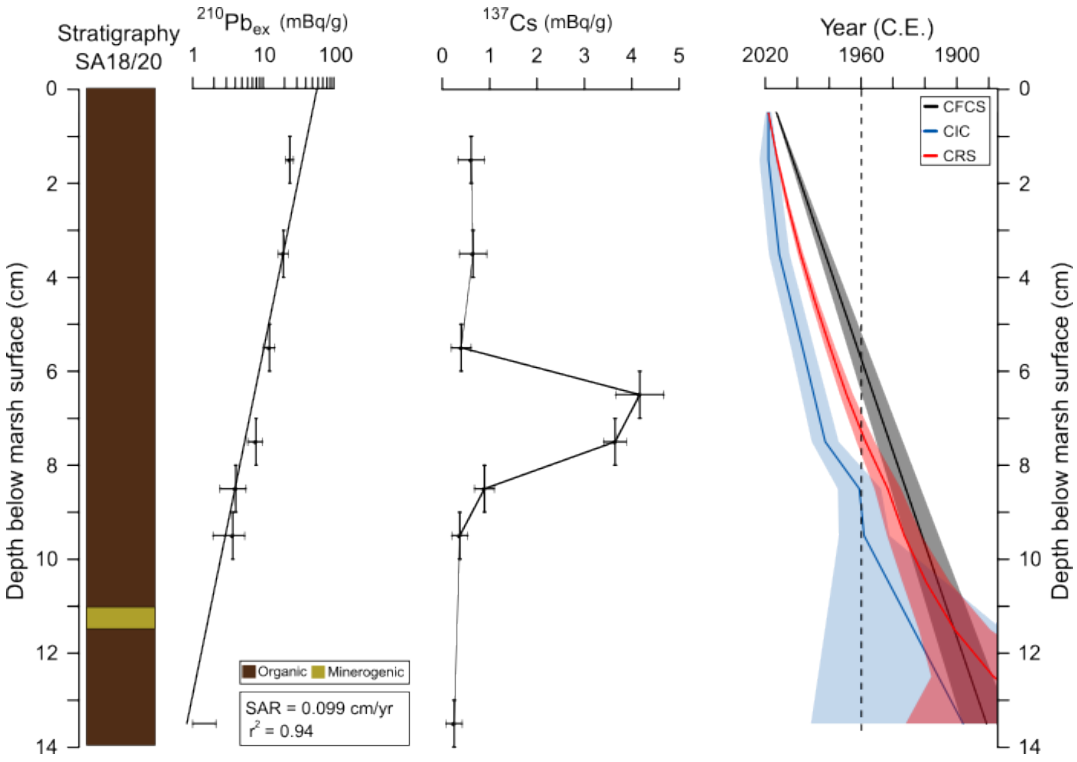

Figure 5.6 : Short-lived radionuclides measurements and age-depth models for SA18/20 core from radionuclide dating and data are plotted against depth. From left to right $^{210}Pb_{ex}$ activity, ^{137}Cs activity, and the age-depth models generated using CRS, CFCS and CIC models (Bruel and Sabatier, 2020). Vertical bars show top and bottom elevation of the subsamples, horizontal bars show uncertainties in the Pb and Cs activities. The black dashed line highlights the year of 1960 CE, SAR: Sediment accumulation rate; r^2 coefficient of determination.

Radiocarbon dating provides an age constraint from the sample at 37.5 cm in the light grey organic silty unit (U2) placing this at 990 - 1024 CE (Table 5.1). Calculating the sedimentation accumulation rate based on this single calibrated radiocarbon age

alone gives a constant rate of 0.0372 cm/yr. This value is substantially lower than the rate of 0.099 cm/yr calculated for the uppermost 13.5 cm of the core from $^{210}Pb_{ex}$ measurement, and therefore it suggests that the sediment accumulation rate has changed through time and the bottom of the core has a higher accumulation rate than the upper part.

Table 5.1: Radiocarbon age of sample provided from plant macrofossils in the core SA18/20 from San Antonio. The result is calibrated to calendar years CE using OxCal 4.3 software (Bronk Ramsey, 2009) with the calibration dataset SHCal20 (Hogg et al., 2020).

Sample Site	Laboratory Code	Sample ID Depth(cm)	Sample type	Radiocarbon age (Years AD ±1σ error)	Calibrated age range (yr CE ±2σ error)
San Antonio	UCIAMS-229618	SA18/20 37.5 cm	seed and stem	1090 ± 15	990 - 1024

In addition to the serac-generated model, there is another method for generating an age-depth model that employs a Bayesian approach for sediment accumulation history and sedimentary chronology. The *rplum* package allows combination of ^{210}Pb, ^{137}Cs and ^{14}C dates (Aquino-López et al., 2018, Blaauw et al., 2020). In contrast to conventional approaches, this model uses prior information in order to generate age-depth models to eliminate uncertainties and poor estimates (see Aquino-López et al., 2018, 2020). The age-depth model agrees with the serac-generated models for the uppermost 13.5 cm for which ^{210}Pb and ^{137}Cs measurements are available (Figure 5.7).

As *plum* uses both ^{210}Pb measurements and the basal radiocarbon date, it generates an age-depth model from 37.5 cm to the top of the core. The complete age model with the timing of historical earthquakes is highlighted in Figure 5.8. As in serac-generated models, the 1960 earthquake corresponds to ~8 cm depth whereas the 1837 rupture corresponds to ~11 cm depth below marsh surface in the stratigraphy, around the sandy silt layer interbedded in the top peat unit (U6). 1575, the date of the earliest historical earthquake, corresponds to ~20 cm, in the dark peat unit (U5).

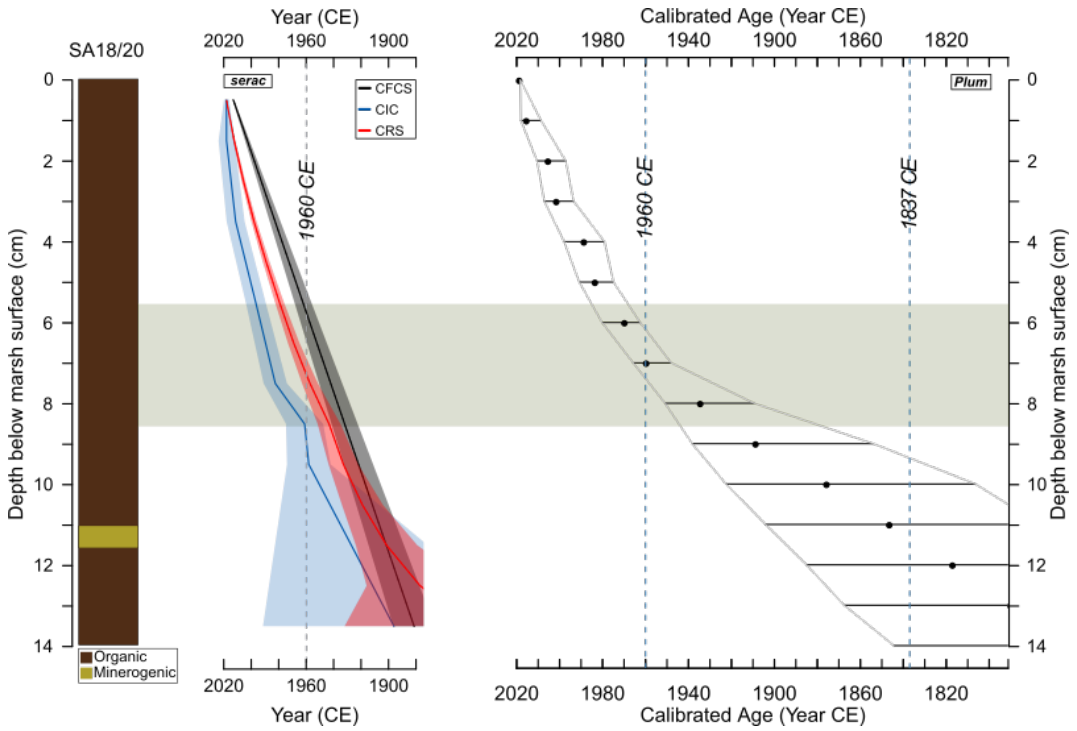

Figure 5.7 : Comparison of age-depth models generated with *serac* and *plum*. Shading highlights the possible depth for the 1960 earthquake based on ^{137}Cs activity. The dashed lines show the timing of historical earthquakes in 1960 and 1837.

5.5.1 Error range in age-depth models

The age-depth model resulting from *serac* yields varying error ranges for each approach. Although all three dating models display similar output at the depth of 8.5 cm, both the CRS and CIC models present substantially larger error ranges than the CFCS model. This issue stems from the lack of any subsamples between 8.5 cm to 14 cm. The main advantage of CFCS is the assumption of a constant sedimentation rate as opposed to the other ones. Provided that more subsamples can be used, better estimates for age-depth and confidence interval could be obtained.

The age-depth model that is generated via the *rplum* package (Blaauw et al., 2020) in R employs the Markov chain Monte Carlo (MCMC) approach (Metropolis et al., 1953, Hastings, 1970) (Figure 5.8). In this method, this approach carries out computer-driven sampling of the flux of ^{210}Pb, supported ^{210}Pb as well as Bayesian statistics to better estimate uncertainties (Aquino-López et al., 2018, Blaauw et al., 2020). The main advantage of this method is to combine ^{210}Pb measurement and radiocarbon determination to provide estimates of the age of each subsample in the core, where there are no radiometric isotope measurements or the lack of dateable

material and generate more realistic estimates of precision and accuracy for the age-depth models (Aquino-López et al., 2018).

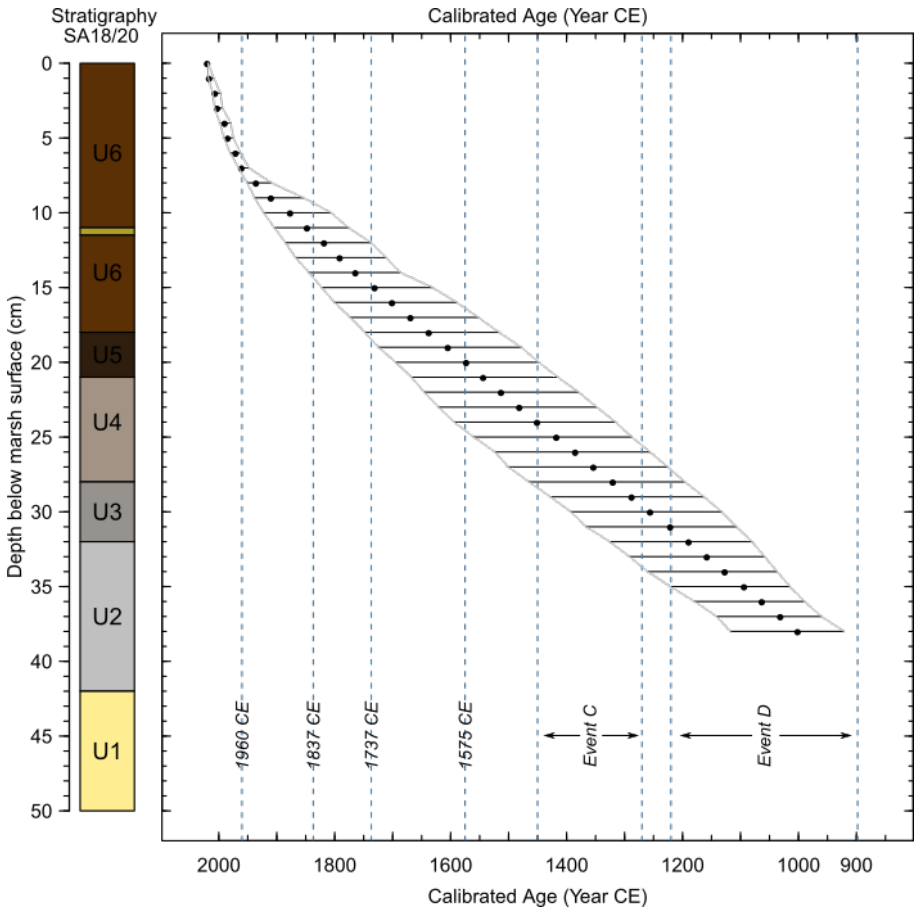

Figure 5.8: Age-depth model combining ^{210}Pb and ^{14}C measurements generated using the *rplum* package in R. The blue dashed lines show the timing of historical earthquakes in 1960, 1837, 1737, 1575 and arrows show the time ranges for events C and D (Cisternas et al., 2005, 2017b, Garrett et al., 2015).

Monte Carlo is an approach that estimates the principal properties of sample distribution by interrogating random samples from that distribution (Metropolis and Ulam, 1949, Hasting, 1970, Gilks et al., 1996, Brooks et al., 2011). When used with a large number of random samples, the Monte Carlo method reflects the main parameter of the distribution; here this parameter is considered as sediment accumulation rate. The simulation of random sampling generates a representative and unbiased group of samples. The MCMC approach is utilised to obtain the posterior distribution of the chronology using millions of pieces (chains) for modelling. The approach takes the data of each sub-sample depth in core and generates samples from the posterior distribution (Aquino-López et al., 2018, Blaauw et al., 2020). In the Bayesian approach, it is assumed that the true value is a random

variable, the posterior probability hinges upon prior conditions (Gilks et al., 1996, Gamerman and Lopes, 2006). For example, the amount of unsupported and supported ^{210}Pb isotopes in a downcore sample depends on the prior sedimentation rate, which is uncertain and lacks any prior information (Aquino-López et al., 2018). Here, the future state of sediments and their radioactive elemental content depend upon the current state which is assumed to exponentially decrease under constant rate of supply (Aquino-López et al., 2018). At the end of the MCMC process the posterior probability converges to its most expected values which is an equivalent best estimate of the parameter (Blaauw and Christen, 2011). It provides millions of outcomes with various likelihood models and prior distributions for one to choose to form resulting chronology (Aquino-López et al., 2018; 2020). This distribution is used to calculate the credible interval (quantiles) for the parameter. In this case, either the mean or median can be chosen and the standard deviation representing uncertainties is the mean of the smaller probabilities (Blaauw and Christen, 2011, Blaauw et al., 2018). Further details and more technical information about this model development can be found in Blaauw and Christen (2011), Aquino-López et al. (2018), Blaauw et al., (2020). Moreover, readers who are interested in more detail about MCMC (Gilks et al., 1996, Gamerman and Lopes, 2006) and Bayesian approaches in R, are referred to books for introduction and tutorials on the topics (e.g., Suess and Trumbo, 2010, Kruschke, 2014, McElreath, 2020).

It is not surprising that sections with fewer dates are less precise. Uncertainties in age estimates demonstrate substantially higher values between 8 cm and 38 cm, and precision decreases depending on the absence of radiometric data due to discrete sampling for ^{210}Pb and the presence of only a single radiocarbon date. Even if there is a basal age for the core from the calibrated radiocarbon date, the confidence interval (technically this is a credible interval) remains large where there is no measurement for ^{210}Pb and radiocarbon dates. This issue is underlined where precision is significantly affected due to missing data (c.f., Aquino-López et al., 2020). The grey lines denote the credible interval range and black points refer to the mean of millions of MCMC simulations in Figure 5.8. As a result, additional ^{210}Pb measurements and radiocarbon ages, for example between 15 and 30 cm depth may reduce uncertainties associated with the age-model in future.

5.6 Reconstruction of palaeomarsh surface elevation

For the purpose of reconstructing palaeomarsh surface elevation (PMSE), here the three transfer function models that were developed in chapter 4 are applied to the fossil dataset. Forty-six samples were analysed for diatoms from monolith SA18/20; 29 samples from organic sedimentary units and 16 from lower sedimentary units. Reconstructions were carried out using the local modern training set (WA-PLS component 3), the regional modern training set using WA-PLS regression (component 2 excluding tidal flat samples and residual outliers) and finally the regional modern training set using LW-WA (with 10% of samples in the local training set, Model D). The transfer function models also produce sample specific error estimates for each fossil sample under bootstrapping cross-validation with 1000 cycles (Birks, 1995). In order to include 95.4 % (2σ) confidence intervals, the sample specific error estimates are multiplied by 2.

In addition to the assessment of transfer function performance described in chapter 4, the reliability of reconstructions is also assessed here by investigating whether the modern training sets provide good modern analogues for fossil samples (Birks et al., 1990, ter Braak, 1995a). The models are compared based on numbers of good, close, and poor analogues in MAT (Birks, 1995, Simpson, 2007, Simpson, 2012) by means of minimum dissimilarity coefficients. The threshold for the minimum dissimilarity values is defined as good (<the 5th percentile), close (between the 5th and the 20th percentiles) and poor (> the 20th percentiles) modern analogues respectively (Watcham et al., 2013).

The statistical performance of the three reconstruction models shows varying results (Table 5.2). The Local Model performs best in terms of r^2 and RMSEP, but provides no good and few close analogues. Model C is favoured over Model D as it provides the greatest number of good and close modern analogues and lower RMSEP. The summary statistics for all three methods are shown for comparison on Figure 5.9.

Table 5.2 : Statistical performance of the transfer function models applied to fossil samples of SA18/20.

Model Name	No. of samples in the modern training set	Transfer Function Method	Av bias	Max bias	r^2	RMSEP	Analogues good/close/poor		
Local Model	26	WA-PLS component3	1.35	8.29	0.96	6.92	0	6	40
Model C	171	WA-PLS component2	-0.32	35.47	0.71	25.10	4	11	31
Model D	279	LW-WA	1.41	64.56	0.88	28.31	2	6	38

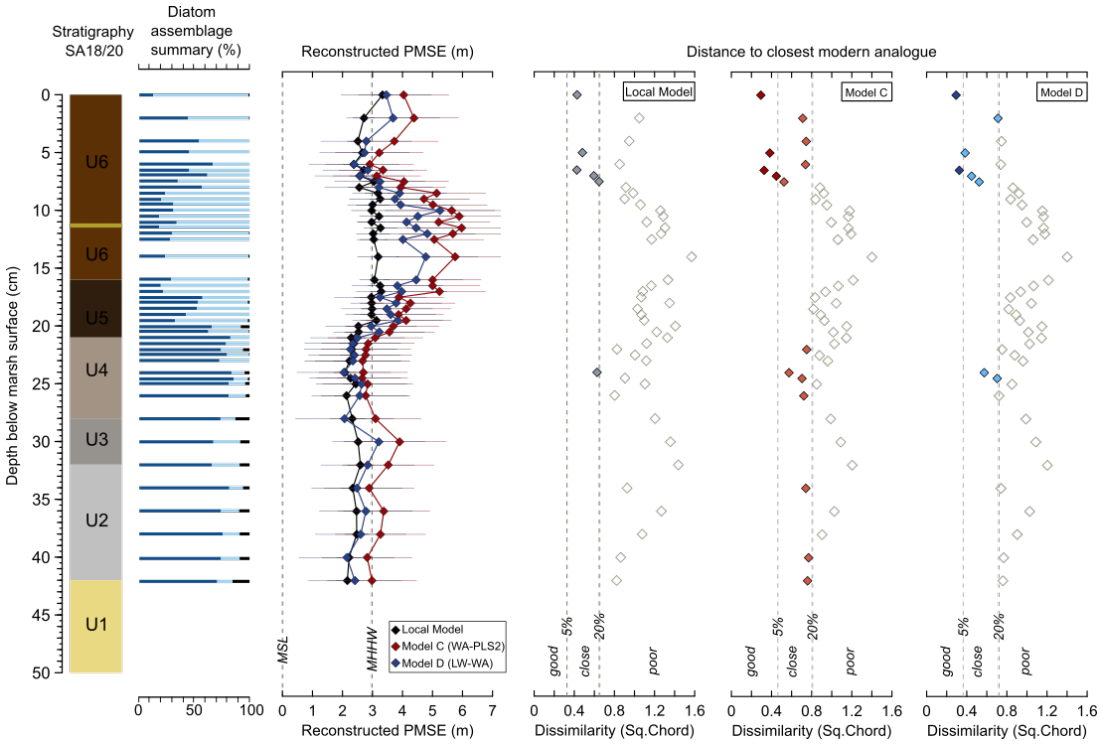

Figure 5.9 : Comparison of the PMSE reconstruction estimates with 95.4% (2σ) errors from the Local Model (WA-PLS3), Model C (WA-PLS2) and Model D (LW-WA), alongside summaries of diatom assemblages and lithostratigraphy. Dissimilarity coefficient values are plotted relative to the threshold for good (the 5th percentile), close (the 20th percentiles) and poor (> the 20th percentiles) modern analogues.

A similar trend is presented in all the two component regional models, whilst the response amount is considerably different especially in the Local Model at shallow elevations points. As expected, the transfer function results yield higher elevations for peat samples than silt samples which is observable in the Model C and Model D. However, there are significant differences between the reconstructions from the three different transfer function models, particularly for the peat samples (8.5 - 17 cm), peaking at a maximum difference between Model C and the Local Model of 2.60 m and 1.52 m between Model D and the local model (Figure 5.9). The main cause of the significant differences between model estimates based on local and regional training sets, stem from different elevation optima for *Cosmioneis pusilla* and *Pinnularia divergentissima* that are calculated from WA-PLS regression. The error values are also smaller for the Local Model whereas Models C and Model D, the regional dataset, have larger error ranges.

The first noticeable change in PMSE is observed between a depth of 34 and 28 cm, where there is a gradual increase followed by a decrease, in both Model C and Model D. The reconstructed estimates are slightly below MHHW (2.98 m) for the Local model and model D and slightly above MHHW using Model C.

The first noticeable change in PMSE is observed within the sedimentary sequence between depths of 34 and 28 cm. In both Model C and Model D, there is an initial gradual increase followed by a decrease in PMSE. The reconstructed estimates obtained from the Local model and Model D are slightly below the Mean Higher High Water (MHHW) level of 2.98 m, while the estimates from Model C are slightly above MHHW.

A major change occurs starting from 21 cm depth at the transition to the dark peat unit (Unit 2). PMSE estimates rise from near the MHHW boundary to a maximum of ~5.97 m at 11.5 cm in the Model C whereas in Model D, PMSE values peak at 5.25 m at 10 cm. These values are above to the highest astronomical tide, which is 4.38 m above MSL. In contrast, the Local Model estimates remain close to MHHW. Both Model C and Model D show a sharp decline in PMSE up to 6 cm depth where the Model C hits a minimum of 2.91 m, below MHHW. Model D returns to 2.38 m, again below MHHW. Again, the Local Model does not show a similar trend compared to the regional models.

The last important variance is seen starting from 6 cm to the top of the core. The reconstructed values exhibit a sharp increase from ~2.90 m to 4.38 m in Model C,

3.69 m in Model D, and subsequently a gradual decrease in both models. Nevertheless, there is no considerable rise in estimates from the Local Model, rather estimates remain relatively stable and show a slight increase ~0.6 m from 2 cm to 0 cm.

The main difference between the models is the sample size: the Local Model contains only 26 modern samples collected from San Antonio estuary while Model D includes the full regional training set (total 279 modern samples) and Model C comprises regional marsh samples (not including tidal flat samples, total 177 modern samples) from the full training set. Employing regional datasets rather than relying on only the local modern samples from the study area increases the confidence level of reconstruction estimates since they provide better modern analogues (e.g., Hocking et al., 2017). Thus, Model C is the most suitable option for further investigation and interpretation of the relative sea-level change. It offers a greater number of good and closely matching analogues compared to the Local Model and Model D.

5.6.1 Significance test

The significance test permits us to evaluate whether tidal elevation is an ecologically important determinant and a statistically significant predictor of the modern diatom species distribution or not. With the aim of assessing whether current quantitative reconstruction estimates in Model C are statistically significant, a random significance test was applied (Telford and Birks, 2011) using measured environmental variables to generate random environmental variables by permuting them.

Apparently transfer function models using random environmental variables explain more variance than Model C in Figure 5.10. Although Model C is rather close to the 95% boundary, it still explains less variance than reconstruction models using a random environmental variable through permutation of SWLI values. The significance test underlines that the reconstructed estimates should be treated with caution, as the transfer function using randomly generated environmental variables (obtained by permuting the measured environmental variable) explains more variance in the fossil diatom assemblage than Model C.

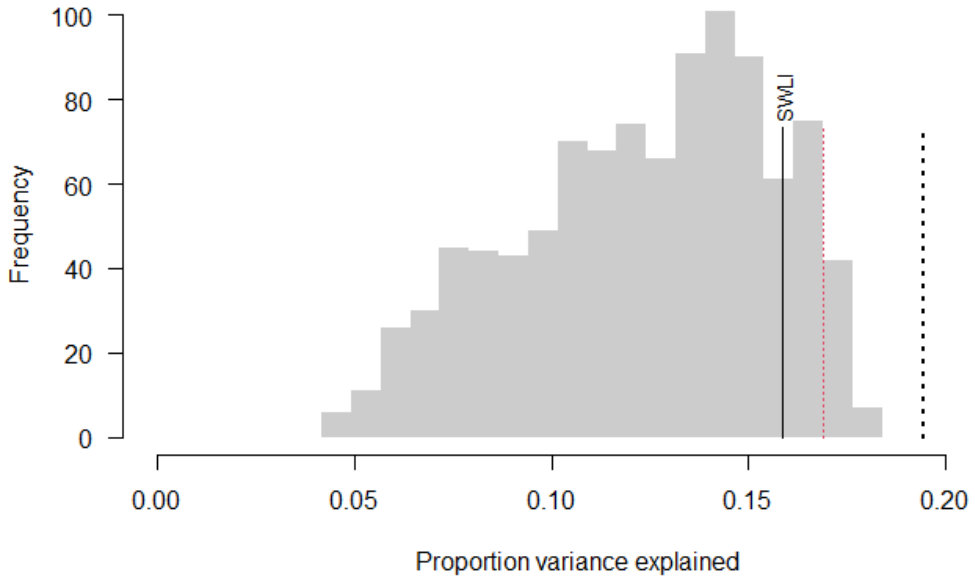

Figure 5.10 : Histogram of the proportion of variance in the SA18/20 diatom record explained by 999 calibration functions (Model C: WA-PLS Component 2) trained with random environmental data. Solid black line displays the proportion of variance explained by PMSE in Model C and the red dotted line marks the proportion of variance below which 95% of the generated random environmental variables which obtained by permuting measured environmental variable calibration functions could be explained. The black dotted line indicates the proportion of variance explained by the first axis of a CA of the fossil data.

5.6.2 Goodness of fit

A goodness-of-fit is a statistical technique that assists in measuring divergence between the observed values (elevation of modern samples) and predicted values (elevation of reconstructed elevation fossil samples) which is critical to evaluate the reliability of transfer function models (Birks et al., 1990, Birks, 1995, Simpson and Hall, 2012). This method permits us to decide which reconstructed samples poorly fit in the models by employing the chi-square distribution to find quantiles for a given confidence level or significance level. By employing CCA to the training set, fossil samples can be fitted and passively plotted on the axis of the environmental variable of interest into ordination space; thus, one can calculate squared residual distance to the axis, and explore which fossil samples are poorly fitted in the transfer function models.

Following Simpson and Hall (2012), goodness-of-fit statistics were carried out by using the training set into CCA with elevation (SWLI) as the sole environmental variable for each core sample in the Model C (WA-PLS). Subsequently, the fossil samples were passively plotted in constrained ordination space. The threshold for the square residual distance between each sample and the first CCA axis was identified at 95th (poor fit) and 99th (very poor fit) percentile thresholds as recommended (Simpson and Hall, 2012). For the fossil assemblage that is preserved in the core SA18/20, goodness-of-fit statistics assessed the validity of reconstructions using Model C. Figure 5.11 demonstrates the goodness-of-fit statistics of the fossil samples that the majority of samples are very poorly fitted with SWLI; however, that some in the upper part of the core (top 7 samples at 0, 2, 4, 5, 6, 6.5 and 7 cm) have lower residual lengths and are well fitted. In contrast, the rest of the fossil samples in which the lower part of the core has higher residual lengths and are very poorly fitted, with the exception of the sample at 24 cm. As a result, we must be more cautious about reconstructions based on these assemblages.

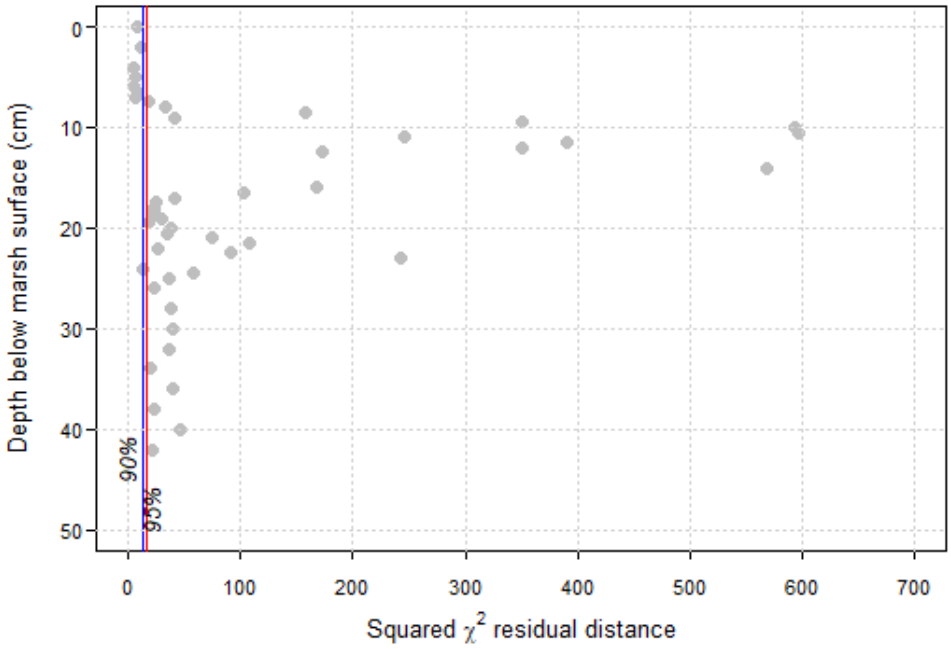

Figure 5.11: Squared residual length for the San Antonio fossil assemblages and core depth. The blue line marks the 90% limit of the calibration set residual lengths (poorly fitted) and the red line marks the 95% limit (very poorly fitted).

5.6.3 Sample-specific error (uncertainty) for reconstruction estimates

Sample-specific error contributors for the reconstruction of palaeomarsh surface elevation of the fossil samples used in the San Antonio core (SA18/20) are calculated using the bootstrap method. Figure 5.12 gives a visual impression of the existing relationship between both contributions. The RMSEP of reconstructed individual fossil samples under bootstrap cross-validation is composed of two contributors, which differs from that used in the wider statistical literature, namely s_1 and s_2 (for details Birks et al., 1990).

The first model named as the Local model employs only modern surface samples that were obtained from the San Antonio estuary. The total number of modern samples is 26 and it is developed by using WA-PLS method with component three. Figure 5.12 shows the standard error of prediction values for each fossil sample in the local model. The total RMSEP estimated for the local model substantially varies due to the amount of error estimated in fossil samples. The contribution of s_1 (sample-specific error) in the prediction errors amongst the fossil samples across the core is the main contributor to the error range. Notably, the majority of fossil samples between 9.5 and 14 cm contribute to approximately 90% of the error values.

The total RMSEP for the Model C is ~60 SWLI units. The contribution of s1 (sample-specific error) in the prediction errors amongst the fossil samples between 9.5 and 16.5 cm and fossil samples at 21 cm and 23 cm are close or larger than 20% (some fossil samples have more than 30%) the overall error in the Model C. The sample specific error of the rest of the fossil samples varies between 10 – 20% of the total error.

In Model D, the amount of contribution error in s1 substantially varies from sample to sample. The fossil samples between 8 cm and 17.5 cm (except for 9 cm and 17 cm) demonstrate larger error than 20%. Moreover, s1 contribution for the fossil samples at 8, 9.5, 10, and 14 cm exceed 50% error contribution to the overall error.

In general, Model D exhibits slightly lower sample-specific errors overall compared to Model C. The large error values are clustered in the range around samples from 8 to 17 cm. The variation in s_1 error arises from the difference in the number of modern analogues in the training set. Model C consists of 171 samples, whereas Model D contains 277 samples in the training set, which impacts the locally weighted regression and calibration using a specific sample size. Having large s_2 values in both cases suggests that the modern training set displays noisy environmental data

generally explaining nearly 80% of error, except for the sub-samples located approximately around at 8 – 17 cm depth.

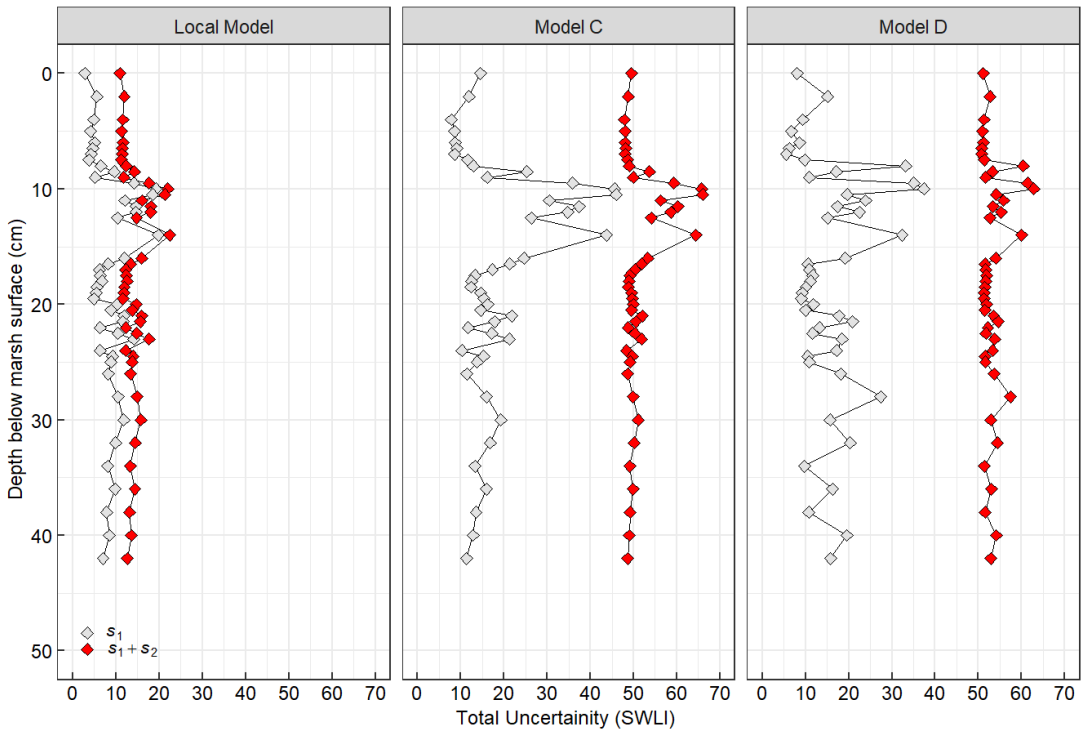

Figure 5.12 : Sample-specific errors for Local Model (a), Model C (b) and Model D (c) that were obtained for each sample in the core as a result of bootstrapped cross-validation. Total uncertainty in SWLI units consist of $s_{1\ fossil}$ is the standard error of the bootstrap estimates of the environment for an individual fossil sample; $s_{2\ model}$ is the average bias, which is the mean of the residuals, from the transfer function model using for the predicted values for the training set samples which is obtained under bootstrapped cross-validation procedure (Birks et al., 1990).

When SWLI units are back-converted to metre scale units by rearranging the original SWLI equation that is employed to convert elevation of the modern surface samples (Hamilton and Shennan, 2005), each output of the sample-specific error values is in order to obtain 95.40% confidence interval as a common practice since they were already multiplied by 1.96. At this step, these values are in SWLI unit, and they are calculated before back-transforming the reconstructed values to the metre scales.

For example, when the error values in SWLI units back converted for Model C, the error values are ± 0.86 m. Table 5.3 shows only reconstructed elevation for samples from 0 to 8 cm. However, sample-specific error for each sample is not multiplied by 1.96; thus, this values only cover ~68% confidence interval. When the error values in

SWLI units are multiplied by 1.96 in order to obtain 95.40% confidence interval and back converted for Model C, the error values range from ± 1.68 to ± 1.69 m (Table 5.4)

Table 5.3 : The sample specific error of the reconstructed elevation of fossil samples in Model C with 68% confidence interval.

Depth	MSL	MHHW	Sample-specific error (1σ) (SWLI)	Sample-specific error (m)
0	0	2.98	28.92	± 0.86
2	0	2.98	28.86	± 0.86
4	0	2.98	28.77	± 0.86
5	0	2.98	28.75	± 0.86
6	0	2.98	28.78	± 0.86
6.5	0	2.98	28.75	± 0.86
7	0	2.98	28.77	± 0.86
7.5	0	2.98	28.82	± 0.86
8	0	2.98	28.87	± 0.86

Due to the standardized water level index (SWLI) formula, when there is a large sample-specific error in SWLI values, the errors are reduced when back-converted to the meter scale. This is evident when multiplying the sample-specific error in SWLI values by 1.96 to obtain a 95.40% confidence interval. The resulting transformation to the metre scale provides a lower error range compared to the 68% confidence interval.

Moreover, it is not surprising that MHHW is playing a significant role in the transform equation when SWLI values are transformed back to metre scale as well. A larger tidal range leads to a greater sample-specific error when SWLI values are converted back to the original scale (see Barlow et al., 2013). Thus, in locations where large tidal ranges are measured, reconstruction models will have large sample-specific error. An example to investigate the role of tidal range is presented in Table 5.5 where MHHW is 1.12 m. It is evident that the sample-specific error is directly proportional to tidal range, and it decreases significantly when comparing the error range of ±1.68 m for MHHW of 2.98 m to the error range of ±0.68 m for reconstruction estimates when MHHW is 1.12 m. As a result, those study sites with a large tidal range yield high uncertainty for reconstruction estimates.

Table 5.4 : The sample specific error of the reconstructed elevation of fossil samples in Model C with 95% confidence interval.

Depth	MSL	MHHW	Sample-specific error (2σ) (SWLI)	Sample-specific error (m)
0	0	2.98	56.68	± 1.69
2	0	2.98	56.57	± 1.69
4	0	2.98	56.39	± 1.68
5	0	2.98	56.35	± 1.68
6	0	2.98	56.41	± 1.68
6.5	0	2.98	56.35	± 1.68
7	0	2.98	56.39	± 1.68
7.5	0	2.98	56.49	± 1.68
8	0	2.98	56.59	± 1.69

Finally, it should be noted that where larger sample-specific error values are estimated in SWLI units, then back-converting these units to metre scale will be smaller due to the original formula. In summary, the size of the sample-specific error values is dependent upon both error values in transfer function models and tidal range. It has been elucidated that the source and variation in the sample-specific error resulting from reconstruction of palaeomarsh surface elevation models (PMSE) in detail.

Table 5.5 : The sample specific error of the reconstructed elevation of fossil samples in Model C with 95% confidence interval if tidal range was 1.12 m.

Depth	MSL	MHHW	Sample-specific error (2σ) (SWLI)	Sample-specific error (m)
0	0	1.12	56.68	± 0.63
2	0	1.12	56.57	± 0.63
4	0	1.12	56.40	± 0.63
5	0	1.12	56.36	± 0.63
6	0	1.12	56.42	± 0.63
6.5	0	1.12	56.35	± 0.63
7	0	1.12	56.38	± 0.63
7.5	0	1.12	56.48	± 0.63
8	0	1.12	56.59	± 0.63

5.7 Interpretation

The quantitative reconstructions of PMSE show noticeable changes at certain depths. The PMSE estimates derived from the regional transfer function models provide better estimates since they provide a larger number of modern analogues compared to the Local Model, as discussed above. The main focus here is therefore on Model C (WA-PLS2). The calibration of assemblages using Model C yields PMSE estimates which are converted to relative sea-level reconstructions by taking the estimates away from the field elevations (Figure 5.13). Model C reconstructions show three main changes along the core and these changes may indicate an association with seismic or non-seismic origins. Although the following sections aim to interpret changes in RSL for all reconstruction estimates, it should be noted that only those estimates based on good and close analogues can be considered reliable.

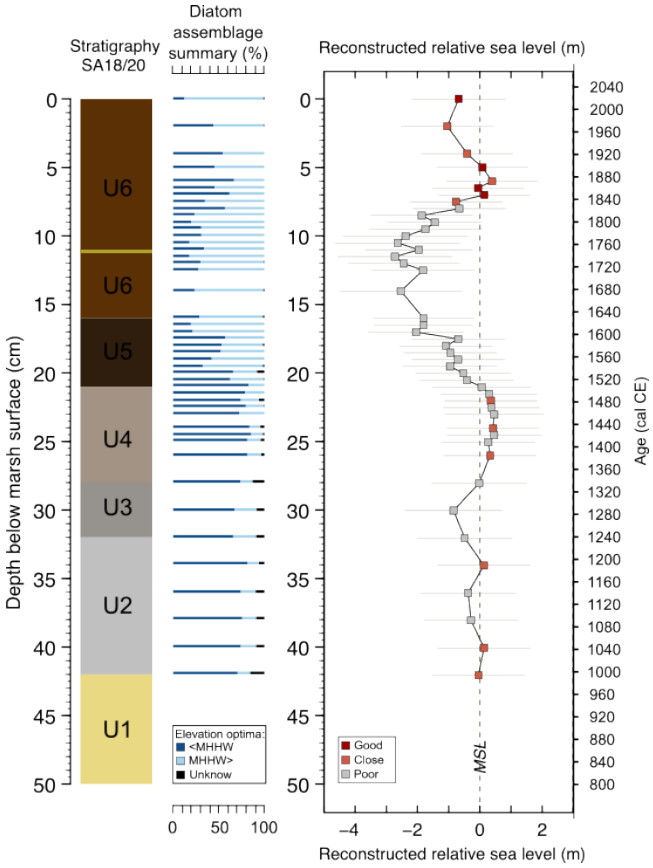

Figure 5.13: Summary of San Antonio diatom assemblages and relative sea-level reconstructions derived from calibration of fossil assemblages using Model C. Species classified as below or above MHHW based on modern species elevation optima derived from the transfer function in Model C. Good, close, and poor modern analogues are calculated using the distance to the closest modern analogue from MAT in order to assess the similarity between modern and fossil assemblages.

From the bottom, where the single radiocarbon date is obtained at 37.5 cm, no significant change is presented, although it is noticeable that this age corresponds to the timing of a prehistoric earthquake named as event D in Maullín and Chucalén (Cisternas et al., 2005, Garrett et al., 2015). However, neither lithostratigraphy nor RSL curve show any noticeable change between depths of 38 and 36 cm.

The earliest change in the RSL starts gradually at 34 cm in the minerogenic unit 2 and falls ~1 m by the transition into minerogenic unit 3 at 32 cm depth. A gradual rise in RSL follows, reaching modern MSL at 28 cm depth. Even though there is an obvious change in the stratigraphy from unit 3 to unit 4, diatom assemblages do not show a substantial change between those units. The same species dominate these samples: *Paralia sulcata, Achnanthes brevipes, Diploneis didyma* with elevation optima sub-MHHW and *Diploneis ovalis* with elevation of optima supra-MHHW. However, only the sample at a depth of 34 cm provides a close analogue, while the samples at depths of 32 cm, 30 cm, and 28 cm do not have any good or close analogues. It is important to note that none of these samples have good or close analogues, suggesting that the change in RSL cannot be regarded as reliable estimations.

The most striking change in the RSL curve occurs with a strong decline from 0.05 ± 1.55 m at 21 cm to 2.36 ± 1.93 m below MSL at 10 cm core depth. This major fall in the RSL corresponds to the change in stratigraphy from silt to peat (U4 to U5, continuing into U6). The number of diatoms with elevation optima sub-MHHW gradually decreases, whereas those with elevation optima supra-MHHW, *Nitzschia vitrea*, *Cosmioneis pusilla*, *Pinnularia cruciformis*, *Nitzschia fruticosa* and *Pinnularia divergentissima,* significantly increase. However, no samples between 21 and 10 cm have good and close analogues in the modern training set. One of the reasons for the lack of good and close analogues is the abundance of Nitzschia vitrea, which is not well represented in the modern training set. As a result, the estimates for samples at these depths cannot be considered reliable for deciphering RSL changes.

Above 10 cm cm, RSL rises sharply to 0.40 ± 1.44 m MSL at 6 cm core depth. The distinct thin sandy-silt layer from 11.5 cm to 11 cm depth within the top organic unit (U6) marks an increase of *Pseudostaurosira perminuta* and decrease of *Cosmioneis pusilla*; however, the change in RSL across this contact is no larger than other sample-to-sample fluctuations. The *serac* and *plum* age models indicate that the occurrence of this unit dark silt-sand unit is approximately concurrent with the timing of the 1837 CE earthquake (Figure 5.7).

RSL rises between 8 cm and 6 cm, before dropping sharply from 0.39 m ± 1.44 above MSL at 6 cm to 1.04 ± 1.43 m below MSL at 2 cm. All age-depth models show that this steep rise in RSL between 8 cm and 6 cm may be coincident with the 1960 earthquake (Figure 5.7), with the following fall concurrent with post-seismic uplift recorded by tide gauge measurements at Puerto Montt (Barrientos et al., 1992) after the 1960 earthquake. There is no change in the lithostratigraphy at this time and unit 6 remains unchanged. The number of good and close modern analogues increases above 8 cm, with four samples with good and four with close analogues. The presence of good and close modern analogues shows confidence in reconstructed RSL estimates. Thus, the fossil samples and diatom-based reconstruction of RSL change show higher confidence compared to the samples at lower depths. However, it is important to note that the estimates from this model fail in the significance test, indicating limitations in their reliability.

5.8 Discussion

The fundamental hypothesis that late Holocene tidal marsh sedimentary sequences may preserve evidence of earthquakes and associated sea level change has been followed throughout this chapter. Stratigraphic and palaeoecological features of the San Antonio estuary have been characterised based on lithostratigraphic exploration of multiple cores, particle size analysis from a representative core (SA18/20), analysis of diatom assemblages and results from radiometric dating.

Since the sequence covers the last 1000 years, the study site has experienced at least four great subduction zone earthquakes which are reported previously (Cisternas et al., 2005, 2017b, Garrett et al., 2015). Nevertheless, while these earthquakes left characteristic peat-mud couplets at other sites, the impacts were not the same at San Antonio as a result of the greater distance of San Antonio from the trench, ~170 km.

5.8.1 The 1960 earthquake

Numerous lines of geological evidence have been presented associated with the 1960 earthquake and ensuing tsunami in south-central Chile (Plafker and Savage, 1970, Cisternas et al., 2005, 2017b, Atwater et al., 2013, Garrett et al., 2013, 2015, Kempf et al., 2015). Compared to these studies, the San Antonio estuary is located farthest from the trench (170-180 km). The age-depth models which are generated using the short-lived radionuclides and combination of them with the single ^{14}C date suggest

the 1960 earthquake should lie between 8.5 cm and ~5 cm (CFCF, CIC, CRS models) and at ~ 7 cm (plum model). The age-depth models indicate the 1960 earthquake does not correspond with the interbedded thin sandy-silt bed in the youngest sedimentary unit (U1) at 11.2-11.6 cm. According to the models that interbedded sandy-silt layer was deposited earlier than atmospheric nuclear testing (1952 to 1963). Neither ^{137}Cs nor ^{210}Pb age-depth models support a correlation between the interbedded sandy-silt layer and the 1960 Great Chilean earthquake.

In contrast to previous studies (Cisternas et al., 2005, 2017b, Garrett et al., 2013, 2015) near to San Antonio, the stratigraphy of the tidal marsh does not display the occurrence of a peat-mud or mud-peat couplet with a sharp contact at depths associated with the 1960 earthquake. In general, the contacts between sedimentary units were interpreted as gradational. The absence of laterally extensive peat-mud couplets with sharp contacts and evidence of suddenness of submergence or emergence (Nelson et al., 1996) indicates the site did not subside or uplift sufficiently to exceed the threshold for evidence creation (see Shennan et al., 2016). The sheltered location of San Antonio may also have prevented inundation by the tsunami and consequently the absence of a deposit as seen at other sites (Cisternas et al., 2005, 2017b, Garrett et al., 2013, 2015).

According to the field investigation carried out 8 years after the 1960 earthquake, four locations close to San Antonio provide observations of subsidence varying from -0.4 to -1 m (Plafker, 1969). While there is no stratigraphic change, diatom-based RSL reconstructions indicate RSL rise around the time of the earthquake and fall after. It is difficult to quantify the magnitude of the rise due to uncertainty over the depth of the earthquake horizon, but RSL rise is consistent with coseismic subsidence. The tide gauge measurements following 1960 indicate post-seismic uplift (RSL fall) near Puerto Montt (Barrientos et al., 1992, Figure 3); thus, RSL fall at San Antonio could be consistent with this deformation.

In contrast, tide gauge measurements obtained from the Permanent Service for Mean Sea Level (PSMSL) at Puerto Montt (41°29'S, 72°56'W) indicate a rise in mean sea-level prior to the 1960 earthquake. While there is no record available between 1960 and 1964, there was a sharp increase in mean sea level between 1960 and 1970. Subsequently, the tide gauge measurements suggest a period of stabilisation starting from 1971. However, it should be noted that there is a lack of data for the years between 1971 and 1980, which limits our ability to fully analyse and understand the variations during that period.

Altimetry data from Guafo Island suggests a rise in RSL following the 1960 earthquake (Melnick et al., 2018) (Figure 5.14). However, these measurements do not agree with the reconstruction estimates from San Antonio. It is important to note that comparing diatom-based reconstruction models and sensitive altimetry measurements (at the mm scale) from satellite data, as used in Melnick et al. (2018), is extremely challenging. Additionally, Guafo Island is located directly above the seismogenic zone, and there is a considerable distance of approximately 250 km between Guafo Island and San Antonio. Furthermore, our geologic findings suggest that San Antonio may be located near the eastern limit of coseismic subsidence, which differs from a place like Guafo Island that experiences evident seismic locking.

These findings suggest that, despite the absence of sedimentary signatures of the 1960 earthquake, diatom-based reconstruction estimates indicate a slight fall in RSL following the 1960 event for a period of nearly a decade. This observation could align with the available tide gauge measurements to some degree, any may be considered as additional evidence for the occurrence of post-seismic uplift in this region. Nevertheless, it is crucial to note that the PSMSL suggests that the measurements may not meet research quality standards, and the reconstruction model failed the significant test, thereby making it challenging to determine the reliability of the reconstruction estimates under these circumstances.

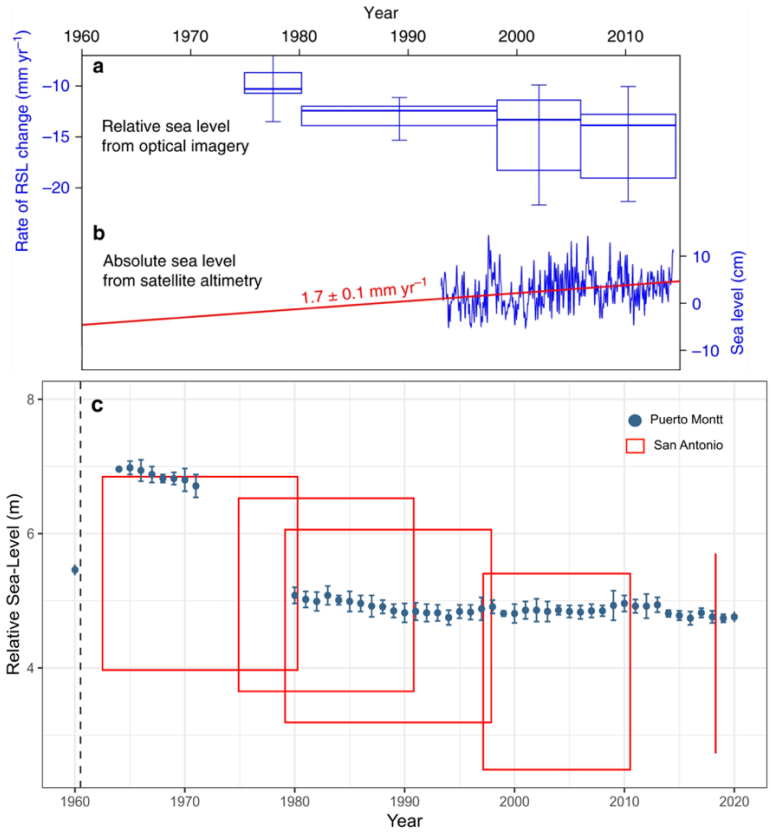

Figure 5.14 (previous page) : Comparison of reconstruction estimates from three different sources. a) and b) show estimated relative RSL changes at Guafo Island after the 1960 earthquake (from Melnick et al., (2018), Figure 5a, b); c) Reconstruction estimates from San Antonio estuary and tide gauge measurements at Puerto Montt from the PSMSL database.

These findings address the first aim of this study “Is there geological evidence of relative land-level change at San Antonio estuary associated with the 1960 earthquake, which can be used to define the limit of inland coseismic deformation?”. Based on analysis of the stratigraphy, sedimentology, and microfossil content of the coastal deposits at San Antonio, even though there is not obvious evidence from a stratigraphical point of view, the RSL reconstructions suggest a slight change may be associated with the 1960 earthquake around 8-6 cm depth. Furthermore, the site may record postseismic uplift as a fall in RSL of up to 1 m. While there are evident traces of the 1960 earthquake in tidal settings close to the trench, as we move away from trench towards the landward limits of surface deformation, the potential for evidence creation decreases. San Antonio was affected by the 1960 earthquake but does not meet the criteria of Nelson et al. (1996) and Shennan et al. (2016). Based on a simple elastic dislocation model (Hyndman and Wang, 1993), the distance from the trench is critical in determining the direction and magnitude of vertical coseismic deformation. This suggests that San Antonio may reside close to eastern edge of coseismic subsidence resulting from the 1960 earthquake due to the geometry of the subduction zone (Moreno et al., 2009, 2012).

The tidal range may play a key role in determining whether sedimentary couplets are formed. For example, the site at Chucalén shows a moderate tidal range where MHHW is 1.02 m above MSL (e.g., Garrett et al., 2015), whilst at San Antonio MHHW is 2.98 m. Due to the occurrence of different sediment types in wider zones, changes in stratigraphy may not occur at sites with larger tidal ranges and larger deformation magnitudes may be needed to observe stratigraphic changes.

5.8.2 The 1837 earthquake

The 1837 CE earthquake mainly affected the southern part of the Valdivia segment (Cisternas et al., 2005, 2017a), potentially including San Antonio. The age-depth models indicate that the presence of the unusual sandy-silt layer which is interbedded within the top peat unit (U1) might correspond to the timing of the 1837 CE earthquake. The layer has sharp contacts and displays a constant thickness in all of

the cores where it was found. However, the presence of this layer is limited to six cores covering a distance of ~30 m (Figure 5.2).

Tsunamis may deposit minerogenic layers with identifiable anomalous marine sediment, landward thinning and fining, and upward fining grain size, rip-up clasts, sharp eroded lower contact and coincident with land-level change, atypical marine diatom assemblage including occurrence of fragmented diatoms in high numbers (Cisternas et al., 2005, 2017b, Garrett et al., 2013, 2015, Ely et al., 2014, Dura et al., 2015, Hong et al., 2017). However, this unit does not match any of these characteristics. Therefore, the presence of this sandy-silt layer probably does not suggest an occurrence of a tsunami as in previous studies (Cisternas et al., 2005, Garrett et al., 2013, 2015) in nearby localities.

Other processes may also produce similar deposits. Processes such as fluvial floods, aeolian processes, tidal channel migration, and storms act as agents which carry sediments into intertidal settings (Allen, 1997, 2000, Long et al., 2006, Williams, 2009, Witter et al., 2001, Switzer and Jones, 2008). As a small river enters the estuary south of the coring locations, a fluvial source is a possible candidate for the occurrence of this sandy-silt layer. Nevertheless, the uniform thickness and lack of evidence in cores at the south of the Y-Y' transect do not favour this process. The sheltered estuary reduces the chance of storm surge deposition. While the uniform thickness might indicate aeolian deposition (e.g., Williams, 2009), there is no obvious local source for the sediment. Analysis of the sediments by Dr Maria Gehrels rules out tephra deposition. Consequently, the origin of the thin interbedded sandy-silt unit found between 11 and 11.5 cm depth in the top peat layer remains unknown.

The diatom-based reconstruction model for PMSE displays a noticeable drop where the sandy silt unit is found in the core. However, similar changes can also be seen in U1, and the errors are large in comparison with the change. The lack of good and close modern analogues also raises the question of the reliability of the reconstruction. There is certainly a need for more modern analogues in order to carry out a more robust assessment.

5.8.3 The 1737 earthquake

The main geological evidence for the 1737 earthquake is inferred from a tidal marsh at Chaihuín, near Valdivia (Hocking et al., 2021) and turbidite records from lakes nearly 250 km to the north (Moernaut et al., 2014). The age models suggest this age would be located between 16.5 cm and 15.5 cm depth. Neither the stratigraphy nor

the RSL reconstruction point to any evidence of the 1737 earthquake. As in previous study sites at Maullín and Chucalén, which are at the same latitude as San Antonio, there is no evidence at San Antonio which can be associated with this earthquake, promoting the idea that the rupture was constrained to the area north of San Antonio (Cisternas et al., 2017a, b).

5.8.4 The 1575 earthquake

Previous studies present evidence for the historical earthquake that occurred in 1575, also named as event B (Lomnitz, 1970, 2004, Cisternas et al., 2005). The earthquake is interpreted as having similar characteristics to the M_w 9.5 1960 earthquake in terms of rupture length, mainly offshore slip, and the generation of a major tsunami (Cisternas et al., 2005, Atwater et al., 2013, Moernaut et al., 2014, Garrett et al., 2015, Cisternas et al., 2017b, Kempf et al., 2017).

Evidence for the 1575 earthquake and accompanying tsunami is found at Maullín and Chucalén, yet there is not any obvious evidence at San Antonio. Neither the sand sheet overlying peat units at Maullín and Chucalén are interpreted as tsunami deposits or the rise in RSL resulting from subsidence is observed in the stratigraphy from San Antonio. The age-depth models indicate 1575 most likely relates to depths of between 21 and 19 cm. This depth corresponds to change in stratigraphy from organic silt (U4) to organic peat (U5). However, this change does not fit criteria for identifying subduction zone earthquakes (Nelson et al., 1996, Shennan et al., 2016). The contact is not abrupt and the RSL reconstructions do not show evidence for sudden emergence. Following the suggestion of the similarity with the 1960 earthquake, this event may have had similar slip distribution and vertical deformation; thus, the location of San Antonio may have been close to the transition from coseismic subsidence to uplift.

5.8.5 Prehistoric events

Based on geological findings, two prehistoric earthquakes are referred to as event C (1270-1450 CE) and event D (898-1220 CE) due to their resemblance to the 1960 (event A) and the 1575 (event B) earthquakes. In addition, smaller events between these large earthquakes are named bc1, bc2 and cd (Cisternas et al., 2005, 2017b, Atwater et al., 2013, Moernaut et al., 2014, Garrett et al., 2015). The basal radiocarbon age range of 990-1024 CE which is obtained at 37.5 cm depth and the age-depth models generated by *plum* include the time period for these prehistoric events. While there is evidence of coseismic deformation and the occurrence of

tsunamis in the stratigraphy at Maullín and Chucalén, San Antonio does not include tsunami deposits or any abrupt change between sedimentary deposits that might correspond to these large prehistoric earthquakes. Moreover, diatom assemblages do not mark any substantial change from marine to freshwater species. That does not suggest that these large prehistoric events did not occur, on the contrary based on these findings San Antonio did not preserve geological records for these large events. However, the reasons for sea-level fall at San Antonio during this period may be associated with its sheltered location and enclosed nature of the estuary; also, it does not preserve stratigraphic evidence as at Maullín, Chucalén and Cocotué. Moreover, the absence or scarceness of sedimentary records associated with coseismic subsidence is also pointed out as a cause of RSL fall such as at the Valdivia estuary (see Nelson et al., 2009). This suggests accommodation space could be an essential problem with RSL fall following the mid-Holocene highstand preventing the preservation of evidence for coseismic deformation (e.g., Nelson et al., 2009). Consequently, the absence of sediment deposit limits further investigation and model developments for PMSE and RSL change.

5.9 Summary

The San Antonio estuary is located in the centre of the 1960 earthquake rupture zone. According to historical records, this region was not only struck by historical events but also by large prehistoric earthquakes. The 50-cm long core that was collected provides a millennial scale record and the analysis of diatom assemblages in fossil samples, along with stratigraphy and sedimentology, aids in characterizing the sedimentation history and allows for quantitative reconstructions of relative sea-level (RSL) change.

While the sedimentary sequence covers the timing of historical great and large earthquakes, there is no geological evidence for coseismic deformation associated with them. Similarly, no evidence is available for prehistoric earthquakes (event B, C and D) over the last 1000 years. The age-depth models suggest that the 1960 earthquake should be recorded at sediment depths between 5.5 and 8.5 cm; however, there is no evidence that would satisfy the criteria of Nelson et al. (1996) and Shennan et al. (2016). The lack of evidence for coseismic deformation at the site could be attributed to its location at the eastern limit of the coseismic subsidence resulting from the 1960 earthquake.

With the aim of reconstructing vertical land-level change, a diatom-based transfer function developed in Chapter 4 is calibrated using the fossil assemblage found in the core. However, due to the limit number of modern good and close analogues, the large number of reconstruction estimates can be deemed not reliable. Moreover, the reconstruction model has failed the significant test, thereby making it challenging to determine the reliability of the reconstruction estimates under these circumstances.

In conjunction with the goodness of fit and significance tests, the reliability of the reconstruction estimates is limited by the number of samples with poor modern analogues (31/46). Further efforts are needed to increase the size of the modern training set to adequately represent the environments found in the San Antonio core which may solve the lack of good analogues problem.

Chapter 6 : Results – Reconstructions of deformation from uplifted beaches in the Valdivia Region

6.1 Introduction

This chapter introduces new stratigraphic and microfossil records from coastal exposures at Rosada, Loncoyén South, Loncoyén North, Calfuco, Chan-Chan and Isla Mancera in the Valdivia Region (Figure 6.1). Historical records show that the Valdivia region was struck by earthquakes in 1960, 1837, 1737 and 1575. As a first step in searching for evidence for these historical earthquakes, an abrupt contact between minerogenic and organic sediments is sought to determine the possible occurrence of coseismic displacement resulting in a sudden change of environment. This chapter presents lithostratigraphic properties, diatom assemblages, radiocarbon dates, as well as reconstructions from diatom-based transfer functions. Finally, I discuss whether these sites provide evidence for historical earthquakes and compare my findings with previous studies.

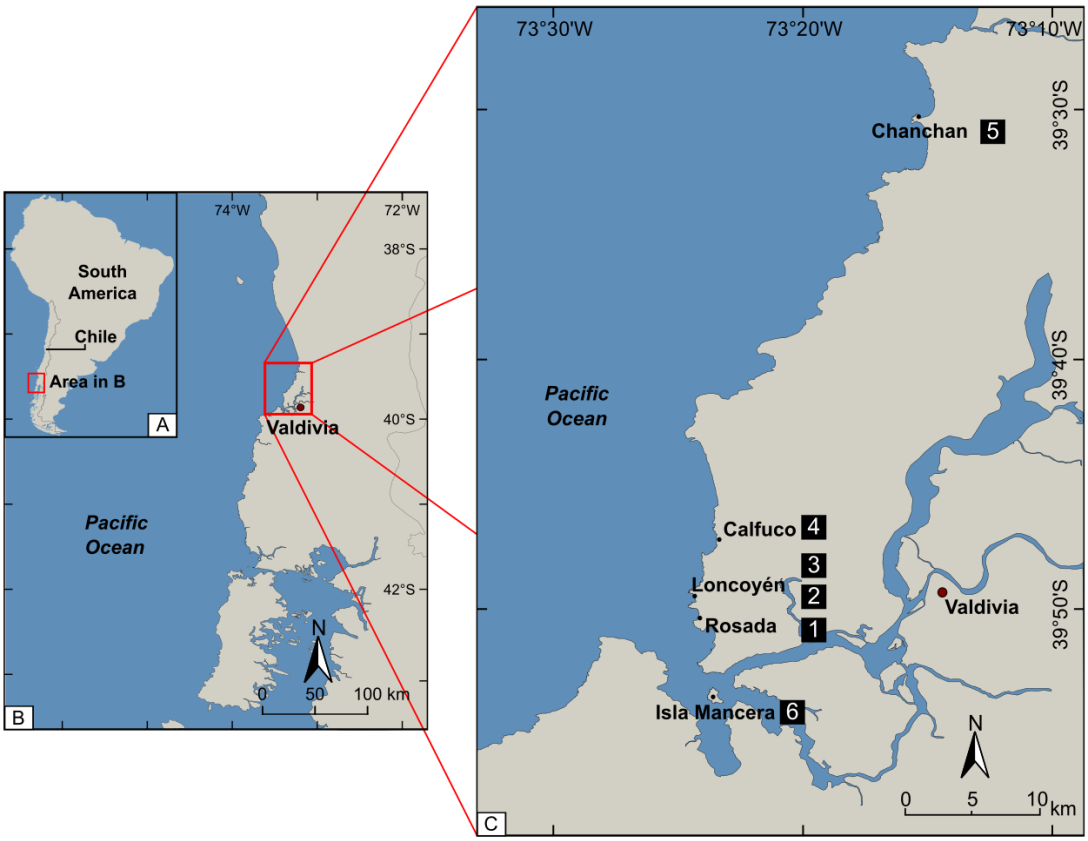

Figure 6.1 : Location of the study area within Chile (A) and the Valdivia region (B). The six sites examined in this chapter are shown in (C): Site 1: Rosada, Site: 2 Loncoyén South, Site: 3 Loncoyén North, Site: 4 Calfuco, Site: 5 Chan-Chan and Site: 6 Isla Mancera.

6.2 Study Sites

Field investigations were carried out at six coastal sites within the northern part of the Valdivia segment (39°53'S - 39°30'S) in January 2019 (Figure 6.1). The coastal geomorphology is shaped by upper marine terraces (also named as Cancagua) of late Pleistocene age, dating to Marine Isotope Stages 5e (MIS 5e) and ranging in elevation from 5 to 67 m (e.g., Astorga and Pino, 2011, Vega et al., 2018, Ditzel, 2019). The lower terraces at the back of the beach are much younger, dating to the late Holocene, and are the focus of this chapter.

6.3 Chronology

The lower terraces at each study site display an organic unit overlying a sand unit. Each exposure was sampled for radiocarbon dating just above the transition from the underlying minerogenic unit to the organic unit. For the purpose of constraining maximum ages, plant macrofossils were collected for radiocarbon dating from the bottom of the organic sedimentary unit where possible. All dates are calibrated to calendar years CE using OxCal 4.3 software (Bronk Ramsey, 2009) with the calibration curve SHCal20 (Hogg et al., 2020). In samples reaching 100% modern carbon, the post-bomb atmospheric southern hemisphere ^{14}C curve (Hua et al., 2013) was used for calibration (Figure 6.2; Table 6.1).

Radiocarbon dates from each sand/silt-peat contact from Rosada, Loncoyén North and Loncoyén South provide similar age ranges (1690 – 1950) (Figure 6.2), while the radiocarbon age for Chan-Chan covers an overlapping but slightly older age range (1515 – 1800 CE) than these three sites. Samples from Loncoyén South (59 cm), Isla Mancera (48 cm) and Calfuco return modern ages. To the south, the calibrated age for the samples at 139-140 cm on Isla Mancera provides the oldest age amongst coastal sites indicating that the organic sediment formed approximately a thousand years ago (1045 – 1216 CE), while the second samples represent the youngest calibrated age as 1956 – 1957 CE.

Table 6.1: Summary information of Accelerator Mass Spectrometry (AMS) ^{14}C dating of sediments collected from Rosada, Loncoyén South, Loncoyén North, Chachan, Calfuco and Isla Mancera, in south-central Chile. Radiocarbon ages are calibrated to calendar years CE using OxCal 4.3 software (Bronk Ramsey, 2009) with the calibration dataset SHCal20 (Hogg et al., 2020) or the post-bomb atmospheric southern hemisphere curve (Hua et al., 2013) where samples exceed 100% modern carbon.

Site	Lab Code	Sample Code	Material	Depth (cm)	Radiocarbon Age (years BP ±1σ)	$F^{14}C$ ± 1σ	Calibrated age range (± 2σ year AD)		
							Minimum	Maximum	Probability (%)
Rosada	D-AMS 033108	RO19/R1	seeds	50-51	116 ± 24		1697 1810	1724 1950	11.9 83.6
Loncoyén North	D-AMS 033110	LO19/R1N	seeds	81-83	196 ± 26		1667 1834 1924	1815 1888 1950	74.5 13.5 7.4
Loncoyén South	D-AMS 033109	LO19/R1S	seeds	41-43	98 ± 24		1699 1810 1876	1723 1870 1945	8.2 28.8 58.4
Loncoyén South	D-AMS 035644	LO19/R2S	seeds	59-60	Modern	1.0394 ± 0.0033	1956 1957	1956 1957	34.7 60.8
Chan-Chan	D-AMS 033111	CC19/R1	seeds stems	62-65	275 ± 27		1514 1626 1735	1543 1677 1800	4.7 58.1 32.6
Calfuco	D-AMS 033112	CF19/R1	seeds	73-74	Modern	0.999 ± 0.0036	1896 1915 1954 1957	1901 1919 1956 1957	1.3 0.8 93.1 0.2
Isla Mancera	D-AMS 035645	IM 19/R2A	seeds	48-49	Modern	1.0368 ± 0.0036	1956	1957	95.4
Isla Mancera	D-AMS 033113	IM19/R1	seeds	139-140	942 ± 24		1045 1105	1090 1216	30.3 65.2

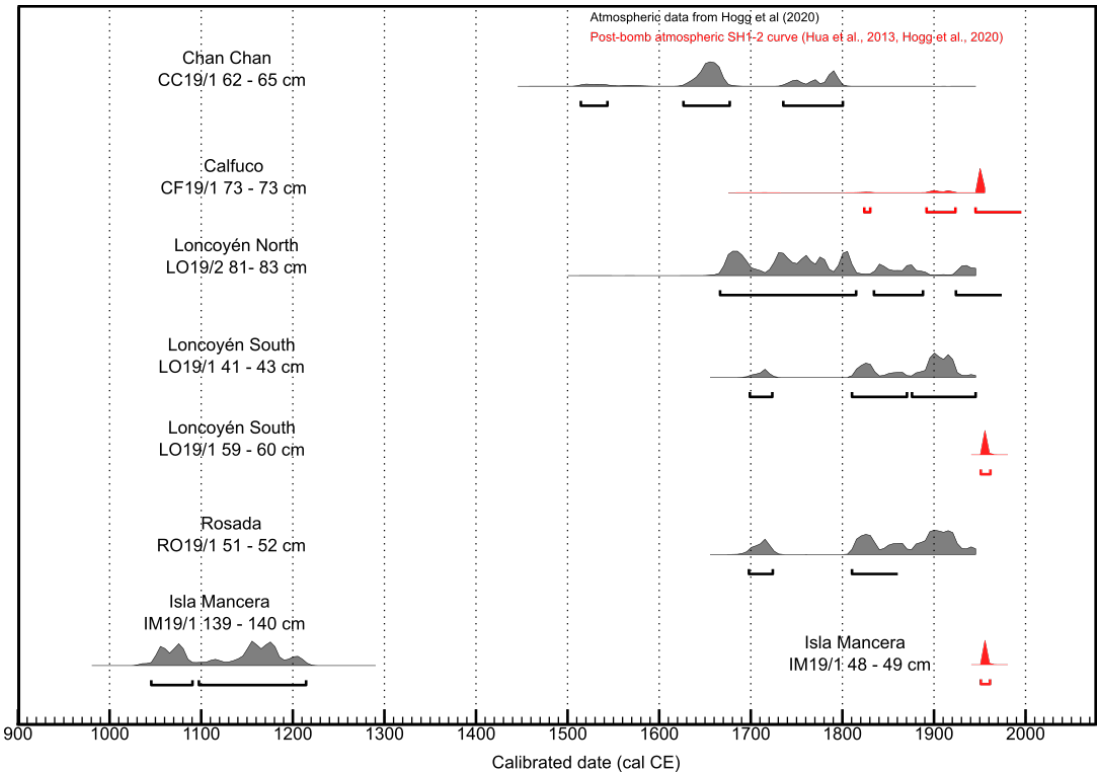

Figure 6.2 : The calibrated age ranges (yr CE ±2σ error) of all dated samples, calibrated with either the SHCal20 curve (grey) or post-bomb curve (red) using OxCal 4.3 (Bronk Ramsey, 2009). The sample sites are positioned in a north-south direction. The distances between sites are exaggerated for illustration and do not show real measures.

6.4 Site 1: Rosada

Rosada beach is nearly a 200 m long bay on the Pacific coast, ~18 km west of Valdivia city (Figure 6.3). It is confined by two headlands and oriented in a north-south direction. At the back of beach there is a low vegetated terrace approximately 0.7 m high. The landward edge of the terrace is backed by a ~30 m high riser of an MIS 5e terrace. The length of the traceable part of an exposure at the seaward side of the terrace is approximately 75 m long. The surface elevation of the described section of the exposure is 3.12 m above mean sea level (m MSL) while the average elevation is 3.51 m MSL (Ditzel, 2019).

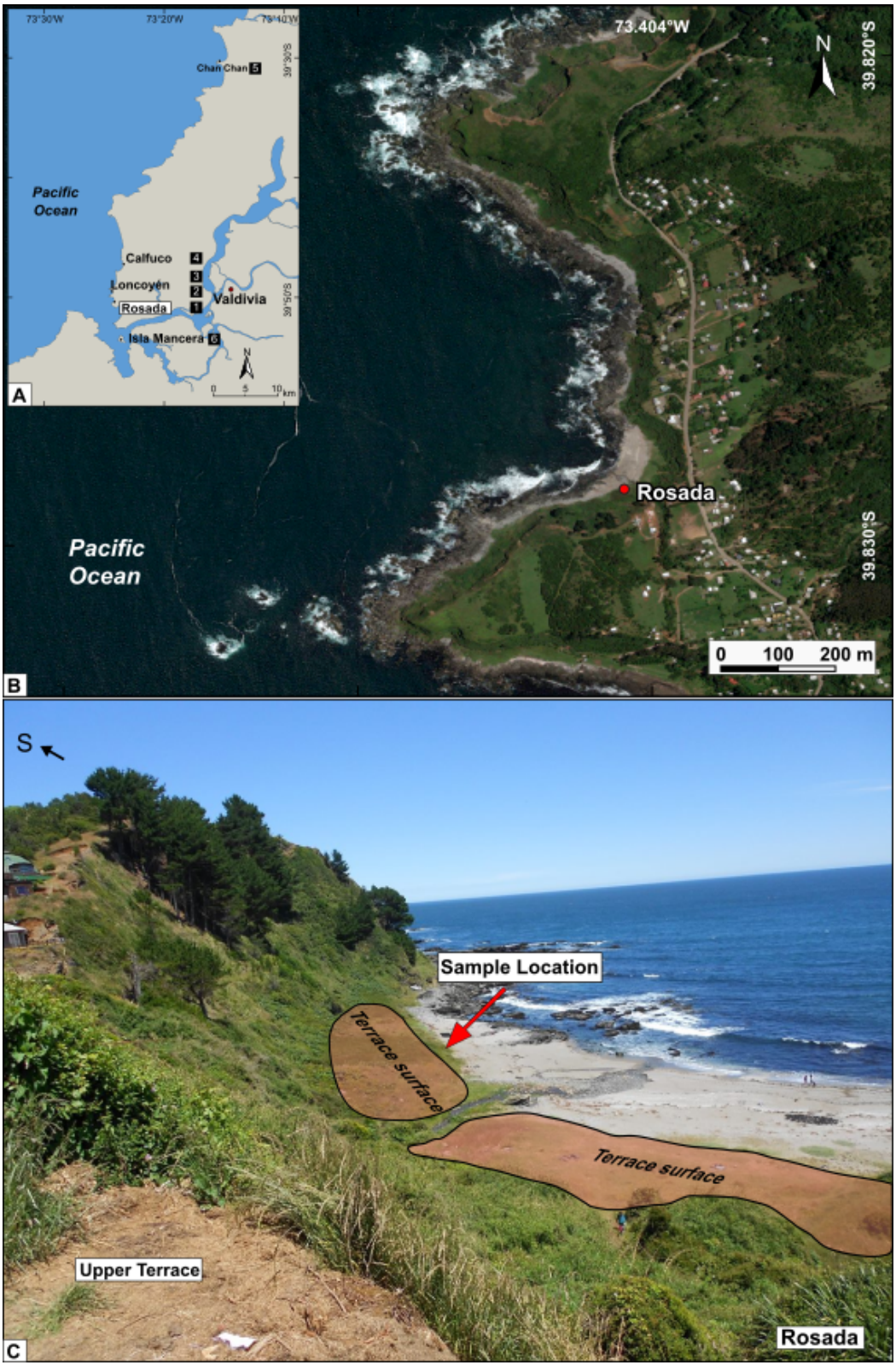

Figure 6.3 : Location map of Rosada beach (A, B). C shows the view of the beach looking southwest.

6.4.1 Lithostratigraphy

The Rosada exposure is ~70 cm high and presents four different sedimentary units (Figure 6.4). A sand unit at the bottom, which is at least 18 cm thick, consists of dark grey very coarse sand with occasional rootlets, containing rounded cobbles up to 12 cm in diameter and occasional shell fragments up to 1 cm long. The organic unit overlying the sand layer is a 28-cm thick dark brown silty humified peat unit. Above the peat layer lies a 14-cm thick mid-brown-orange organic silty coarse-grained sand unit with abundant roots with occasional rounded cobbles (up to 8 cm) and occasional shell fragments. The uppermost layer is formed by a 10-cm thick grey coarse sand containing living roots. All contacts are gradual, with no sharp contacts between any layers observed.

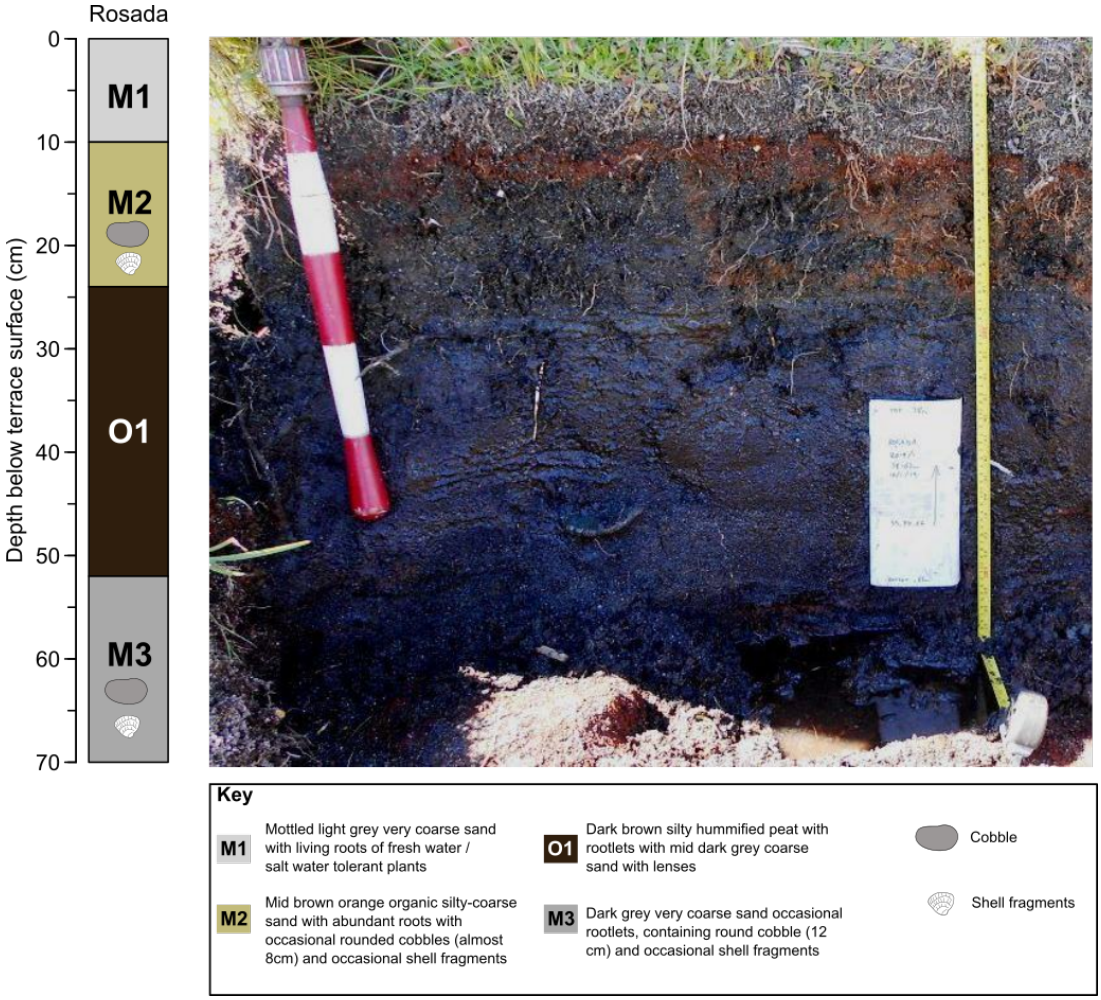

Figure 6.4 : Stratigraphy of the sampled exposure at Rosada. The sketch on the left-hand side and photo, which was taken in January 2019, on the right-hand side describe the exposure. Red and white scale bar divisions on the shovel are 10 cm.

6.4.2 Radiocarbon results

In order to constrain the timing of stratigraphic change at Rosada, AMS radiocarbon dating was carried out by selecting datable materials from the base of the peat unit. Multiple seeds found at 50-51 cm provided a calibrated age of 1697 – 1950 CE (Table 6.1).

6.4.3 Diatom assemblages

Diatom assemblages were analysed from sub-samples collected between 44 and 59 cm below the terrace surface where a clear change in stratigraphy from minerogenic to organic sediment was present. Diatom assemblages at Rosada are dominated by species with elevation optima above mean higher high water (MHHW) and there is no clear transition in the diatoms corresponding to the lithological change from sand to peat (Figure 6.5). *Rhopalodia constricta* (12 - 31%) and *Diploneis ovalis* (11 - 35%) are the most ubiquitous species across the exposure. The only common species with a modern optima below MHHW is *Navicula viridula*. Except for *Navicula viridula*, species with elevation optima below MHHW never exceed more than 10% of any fossil sample.

6.4.4 Reconstruction of elevation change

Transfer function models (regional Models C and D, see chapter 4) are applied to derive estimates of the palaeosurface elevation (PSE) associated with each fossil diatom assemblage in the coastal exposures. In spite of the fact that there is an observable transition from a minerogenic to an organic layer, PSE estimates do not underscore an evident change. Reconstruction values for all fossil samples remain above MHHW (0.65 m MSL) with both applied models (Figure 6.5). Minimum dissimilarity coefficients between modern and fossil samples show that all samples only have close and poor analogues in the modern training set. However, Model C has more close analogues than Model D, which becomes the preferable model of choice. The PSE estimates are converted to relative sea-level change (Figure 6.5), and the reconstruction suggests RSL has been relatively stable throughout the record.

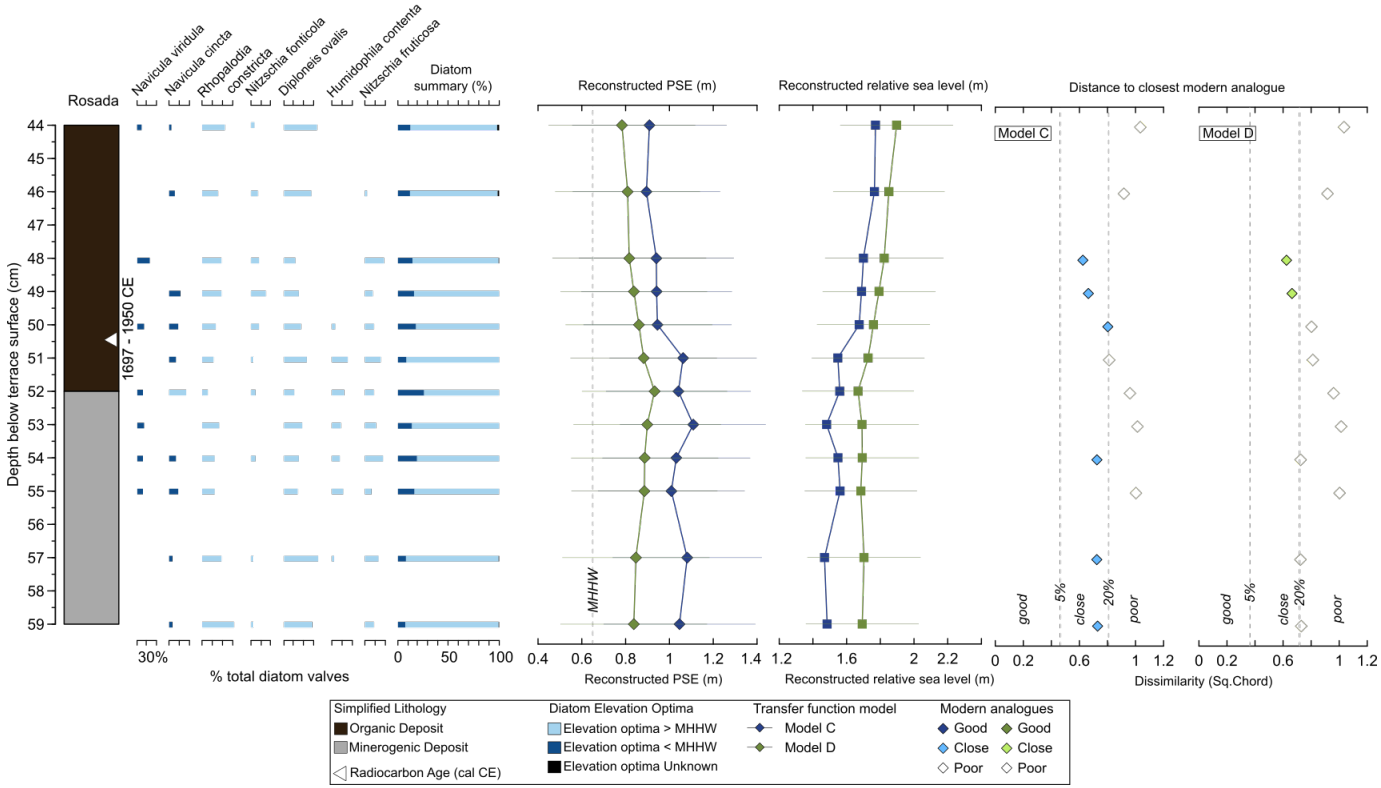

Figure 6.5 : Summary of Rosada diatom assemblages and palaeoterrace surface elevation (PSE) reconstructions derived from calibration of assemblages using the transfer function models, with the 95.4% (2σ) errors shown for both models. Species are classified as above and below MHHW based on modern species elevation optima derived from the weighted averaging (see chapter 4). The modern analogue graphs on the right-hand side display dissimilarity measure (square chord distance) and are employed to assess the similarity between the modern analogues and the fossil assemblages with good (5th percentile), close (20th percentile) and poor (> 20th percentile) as thresholds.

6.5 Site 2: Loncoyén South

Loncoyén bay is located ~18 km west of the city of Valdivia (Figure 6.6). The bay is split into two by a rocky headland, with the southern and northern sections each bounded by further rocky headlands. The southern part of the bay is ~ 700 m long. At the back of the beach there is a low terrace, with a visible exposure extending 100 m in length. Its upper surface is heavily vegetated. The elevation of the top of the described part of the terrace riser is 4.72 m MSL and the average elevation of the terrace surface is 4.90 m MSL (Ditzel, 2019).

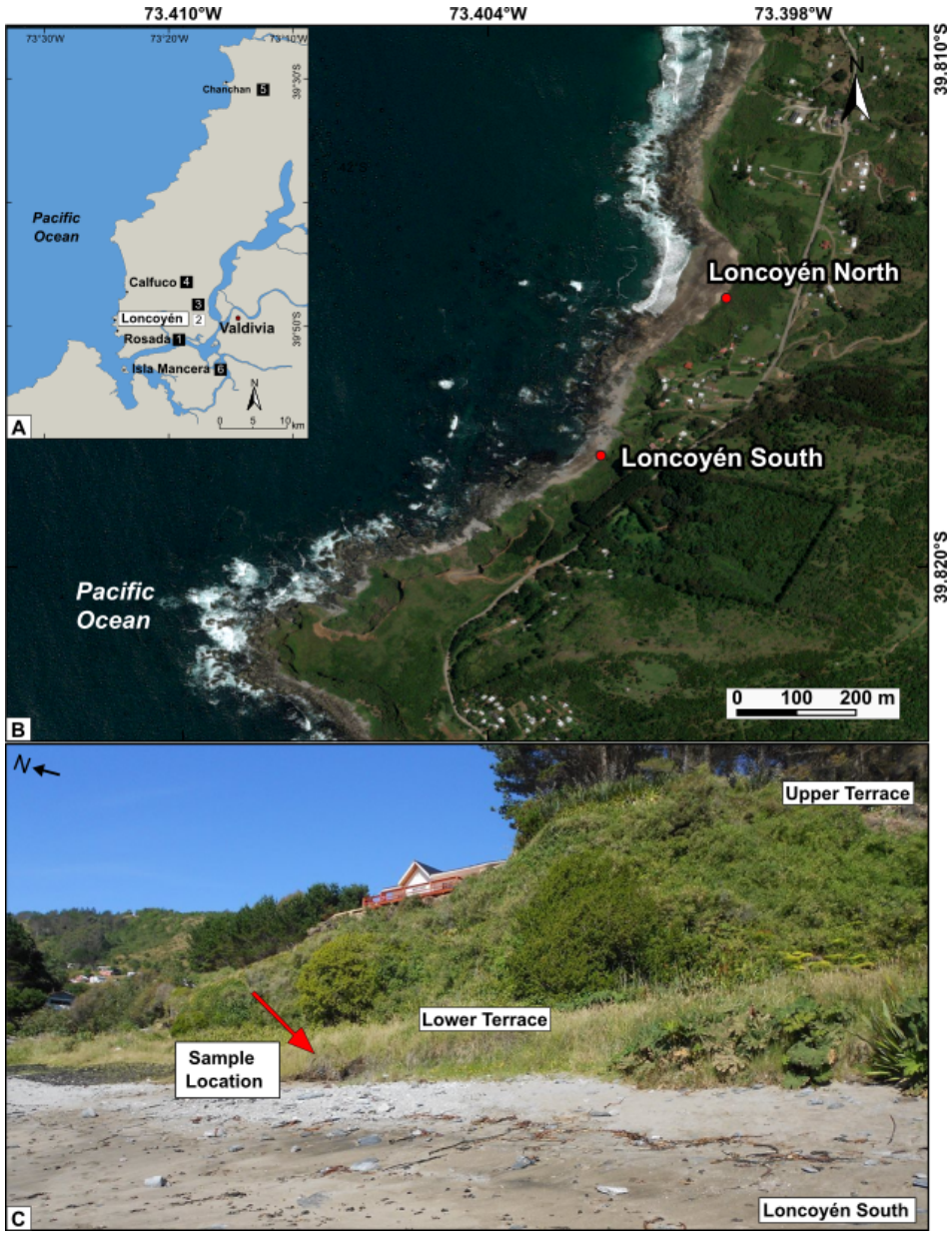

Figure 6.6 : Map of Loncoyén South beach and location of the sampled exposure (A, B). C shows the view of the beach looking northeast.

6.5.1 Lithostratigraphy

The sampled part of the Loncoyén South exposure is 94 cm high and displays six minerogenic layers and one organic layer (Figure 6.7). Four different minerogenic layers starting from the base of the exposure are composed of various colours and sizes of sand, with all but one incorporating rounded gravels ranging from 2 to 3 cm in diameter. Overlying these four layers is a light brown organic sand layer containing occasional rootlets and rounded gravels that vary in size between 1 and 2 cm. Another light grey very coarse sand unit occurs above the organic sand layer. The third layer from the top is a 22-cm thick organic mid-brown sandy peat with sand lenses thinner than 1 cm at the bottom. The unit contains roots as well as occasional gravels. The uppermost two layers are sand units containing rootlets. None of these layers showed sharp contacts.

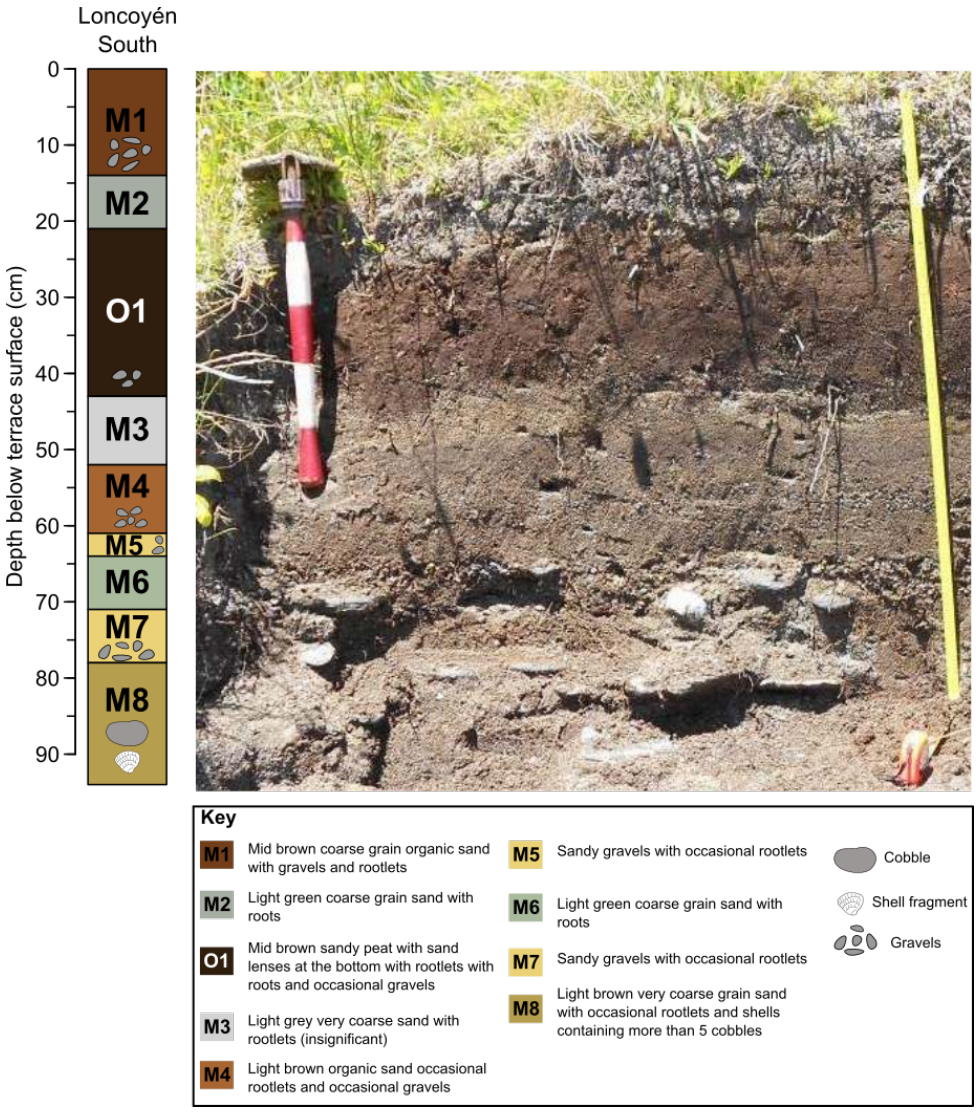

Figure 6.7 (Previous page): Stratigraphy of the sampled exposure at Loncoyén South. The sketch on the left-hand side and photo, which was taken in January 2019, on the right-hand side describe the exposure. Red and white scale bar divisions on the shovel are 10 cm.

6.5.2 Radiocarbon results

In order to constrain the timing of the initiation of peat deposition at Loncoyén South, AMS radiocarbon dating was carried out by selecting datable materials from the base of the peat unit. Multiple seeds at 41 – 43 cm provided an age of 1699 – 1945 CE, and a second sample at 59 – 60 cm exceeded 100% modern carbon, providing a modern age range of 1955 – 1956 CE (Table 6.1).

6.5.3 Diatom assemblages

Diatom assemblages were investigated from sub-samples between 36 and 61 cm below the terrace surface across an obvious change in stratigraphy from minerogenic to organic. There are clear changes in diatom assemblages within this sampled section, but these do not correlate with the change in stratigraphy (Figure 6.8). The top (36-40 cm) and bottom (47-51 cm) of the sampled section contain higher relative abundances of species with elevation optima below MHHW (ranging between 35 and 60% of the total assemblage) and dominated by *Pseudostaurosira aff. diablarum*. There is a relatively sharp transition in diatom composition between 47 and 46 cm, with the disappearance of *Pseudostaurosira aff. diablarum* and increase in relative abundance of species with elevation optima above MHHW (constituting 40% of the assemblage at 47 cm and 90% at 46 cm). *Diploneis ovalis* remains the most dominant species in the middle section, across the lithologic boundary and <10% of the assemblage is composed of low elevation taxa until another transition between 41 and 40 cm.

6.5.4 Reconstruction of elevation change

The PSE reconstructions for Loncoyén South derived from transfer function calibration do not demonstrate significant differences between estimates in general (Figure 6.8). There is some variation in the model outputs at 41 cm, where *Eunotia praerupta* seems to be driving the difference. However, this variation is still within error, and it also must be noted that the modern training sets do not provide fossil samples with even close modern analogues.

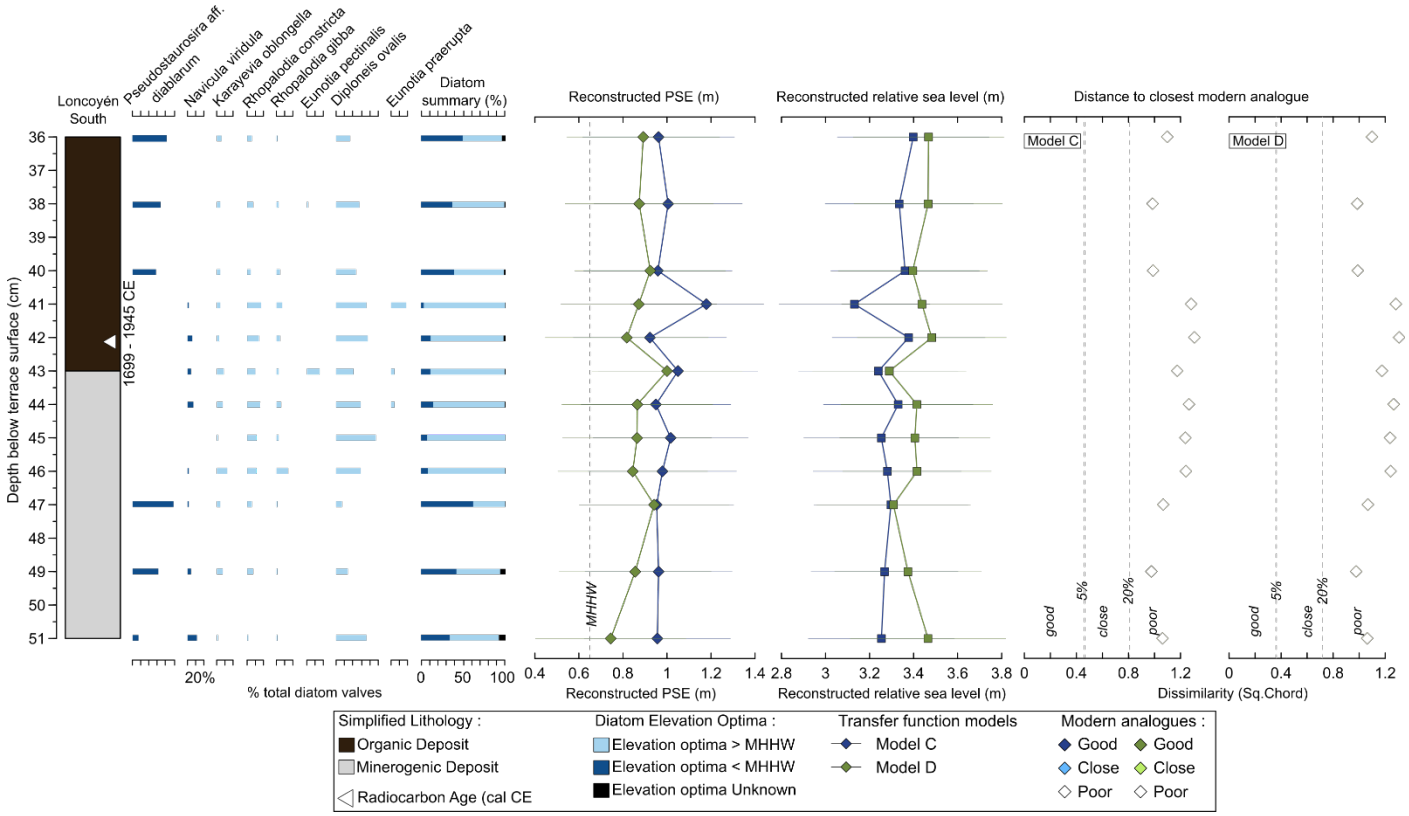

Figure 6.8 : Summary of Loncoyén South diatom assemblages and palaeoterrace surface elevation (PSE) reconstructions derived from calibration of assemblages using the transfer function models, with the 95.4% (2σ) errors shown for both models. Species are classified as above and below MHHW based on modern species elevation optima derived from the weighted averaging (see chapter 4). The modern analogue graphs on the right-hand side display dissimilarity measure (square chord distance) and are employed to assess the similarity between the modern analogues and the fossil assemblages with good (5th percentile), close (20th percentile) and poor (> 20th percentile) as thresholds.

6.6 Site 3: Loncoyén North

The exposure in the north of Loncoyén bay is located around 340 m north of the southern exposure and bounded by a rocky headland in the north. The length of the terrace at the back of the beach is 200 m (Figure 6.9). The elevation of the top of the exposure is 4.43 m MSL and the average elevation of the terrace surface is 4.64 m MSL (Ditzel, 2019).

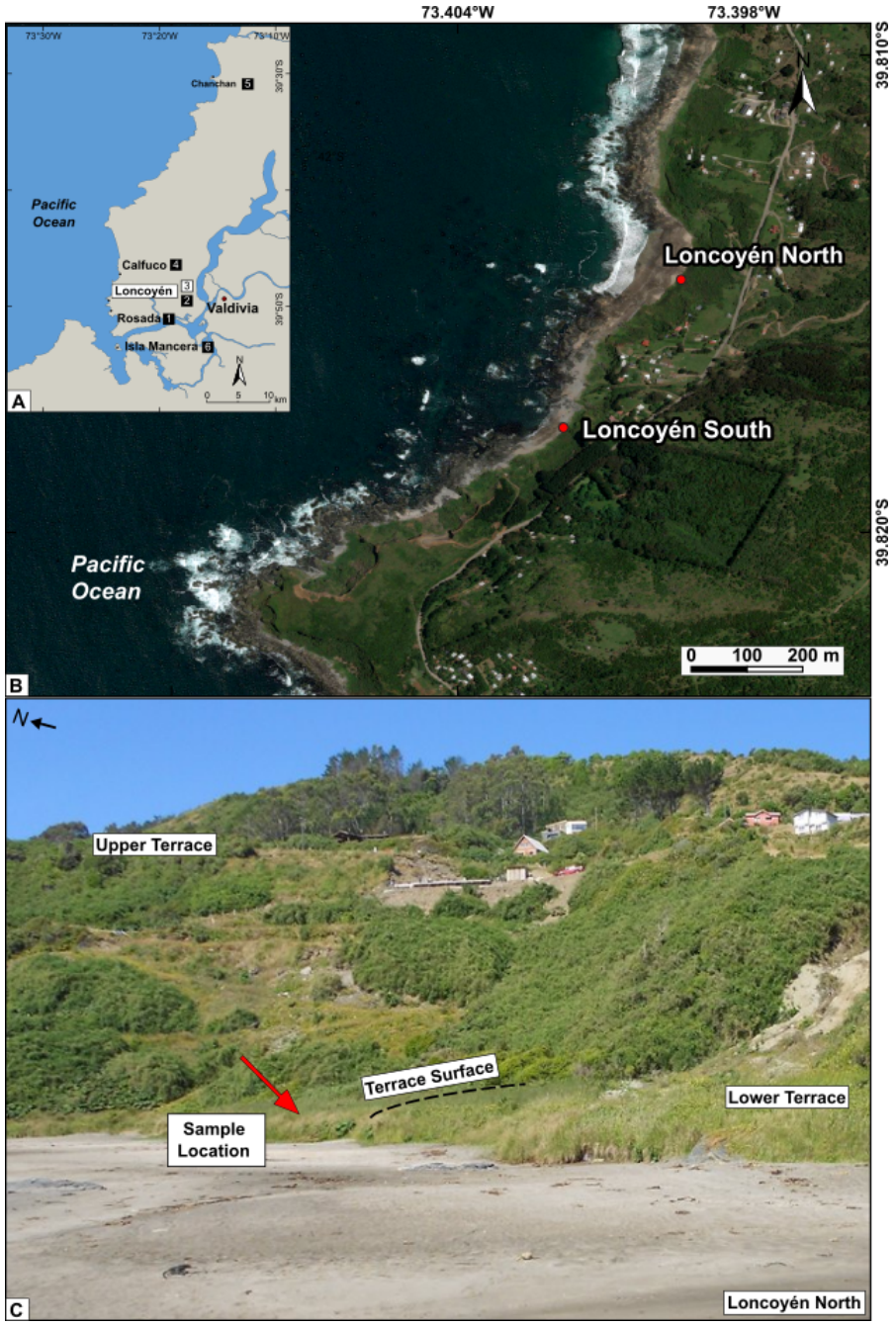

Figure 6.9 : Location map of Loncoyén North (A, B). C shows the view of the beach looking northeast.

6.6.1 Lithostratigraphy

The terrace riser at Loncoyén North is 130 cm high and exhibits four sediment units (Figure 6.10). The basal layer constitutes mid grey sand with rootlets. The overlaying organic unit is made up from 18-cm-thick mid-brown peat with rootlets containing occasional sand grains. The two layers at the top consist of mid-brown organic medium-grained sand with rootlets and dark grey fine to medium-grained sand with rootlets. There is no sign of any sharp contact across the exposure.

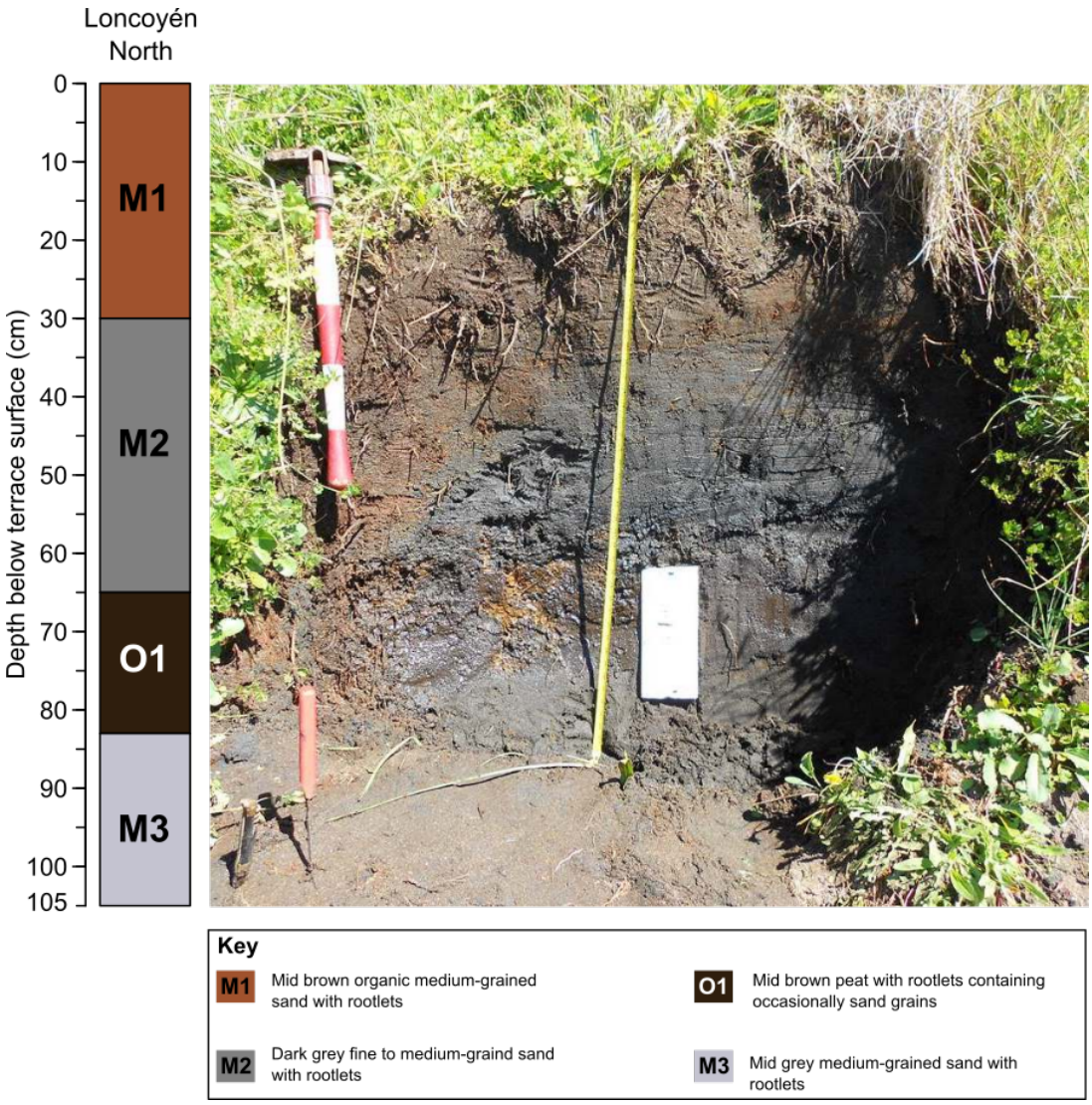

Figure 6.10 : Stratigraphy of the sampled exposure at Loncoyén North. The sketch on the left-hand side and photo, which was taken in January 2019, on the right-hand side describe the exposure. Red and white scale bar divisions on the shovel are 10 cm.

6.6.2 Radiocarbon results

The timing of stratigraphic change from the sand unit to peat found in the exposure at Loncoyén North is determined using radiocarbon dating of seeds from the base of the peat unit. A sample at 81 – 83 cm provides a calibrated age of 1697 – 1950 CE (Table 6.1).

6.6.3 Diatom assemblages

Assemblages of diatoms were explored from sub-samples collected between 75 and 91 cm below the terrace surface where a clear change in stratigraphy from minerogenic to organic unit occurs. The sampled part of the Loncoyén North exposure is dominated by species with optima above MHHW, particularly *Diploneis ovalis*. There are no distinct transitions in diatom assemblage coinciding with the lithological change from sand to peat (Figure 6.11).

6.6.4 Reconstruction of elevation change

There is no significant change in PSE estimates from the Loncoyén North exposure derived from the transfer function (Figure 6.11). There is a small but noticeable change at 86 cm in Model C, but all fossil samples have poor modern analogues in both models. A larger modern training set containing more samples from elevations above MHHW is required in order to improve the transfer function models.

The PSE estimates are converted to relative sea-level reconstructions (Figure 6.11), and reconstructions are very similar between models. There is potentially a very minor increase in RSL across the sand-peat contact, but this is very small and well within error, so it is impossible to conclude with any certainty that RSL change occurred within the sampled interval.

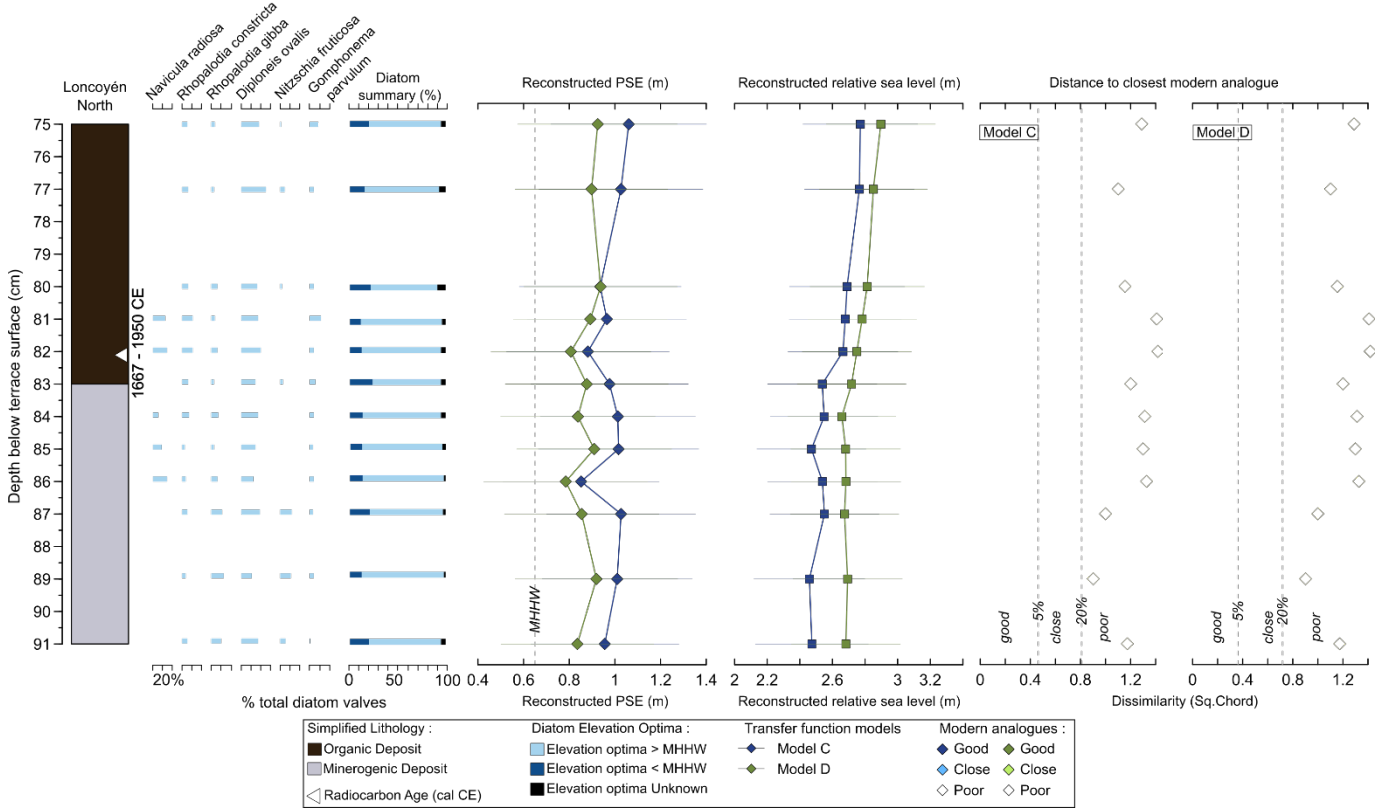

Figure 6.11 : Summary of Loncoyén North diatom assemblages and palaeoterrace surface elevation (PSE) reconstructions derived from calibration of assemblages using the transfer function models, with the 95.4% (2σ) errors shown for both models. Species are classified as above and below MHHW based on modern species elevation optima derived from the weighted averaging (see chapter 4). The modern analogue graphs on the right-hand side display dissimilarity measure (square chord distance) and are employed to assess the similarity between the modern analogues and the fossil assemblages with good (5th percentile), close (20th percentile) and poor (> 20th percentile) as thresholds.

6.7 Site 4: Calfuco

Calfuco beach is located nearly 14 km northwest of Valdivia (Figure 6.12). The coastal exposure is 320 km long with a densely vegetated terrace with an average elevation of 4.46 m MSL at the back of beach and the landward edge of the terrace is backed by a 20 - 30 m high riser of an MIS 5e age terrace. The elevation of the top of the sampled profile of the exposure is 4.25 m MSL (Ditzel, 2019).

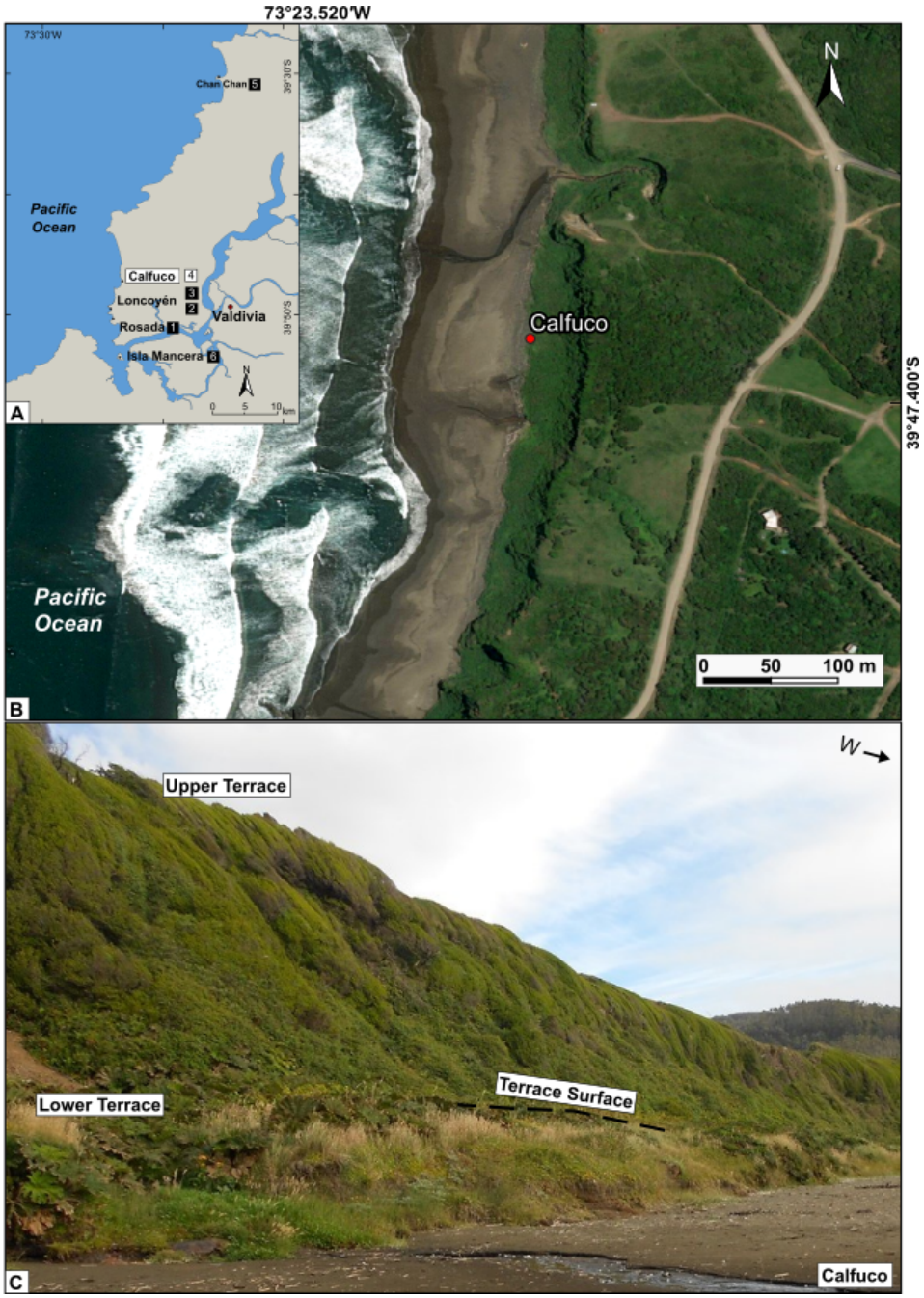

Figure 6.12 : Location map of Calfuco beach (A, B). C shows the view of the beach looking southeast.

6.7.1 Lithostratigraphy

The Calfuco exposure is comprised of nine stratigraphic units, with four abrupt transitions between minerogenic and organic layers (Figure 6.13). Note the cleaned section logged in Figure 6.13 was from a different part of the exposure to where the monoliths were taken for diatom analysis, hence the depths of stratigraphic boundaries vary slightly in subsequent figures.

The basal sand (M5) unit is 37-cm thick and comprises fine to medium-grained sand that consists of dark grey blue-dark yellow and mid yellow colour altered heavy minerals. This bottom unit is overlain by a 3 cm-thick dark brown fine to medium-grained organic silty-sand (M4) with sharp contact (2-3 mm) with the overlying organic unit, which is a 10-cm thick dark brown well-humified herbaceous peat containing roots (O4). This organic unit is overlain by mid brown humified silty-peat (O3). The next unit (M3) is a 2-cm thick dark yellow fine to mid grain sand with rootlets; however, it pinches out and is not continuous along the cross section. It is capped by a 3-cm thick dark brown well-humified herbaceous peat (O2) containing roots with a sharp contact (2 mm) with the upper minerogenic dark yellow fine to medium-grained sand with rootlets (M2); yet this unit also pinches out and is not continuous along the cross section as M3. The layer above M2 is a 9-cm thick dark brown well-humified herbaceous peat layer (O1) that contains roots with sharp contact (1 mm) with the top unit. The top unit is a 42-cm thick fine to medium mottled sand with abundant roots.

6.7.2 Radiocarbon results

The timing of stratigraphic change at Calfuco is constrained using AMS radiocarbon dating by selecting datable materials from the base of the peat unit. At 73 – 74 cm multiple seeds were found and used to provide the age of the lowermost sand to peat contact. That age is calibrated using the post-bomb atmospheric southern hemisphere ^{14}C curve (Hogg et al., 2020) and provides a calibrated age of 1896 – 1957 CE (Table 6.1).

6.7.3 Diatom assemblages

Diatom analysis was focussed between 66 and 81 cm below the terrace surface to cover the lowermost transition from minerogenic sediment to peat (Figure 6.14). Below 76 cm, sand samples are dominated by species with elevation optima below MHHW including *Navicula cincta* and *Fallacia pygmaea*. There is a sharp transition between 75 and 76 cm, above which diatoms with higher elevation optima above

MHHW dominate. From 75 to 66 cm, species assemblages are consistent with taxa including *Planothidium lanceolatum, Rhopalodia constricta, Diploneis ovalis* and *Lemnicola hungarica* dominating.

6.7.4 Reconstruction of elevation change

Both transfer function models provide estimation for the PSE at Calfuco and present very similar trends (Figure 6.14). The change in stratigraphy does not correspond to a change in the PSE. The same circumstance can be seen for reconstructed RSL. However, again it must be noted that neither model performs well in terms of providing fossil samples with any good or close modern analogues.

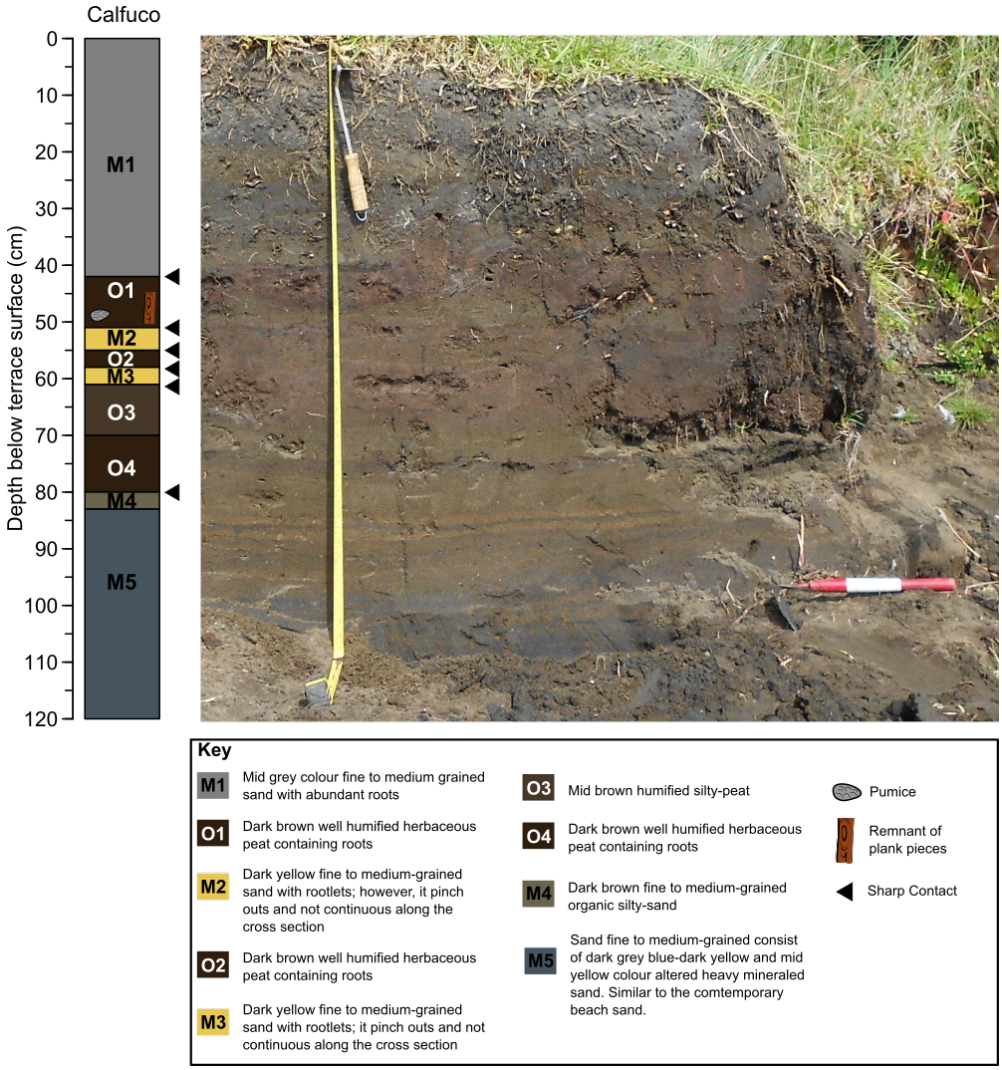

Figure 6.13 : Stratigraphy of the sampled exposure at Calfuco. The sketch on the left-hand side and photo, which was taken in January 2019, on the right-hand side describe the exposure. Red and white scale bar divisions on the shovel are 10 cm.

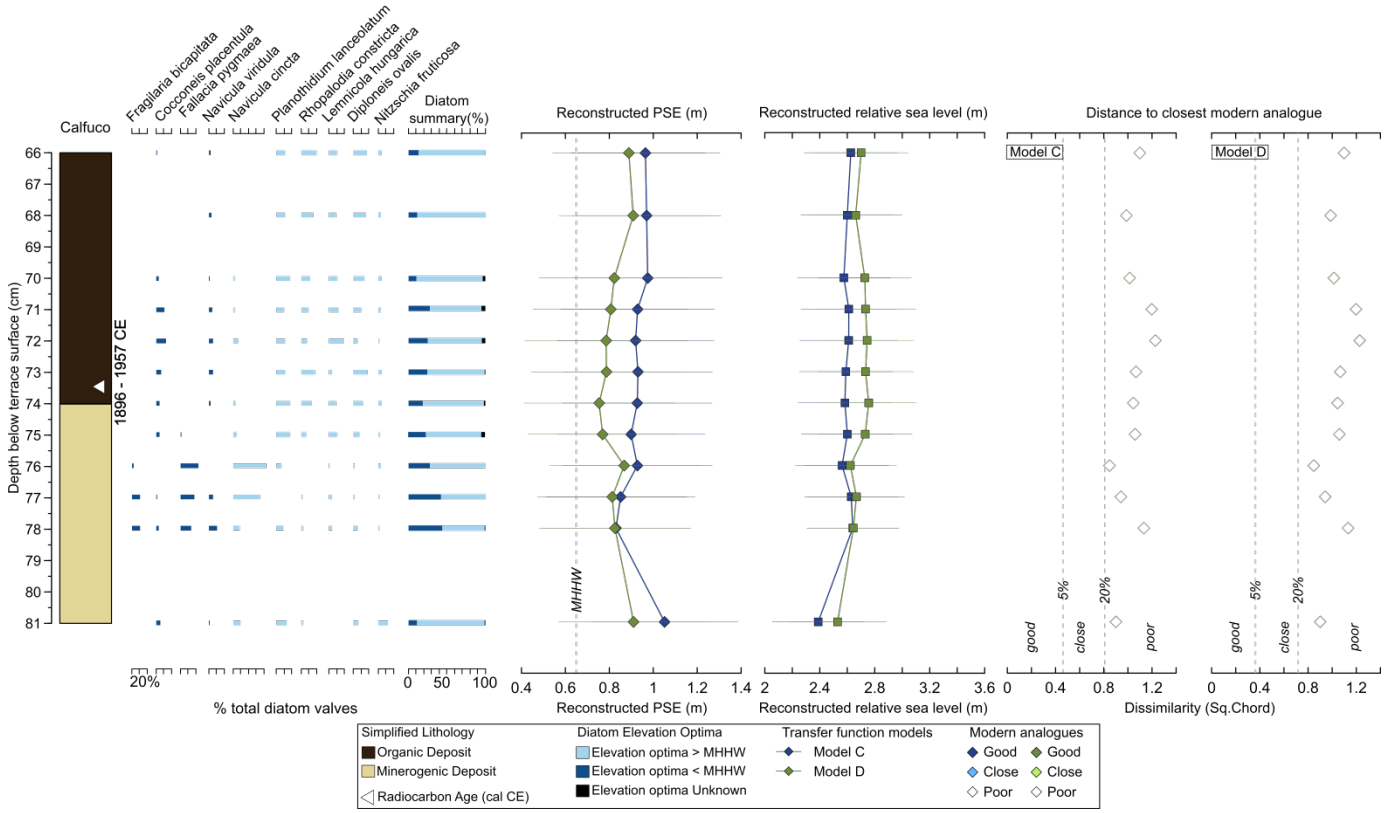

Figure 6.14 : Summary of Calfuco diatom assemblages and palaeoterrace surface elevation (PSE) reconstructions derived from calibration of assemblages using the transfer function models, with the 95.4% (2σ) errors shown for both models. Species are classified as above and below MHHW based on modern species elevation optima derived from the weighted averaging (see chapter 4). The modern analogue graphs on the right-hand side display dissimilarity measure (square chord distance) and are employed to assess the similarity between the modern analogues and the fossil assemblages with good (5th percentile), close (20th percentile) and poor (> 20th percentile) as thresholds.

6.8 Site 5: Chan-Chan

Chan-Chan is located 26 km north of Valdivia and the bay is confined by a headland to the west which is connected to the mainland through Huezhui tombolo (Figure 6.15). This site does not represent an obvious exposure contrary to the southern sites and the present exposure is ~90 m long. It is densely vegetated but dry; thus, describing the stratigraphy of the terrace riser was challenging. The average elevation of the top of the exposure is measured as 3.02 m above mean sea level (Ditzel, 2019).

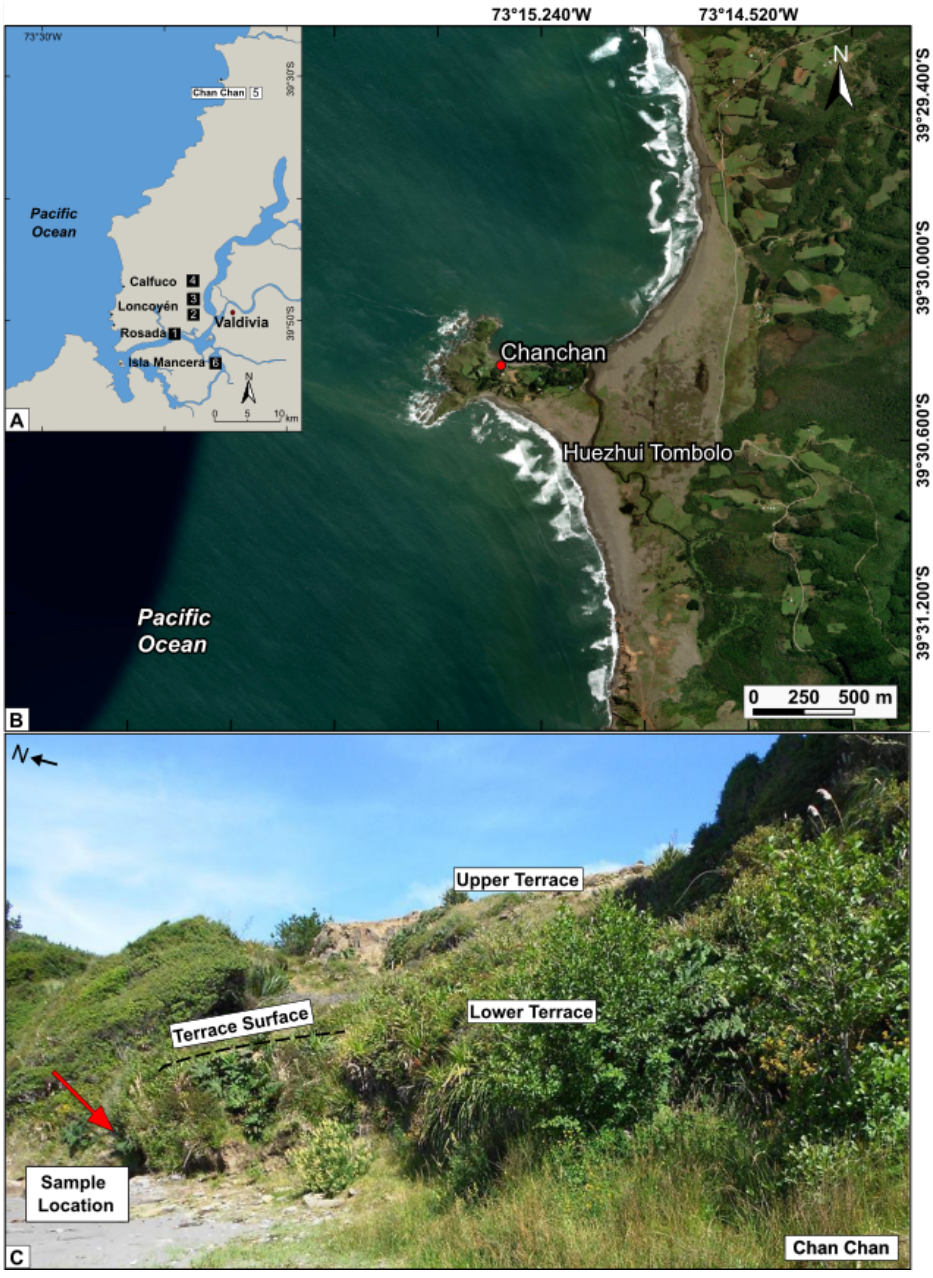

Figure 6.15 : Location map of Chan-Chan beach (A, B). C shows the view of the beach looking northeast.

6.8.1 Lithostratigraphy

The coastal exposure at Chan-Chan is 70 cm high and characterised by four units (Figure 6.16). The basal 5 cm thick unit is a dark brown sand with rootlets containing boulders (larger than 25 cm) and angular rocks and is sharply overlain by light brown peat. The peat is overlain by two sand units: the mid brown sand unit (M2) containing rootlets and boulder between 21 and 27 cm which is overlain by light brown sand (M1) including herbaceous organic matter with rootlets and gravels as a the top unit.

Figure 6.16 : Stratigraphy of the sampled exposure at Chan-Chan. The sketch on the left-hand side and photo, which was taken in January 2019, on the right-hand side describe the exposure. The length of monolith is 25 cm as reference to the scale.

6.8.2 Radiocarbon results

The timing of peat deposition overlying the basal sand at Chan-Chan is constrained using radiocarbon dating. Multiple seeds and stems were selected from the base of the peat unit at 62 – 65 cm. These provided a calibrated age of 1515 – 1800 CE (Table 6.1).

6.8.3 Diatom assemblages

Diatoms were analysed between 60 and 70 cm below the terrace surface where an evident change in stratigraphy from minerogenic to organic units occurs. Species typically found above MHHW are present above and below the lithological transition at 65 cm depth, however the preservation of diatoms is extremely limited from the exposure and counts could not reach the minimum level of 250 valves in 3 samples (Figure 6.17). Under this circumstance, it is therefore challenging to make interpretations upon zonation and transitions based on very limited diatom assemblage data.

6.8.4 Reconstruction of elevation changes

Diatom preservation in the peat and sand units was very poor, and it was not possible to acquire representative counts (>250 valves) from both peat and sand units. Only 2 of out 8 samples provided a minimum count of diatom valves, and therefore the reconstruction of PSE was only possible from two fossil samples at 61 and 66 cm (Figure 6.17). Reconstruction estimates confirm an elevation above MHHW, and fossil samples have only close modern analogues in the training set; however, it is not possible to reconstruct PSE at higher resolution due to the lack of diatoms in other samples. The PSE estimates from Model C and Model D are converted to relative sea-level reconstructions. The values for RSL estimates are close to the MHHW (0.66 m) boundary and differences in the estimates are low amongst models.

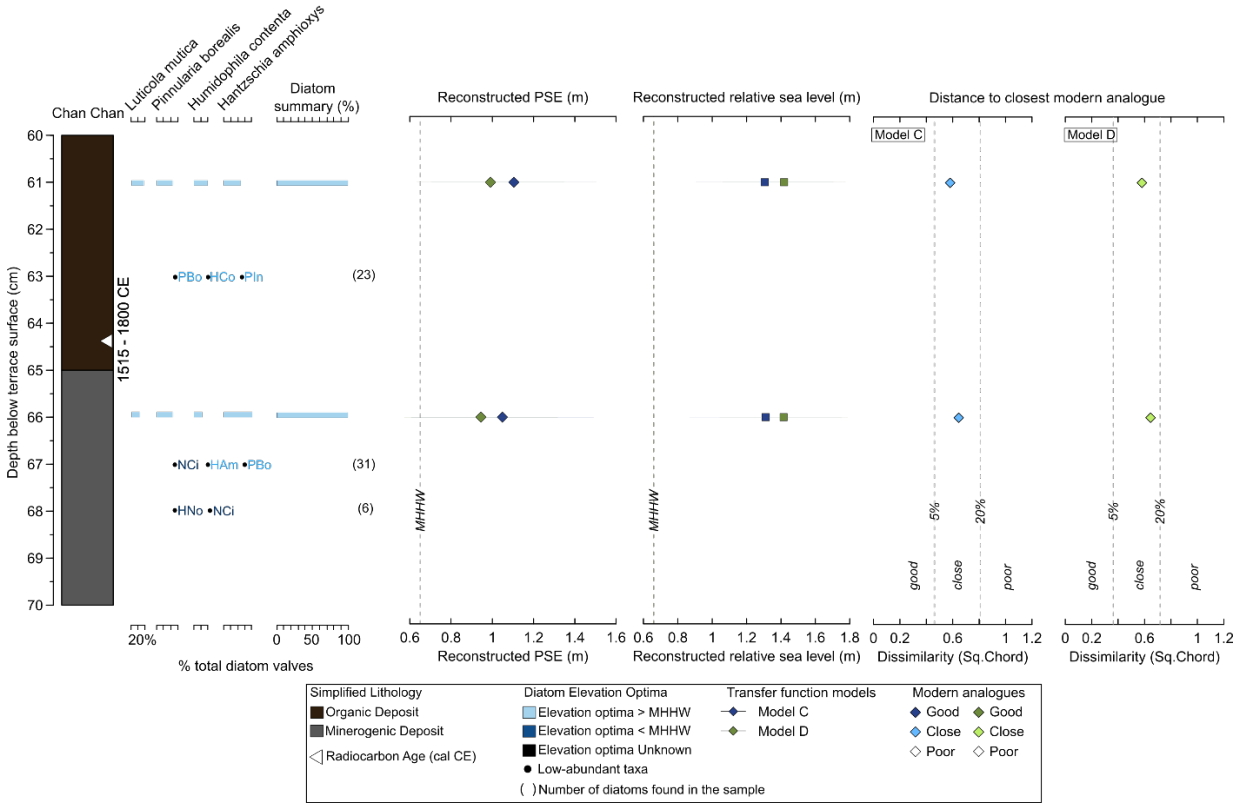

Figure 6.17 : Summary of Chan-Chan diatom assemblages and palaeoterrace surface elevation (PSE) reconstructions derived from calibration of assemblages using the transfer function models, with the 95.4% (2σ) errors shown for both models. Species are classified as above and below MHHW based on modern species elevation optima derived from the weighted averaging (see chapter 4). The modern analogue graphs on the right-hand side display dissimilarity measure (square chord distance) and are employed to assess the similarity between the modern analogues and the fossil assemblages with good (5th percentile), close (20th percentile) and poor (> 20th percentile) as thresholds.

6.9 Site 6: Isla Mancera

Isla Mancera is an island approximately 560 m^2 and located approximately 30 km southwest of the city of Valdivia. The coastal exposure occurs on the western side of the island (Figure 6.18). The elevation of the top of the exposure is 2.64 m MSL and the average elevation of the terrace surface is 2.70 m MSL (Ditzel, 2019). The described profile of the terrace riser is covered by dense vegetation and nearly 90 m long.

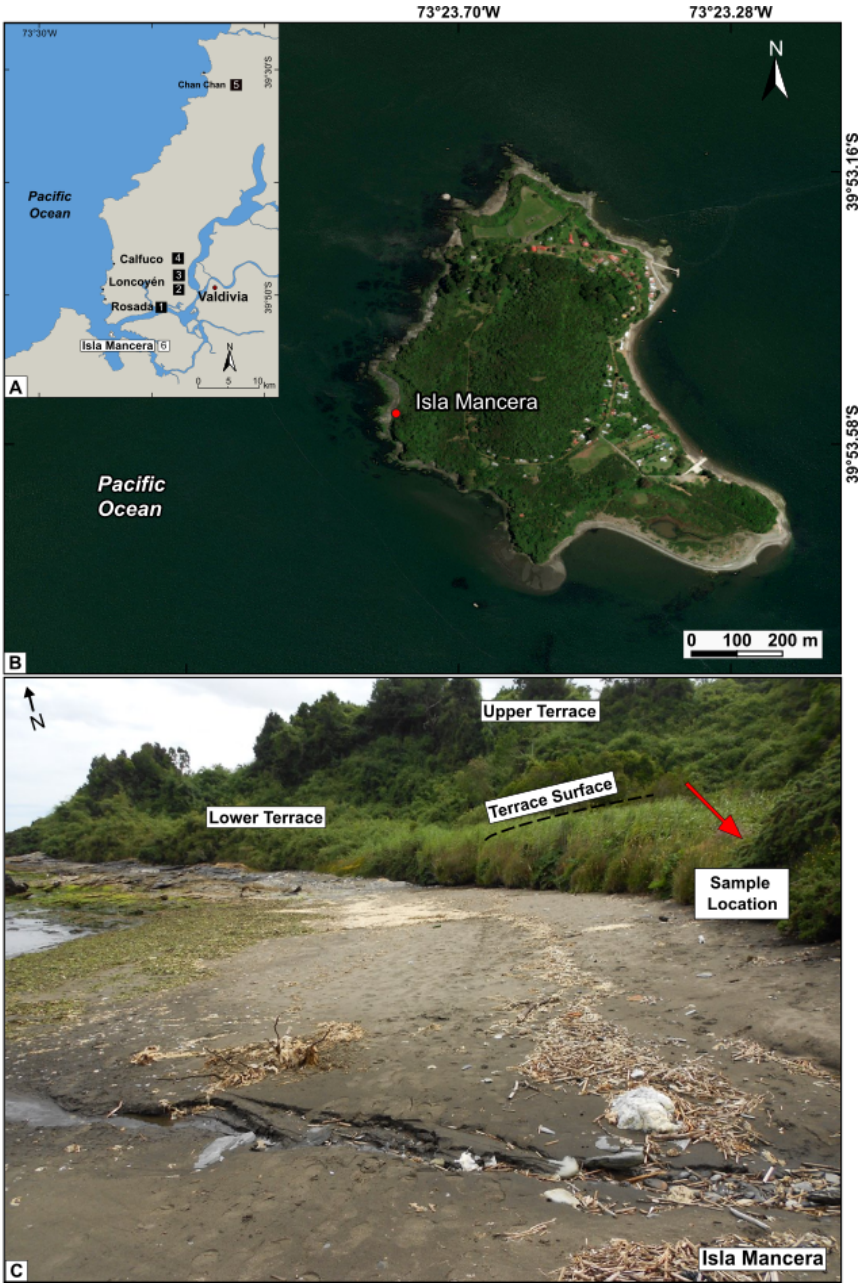

Figure 6.18 : Location map of Isla Mancera (A, B). C shows the view of the beach looking northwest.

6.9.1 Lithostratigraphy

The exposure at Isla Mancera is 150 cm high and comprises eight sedimentary units overlying bedrock (Figure 6.19). The base of the section consists of cobbles, gravels, pebbles, and sand, and is overlain by a peat unit (O3), separated by a sharp contact at 140 cm. The peat also has a sharp upper contact with the overlying mid grey sand unit (M3) containing gravels. The unit above is a 58-cm thick dark brown humified herbaceous peat containing rootlets, sharply overlain by another grey sand unit (M2). The organic unit (O1) right above this layer comprises mid brown silty herbaceous peat which also has sharp contact with the overlying coarse grey sandy unit above (M1).

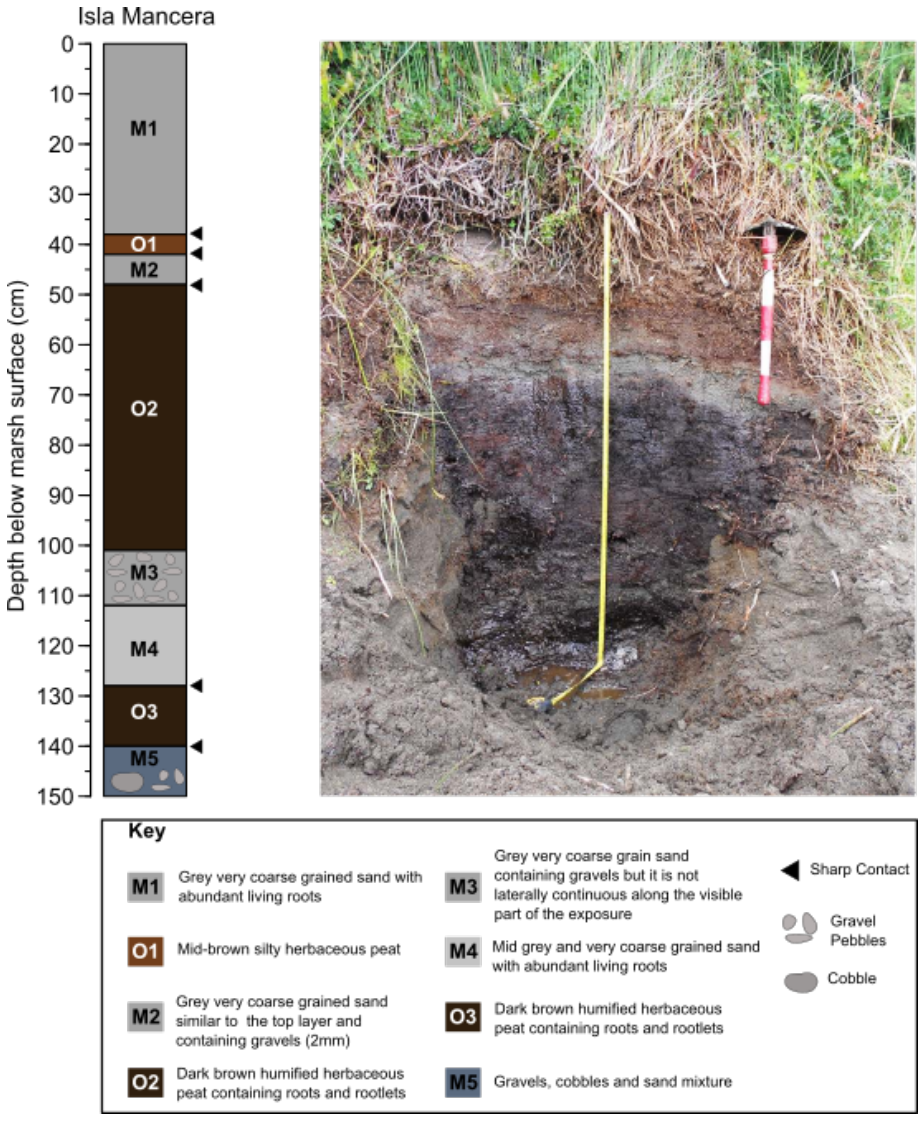

Figure 6.19 : Stratigraphy of the sampled exposure at Isla Mancera. The sketch on the left-hand side and photo, which was taken in January 2019, on the right-hand side describe the exposure. Red and white scale bar divisions on the shovel are 10 cm.

6.9.2 Radiocarbon results

Two AMS radiocarbon samples provide a constraint on the chronology for the Isla Mancera sedimentary sequence. The chronology of the exposure was determined using radiocarbon dating of seeds from peat units. The calibrated age range for the first organic sediment occurring 139 – 140 cm is 1045 – 1216 CE and the youngest organic sediment found at 48 – 49 cm is 1955 – 1971 CE (Table 6.1).

6.9.3 Diatom assemblages

Diatom assemblage data from Isla Mancera is discrete and extracted only from peat layers at 38 cm, 48 cm, 80 cm, 112 cm, 128 cm, and 139 cm, due to very limited time in the field to collect samples (Figure 6.20). The species with lower elevation optima decrease in abundance from 139 to 80 cm (from 48 to 0 % of the assemblage). At 80 cm diatom assemblages are dominated by a relatively high percentage of *Eunotia sp.1*. As this taxon could not be identified to species level, it has an unknown elevation optimum. While diatoms with sub-MHHW optima dominate the organic sample at 48 cm, particularly *Aulacoseira distans*, the upper organic unit (O1) is dominated by species with supra-MHHW optima.

6.9.4 Reconstruction of elevation change on Isla Mancera

Overall, both PSE reconstructions from both transfer function models are similar. However, due to the small number of fossil samples it is challenging to understand the overall pattern of PSE change (Figure 6.20). There is slight RSL fall of 0.27 ± 0.57 m (model D) between 140 and 128 cm, although this is within error. This is followed by a period of RSL rise. The sharp change from unit O1 to unit M1 is dated to 1956 – 1957 CE, and therefore it is suggested that this is associated with the 1960 earthquake. Moreover, Model D reconstructs a 0.36 m fall in the RSL while the Model C display only 0.02 m fall. However, these RSL changes must be viewed with caution, as the analogue matching technique showing that neither model reach good and close analogue thresholds and emphasising the requirement for a larger modern dataset to improve reconstruction estimates.

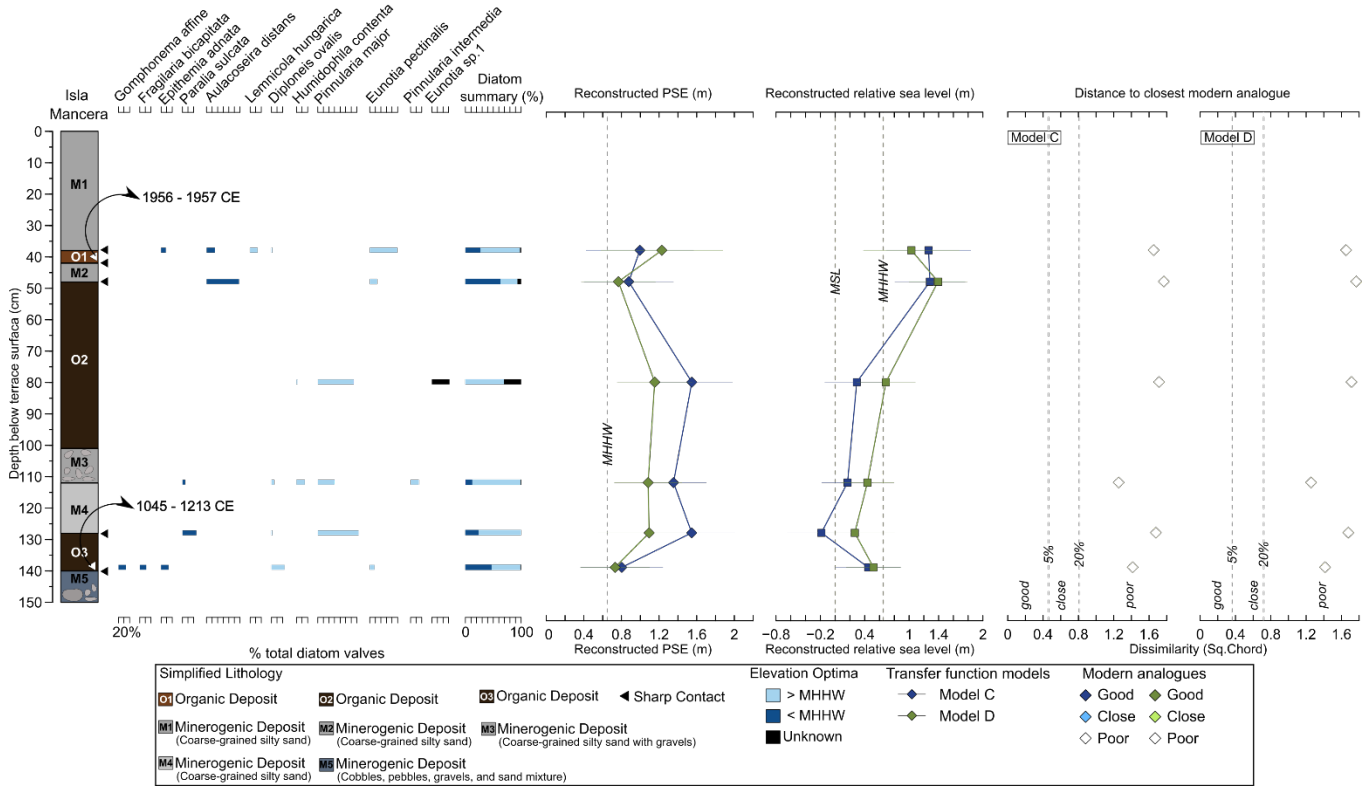

Figure 6.20 : Summary of Isla Mancera diatom assemblages and palaeoterrace surface elevation (PSE) reconstructions derived from calibration of assemblages using the transfer function models, with the 95.4% (2σ) errors shown for both models. Species are classified as above and below MHHW based on modern species elevation optima derived from the weighted averaging (see chapter 4). The modern analogue graphs on the right-hand side display dissimilarity measure (square chord distance) and are employed to assess the similarity between the modern analogues and the fossil assemblages with good (5th percentile), close (20th percentile) and poor (> 20th percentile) as thresholds.

6.10 Assessment of the reconstructions

Quantitative reconstructions of relative palaeosurface elevation based on diatom assemblages from six sites provide results where there are sufficient diatom counts available. However, it is suggested that the reliability of a reconstruction model hinges upon similarity between fossil samples and modern analogues within the training set (ter Braak, 1995a), as calculated by the modern analogue technique. Unfortunately, the regional modern training set used does not provide fossil samples from Loncoyén South, Loncoyén North, Calfuco, Isla Mancera with either “good” or “close” modern analogues and provides only “close” modern analogues for fossil samples from Rosada and Chan-Chan (Table 6.2). Model C (WA-PLS) performs slightly better than Model D (LW-WA) in terms of the modern training set providing closer analogues for fossil samples at Rosada. However, a key conclusion is that the modern training set should be expanded, particularly with samples from the extremes of the elevation gradient, in order to generate better and more reliable reconstructions.

Table 6.2 : Percentages of close analogues from the modern samples calculated using MAT from coastal sites in the Valdivia Region.

Site and Core number (no. of samples)	Transfer Function Model	% of samples with ‘good’ modern analogues	% of samples with ‘good/close’ modern analogues
Rosada	Model C	0	50
RO19/1 (12)	Model D	0	16.67
Loncoyén South	Model C	0	0
LO19/1 (12)	Model D	0	0
Loncoyén North	Model C	0	0
LO19/2 (12)	Model D	0	0
Calfuco	Model C	0	0
CF19/1 (12)	Model D	0	0
Chan-Chan	Model C	0	*
CC19/1 (2)	Model D	0	*
Isla Mancera	Model C	0	0
IM19/1 (6)	Model D	0	0

* Number of fossil diatom is below the minimum count of 250 valves; hence, reconstruction model for Chan-Chan do not provide reliable estimates.

6.11 Discussion

Depositional environments are characterised based on lithostratigraphy, diatom assemblages and radiocarbon ages. It was initially hypothesised that the deposition of organic sediment overlying sand was concurrent across the six sites. However, the radiocarbon ages suggest this may not be the case. As reported by historical records these coastal sites were affected by both the 1837 and 1737 CE earthquake (Lomnitz, 1970, 2004, Cisternas et al., 2005, 2017b) in addition to the M_w 9.5 1960 and 1575 CE earthquakes. The radiocarbon ages suggest that organic units overlaying sand units at Rosada, Loncoyén North, Loncoyén South, and Chan-Chan cover and fit the timing of the 1737 earthquake (1500 – 1950 CE) (Figure 6.21). However, radiocarbon age ranges encompassing both historical earthquakes occurred in 1837 CE and 1737 CE with the exception for Calfuco and Isla Mancera exposures. Moreover, this age constraint permits correlation of these peat units with both historical earthquakes. One of the common issues of radiocarbon dating is its inability to differentiate sediments from a short timescale due to plateaux in the radiocarbon calibration curve covering a large age range for the last 500 years (McCormac et al., 2004; Hua, 2009). Despite the radiocarbon age range for Chan-Chan including the 1575 CE earthquake, historical records show the occurrence of coseismic subsidence and large tsunami which does not match with coastal stratigraphy. However, there is a discrepancy between the radiocarbon ages from Loncoyén South because of the stratigraphic position of samples and dating results. The age range for the sample between 41 - 43 cm yields 1699 – 1945 CE while the sample at 59 - 60 cm provides a younger age range of 1956 – 1957 CE. The younger age at 59 - 60 cm may have been derived from penetration of roots or the older age at 41 - 43 cm may have been associated with reworking materials; thus, the calibrated result was rejected on stratigraphic grounds. Nonetheless the old age is independently correlated with and provides a similar radiocarbon age at Loncoyén North which is the same beach and is separated by ~0.4 km. Thus, here the younger radiocarbon age is discounted for interpretation.

At Calfuco and Isla Mancera, dated intervals do not include the 1737 rupture; however, with only limited radiocarbon ages it is not possible to rule out preservation of the 1737 CE earthquake on the basis of chronology alone. Additional samples are required in order to establish a more robust chronology and confirm whether observed sand-peat contacts relate to land-level change associated with the 1737 earthquake.

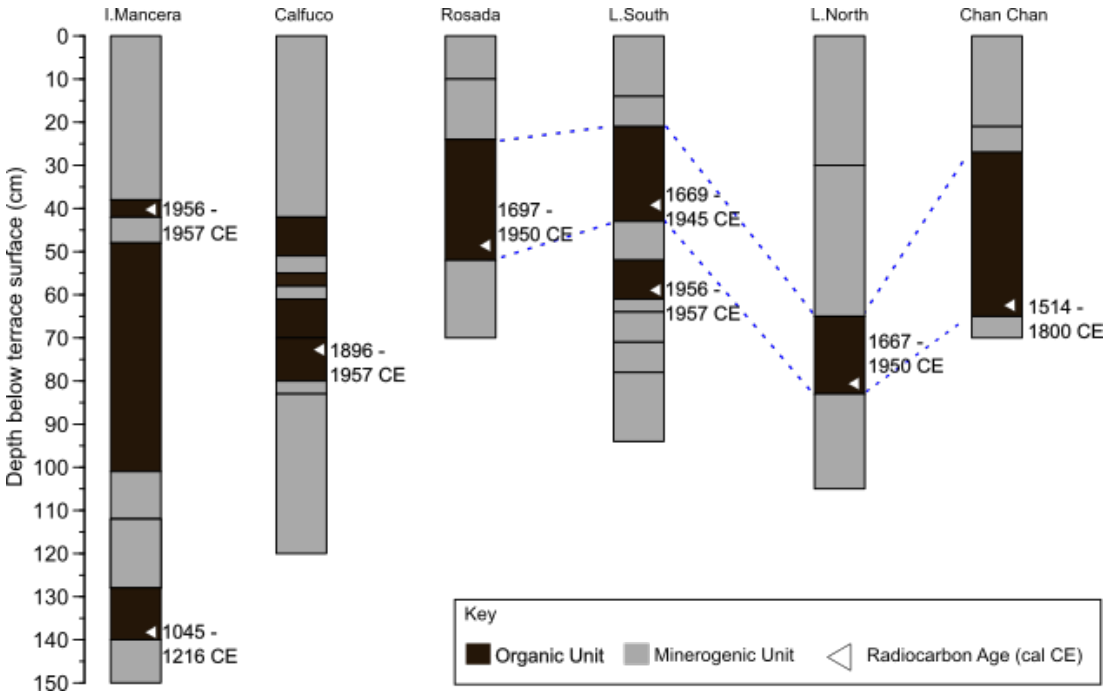

Figure 6.21 : Illustration of the coastal exposures showing their radiocarbon ages and correlations. Simplified sedimentary units with dark brown colours show organic whereas same grey colours are used for simplifying different minerogenic units. White triangles show depth of subsamples used for radiocarbon dating.

Finally, at Isla Mancera, the basal sand-peat contact dated to 1045 – 1216 CE could correspond to the prehistoric earthquake (event D) reported at Chucalén and Maullín, dated to 1070 – 1220 and 1020 – 1180 CE respectively (Cisternas et al., 2005, Garrett et al., 2015). However, only one of the essential criteria for detection of large subduction zone earthquakes (developed by Nelson et al. (1996) and modified by Shennan et al. (2016)) can be tested for the contact at 139 – 140 cm a mud-peat couplets with sharp contacts parallel to the coast (Figure 6.19). Hence, this insufficient information cannot provide evidence regarding a possible origin of the lithostratigraphic change and suggests the need for further investigation.

6.11.1 The 1960 earthquake

The nearest locations to the study sites providing observations of land-level change in the 1960 earthquake suggest subsidence ranging from 0.7 m to 2.7 m (Plafker and Savage, 1970), with Ho et al. (2019) suggesting an average of 1.71 m subsidence. It is reported that the presence of low-level marine terraces in the study area and to the south (38° S – 41° S) with elevations of 1.2 - 1.5 m before the 1960 earthquake were submerged (Fuenzalida et al., 1965). It is also well known that this stretch of coast

was inundated by a tsunami in 1960, with a reported run-up height of 10 - 15 m (Cisternas et al., 2005). Moreover, however, as the contemporary elevation of the investigated exposures is ~4 m above MSL and the elevation of these lowest marine terraces at similar latitudes immediately prior to the 1960 earthquake was 1.2 - 1.5 m above MSL, it appears the terraces studied are too high to record subsidence in their stratigraphy.

6.11.2 The 1837 earthquake

In spite of the fact that there are historical records for seismic shaking (Lomnitz, 1970, 2004, Cisternas et al., 2005, 2017b) and turbidite deposits triggered by seismic shaking associated with the 1837 CE earthquake (Moernaut et al., 2014) (St-Onge et al., 2012) at similar latitudes, it is suggested that the 1837 CE earthquake ruptured in the southern sector of the Valdivia segment (Cisternas et al., 2017b), further south of Valdivia. This is on the basis of model simulations of rupture scenarios (Cisternas et al., 2017b), and the lack of any geological evidence for coseismic deformation associated with the 1837 rupture. The most northerly evidence for the 1837 event from a coastal site comes from Cocotué on Isla de Chiloé, which is approximately 230 km to the south of Valdivia (Cisternas et al., 2017a). The preservation of turbidites from 1837 at sites to the north of Valdivia can easily be explained and is consistent with observations of earthquake-triggered turbidites some distance outside the rupture zone, as observed for the Mw 8.8 2010 Maule earthquake (Moernaut et al., 2014). Models considering various hypothetical ruptures, suggest that the 1837 CE earthquake likely resulted in a widespread rupture and involved slipping over a wide range of depths in the southern part of the Valdivia segment (Cisternas et al., 2017b). Therefore, in line with the compelling findings from Hocking et al. (2021), this study recognises that changes observed at coastal sites could potentially be associated with the 1737 CE earthquake. Further discussion of evidence for the 1837 versus 1737 events is in sections 7.5.1 and 7.5.2 respectively.

6.11.3 The 1737 earthquake

Historical records show that the 1737 earthquake caused considerable shaking along a ~500 km section of the Valdivia segment, stretching from Concepción to Isla Chiloé (Lomnitz, 1970; 2004, Cisternas et al., 2005, 2017a). Despite the large extent of shaking, the occurrence of a tsunami was not reported in documentary records. In addition, geological evidence including occurrence of tsunami for this event has been reported in tidal marsh sediments at Chaihuín, located 20 km southwest of the mouth

of the Valdivia estuary (Hocking et al., 2021) and inland in lake turbidite records from Riñihue, Calafquén and Villarrica lakes (Moernaut et al., 2014).

In this study, the stratigraphy within the coastal exposures demonstrates evident changes from a minerogenic unit to an organic unit. Moreover, these similar transitions coincided with the timing of the historical 1737 CE earthquake at four of the six sites, and the evidence presented here constrains the length of the rupture to at least the ~40 km from Chan-Chan to Rosada. Previous studies reported that stratigraphical change associated with megathrust earthquakes preserved as peat-mud couplets (e.g., 1960, 1575) in south-central Chile (Cisternas et al., 2005, Garrett et al., 2015), Alaska (Shennan et al., 1999), Cascadia (Witter et al., 2003) and New Zealand (Hayward et al., 2006) indicate coseismic subsidence whilst the stratigraphic evidence for this earthquake is presented as sand-peat couplets, which points to coseismic uplift as in Chile (Dura et al., 2015, Ely et al., 2014) and the Pacific Northwest (Shennan et al., 2009, 2014a, 2014b, Briggs et al., 2014). Thus, the observed transition from sand units to peat units in these four coastal stratigraphies is inferred as possible coseismic uplift related to the 1737 earthquake.

It is suggested that the type of coseismic deformation that is observed in coastal stratigraphy is governed by the geometry of the subduction interface and both the amount and distribution of coseismic slip on that interface (Moreno et al., 2009). Accordingly, possible coseismic uplift recorded at coastal sites resulting from the 1737 earthquake suggests that seismic locking may have occurred on a landward and deeper part of the subduction interface, as previously suggested by Cisternas et al. (2017a) and in contrast to the larger and shallow ruptures (e.g., 1960, 1575) based on distribution of coseismic slip models (Moreno et al., 2009, 2012, Ely et al., 2014). The interpretation that the 1737 event was of modest size and a deep rupture was previously suggested on the basis of a lack of evidence for a tsunami (Cisternas et al., 2005; 2017b) and based on turbidite thickness (Moernaut et al., 2014). Likewise, tsunami deposits are also absent from the study sites here. This interpretation is also guided by comparisons to similar behaviour suggested for the 1906 central Chile earthquake (see Carvajal et al., 2017).

Whilst in agreement with most previous research (Cisternas et al., 2017a, b; Moernaut et al., 2014), the evidence for possible coseismic uplift in 1737 that is presented here contradicts new evidence very recently reported from Chaihuín tidal marsh, which is located 19 - 23 km to the southwest of this study's sites, of coseismic subsidence and tsunami deposition (Hocking et al., 2021). This presents an important challenge to

address in future research to explain such apparently contradictory evidence at sites which are relatively close. However, with the caveat that further local comparisons to Chaihuín are required, on the basis of this studies' findings and in conjunction with previous research suggestions, the hypothesis for the 1737 earthquake being of moderate to small size magnitude and being a deep rupture is preferred provided that sedimentary signatures resulted from this earthquake. The sedimentological records showing both subsidence and uplift along the coast may originate due to the presence of subduction megathrust geometry and heterogeneity along-strike structure of the plate interface could be potential reasons for this differential land-level change (e.g., Moreno et al., 2009, Wang and He, 2008, Suito and Freymueller, 2009, Kopp, 2013, Liu and Zhao, 2018, van Zelst et al., 2019, Plescia and Hayes, 2020, Fan and Zhao, 2021) and or along-strike slip variation (e.g., Wang et al., 2013). Therefore, this leads to the idea that shaking may emanate from a variable seismic coupling in this region, which certainly requires further investigation. This points to further investigation to find the reason for variable coseismic deformation during the same earthquake that were observed at different coastal sites which are very close to one another. Hypotheses for potential reasons are presented in Chapter 7.

Finally, due to the absence of good and close analogue, it is not possible to obtain reliable estimate for vertical land-level changes under these circumstances. Alternative proxies may be helpful for generating reconstruction estimates (see section 7.3 for detailed discussion and recommendations).

6.11.4 Prehistoric Earthquakes

Previous studies also reported the presence of prehistoric earthquakes based on sedimentary evidence in south-central Chile (Cisternas et al., 2005, 2017b, Atwater et al., 2013, Moernaut et al., 2014, Garrett et al., 2015). Two prehistoric earthquakes are referred to as the event C between 1270 – 1450 CE and event D around 898 – 1220 CE. Both are suggested to share similarities to the 1960 (event A) and the 1575 (event B) earthquakes. In addition, smaller events between these large earthquakes are named bc1, bc2 and cd (Cisternas et al., 2005, 2017b, Moernaut et al., 2014, Garrett et al., 2015). Radiocarbon dating of an abrupt sedimentary contact at Isla Mancera, dated to 1045 – 1216 CE, correlates in terms of timing with Event D reported by Cisternas et al. (2005) at Maullín and also corresponding to the same event suggested by Garrett et al. (2015) at Chucalén as well as from Lago Calafquén (Moernaut et al., 2014). However, the stratigraphy presents contrasting evidence, which is a sharp transition from minerogenic (gravel, pebble, cobble, and sand

mixtures) to organic (peat) unit suggesting a RSL fall (Figure 6.20), rather than a RSL rise that was found at Maullín and Chucalén. Notwithstanding that Isla Mancera is located approximately 200 km to the north of Chucalén and Maullín suggesting that coseismic deformation may present a different response along-strike (e.g., Ely et al., 2014). Despite generating reconstruction estimates for the fossil sequence at Isla Mancera, none of these estimates can be deemed meaningful due to the lack of good and close modern analogues. Moreover, with only six fossil samples there is the necessity for analysis of more subsamples in order to generate higher resolution reconstructions of RSL change. In addition, the current modern training set does not provide good and/or close analogues for fossil samples; thus, there is need for a larger modern training set in order to generate reliable reconstruction estimates (ter Braak, 1995a). Additional age control is also required to better constrain the change in stratigraphy; thus, ^{210}Pb dating together with more radiocarbon dates from lower elevations would be useful for improving the age model and reducing uncertainties.

6.11.5 Limitations of the quantitative reconstruction models

There are two main limitations with quantification of RSL change at the study sites: preservation of diatoms in basal sands and poor modern analogues provided by the modern training set. Firstly, the indicative meaning of the sand units found at the base of all exposures can be found at a wide range of elevations (see Garrett et al., 2020); thus, making inferences of RSL change difficult. Also, whilst reconstructions can be generated by applying a transfer function, the absence of species with sub-MHHW elevation optima in sand deposits yields reconstruction estimates which change near and above MHHW boundaries. Hence, it is not possible to quantify RSL change in transfer function methods due to the lack of diatoms with sub-MHHW elevation optima in the modern training set.

The lack of diatom taxa with sub-MHHW elevation optima was also observed at Cocotué (Cisternas et al., 2017b), where basal sands contained very low abundances of diatoms initially, and then subsequently, freshwater species from the overlying peats have percolated into the sands due to ponding of freshwater and the infiltration of freshwater. Such ponding and infiltration was observed during the fieldwork, which could have introduced freshwater diatoms into the sands. Consequently, apparently the post-deposition diatom assemblages have changed and do not provide an accurate reconstruction of elevation at the time of deposition. The second issue is the lack of good and close modern analogues that the modern training set provides for fossil samples, which reduces the reliability of the reconstructions, and stresses the

need for a larger modern dataset in order to generate ecologically reasonable reconstruction models. The third and most critical issue is the predictive ability of the transfer function models originating from the limited relationship between modern diatom assemblages and elevation as the main environmental variable (see Chapter 7).

6.11.6 Limitation of radiocarbon-based age models

Due to large fluctuations in the concentration of the ^{14}C isotope in the atmosphere as a result of changes in Earth's geomagnetic field intensity, solar activity and in the carbon cycle (e.g., Stuiver and Quay, 1980, Damon and Sonett, 1991, Stuiver, 1994, Hughen et al., 2004), the age estimates calculated from a single radiocarbon date from a sediment possibly reflects wide calibrated age ranges (e.g., Trumbore et al., 2016). Therefore, a calibration curve for ^{14}C is required to calibrate radiocarbon ages to calendar dates (Figure 6.22). The calibration step is carried out by comparing the radiocarbon measurement on the sample with the material of known age which is usually tree rings for the Holocene in particular (Hogg et al., 2020, Reimer, 2020).

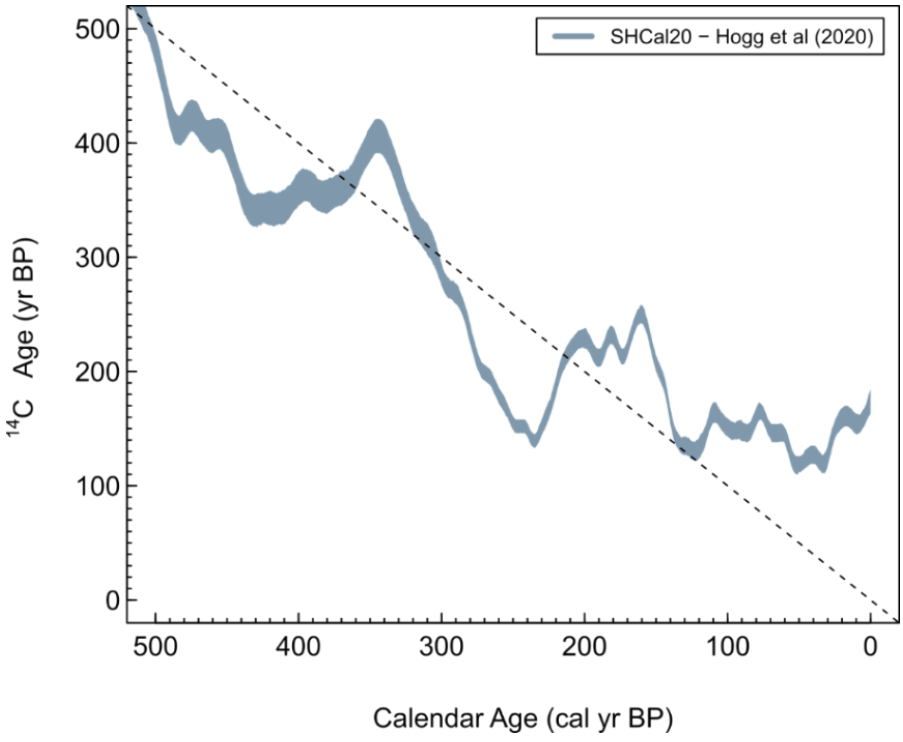

Figure 6.22 : Relationship between radiocarbon and calendar ages over during the last 500 years. The dashed line is the 1:1 line where radiocarbon age equals calendar age. The shaded blue curve is the Southern Hemisphere SHCal20 calibration curve with 1 standard deviation (SD) from Hogg et al. (2020).

The calibrated age ranges are probability based and do not show a normal distribution. Instead, the highest probability density range, typically 95.4% (Bronk Ramsey, 2009), is selected, resulting in distinct separate ranges due to fluctuations in the calibration curve. This probability distribution is very far from being normally distributed and demonstrates multiple peaks not normally distributed (Bronk Ramsey, 2009).

This is a common problem where multiple plateaux are present along the calibration curve (McCormac et al., 2004, Hua, 2009) especially when ages of samples cover the last 500 years. The radiocarbon ages from Rosada, Loncoyén North, Loncoyén South and Chan-Chan fall into this range; therefore, it is crucial to consider any event that occurred in these large age ranges (Figure 6.23). This range precludes inferring where multiple events occurred. Perhaps, employing other isotopes for developing age-depth models via ^{137}Cs and ^{210}Pb together with radiocarbon dating can yield better results since the "rplum" package (Blaauw et al., 2020) in R is able to combine these two techniques. This generated age-depth model uses a Bayesian approach and error ranges which are known as credible intervals, reflect the central portion of the posterior distribution that contains 95% of the estimated age values; hence, such age-depth models include realistic uncertainties that enable us to obtain better results and robust estimates for sediment ages.

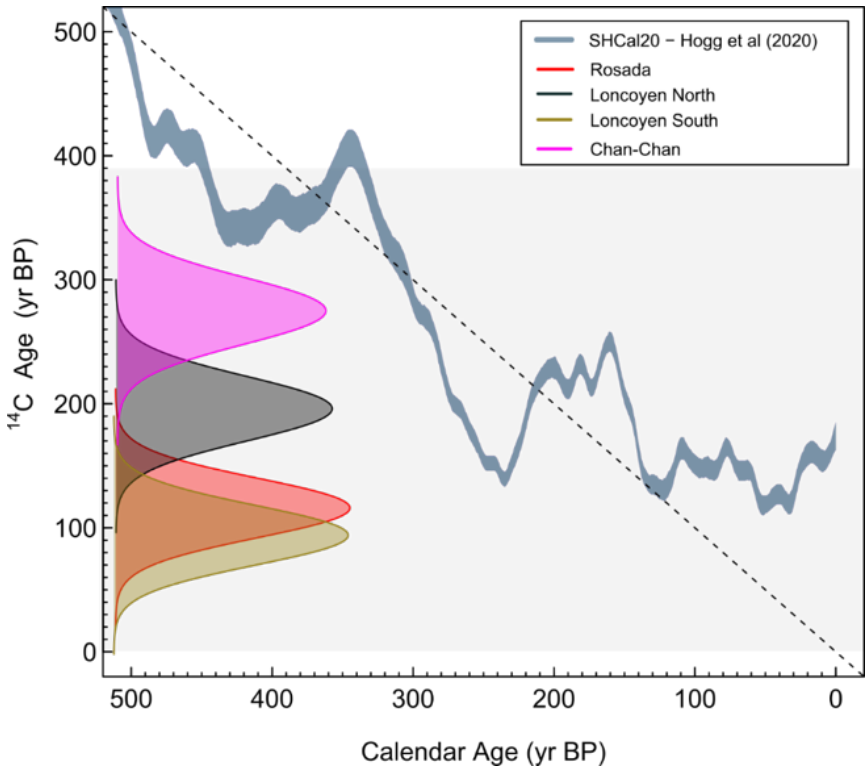

Figure 6.23 (previous page) : Gaussian distribution of uncalibrated ^{14}C ages for the samples from Rosada, Loncoyén North, Loncoyén South and Chan-Chan. The dashed line is the 1:1 line where radiocarbon age equals calendar age. The grey shaded area represents the age range of samples from this study. The shaded blue curve is the Southern Hemisphere SHCal20 calibration curve with 1 standard deviation (SD) from Hogg et al. (2020).

The age-depth model for the core obtained from San Antonio, as described in chapter 5, utilises a novel approach using the *rplum* package in R. This approach incorporates ^{137}Cs and 210Pb measurements along with radiocarbon dating (Aquino-López et al., 2018; Blaauw et al., 2020). Unlike traditional dating techniques, this Bayesian framework provides uncertainty ranges that encompass the central portion of the posterior distribution, containing 95% of the estimated age values (Aquino-López et al., 2018, 2020). Furthermore, this approach has the capability to generate age estimates even in the absence of direct measurements. Thus, it has the potential to address the limitations of radiocarbon dating in future studies by requiring at least two radiocarbon dates per millennium (Blaauw et al., 2018).

6.12 Summary

This chapter analyses sedimentological records from coastal sites and presents possible geological evidence for the 1737 CE earthquake in south-central Chile. The stratigraphy of coastal exposures was analysed, and diatom-based reconstructions of PSE were generated for coastal sites at Rosada, Loncoyén South, Loncoyén North, Calfuco, Chan-Chan and Isla Mancera. The lithological change found in the stratigraphy at Rosada, Loncoyén South, Loncoyén North and Chan-Chan suggest a transition from minerogenic to organic units. These changes are constrained by radiocarbon dating which indicates the timing of the initiation of peat deposition may correspond to the earthquake which occurred in 1737 CE suggesting coseismic uplift at these sites. However, diatom-based reconstruction models do not suggest an abrupt change in the RSL associated with the 1737 earthquake, likely due to the percolation of freshwater diatoms into the beach sand. Moreover, due to the lack of good and close analogues and high numbers of poor analogues, there is the requirement for a larger modern dataset in order to improve the transfer function models. Initial interpretations from Isla Mancera may also suggest the occurrence of an earthquake around 1045 – 1216 CE, which has previously been reported in south-central Chile as event D. However, it should be noted that this record alone cannot meet the criteria established by Nelson et al. (1996) and Shennan et al. (2016).

Chapter 7 : Discussion

This chapter synthesises and discusses the use and reliability of diatom-based transfer function models from the San Antonio estuary and coastal sites in the Valdivia region. Moreover, it discusses the sedimentological findings from Chapter 5, and Chapter 6 whether they present evidence for subduction earthquakes in south-central Chile.

7.1 Is it sufficient to use elevation as a single environmental gradient explaining total variance in diatom assemblage?

In combination with the use of previous studies' datasets (Hocking et al., 2017), diatom assemblages in surface samples from seven intertidal environments produce the modern dataset employed to generate various transfer function models with an attempt at estimating the RSL changes associated with subduction zone earthquakes during the late Holocene at coastal sites in south-central Chile. However, can elevation, which is a function of tidal duration and frequency, be considered the sole environmental gradient that determines species composition in this dataset? The following paragraphs discuss this assumption and the relationship between elevation and species composition.

Numerous studies employ elevation as the main environmental variable to reconstruct relative sea-level change and explore the relationship with tectonics (for reviews see Pilarczyk et al., 2014, Dura et al., 2016b). With the modern diatom training set, elevation explains about 5% of the variance (which is low but not unexpected since previous studies reported a close figure) (Sawai et al., 2004a; Roe et al., 2009, Watcham et al., 2013; Barlow et al., 2014), and the ratio of the eigenvalue of the constrained CCA axis (λ_1) to the eigenvalue of the first unconstrained (λ_2) CA axis is 0.49. This ratio points to the importance of elevation as an environmental gradient that controls the variability of diatoms; where elevation correlates with the most important ecological gradient in the dataset, it is expected that this ratio ($\lambda_1 \backslash \lambda_2$) is greater than one (ter Braak, 1988; Juggins, 2013). Nevertheless, although this ratio is below 1.0, it is suggested that transfer functions may still have a value for reconstructing RSL from assemblages of fossil diatoms (Dixit et al., 1993, Kemp et al., 2013). It should be noted that no certain statistical evidence has been presented as to why they could be valuable especially for quantitative model development since this ratio is an important metric. Yet, it is still limited to explain variance and explore the relationships between environmental variables and species response.

Although CCA demonstrates that the first unconstrained axis 1 with an eigenvalue of 0.48 is the largest eigenvalue, the following unconstrained axes gradually decrease, and the difference between them and the first axis is relatively small. Moreover, CCA produced an eigenvalue of 0.23 for axis 1, accounting for 5% of the total variation in the diatom assemblages. Considering that elevation is the sole known environmental variable, this single elevation gradient explains 100% of the variation. Furthermore, when tidal flat samples were removed from the regional training set, CCA axis 1, which equates to WAPLS component 1 (ter Braak and Verdonschot, 1995; Birks, 1998) still only explains 5.94% of the total variation in modern assemblages; thus, this improvement is not a substantial change. This variance, hence, indicates that diatom response to elevation may be considered insignificant. However, one recent study shows that elevation can be considered as the major driving factor that governs variability of diatom assemblage in intertidal environments, while the other factors such as salinity, grain-size, total organic carbon content can also control diatom variability in Willapa Bay, Washington, USA (Hong et al., 2021). Furthermore, it is suggested that incorporating additional environmental variables can account for up to 40% of the variation observed in the diatom assemblage at tidal wetlands and salt marshes (e.g., Szkornik et al., 2006, Hong et al., 2021). The modern dataset from intertidal sites in south-central Chile reflects less variability than can be explained with diatom assemblages as in earlier studies which produce utilise earlier versions of this modern training set in the same region (Garrett et al., 2013, Hocking et al., 2017). All this suggests, yet again, diatom assemblages and environmental variables display a complex relationship, and that elevation is not the most important control on diatom assemblages in south-central Chile; hence, it can invalidate one of the essential assumptions of the approach that other environmental variables have negligible influence, or their joint distribution with elevation in the fossil dataset is the same as in the training set (Birks, 1995, Juggins, 2013). Further investigation is required to obtain information about whether other environmental variables including salinity, total organic carbon, and mud-fraction are positively correlated with elevation as well as how much variability is explained by these factors (Hong et al., 2021). This information may reflect which environmental variables are the major drivers of diatom variability in the modern training set.

7.2 The role of the transfer function approach

In coastal palaeoseismology, quantitative reconstructions using diatoms and foraminifera have been developed to estimate RSL change emanating from

subduction zone earthquakes. Where the same diatom taxon is present in both modern and fossil sediments, any transfer function methods yield reconstruction estimates for environmental gradients of interest. The main concern here, however, is how reliable these reconstruction models are for inferring land-level and RSL change in the past (Barlow et al., 2013, Kemp and Telford, 2015, Dura et al., 2016b).

This study has set out to attempt to reconstruct palaeo-surface elevation and relative sea level in the past associated with subduction zone earthquakes by utilising diatom assemblages recorded within coastal sedimentary sequences in south-central Chile, following widespread successful adoption of this approach in this area (e.g., Garrett et al., 2015, Hocking et al., 2017, Brader et al., 2021, Hocking et al., 2021).

This study follows the assumption that elevation (as a surrogate for tidal inundation and duration) reflects the strongest influence on diatom assemblages and that other environmental variables have negligible effects through time and their collective response has remained the same in the past (Birks, 1995, Juggins, 2013). Notwithstanding, this assumption does not provide reliable outputs, due to the large number of poor analogues for fossil assemblages indicating diatom assemblages could be governed by other environmental variables and their effect probably changes through time. In order to determine whether there are other dominant controls on diatom distribution besides elevation, or whether the poor modern analogues situation is simply a function of not sampling the full environmental gradient, both additional environmental variables of interest (e.g., salinity, grain size, nutrition) and modern sampling below MTL and above MHHW would be required.

Where microfossil taxa are available in sediment, reconstruction models can provide estimates when modern taxa match with the corresponding fossil taxa. Despite the local training set exhibiting relatively low diversity in diatom assemblages, it can still yield reconstruction estimates for the past environment, as the same diatom taxa are found in both modern and fossil assemblages. However, considering the limited diversity in the local training set, it is essential to incorporate the regional dataset to obtain more reliable and representative models for understanding past environmental changes. Numerous studies have already stressed the importance of utilising regional training sets in order to strengthen the predictive ability and to capture the variation in diatom assemblages from a wide range of coastal environment for sea level-change (Gehrels et al., 2001, Zong et al., 2003, Horton and Edwards, 2005, Nelson et al., 2008, Wilson and Lamb, 2012, Watcham et al., 2013, Shennan et al., 2014b, Sawai et al., 2016, Hocking et al., 2017), while the precision of the reconstruction models

tends to decline. The construction of modern datasets and enumerating diatoms requires significant collective efforts, substantial time and commitment that have been undertaken by many studies. The combined regional training set consists of 289 modern samples including 26 new modern samples from this study. While transfer function models with the local training set show favourable performance over the models generated with the regional training set, they do display poor statistical performance especially for samples found below 125 – 130 SWLI. The same regional training set (without modern samples from San Antonio) was also used by Hocking et al. (2017) and they emphasise this situation and excluded samples below 125 SWLI elevation to improve statistical performance. A similar approach was also adopted in similar studies in Alaska, with systematic removal of samples below a certain elevation found to improve statistical performance (Hamilton and Shennan, 2005).

Since some diatoms (*Planothidium delicatulum, Fallacia tenera, Pseudostaurosira perminuta, Opephora pacifica* small form) are available across all tidal frames and their ecological amplitude (tolerance) is broad (>50 SWLI), they influence the predictive ability of the transfer function models and also display larger error. Therefore, this led to removal of all tidal flat samples from the regional training set to improve the accuracy and precision of the reconstructions; however, this removal resulted in employing only 176 modern samples for developing transfer function models that nearly used 60% of the regional training set. Yet, an extra step was taken by excluding tidal flat samples from the regional dataset so as to improve statistical performance of the transfer function which causes an obvious bias for species optima. The Bayesian transfer function method introduces a more flexible multimodal approach in contrast to the unimodal approach used for species response curves (Cahill et al., 2015, Holden et al., 2017); nonetheless, this method does not solve the issue of the lack of modern analogues for fossil assemblages and is also still liable to essential assumptions for developing transfer function models.

In spite of the statistical performance of the transfer function being considered good, the major arising issue is the modern analogues for fossil assemblages. In order to attain robust and reliable reconstruction models, the calibration step of transfer function development must have modern analogues for fossil diatoms preserved in core (ter Braak, 1995a). It is suggested that when there are no good modern analogues for fossil assemblages, using a regional dataset that incorporates taxa from multiple sites extends spatial diversity and varying environmental settings and spans a large range of intertidal environments (i.e., large range of marshes), and may

aid in providing better modern analogues for fossil assemblages (Birks, 1998). It is suggested that the lack of modern analogue situation emanates from substantial changes in environmental conditions through time (Watcham et al., 2013). This situation, consequently, invalidates one of the main assumptions which is diatom assemblages in the modern training set are the same as in the fossil assemblage and their ecological responses have not changed significantly over the timespan represented by the fossil assemblage (Birks, 1995, Juggins, 2013). Where modern analogues for fossils assemblages are absent, employing a regional training set becomes a mandatory step for the purpose of finding modern analogues to fossil samples especially in south-central Chile (e.g., Hocking et al., 2017). Notwithstanding, we cannot be sure that regional dataset will provide enough modern analogues for fossil samples. When certain taxa dominate the fossil samples (e.g., *Nitzschia vitrea, Pseudostaurosira perminuta, Cosmioneis pusilla*), the species optima estimated using the WA method, along with the regression coefficient determined by the WA-PLS method, collectively influence the reconstructed SWLI values. As a result, these reconstructed estimates may demonstrate extreme values that exceed the maximum elevation of modern sampling. This phenomenon has been observed in the reconstruction estimates for the San Antonio core samples at depths ranging between 9 cm and 14 cm (Figure 5.13). Hence, caution must be taken when interpreting reconstruction points and curves for the past sea-level and reliance upon precision of the reconstructed values. This does not mean that diatom analysis is not always fruitful; there are better examples where the number of modern analogues is rather favourable and representative for fossil assemblages (Zong et al., 2003, Hamilton and Shennan, 2005, Hawkes et al., 2011). More work in this region of study, however, is needed to be done collecting a large number of modern samples from different regions.

One of the main challenges is the availability of modern analogues for fossil diatom assemblages. The quantitative approaches hinge upon similarity between modern and fossil diatom assemblage; hence, when there are no modern analogues for the fossil samples, the reconstruction models could be unwarranted to estimate and understand past changes in tidal elevation (Juggins, 2013). Moreover, there is no easy way to determine the threshold for the dissimilarity measures and it can be a subjective choice. Given that diatoms are collected from intertidal environments they may exhibit high diversity in sediments both within and between sites and form diverse training sets. Therefore, it may be deemed welcome to select a relatively “high” percentile threshold in the dissimilarity threshold in order to improve statistics for the

number of good/close analogues. However, it has been emphasised that these thresholds were based on visual observation (see Watcham et al., 2013), and elsewhere the conventional thresholds are 2nd, 5th and 10th percentiles for dissimilarity cut-offs (Simpson, 2007, 2012, Simpson and Oksanen, 2020). This change in thresholds plays an important role in deciding the number of good, close, and poor analogues. It is evident that any taxon present in the fossil samples that is also available in the modern training set will exhibit identical elevation optima and tolerances. Therefore, even a single fossil taxon yields an estimate for a reconstruction model in calibration step which reflects a misleading estimate for RSL change. Moreover, where the dissimilarity measure between the number of fossils and modern taxa is large, reconstruction models will not provide reasonable outputs. Furthermore, the relatively younger samples located at the top of the core can be compared with tide gauge measurements, which provides some validation. However, for the samples at the bottom of the core, historical records are lacking, making it impossible to compare them with known periods.

This study considers and only uses elevation as the sole environmental variable and does not include other environmental variables (e.g., salinity, grain size, nutrition) to explore which of these environmental components explain substantial variance and exerts the greatest influence upon the diatom distributions in south-central Chile. Although the results of CA show that the first axis has the largest eigenvalue, the differences between the first axis and the other three axes are not significant enough to suggest that elevation is the sole or dominant driving factor for diatom assemblage. Hence, it would be unrealistic to assume that elevation is the sole governing factor controlling diatom distributions in saltmarsh environments (Juggins, 2013). Notwithstanding, analysing multiple environmental gradients also may not explain the greatest variance in the diatom data and the large, some or only small part of total variation can be left unexplained (Horton et al., 2006, Barlow et al., 2013, Watcham et al., 2013, Hong et al., 2021). Consequently, elevation, which serves as a surrogate for tidal exposure in reconstructions, cannot be considered independent of other environmental variables. Thus, reconstruction models should be treated with caution, as many environmental variables can influence the ecological response of the diatoms.

Diatom assemblages have a complex relationship with environmental variables (e.g., Juggins and Birks, 2012, Desianti et al., 2019, Hong et al., 2021). It is critically important whether a secondary environmental variable has a larger impact or not

since assumption 5 “environmental variables other than the one of interest have negligible influence, or their joint distribution with the environmental variable does not change with time.” relies upon it (see Section 3.5.3.1). It is substantially important follow ter Braak (1988)’s rule of thumb for the useful reconstruction model, that λ_1/λ_2 ratio at least should be 1.0, must be carried out which generally has not received much attention at all (see Juggins, 2013). The relative explanatory power of environmental variables of interest decreases as when the effect of confounding variables is strong. We may observe this effect when the regional and the local training sets are compared. Application of the local training set generally presents a large value for λ_1/λ_2 ratio which indicates the relative explanatory power of the tidal elevation evidently decreases. The assumption 5, hence, may not be met as expected.

Moreover, the lack of modern analogues and/or good analogues leading to advantages of using regional datasets have been stressed in the earlier studies from the UK (Gehrels et al., 2001, Horton and Edwards, 2005), Pacific Northwest (Watcham et al., 2013, Nelson et al., 2008, Sawai et al., 2016), Chile (Hocking et al., 2017) and Atlantic Northeast (Desianti et al., 2019). Apparently, the lack of modern analogue situation is a common trait of diatom assemblage data in south-central Chile since this study is using the previous works when constructing the regional data as well. However, the relative explanatory power of the training set (λ_1/λ_2) significantly declines and variance in the modern dataset explained by elevation also decreases, in this case ~75% decrease was calculated (from 22% to 6% for San Antonio) when the regional dataset is employed to generate reconstruction models. This decline introduces another crucially important question of how credible these reconstruction models are for RSL change studies as the use of the regional training set palpably weakens the explanatory power of transfer function models. The predictive capabilities of transfer function models should always be borne in mind and estimates must be carefully used for further analyses.

Should bootstrapped cross validation be applied, the sample-specific errors exhibit a large range when the ~95% confidence interval is used. This approach comes from the assumption that reconstructed values are normally distributed; nevertheless, this range is too broad to interpret reconstruction results, especially where tidal range is large (macrotidal regime 4 – 6 m or more). Although sample-specific errors were obtained by means of bootstrap cross-validation, they do not account for the extra uncertainty arising from poor analogue quality. The present error range only emerges

from the modern training set and fossil diatom assemblages. Notwithstanding, it is suggested that reconstruction models when cross validated by means of bootstrapped method provide an acceptable level of uncertainty (Kemp and Telford, 2015, cf. Juggins and Birks, 2012) since they encompass error from fossil samples and the difference between predicted and measure samples (Birks et al., 1990). Consequently, reporting default outputs for sample-specific errors, at a confidence interval of 68% (1σ) derived from model output, may facilitate easier interpretation of the reconstruction results. However, it is noteworthy that in the present study, the presentation of uncertainty ranges at the 95% (2σ) confidence interval posed challenges in interpreting the results.

One of the most challenging circumstances is the tidal range of the study area. Despite the possibility of obtaining precise transfer function models (low sample-specific error) where the tidal range is large, in this case the tidal range is approximately 6 m at San Antonio, and the outputs provide large uncertainty ranges for the reconstructed values in contrast to micro-tidal environments where estimated error ranges of typical transfer function models are ~10 – 15% of the tidal range (see Barlow et al., 2013, Williams et al., 2021). As a result, the reconstructed values exhibit a large error range in macro-tidal environments. Perhaps the most important lesson from San Antonio is that the regardless of the statistical performance of the transfer function, the reconstructed elevation must be treated with caution when studying those sites that have large tidal range (see Sawai et al., 2017) as they can provide large error range without a doubt (see section 5.6.3). Otherwise, the resulting reconstruction models are unable to reflect environmental change in the past and do not have considerable practical values in understanding palaeoenvironmental change at studied coastal sites.

Another crucial concern is the low preservation of diatoms in fossil samples. In the absence of fossil diatoms or where a minimum count of 250 valves could not be met, reconstruction models cannot be carried out to explore past sea-level change. Furthermore, in the case of the lack of fossil taxa, especially with optima sub-MHHW (or marine diatoms), the reconstruction curve does not show palpable change that coincides with the transition from organic to minerogenic sedimentation (vice versa). Although the lack of diatoms may not be seen as a major problem in general, there is no certainty that sediments always contain diatoms. As a result, employing a multiproxy approach could be a better choice for the future endeavours so as to generate reconstruction models.

When it comes to the evaluation and validation of reconstruction models, comparing them with historical records is a critical step which must be carried out where they are available, especially for the recent past (Birks, 2010, Juggins and Birks, 2012). Where there is not any historical record the main alternative is employing independent palaeoenvironmental data. Fortunately, tidal gauge measurements, spanning nearly the last 80 years, are available at Puerto Montt, ~40 km away from San Antonio; thus, reconstruction estimates, and these tidal measurements have been compared in section 5.8 (Figure 5.14). As for the older samples, the only possible means to assess reconstruction estimates is to carry out numerical evaluation. Besides, tidal elevation as the variable of interest is important in space at San Antonio when modern samples are collected, might not have been important in the past. Consequently, these estimates will always be challenging to evaluate without historical records, or any comparable outputs and it behoves us all for this reason to be cautious.

The reconstruction of PMSE can be achieved to some degree; nevertheless, it may not provide a meaningful reconstruction model at San Antonio tidal marsh or other coastal sites in the Valdivia region. The results suggest that the diatom-based reconstructions derived from intertidal settings do not hold the most promise for estimating RSL change. Furthermore, tidal elevation does not exhibit a dominant signal and may not be the primary environmental gradient governing diatom assemblages Hence, it cannot be considered that assumption 5 to have been met (Juggins, 2013).

7.3 Alternative approaches to diatom analysis

A potentially promising method is available by determining isotopes of $\delta^{13}C$, total organic carbon, carbon-nitrogen ratios, and total nitrogen to quantify palaeoenvironmental or relative sea-level change when microfossils are absent, poorly preserved or they can be used together. The continuous preservation of organic matter in coastal sediment, and thereby $\delta^{13}C$ and C/N values, can provide information about relative sea-level (Törnqvist et al., 2004, Kemp et al., 2010, 2012, Milker et al., 2022). Moreover, this approach of analysing $\delta^{13}C$ and C/N has been employed to yield information about relative sea-level change resulting from subduction zone earthquakes (Dura et al., 2011, Hawkes et al., 2011, Engelhart et al., 2013a, 2013b). Although other biota such as foraminifera and testate amoebae were not examined in this study, their inclusion could be valuable for comparison purposes with diatom findings in future studies (Horton and Edwards, 2006, Pilarczyk et al., 2014, Barnett et al., 2017). Furthermore, incorporating these additional biota

could provide a better understanding of the variability in tidal elevation. Lastly, Bayesian approaches allow multiple proxies to be employed together with differing uncertainties thereby such an approach may provide more robust reconstruction models for future studies (Cahill et al., 2016, Holden et al., 2017); although it still invokes the basic assumptions (see section 3.5.3.1) for developing transfer function models and it does not solve the lack of modern analogue situation.

7.4 Comparisons between the reconstruction model and the indicative range of the different sea-level indicators in the Valdivia Region

Investigating biostratigraphic data may aid in distinguishing the initiation and/or termination of marine influence and constraining estimation of past RSL. Diatom-based transfer function models were unable to confirm the formation of any contacts through uplift resulting from subduction zone earthquakes, due to the lack of marine diatom assemblages in sand deposits and reconstructions. They were also unable to differentiate lithostratigraphy and could not provide distinct curves for palaeo surface elevation changes at all studied coastal sites in the Valdivia region. The use of quantitative reconstruction approaches, thus, may not be deemed effective in estimating relative sea-level changes associated with the subduction zone earthquakes of interest. Furthermore, inferring the occurrence of coseismic rupture may also be contingent upon the degree of overlap on the indicative meaning of the different sea-level indicators. As a result, rather than focusing on only quantitative results from reconstruction estimates, we can investigate the indicative meaning of sedimentary deposits to decipher the extent of correlation among the indicative significance of distinct sea-level markers.

In this case, employing one of the most essential and conventional practices of assessing indicative meaning based on lithostratigraphic features of sedimentary sequences may allow RSL to be constrained (Shennan, 1986, Van de Plassche, 1986). The indicative meaning is composed of the reference water level (RWL) that denotes tidal level such as MSL or MHHW, and indicative range (IR) expresses the vertical range in which the sample might be found (e.g., below MHHW, above MSL).

Following Garrett et al. (2020), which presents a comprehensive RSL dataset from Chile (see also section 2.4.1), it is suggested the indicative meaning of the sand units found at the base of all exposures can be found at a wide range of elevations (between MLLW and HAT). Furthermore, those sand units are dominated by diatom species with elevation optima above MHHW, thereby the index points are conservatively

estimated to have formed between MLLW and HAT. Hence, this poses limitations in reducing the indicative range and presents difficulties in evaluating sand layers as reliable sea level indicators, as they cannot be clearly distinguished from the overlying organic layers.

7.5 Do the coastal sites in the Valdivia Region contain any evidence for earthquakes in 1837 and/or 1737?

This study has sought to identify sudden changes in RSL that might correlate with occurrences of earthquakes and tsunamis at the studied coastal sites. Coastal sedimentary deposits can be used to identify relative land-level change associated with subduction zone earthquakes (Nelson, 2007). However, it is suggested that the presence of any change in coastal sedimentary deposit can be stem from non-seismic origins as well; hence, it is imperative to assess whether deposits meet a range of criteria to discriminate the origins of any changes in stratigraphy (Nelson et al., 1996, Shennan et al., 2016).

The striking features of coastal geomorphology are the MIS 5e interglacial terraces and cliffs across the Valdivia region (Astorga and Pino, 2011, Vega et al., 2018). In front of these interglacial terraces at each study site there are lower terraces demonstrating similar sedimentary sequences where sand units are overlain by peat units in the coastal exposures. This study tests the hypothesis that each sand-peat couplet at the examined coastal sites in the Valdivia region provide evidence for the occurrence of pre-1960 earthquakes in 1837 CE or 1737 CE by adapting the combined criteria outlined Nelson et al. (1996) and Shennan et al. (2016) together with radiocarbon dates of each organic unit and fossil diatom assemblages.

In order to infer a possible origin of sedimentary deposition whether due to seismic or non-seismic processes, six criteria that were established by Nelson et al. (1996) and updated by Shennan et al. (2016) were investigated : 1) lateral extent of peat-mud or mud-peat couplets with sharp contacts; 2) suddenness of submergence or emergence, and replication within each site; 3) amount of vertical motion, quantified with 95% error terms and replicated within each site; 4) synchroneity of submergence and emergence based on statistical age modelling; 5) spatial pattern of submergence and emergence; 6) possible additional evidence, such as evidence of a tsunami or liquefaction concurrent with submergence or emergence.

The studied sedimentary deposits on coastal exposures may not be suitable locations for application of all criteria (3, 5, 6) for detection of subduction zone earthquakes and

identifying land-level change owing to the lack of marine diatoms, limited spatial distribution of marine terraces, and the absence of a tsunami deposit as suggested by Ditzel (2019). However, the other three criteria can be assessed (lateral extent of abrupt contacts, and the suddenness and synchronicity of land-level change between sites) and they are critical in evaluating a possible co-seismic origin of lithostratigraphic change.

Analyses of the coastal exposures indicates changes in sediment stratigraphy at Rosada, Loncoyen North, Loncoyen South and Chan-Chan. The presence of peat overlying sand layers with an abrupt contact (<10 mm) in the coastal exposures, in conjunction with radiocarbon dating at these sites, may suggest a change in land level associated with subduction zone earthquakes. Furthermore, none of these coastal exposures demonstrate any obvious signs of tsunamis arising from these historical earthquakes, since sand layers show similarity to modern sand accumulated on those beaches (Ditzel, 2019). Moreover, quantitative reconstructions are not able to support a rise in palaeo surface elevation owing to the lack of marine diatoms in those sand units.

Table 7.1 : Assessment of essential criteria for detection of large subduction zone earthquakes, as developed by Nelson et al. (1996) and modified by Shennan et al. (2016).

No	Criteria	Site
1	lateral extent of peat-mud or mud-peat couplets with sharp contacts	Rosada (M3-O1), Loncoyén North(M3-O1), Loncoyén South (M3-O1), Chan-Chan (M3-O1)
2	suddenness of submergence or emergence, and replicated within each site	Rosada (M3-O1), Loncoyén North(M3-O1), Loncoyén South (M3-O1), Chan-Chan (M3-O1)
3	amount of vertical motion, quantified with 95% error terms and replicated within each site	-
4	synchroneity of submergence and emergence based on statistical age modelling	Rosada (M3-O1), Loncoyén North(M3-O1), Loncoyén South (M3-O1), Chan-Chan (M3-O1)
5	spatial pattern of submergence and emergence	-
6	possible additional evidence, such as evidence of a tsunami or liquefaction concurrent with submergence or emergence	-

It is suggested that the sand units found at the coastal exposures mainly originated locally (beach deposits), with the exception of the sandy units at Calfuco, which are inferred to have been transported by wind, according to granulometric analysis (Ditzel, 2019). Furthermore, the bottom sand units do not contain upward fining grain size, rip-up clasts, well-defined upper contacts, atypical marine diatom assemblages including occurrence of fragmented diatoms in high numbers which are characteristic of tsunami deposits (Cisternas et al., 2005, 2017b; Garrett et al., 2013, 2015, Ely et al., 2014, Dura et al., 2015, Hong et al., 2017). Therefore, it is concluded that the Holocene marine terraces do not contain any tsunami-lain sand layers.

Even though both 1837 CE and 1737 CE earthquakes caused extensive shaking across coastal sites as noted in written accounts, the sedimentary deposits at coastal sites do not suggest any similarity with those associated with 1960 type earthquakes (Lomnitz, 2004, Cisternas et al., 2005, 2017a, Garrett et al., 2015). Here at sites around Valdivia, coseismic land uplift (relative sea-level fall) is indicated by

minerogenic-organic sedimentary couplets. The occurrence of coseismic uplift compared to coseismic subsidence observed in 1960 and 1575 at Valdivia, possibly stems from the complex geometry and heterogeneity that suggest different strike and dip patterns, as well as slip distributions in the rupture zone across this segment, between the earthquakes (e.g., Moreno et al., 2009, Wang et al., 2013, Klein et al., 2016). Several hypotheses for this possibility are presented in 7.5.2.

Radiocarbon ages from each exposures' peat unit (except for Calfuco and Isla Mancera) constrain the chronology of the coastal stratigraphy. Deposition of each peat layer dates to the past 300 – 500 yr, from radiocarbon dating. Unfortunately, this is a broad age range, due to plateaux in the radiocarbon calibration curve in this period (McCormac et al., 2004, Hua, 2009, Williams, 2012), and therefore the radiocarbon age range encompasses both historical earthquakes that occurred in 1837 CE and 1737 CE. In the following sections, therefore, focus is on discriminating between these two different earthquakes.

7.5.1 Is there any evidence for the 1837 earthquake?

Lake turbidite records have been used to suggest that the 1837 CE earthquake may have been of magnitude Mw ~9, a similar magnitude to the 1960 and 1575 CE events (Moernaut et al., 2014). Modelling suggests these ruptures occurred at shallow fault depths (Cisternas et al., 2017b). Yet, coastal sites do not provide a comparable sedimentological record in terms of coseismic subsidence and accompanying tsunamis (Cisternas et al., 2005, Cisternas et al., 2017b, Garrett et al., 2015). Should the 1837 CE earthquake have occurred in the shallow part of the fault, we would expect coastal sites to exhibit organic-minerogenic couplets (peat unit overlain by sand or mud units) indicative of coseismic submergence. By contrast, around Valdivia, the coastal exposures demonstrate minerogenic-organic couplets, thus giving rise to support for an occurrence of an earthquake that ruptured the deeper part of the megathrust as in other subduction zones (Nelson et al., 1996). Moreover, neither this study nor previous studies at coastal sites report any occurrence of tsunami deposits. In addition, inland lake turbidite records from Riñihue, Calafquén and Villarrica lakes (Moernaut et al., 2014), a marine turbidite from the Reloncaví Fjord shows anomalous thickness of turbidites, distinct geochemistry and fining upward grading related to the 1837 CE earthquake supporting more southern rupture (St-Onge et al., 2012). Lastly, one of the recent studies utilising coseismic slip models with various depths suggests that the 1837 earthquake resulted from a wide rupture reaching depths of about 60 km of the plate interface within the southern part of the

Valdivia segment of the subduction zone (Cisternas et al., 2017a). This difference, therefore, leads us to consider that the earlier earthquake which occurred in 1737 CE may cause the change in coastal stratigraphy at study sites in the Valdivia region. Based on this assumption, the following section discusses possible reasons for coseismic deformation patterns.

7.5.2 The 1737 earthquake and coseismic deformation patterns

The stratigraphy of the coastal exposures at Rosada, Loncoyén South, Loncoyén North, and Chan-Chan exhibit a sedimentological change from minerogenic to organic units. The similarity in stratigraphy and synchronous signatures observed at the coastal sites along the northern part of the subduction margin within the Valdivia segment, suggest these couplets indicate coseismic uplift in the same earthquake. The timing fits with both the 1837 and 1737 events but having ruled out the occurrence of the 1837 event, it can be considered that these findings are indicative of the occurrence of the 1737 CE earthquake in the region. This deduction provides critical information for this rupture regarding the type of slip distributions that cause uplift at Rosada, Loncoyén and Chan-Chan and coseismic subsidence at Chaihuín, which is ~20 km southwest of Rosada. At Chaihuín, organic sediments are overlain by intertidal clays, with diatom assemblages indicating coseismic subsidence as well as tsunami inundation (Hocking et al., 2021). It appears that the city of Valdivia and its surrounding region could possibly be located near, or lie within, the centre of the rupture area of the 1737 CE earthquake. This apparent contradiction in stratigraphic signatures and direction of coseismic deformation (uplift versus subsidence leads to difficulty in distinguishing the possible sources of nucleation depth of this rupture. Also, contrasting vertical deformation patterns suggest a complex rupture model rather than using a simple elastic dislocation model. simple elastic dislocation models (e.g., Nelson et al., 1996) assume earthquake scenarios with spatially uniform slip on planar faults and may be inadequate and unable to explain complex rupture patterns (e.g., Moreno et al., 2012, Hamling Ian et al., 2017, Diederichs et al., 2019). Hence, it is undoubtedly challenging to account for the asymmetry of observed vertical displacements due to limited information about the rupture. The following section discusses possible sources of nucleation depth and along-strike changes in coseismic deformation patterns under the assumption that both coseismic uplift observed from Chan-Chan to Rosada beach and coseismic subsidence and tsunami inundation at the Chaihuín tidal marsh stem from the 1737 CE earthquake.

The first possible hypothesis is that differing vertical coseismic deformation patterns could be attributed to dislocations at different depths and different spatial distribution of slip on the plate interface owing to complex geometric irregularities along the subduction interface (e.g., Dmowska et al., 1996, Subarya et al., 2006, Lay et al., 2012, Hamling Ian et al., 2017, Diederichs et al., 2019). This would indicate that the depth of the down-dip end of the locked zone may asymmetrically vary where this earthquake nucleated. One of the most recent examples generating substantial crustal deformation as both coseismic uplift and subsidence across the coastline is the 2010 M_w 8.8 Maule earthquake, which nucleated at the Nazca-South America plate boundary in south-central Chile with a total rupture length of ~500 km. Geodetic observations indicate that before the rupture there were two regions where high asperities appeared to be nearly wholly locked (Moreno et al., 2010). The 2010 Maule earthquake coseismic slip along the northern section was located mainly offshore causing coseismic subsidence of the adjacent coastline coastal line whilst the southern section of the rupture slipped mainly landward below the coastline generating coseismic uplift (Vigny et al., 2011, Moreno et al., 2012). Departing from this analogy, this suggests that the southern section of the rupture remained confined to the shallow portion of the fault zone while the northern margin is confined to the intermediate and/or deep portion of the plate interface resulting from significant variations in the degree of locking across a plate interface (e.g., Correa-Mora et al., 2008).

The second possible reason for along-strike variability in vertical coseismic deformation patterns may be because this earthquake might have occurred due to two or multiple persistent asperities (Figure 7.1), rather than consisting of a rupture dominated by one main asperity which is large slip/large slip patches or stress drop areas (e.g., Bürgmann et al., 2005, Correa-Mora et al., 2008, Yomogida et al., 2011, Chlieh et al., 2014, Bletery et al., 2016, Hamling Ian et al., 2017, Ye et al., 2018; Zhao et al., 2022). Provided that the first asperity occurred in the shallow and mostly offshore section, while the second asperity propagated beneath the coastline. Furthermore, it is suggested that the lack of asperity may lead to the occurrence of large megathrust earthquakes (Bletery et al., 2016); hence, the 1737 event may have ruptured two or more asperities which makes it a relatively moderate rupture. Consequently, the presence of multiple asperities implies that this rupture may have originated from the subduction zone rather than an intraplate earthquake since it is suggested that great subduction zone earthquakes could be influenced by varying the scale of asperities (c.f. Moreno et al., 2010).

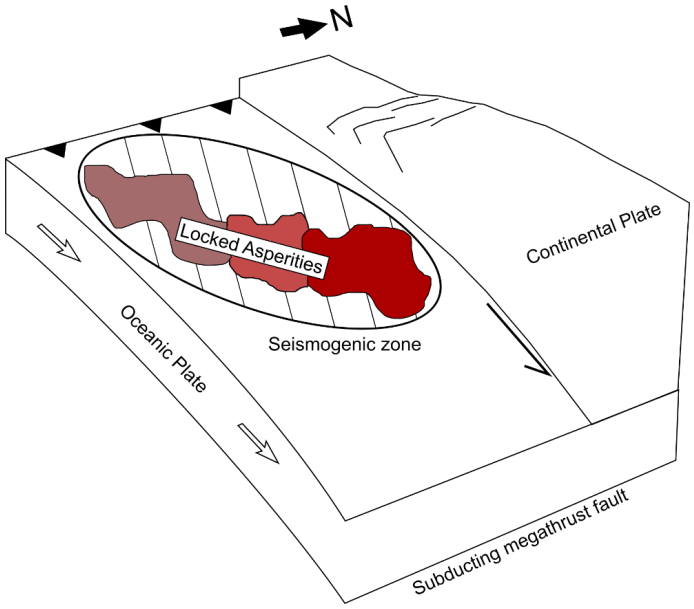

Figure 7.1 : Sketch illustrating a subduction zone with three different asperities of varying degrees in-between, suggesting different levels of coseismic deformation at coastal sites to the south and north.

Along-strike variations in vertical coseismic deformation of the coastline can also be considered as a form of patchy seismic behaviour resulting from a patchy and highly variable suite of plate interface complex lithological features (Tassara et al., 2006, Pérez-Gussinyé et al., 2008, Barnes et al., 2020). Furthermore, contrasting coseismic deformation patterns could be linked to along-strike variations in frictional stress, asperities, non-uniform slip on the megathrust interface, down-dip angle and also due to variation in shear strength and/or variation in locking (Bletery et al., 2016, Shrivastava et al., 2019).

Another possible reason for along-strike variability in vertical coseismic deformation can be attributed to megathrust events or the activation of inland (crustal) faults through ruptures and/or reactivation. Recent studies have compiled a database of active and potentially-active continental faults in Chile (Santibáñez et al., 2019; Maldonado et al., 2021). Furthermore, it has been suggested that the presence of faults capable of generating earthquakes with magnitudes of 7 to 7.5 in the coastal region coincides with the coastal sites in the Valdivia region (Santibáñez et al., 2019; Maldonado et al., 2021).

There are examples of inland faults being triggered by megathrust earthquakes both before and after the main event (e.g., Farías et al., 2011; González et al., 2015; Mitogawa and Nishimura, 2020). Moreover, interseismic locking models propose that

strain accumulation during the interseismic period and coseismic deformation along the subduction megathrust may also induce the rupture of crustal faults within the overriding South American plate (e.g., ten Brink and Lin, 2004; Loveless et al., 2010). Similar occurrences are also reported for Japan (e.g., Komura et al., 2019). Moreover, simultaneous activation and stress transfer from megathrust or strike-slip faults can also trigger the rupture of nearby faults (e.g., Loveless and Pritchard, 2008; Toda and Tsutsumi, 2013). Notwithstanding, it should be noted that currently there is no compelling evidence to support this hypothesis. Furthermore, when we consider the proximity of these coastal sites to the city of Valdivia, coupled with the absence of historical records for the occurrence of earthquakes before or after this event, it further complicates the issue.

Numerous factors may cause the change in coastal stratigraphy pointing to possible coseismic deformation. Provided that both findings from this study and the Chaihuín tidal marsh reflect vertical coseismic deformation associated with the 1737 rupture, the slip along the northern patch occurred mostly below the coastline and thus the adjacent coastline uplifted, whilst slip along the southern patch was located mostly offshore resulting in coastal subsidence. However, based on available data it is rather challenging to establish robust estimates for how slip may have varied in space for this historic rupture and suggests the necessity for further investigation to constrain the magnitude, depth, and amount of coseismic slip resulting from this earthquake.

7.6 San Antonio tidal mashes

7.6.1 Do the tidal marsh sediments at San Antonio estuary reflect evidence for subduction zone earthquakes?

At first glance, the stratigraphy of the San Antonio tidal marsh does not reflect any obvious peat-mud, peat-sand, or mud-peat couplets with sharp contacts. From bottom to the top, lithological changes appear to be gradual, changing from minerogenic units (silty-sand and silty sediments) to herbaceous peaty units. This points to decreasing tidal influence at the estuary through time.

Diatom-based transfer functions using a regional-scale modern training set are applied to construct a new RSL curve from fossil assemblages within sediment core SA18/20 from the San Antonio estuary. However, the reconstruction models do not agree with inferred subsidence at nearby localities which was reported by Plafker and Savage (1970) for the 1960 rupture. Moreover, the coastal sediments do not

demonstrate any sharp changes in the stratigraphy implying occurrence of subduction zone earthquakes.

The striking feature of the sandy-silt unit is that it is not laterally continuous, it only presents in six cores perpendicular to the estuary. Moreover, this unit does not demonstrate any sharp and erosional lower contacts, or a coarser grain size pointing to high-energy deposition characteristics in depositional environment. In addition, the absence of any indicative criteria of tsunami deposition, including lack of abrupt lower or upper contacts often with flattened vegetation rooted in the underlying unit, laterally extensive, landward thinning, upward fining, rip-up clasts, mixed diatom assemblages, this unit is not interpreted as being deposited in a tsunami event (Morton et al., 2007, Peters and Jaffe, 2010, Engel and Brückner, 2011). In addition, the sheltered location of the estuary suggests that this unit may be beyond the reach of storm surges. Due to these characteristics, it is difficult to estimate its origin, and it remains unknown.

Those cores that were examined across the San Antonio estuary suggest a succession from minerogenic sediments (from sand to silty-clay to clayey-silt) to organic sediment (peat deposits), suggesting increasing freshwater influence. The cores are suitable to test those criteria 1, 2, 4, and 5 in (see Table 7.2) addressed by Nelson et al. (1996), Shennan et al. (2016). The first criterion suggests there is no sharp contact between units except for the sandy-silt unit at 11-11.5 cm. The second criterion indicates that there is no evident submergence or emergence observed. Third one cannot be testable as there is only one study site. The fourth criterion highlights that the age-depth model covers approximately 1000 years but does not align with the timing of historical and prehistoric earthquakes. The fifth criterion reflects that the distribution of sedimentary deposits points out neither emergence nor submergence where the distribution of sedimentary units within cores follows certain pattern. The last criterion suggests that there is no additional evidence to meet this criterion.

Table 7.2 : Essential criteria for detection of large subduction zone earthquakes, as developed by Nelson et al. (1996) and modified by Shennan et al. (2016).

No	Criteria	Check
1	lateral extent of peat-mud or mud-peat couplets with sharp contacts	NA
2	suddenness of submergence or emergence, and replicated within each site	NA
3	amount of vertical motion, quantified with 95% error terms and replicated within each site	NA
4	synchroneity of submergence and emergence based on statistical age modelling	NA
5	spatial pattern of submergence and emergence	NA
6	possible additional evidence, such as evidence of a tsunami or liquefaction concurrent with submergence or emergence	NA

- NA: Not Available

The absence of evidence for coseismic deformation in tidal marsh sediments that was analysed from San Antonio estuary may imply that the study site may be placed near at the eastern limit of coseismic subsidence resulting from the 1960 earthquake (Plafker, 1972, Cifuentes, 1989; Wang et al., 2007, Moreno et al., 2009, Cisternas et al., 2017b). If this assumption is true, under these circumstances this range can result in constraining the width of plate-boundary fault rupture across the Valdivia segment at the Chilean subduction zone which is a pivotal aspect of generating geophysical models of the next great Chilean earthquake.

Furthermore, in addition to the 1960 earthquake, the stratigraphy at San Antonio does not present any geological evidence for event B, C, and D. The lack of evidence for these large earthquakes, which are comparable to the 1960 earthquake, may also aid in constraining the extent of coseismic subsidence associated with these ruptures (Cisternas et al., 2005, 2017a, Garrett et al., 2015).

7.6.2 Long-term relative sea-level change

With the aim of assessing the processes driving RSL change, this section compares transfer function-derived RSL reconstructions with a suite of glacial isostatic adjustment models.

It is suggested that long-term interseismic sea-level rise between large earthquakes is the driving factor in intertidal settings during the Holocene (Dura et al., 2011, Grand

Pre et al., 2012, Garrett et al., 2015, 2020). For example, during an extended interseismic period where the rate of land uplift is greater than the rate of eustatic sea level rise, there is a decline in RSL that leads to a gradual transition from a salt marsh to organic-rich terrestrial soil. This transition occurs due to the decreasing influence of marine conditions (e.g., Leonard et al., 2010). Previous palaeoseismic studies that have been carried out on coastal lowlands and intertidal marshes in south-central Chile (Atwater et al., 1992, Cisternas et al., 2005, 2017b, Garrett et al., 2015, 2020) present evidence for falling RSL over the late Holocene, but a rise in the last 1000 years.

Index points, which are estimates for the specific position of RSL in time and space, that were obtained from Maullín (six) and Chucalén (twelve) show that RSL was almost 1 m below the present sea level at around 1050 CE (Cisternas et al., 2005, Garrett et al., 2015), while reconstructions from San Antonio suggest RSL was between 0.28 ± 1.50 and 0.37 ± 1.53 m at this time. Subsequently, at both Maullín and Chucalén, RSL rose due to coseismic subsidence (Cisternas et al., 2005, Garrett et al., 2015). In contrast, at San Antonio, RSL experienced a significant drop of approximately 2 meters below the present MSL between approximately 1550 CE and 1850 CE (Figure 7.2 and Figure 5.8). Sea level index points from San Antonio (Table 7.3) do not exhibit a similar trend as those in Maullín and Chucalén. Furthermore, the presence of a large error range makes it challenging to compare the reconstruction estimates.

The studies on glacio isostatic adjustment models show that as well as evident tectonic control, land-level change along subduction margins and convergent settings has been substantially modified by the advance and retreat of glaciers (e.g., Peltier et al., 2015). By investigating the late Holocene deposits of this segment of the subduction zone, a better understanding and comparison of the role of glacio-isostatic forcing and tectonic controls on the sedimentation patterns across the San Antonio tidal marsh can be inferred.

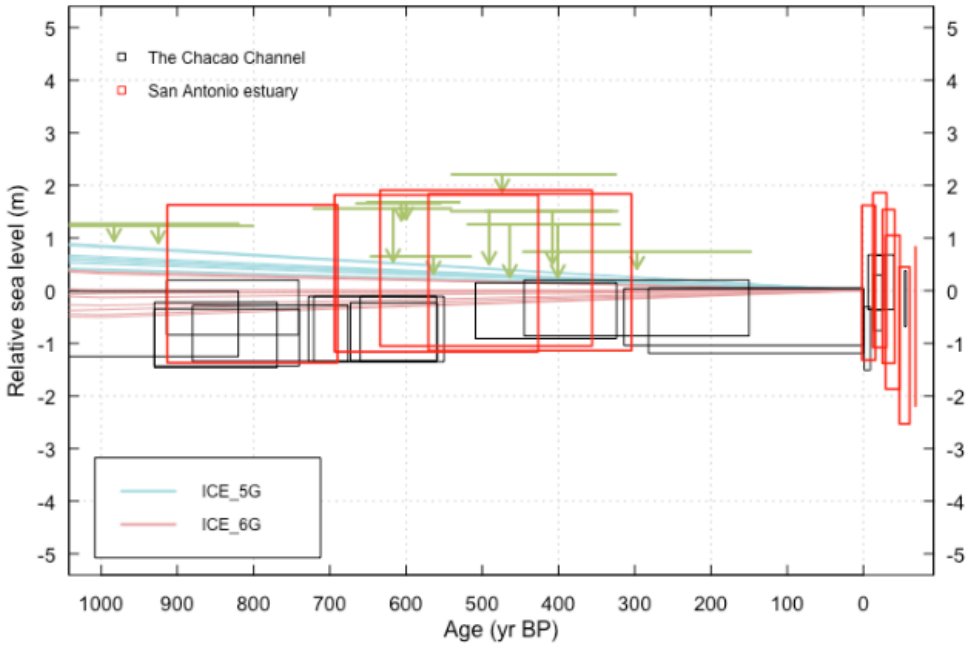

Figure 7.2 : Comparison of the age-elevation distribution of sea-level data points with GIA model predictions. The black rectangles are sea-level index points from the Chacao Channel while the red rectangles are sea-level index points from the San Antonio estuary (only showing good and close analogues); terrestrial limiting points are blue T-shaped symbols and marine limiting points are green ⊥- shaped symbols. GIA model predictions are light blue (ICE_5G) and pink (ICE_6G) curves (Peltier, 2004; Peltier et al., 2015) with varying lithospheric thickness and upper mantle viscosities (see Garrett et al., 2020).

Glacial isostatic adjustment (GIA) models allow us to investigate RSL change for longer time periods (c. 20 ka BP) than current geological records (Peltier, 2004; Peltier et al., 2015). Also, GIA models generate various outputs employing past global ice sheet change and different rheological features such as thickness of lithosphere and various viscosity values for both lower and upper mantle (Peltier, 1998b). The available GIA models comprising ICE-6G (Peltier et al., 2015) and ICE-5G (Peltier, 2004) enable us to compare RSL estimates inferred from sedimentary records. GIA models also indicate RSL has been gradually decreasing since the mid-Holocene (Garrett et al., 2020). As the San Antonio tidal marsh record covers the last 1000-years, comparison to the RSL records from Maullín (Cisternas et al., 2005) and Chucalén (Garrett et al., 2015) is possible. Notwithstanding, the predictive ability of the reconstruction model is rather limited, and the number of good and close analogues are mainly available in the last 100 year; thus, the following section only investigates this period (Figure 7.2). According to GIA estimates using ICE-5G ice

models (Peltier, 2004), RSL shows a gradual decrease during the late Holocene. However, contrasting estimates based on ICE-6G ice models (Peltier et al., 2015) suggest a rise in RSL during the same period, except for a model that incorporates a relatively large lithospheric thickness and relatively strong upper mantle viscosity, which indicates a fall in RSL. This pattern is observed in the Chacao Channel region of the Pacific coast of South America over the past 2000 years. Thus, it is suggested that the increase in RSL creates accommodation space for the deposition of sedimentary deposits, which plays a crucial role in the preservation of evidence for subduction zone earthquakes near the study sites in the region (Cisternas et al., 2005, 2017b, Garrett et al., 2015, 2020).

As discussed in chapters 4 and 5, there is no strong relationship between elevation and diatom assemblages. The significance test indicates that the relative predictive ability of the transfer function is somewhat limited. Additionally, there are a limited number of good and close analogues for the fossil assemblages. The results of the goodness-of-fit analysis suggest that reliable estimates can only be obtained from the samples in the top section of the core. Therefore, it is necessary to focus on a specific set of fossil samples in the upper part of the core to evaluate changes in relative sea level (RSL). The age-depth model for the top eight samples, which provides good and close analogues, only covers the period from approximately 1965 to 2018 CE. In conjunction with these analyses, taking into account tide gauge measurements from Barrientos et al. (1992) and additional measurements from the Permanent Service for Mean Sea Level (PSMSL), it is suggested that there may have been post-seismic uplift (RSL fall) near Puerto Montt following the 1960 earthquake (Barrientos et al., 1992) (section 5.8.1).

Although the San Antonio marsh stratigraphy does not reflect any change, diatom-based reconstruction models indicate a RSL rise around the time of the earthquake in 1960 and fall after at core depths of around 7.5 cm and 0 cm. These estimates are statistically reliable due to the number of good and close analogues for fossil diatom assemblages in this part of the core (Figure 5.13). Nonetheless, it is difficult to quantify the magnitude of the rise in RSL due to large uncertainty over the depth of the earthquake horizon. These findings suggest that even though the stratigraphy did not respond to the 1960 earthquake, diatom-based reconstruction and relative sea-level change reconstruction may be in agreement with observations and tide gauge measurements. Nonetheless, the reconstruction estimates must be treated with caution as discussed in section 7.2.

Table 7.3 : Sea level index points from the San Antonio following Hijma et al., (2015).

Unique sample ID	Reference	Regior code	Sub-region	Latitude	Longitude
SA18/20 - 0 cm	This study	18	San Antonio, Los Lagos Region	-73.13	41.46
SA18/20 - 2 cm	This study	18	San Antonio, Los Lagos Region	-73.13	41.46
SA18/20 - 4 cm	This study	18	San Antonio, Los Lagos Region	-73.13	41.46
SA18/20 - 5 cm	This study	18	San Antonio, Los Lagos Region	-73.13	41.46
SA18/20 - 6 cm	This study	18	San Antonio, Los Lagos Region	-73.13	41.46
SA18/20 - 7 cm	This study	18	San Antonio, Los Lagos Region	-73.13	41.46
SA18/20 - 22 cm	This study	18	San Antonio, Los Lagos Region	-73.13	41.46
SA18/20 - 24 cm	This study	18	San Antonio, Los Lagos Region	-73.13	41.46
SA18/20 - 26 cm	This study	18	San Antonio, Los Lagos Region	-73.13	41.46
SA18/20 - 34 cm	This study	18	San Antonio, Los Lagos Region	-73.13	41.46

Table 7.3 (continued): Sea level index points from the San Antonio following Hijma et al., (2015).

Corrected age (^{14}C a BP)	Corrected age uncertainty (^{14}C a)	Age (cal a CE)	Age 2σ Uncertainty + (cal a)	Age 2σ Uncertainty - (cal a)	Sample depth/overburden thickness (m)
n/a	n/a	2018.30	0.01	0.01	n/a
n/a	n/a	2004.91	7.76	5.61	n/a
n/a	n/a	1988.20	9.08	9.69	n/a
n/a	n/a	1983.06	8.17	7.77	n/a
n/a	n/a	1969.30	6.79	10.96	n/a
n/a	n/a	1959.18	11.10	6.57	n/a
n/a	n/a	1511.33	131.91	134.26	n/a
n/a	n/a	1449.21	133.41	144.75	n/a
n/a	n/a	1383.39	127.08	139.90	n/a
n/a	n/a	1125.43	88.54	134.63	n/a

Table 7.3 (continued): Sea level index points from the San Antonio following Hijma et al., (2015).

Depth to consolidated substrate (m)	Intercalated	Sample elevation (m MSL)	Sample elevation uncertainty + (m)	Sample elevation uncertainty - (m)	Type
nd	1	3.360	0.07	0.07	0
nd	1	3.340	0.07	0.07	0
nd	1	3.320	0.07	0.07	0
nd	1	3.310	0.07	0.07	0
nd	1	3.300	0.07	0.07	0
nd	1	3.290	0.07	0.07	0
nd	1	3.140	0.07	0.07	0
nd	1	3.120	0.07	0.07	0
nd	1	3.100	0.07	0.07	0
nd	1	3.020	0.07	0.07	0

Table 7.3 (continued): Sea level index points from the San Antonio following Hijma et al., (2015).

Primary indicator type	Secondary indicator type	Supporting evidence	Sample indicative meaning
5 = Sedimentary (e.g., deltaic, estuarine, wetland, lacustrine, marine facies)	Specified tidal marsh environment	Quantitative palaeomarsh surface elevation reconstructions from diatom transfer function	Uniquely defined
5 = Sedimentary (e.g., deltaic, estuarine, wetland, lacustrine, marine facies)	Specified tidal marsh environment	Quantitative palaeomarsh surface elevation reconstructions from diatom transfer function	Uniquely defined
5 = Sedimentary (e.g., deltaic, estuarine, wetland, lacustrine, marine facies)	Specified tidal marsh environment	Quantitative palaeomarsh surface elevation reconstructions from diatom transfer function	Uniquely defined
5 = Sedimentary (e.g., deltaic, estuarine, wetland, lacustrine, marine facies)	Specified tidal marsh environment	Quantitative palaeomarsh surface elevation reconstructions from diatom transfer function	Uniquely defined
5 = Sedimentary (e.g., deltaic, estuarine, wetland, lacustrine, marine facies)	Specified tidal marsh environment	Quantitative palaeomarsh surface elevation reconstructions from diatom transfer function	Uniquely defined
5 = Sedimentary (e.g., deltaic, estuarine, wetland, lacustrine, marine facies)	Specified tidal marsh environment	Quantitative palaeomarsh surface elevation reconstructions from diatom transfer function	Uniquely defined
5 = Sedimentary (e.g., deltaic, estuarine, wetland, lacustrine, marine facies)	Specified tidal marsh environment	Quantitative palaeomarsh surface elevation reconstructions from diatom transfer function	Uniquely defined
5 = Sedimentary (e.g., deltaic, estuarine, wetland, lacustrine, marine facies)	Specified tidal marsh environment	Quantitative palaeomarsh surface elevation reconstructions from diatom transfer function	Uniquely defined
5 = Sedimentary (e.g., deltaic, estuarine, wetland, lacustrine, marine facies)	Specified tidal marsh environment	Quantitative palaeomarsh surface elevation reconstructions from diatom transfer function	Uniquely defined
5 = Sedimentary (e.g., deltaic, estuarine, wetland, lacustrine, marine facies)	Specified tidal marsh environment	Quantitative palaeomarsh surface elevation reconstructions from diatom transfer function	Uniquely defined

Table 7.3 (continued): Sea level index points from the San Antonio following Hijma et al., (2015).

RSL (m)	RSL 2σ Uncertainty + (m)	RSL 2σ Uncertainty - (m)	Corrected RSL (m)	Corrected RSL error + (m)	Corrected RSL error - (m)	Correction type
-0.67	1.48	1.48	nd	nd	nd	0
-1.03	1.46	1.46	nd	nd	nd	0
-0.40	1.43	1.43	nd	nd	nd	0
0.08	1.43	1.43	nd	nd	nd	0
0.40	1.44	1.44	nd	nd	nd	0
0.15	1.43	1.43	nd	nd	nd	0
0.36	1.46	1.46	nd	nd	nd	0
0.43	1.44	1.45	nd	nd	nd	0
0.33	1.46	1.46	nd	nd	nd	0
0.13	1.47	1.47	nd	nd	nd	0

Table 7.3 (continued): Sea level index points from the San Antonio following Hijma et al., (2015).

Reject	Why reject?	Notes
0	n/a	Dating Method is Bayesian approach by rplum package in R (Aquino-López et al., 2018, Blaauw et al., 2020). Tidal datums modelled using TPXO8-ATLAS global model of ocean tides (Egbert and Erofeeva, 2010)
0	n/a	Dating Method is Bayesian approach by rplum package in R (Aquino-López et al., 2018, Blaauw et al., 2020). Tidal datums modelled using TPXO8-ATLAS global model of ocean tides (Egbert and Erofeeva, 2010)
0	n/a	Dating Method is Bayesian approach by rplum package in R (Aquino-López et al., 2018, Blaauw et al., 2020). Tidal datums modelled using TPXO8-ATLAS global model of ocean tides (Egbert and Erofeeva, 2010)
0	n/a	Dating Method is Bayesian approach by rplum package in R (Aquino-López et al., 2018, Blaauw et al., 2020). Tidal datums modelled using TPXO8-ATLAS global model of ocean tides (Egbert and Erofeeva, 2010)
0	n/a	Dating Method is Bayesian approach by rplum package in R (Aquino-López et al., 2018, Blaauw et al., 2020). Tidal datums modelled using TPXO8-ATLAS global model of ocean tides (Egbert and Erofeeva, 2010)
0	n/a	Dating Method is Bayesian approach by rplum package in R (Aquino-López et al., 2018, Blaauw et al., 2020). Tidal datums modelled using TPXO8-ATLAS global model of ocean tides (Egbert and Erofeeva, 2010)
0	n/a	Dating Method is Bayesian approach by rplum package in R (Aquino-López et al., 2018, Blaauw et al., 2020). Tidal datums modelled using TPXO8-ATLAS global model of ocean tides (Egbert and Erofeeva, 2010)
0	n/a	Dating Method is Bayesian approach by rplum package in R (Aquino-López et al., 2018, Blaauw et al., 2020). Tidal datums modelled using TPXO8-ATLAS global model of ocean tides (Egbert and Erofeeva, 2010)
0	n/a	Dating Method is Bayesian approach by rplum package in R (Aquino-López et al., 2018, Blaauw et al., 2020). Tidal datums modelled using TPXO8-ATLAS global model of ocean tides (Egbert and Erofeeva, 2010)
0	n/a	Dating Method is Bayesian approach by rplum package in R (Aquino-López et al., 2018, Blaauw et al., 2020). Tidal datums modelled using TPXO8-ATLAS global model of ocean tides (Egbert and Erofeeva, 2010)

7.7 Further recommendations

Although diatoms are generally well preserved in fossil sediments, in sediments where they are absent or sparse (e.g., in sands of the Valdivia coastal exposures), it precludes our ability of acquiring robust reconstruction estimates. Thus, the use of multiproxy methods including alternative microfossil proxies (foraminifera, testate amoebae) or employing geochemistry approaches (see section 7.3) may not only overcome the lack of diatoms and their limited availability but also provide independent test and cross validation opportunities from different models (e.g., Gehrels et al., 2001, Kemp et al., 2010, Wilson and Lamb, 2012, Engelhart et al., 2013b). The Bayesian framework provides a more flexible approach and allows the use of multiple microfossils and geochemistry data (Cahill et al., 2015, Holden et al., 2017). Notwithstanding, this method is not the promised panacea for solving the non-modern analogue issue either and also revokes basic assumptions for developing transfer function models which is not independent from assumption 5 “environmental variables other than the one of interest have negligible influence, or their joint distribution with the environmental variable does not change with time” (see Section 3.5.3.1).

Where both modern and fossil diatoms are available, any transfer function method will generate estimates for reconstructed elevations. Under bootstrapped cross-validation, models also calculate standard error of the bootstrap prediction for each sample (uncertainty) in $\pm 1\sigma$ (68%) range and this value is to be multiplied by 1.96 in order to have 95% confidence interval. However, when SWLI units are back-converted to elevation in metres by utilising the original equation (Eq. 3.1 in Chapter 3), the difference between MSL and MHHW plays an important role to delimit confidence interval for the reconstructed estimates. Where the difference between MSL and MHHW is large, reconstructions have large vertical errors. Therefore, further studies need to consider the role of tidal range (e.g., Horton and Edwards, 2005, Barlow et al., 2013) that can cause large error ranges in reconstructed elevation regardless of the quality of modern analogues.

When employing diatom-based transfer functions to reconstruct former sea-level change, regional training sets are essential to provide better analogues to fossil samples compared to the local training set (Wilson and Lamp, 2012, Barlow et al., 2013, Watcham et al., 2013). Despite the fact that regional training sets generally provide large errors for reconstruction estimates, the lack of modern analogues is still the major obstacle to obtaining reliable reconstruction models. Hence, in order to

increase the likelihood of finding better analogues for fossil samples, new modern samples need to be collected where possible, even if this does not resolve the issue entirely.

Accurate dating by any radiometric methods is of utmost importance to constrain and infer the timing of large earthquakes, especially where recurrence intervals are short, such as the 1737 CE and 1837 CE earthquakes. This is an evident issue especially for radiocarbon dating owing to large fluctuations in the atmospheric carbon content, and radiocarbon dating yielding large age ranges when calibrated to calendar dates especially for the last 500 years (Hua, 2009). Consequently, employing multiple samples for radiocarbon dating as well as ^{137}Cs and ^{210}Pb dating could be effective in creating age models with higher resolution and increased precision for the last 100 years. To do that, age-depth models generated by means of *plum* program (Aquino-López et al., 2018) using rplum package (Blaauw et al., 2020) in R (R Core Team, 2021) could serve this purpose including at least two radiocarbon dates per millennium (Blaauw et al., 2018).

7.8 Summary

This chapter compares and contrasts reconstructions of RSL from this study with previous studies' findings of RSL change associated with subduction zone earthquakes by employing diatom-based quantitative transfer function models and sedimentological findings from coastal sites in south-central Chile. Deciphering the behaviour of subduction zone earthquakes such as rupture length, amount of vertical deformation and timing and recurrence intervals is vitally important to assess the seismic hazard of the region.

Changes from minerogenic to organic sediment deposition in coastal exposures north of Valdivia are interpreted to reflect uplift in the 1737 CE earthquake, although it was not possible to quantify this uplift due to the lack of marine diatoms limiting transfer function reconstructions. It is tentatively suggested that this rupture may emanate from deeper on the subduction zone than the well documented 1960 rupture, in agreement with some previous studies (Cisternas et al., 2017a, b). However, differing patterns of coseismic land-level change to the Chaihuín site to the south, points to the necessity for further investigation to constrain the magnitude, rupture depth, and amount of coseismic slip for this earthquake.

The San Antonio estuary is a potentially promising tidal marsh environment to constrain slip distribution in great and large subduction zone earthquakes, particularly

event B, C and D, in south-central Chile. Key uncertainties remain in Chile, with knowledge of surface deformation in the 1960 earthquake being dominated by studies at the coastal sites (Ely et al., 2014, Dura et al., 2017, Hong et al., 2017, Cisternas et al., 2005; 2017, Garrett et al.,2015; Hocking et al., 2021, Kempf et al., 2015) and patterns of deformation inland are less well known, including the eastern inland limit of coseismic subsidence. The results from diatom-based transfer function models and coastal sedimentary deposits from San Antonio estuary indicate that the 1960 earthquake did not cause any evident coseismic land-level change but do reveal post-seismic uplift that matches with tide gauge records. The lack of evidence for coseismic deformation suggests that the San Antonio estuary can constrain the possible location as the eastern limit of coseismic subsidence resulting from the 1960 earthquake. However, it should be noted that the tidal marsh stratigraphy does not suggest any evidence for earlier great subduction zone earthquakes based on established criteria by Nelson et al. (1996) and updated Shennan et al. (2016).

Due to a number of reasons such as a noisy dataset, large tolerance ranges of diatom taxa, as well as insufficient numbers of modern analogues, the ability of the transfer function models to produce reliable estimates of RSL is substantially limited. This study shows that even though the local training set outperforms the regional training set, the lack of modern analogues is the main problem for the credibility of the reconstruction models. More importantly, the results of CCA and CA must be reported, and the ratio of λ_1/λ_2 should be presented before running any transfer function methods. Furthermore, elevation as the main and only environmental variable of interest explains ~5% of the total variation in the diatom assemblages; hence, caution must be taken when interpreting reconstruction models, especially environmental variables that explain a very small part of the variance in diatom assemblages. We should be extremely cautious of the limitations and assumptions of the transfer function approach otherwise results can be overoptimistic and may not be reliable to understand the past environmental changes.

Chapter 8 : Conclusions

The work presented in this thesis focuses on coastal sediments in order to provide evidence for historical subduction zone earthquakes in south-central Chile. The results from this study can be used to characterise and constrain rupture length and width, the amount of vertical deformation and the timing of past earthquakes. These findings can contribute to the seismic hazard assessment of the region.

This study has sought to find evidence for the 1960, 1837 and 1737 earthquakes (and its predecessors) through analysing sedimentary deposits and their diatom assemblages from coastal outcrops in the Valdivia region and tidal marsh samples from the San Antonio estuary in south-central Chile, in order to contribute to the seismic hazard assessment of the region.

In order to achieve these aims, the following three questions have been investigated:

1. Is there geological evidence of relative land-level change at San Antonio estuary associated with the 1960 earthquake, which may corroborate the location of the eastern limit of coseismic subsidence?

Chapter 5 introduces the analysed sedimentary deposits from San Antonio estuary. Tidal marsh stratigraphy, sedimentology and diatom-based transfer function reconstructions suggest no coseismic deformation took place at San Antonio in the 1960 earthquake. Therefore, it is considered that the San Antonio estuary is the possible location for the eastern limit of coseismic subsidence associated with the 1960 earthquake. Comparison to observations from sites further inland to the east (Plafker and Savage, 1970), suggests San Antonio lies on the hingeline between coseismic uplift and subsidence in 1960.

2. Is there any evidence in tidal marsh sediments at San Antonio for pre-1960 earthquakes (e.g., event B, C and D) that may help constrain the width and magnitude of these ruptures?

Chapter 5 of the thesis focuses on the examination of the litho- and bio-stratigraphy of tidal marsh sediments at San Antonio. The primary aim is to assess the transitions in stratigraphy using established criteria for detecting large subduction zone earthquakes, as described by Nelson et al. (1996) and Shennan et al. (2016). Additionally, the chapter includes the reconstruction of relative sea level (RSL) changes based on the analysis of diatom assemblages. Neither the lithostratigraphy nor diatom-based reconstruction models provide evidence for historically documented earthquakes in 1837, 1737 or 1575 (events B, C, D). Hence, it is not possible to

compare the geological signals of these large/great subduction zone earthquakes. However, the most reliable part of the reconstruction estimates for PMSE change comes from where good and close modern analogues exist (the top 7.5 cm of the core) and estimates of post-1960 RSL fall agree with tide gauge measurements from Puerto Montt (Barrientos et al., 1992). These findings suggest that even though the stratigraphy did not respond to the 1960 earthquake, diatom-based reconstruction and RSL change reconstruction may be in agreement with observations and tide gauge measurements.

3. Do peat deposits on beach terraces in the Valdivia region represent possible occurrence of uplift during a pre-1960 earthquake?

Chapter 6 presents the stratigraphy and diatom assemblages from coastal exposures at Rosada, Loncoyén, Calfuco, Chan-Chan and Isla Mancera in the Valdivia region. Sand-peat couplets at Rosada, Loncoyén and Chan-Chan provide evidence for possible uplift associated with the 1737 CE rupture of the Chilean subduction zone. Findings imply that pre-earthquake beach ridges do not preserve diatoms well, and subsequent post-earthquake percolation of freshwater diatoms into the sands prevents reconstruction of land-level change across sand-peat contacts. Notwithstanding that, these findings introduce the second and contrasting geologic evidence for the possible 1737 earthquake along the south-central Chile coast and highlight the variability of coseismic patterns and seismic hazard in the region.

The main conclusions of this study are:

- Tidal marsh sediments from the San Antonio estuary suggest that there is no evidence for coseismic deformation associated with the 1960 earthquake. This suggests that San Antonio is located at the eastern limit of coseismic subsidence in 1960.
- There is no evidence of pre-1960 earthquakes preserved at San Antonio.
- The stratigraphy of coastal exposures north of Valdivia suggest that sand-peat couplets that are found at Rosada, Loncoyén North, Loncoyén South, and Chan-Chan possibly represent coseismic uplift and may relate to the 1737 earthquake.
- Further investigation of the 1737 earthquake is required as findings here suggest that this earthquake may have been nucleated in the deeper and narrow part of the megathrust in the northern half of the Valdivia segment of Chilean subduction zone, but contradict evidence for coseismic subsidence

associated with the 1737 earthquake that was reported at Chaihuín tidal marsh ~20 km to the south of the study sites (Hocking et al., 2021). This highlights the need for further investigation in order to explain these variable coseismic deformation patterns observed at coastal sites that are very close to one another.

- The reliability of the reconstruction estimates is rather limited due to the number of samples with poor modern analogues. Further efforts are needed to increase the size of the modern training set to adequately represent the environments found in the San Antonio core and coastal exposures in the Valdivia region.
- This study demonstrates that the relationship between diatom assemblages and elevation, which is surrogate for both tidal frequency and duration is not strong, especially when a regional modern training set is employed to generate reconstruction models and elevation may not be an ecologically important determinant for diatom assemblages in modern tidal marshes at the regional scale. This relationship was investigated in detail using a range of statistical methods in Chapter 5 and detailed discussion was provided in Chapter 7. Although local samples collected from the San Antonio tidal marsh display a statistically robust relationship with elevation as a sole environmental variable and provide a relatively small RMSEP compared to the regional training set (Chapter 5), the main issue is the limited number of good analogues for the fossil diatom assemblages and a macrotidal range causing large error ranges on reconstruction estimates. Where tidal range is large or macro level, even if reconstruction estimates have a low RMSEP (for sample-specific error), back-conversion to metre scale introduce large error range. Furthermore, in spite of the number of good and close modern analogues, it is vitally important to employ goodness-of-fit analysis (Birks, 1995, Simpson and Hall, 2012) and significance tests to investigate the robustness of reconstruction estimates (Telford and Birks, 2011). The results of CCA must also be reported, especially the percentage of variance explained by the environmental variable and the relative explanatory power of the environmental variable of interest when different sized training sets are used. Perhaps most importantly, ter Braak (1988)'s criterion for a useful calibration must also be carried out, which generally has received not much attention at all (Juggins, 2013). Otherwise, when the same diatom taxon is present in both modern and fossil sediments, any transfer function methods provide reconstruction estimates for any variable. Our main concern is to obtain reliable reconstruction models to infer

change in elevation in the past; hence, both basic assumptions for developing transfer function models and detailed statistical analysis are vitally important to critically analyse reconstruction estimates and inform further studies.

- On the basis of this study, elevation which is a surrogate function of tidal exposure, cannot be considered independent of other environmental variables and reconstruction models should be treated with caution as many environmental variables influence the ecological response of the diatoms. Considering the reconstruction of PMSE and RSL change associated with subduction zone earthquakes are vitally important to policy makers as well as further research that employs geophysical modelling using vertical and lateral deformation estimates not only in south-central Chile but also all around the edge of the Pacific Ocean and where plate collision exist, an explicit discussion about the reliability upon reconstruction estimates and cautious interpretation must be carried out.
- Development of modern training sets and further reconstruction models utilising fossil assemblages necessitates a substantial diligent effort. Hence, our endeavours require extra caution when interpreting the results of reconstruction models and always bear in mind those basic assumptions and limitations.
- Future studies should aim to consider the problems of large tidal ranges before collecting modern samples, the relative explanatory power of environmental variable of interest (λ_1/λ_2) and goodness-of-fit analysis, significance test, which may lead to poor judgement of contemporary relationships between species and marsh surface elevation and over-reliance on estimations from reconstruction models via transfer function models.

Finally, it must be always borne in mind two more crucial points. Firstly, regardless of the method choice, transfer function models invoke six basic assumptions, one of which is unrealistic in most situations, and that is “environmental variables other than the one of interest have negligible influence, or their joint distribution with the environmental variable does not change with time” (see Section 3.5.3.1). Secondly, in a statistical sense all models are wrong (Box, 1976), following the principle of falsifiability is a substantially important or perhaps the most crucial aspect to measure the validity of the results of our research (Popper, 1962).

References

ABE, K. 1979. Size of great earthquakes of 1837–1974 inferred from tsunami data. *Journal of Geophysical Research: Solid Earth,* 84**,** 1561-1568.

ADMIRAAL, W. 1984. The ecology of estuarine sediment-inhabiting diatoms. *Progress in phycological research,* 3**,** 269-322.

ALLEN, J. R. L. 1997. Simulation models of salt-marsh morphodynamics: some implications for high-intertidal sediment couplets related to sea-level change. *Sedimentary Geology,* 113**,** 211-223.

ALLEN, J. R. L. 2000. Morphodynamics of Holocene salt marshes: a review sketch from the Atlantic and Southern North Sea coasts of Europe. *Quaternary Science Reviews,* 19**,** 1155-1231.

AMANTE, C. & EAKINS, B. W. 2009. ETOPO1 1 Arc-Minute Global Relief Model: Procedures, Data Sources and Analysis. NOAA Technical Memorandum NESDIS NGDC-24. National Geophysical Data Center, NOAA. *doi:10.7289/V5C8276M*.

ANDERSON, M., ALVARADO, P., ZANDT, G. & BECK, S. 2007. Geometry and brittle deformation of the subducting Nazca Plate, Central Chile and Argentina. *Geophysical Journal International,* 171**,** 419-434.

ANGERMANN, D., KLOTZ, J. & REIGBER, C. 1999. Space-geodetic estimation of the nazca-south america euler vector. *Earth and Planetary Science Letters,* 171**,** 329-334.

ANIYA, M. 1996. Holocene variations of Ameghino glacier, southern Patagonia. *The Holocene,* 6**,** 247-252.

APPLEBY, P. 2001. Chronostratigraphic techniques in recent sediments. *Tracking environmental change using lake sediments.* Springer.

APPLEBY, P. & OLDFIELDZ, F. 1983. The assessment of 210Pb data from sites with varying sediment accumulation rates. *Hydrobiologia,* 103**,** 29-35.

APPLEBY, P. G. 1998. Dating recent sediments by 210 Pb: problems and solutions. Finland.

APPLEBY, P. G. & OLDFIELD, F. 1978. The calculation of lead-210 dates assuming a constant rate of supply of unsupported 210Pb to the sediment. *CATENA,* 5**,** 1-8.

AQUINO-LÓPEZ, M. A., BLAAUW, M., CHRISTEN, J. A. & SANDERSON, N. K. 2018. Bayesian Analysis of 210Pb Dating. *Journal of Agricultural, Biological and Environmental Statistics,* 23**,** 317-333.

AQUINO-LÓPEZ, M. A., RUIZ-FERNÁNDEZ, A. C., BLAAUW, M. & SANCHEZ-CABEZA, J.-A. 2020. Comparing classical and Bayesian 210Pb dating models in human-impacted aquatic environments. *Quaternary Geochronology,* 60**,** 101106.

ARANEDA, A., TORREJÓN, F., AGUAYO, M., TORRES, L., CRUCES, F., CISTERNAS, M. & URRUTIA, R. 2007. Historical records of San Rafael

glacier advances (North Patagonian Icefield): another clue to'Little Ice Age'timing in southern Chile? *The Holocene,* 17**,** 987-998.

ARNAUD, F., MAGAND, O., CHAPRON, E., BERTRAND, S., BOËS, X., CHARLET, F. & MÉLIÈRES, M. A. 2006. Radionuclide dating (210Pb, 137Cs, 241Am) of recent lake sediments in a highly active geodynamic setting (Lakes Puyehue and Icalma—Chilean Lake District). *Science of The Total Environment,* 366**,** 837-850.

ASTORGA, G. & PINO, M. 2011. Fossil leaves from the last interglacial in central-southern Chile: Inferences regarding the vegetation and paleoclimate. *Geologica Acta*.

ATWATER, B. F. 1987. Evidence for Great Holocene Earthquakes Along the Outer Coast of Washington State. *Science,* 236**,** 942-944.

ATWATER, B. F., CISTERNAS, M., YULIANTO, E., PRENDERGAST, A., JANKAEW, K., EIPERT, A., FERNANDO, W., TEJAKUSUMA, I., SCHIAPPACASSE, I. & SAWAI, Y. 2013. The 1960 tsunami on beach-ridge plains near Maullín, Chile: Landward descent, renewed breaches, aggraded fans, multiple predecessors. *Andean Geology,* 40**,** 393-418.

ATWATER, B. F., CISTERNAS, M. V., BOURGEOIS, J., DUDLEY, W. C., HENDLEY II, J. W. & STAUFFER, P. H. 2005a. Surviving a tsunami: lessons from Chile, Hawaii, and Japan. *Circular.* Version 1.1 2005 ed.

ATWATER, B. F., MUSUMI-ROKKAKU, S., SATAKE, K., TSUJI, Y., UEDA, K. & YAMAGUCHI, D. K. 2005b. The orphan tsunami of 1700—Japanese clues to a parent earthquake in North America. *Professional Paper.* First Edition: Originally posted 2005; Second Edition: 2015 ed.

ATWATER, B. F., NÚÑEZ, H. J. & VITA-FINZI, C. 1992. Net Late Holocene emergence despite earthquake-induced submergence, south-central Chile. *Quaternary International,* 15-16**,** 77-85.

BARAZANGI, M. & ISACKS, B. L. 1976. Spatial distribution of earthquakes and subduction of the Nazca plate beneath South America. *Geology,* 4**,** 686-692.

BARLOW, N. L. M., LONG, A. J., SAHER, M. H., GEHRELS, W. R., GARNETT, M. H. & SCAIFE, R. G. 2014. Salt-marsh reconstructions of relative sea-level change in the North Atlantic during the last 2000 years. *Quaternary Science Reviews,* 99**,** 1-16.

BARLOW, N. L. M., SHENNAN, I., LONG, A. J., GEHRELS, W. R., SAHER, M. H., WOODROFFE, S. A. & HILLIER, C. 2013. Salt marshes as late Holocene tide gauges. *Global and Planetary Change,* 106**,** 90-110.

BARLOW, N. L. M., LONG, A. J., SAHER, M. H., GEHRELS, W. R., GARNETT, M. H. & SCAIFE, R. G. 2014. Salt-marsh reconstructions of relative sea-level change in the North Atlantic during the last 2000 years. Quaternary Science Reviews, 99, 1-16.

BARNES, P. M., WALLACE, L. M., SAFFER, D. M., BELL, R. E., UNDERWOOD, M. B., FAGERENG, A., MENEGHINI, F., SAVAGE, H. M., RABINOWITZ, H. S., MORGAN, J. K., KITAJIMA, H., KUTTEROLF, S., HASHIMOTO, Y.,

ENGELMANN DE OLIVEIRA, C. H., NODA, A., CRUNDWELL, M. P., SHEPHERD, C. L., WOODHOUSE, A. D., HARRIS, R. N., WANG, M., HENRYS, S., BARKER, D. H. N., PETRONOTIS, K. E., BOURLANGE, S. M., CLENNELL, M. B., COOK, A. E., DUGAN, B. E., ELGER, J., FULTON, P. M., GAMBOA, D., GREVE, A., HAN, S., HÜPERS, A., IKARI, M. J., ITO, Y., KIM, G. Y., KOGE, H., LEE, H., LI, X., LUO, M., MALIE, P. R., MOORE, G. F., MOUNTJOY, J. J., MCNAMARA, D. D., PAGANONI, M., SCREATON, E. J., SHANKAR, U., SHREEDHARAN, S., SOLOMON, E. A., WANG, X., WU, H.-Y., PECHER, I. A. & LEVAY, L. J. 2020. Slow slip source characterized by lithological and geometric heterogeneity. *Science Advances,* 6**,** eaay3314.

BARNETT, R. L., NEWTON, T. L., CHARMAN, D. J. & ROLAND GEHRELS, W. 2017. Salt-marsh testate amoebae as precise and widespread indicators of sea-level change. *Earth-Science Reviews,* 164**,** 193-207.

BARRIENTOS, S. E., PLAFKER, G. & LORCA, E. 1992. Postseismic coastal uplift in southern Chile. *Geophysical Research Letters,* 19**,** 701-704.

BARRIENTOS, S. E. & WARD, S. N. 1990. The 1960 Chile earthquake: inversion for slip distribution from surface deformation. *Geophysical Journal International,* 103**,** 589-598.

BARTSCH-WINKLER, S. & SCHMOLL, H. R. 1993. Evidence for Late Holocene Relative Sea-Level Fall from Reconnaissance Stratigraphical Studies in an Area of Earthquake-Subsided Intertidal Deposits, Isla Chiloé, Southern Chile. *Tectonic Controls and Signatures in Sedimentary Successions.*

BASSETT, D. & WATTS, A. B. 2015. Gravity anomalies, crustal structure, and seismicity at subduction zones: 2. Interrelationships between fore-arc structure and seismogenic behavior. *Geochemistry, Geophysics, Geosystems,* 16**,** 1541-1576.

BURRIDGE, R. & KNOPOFF, L. 1967. Model and theoretical seismicity. *Bulletin of the seismological society of america,* 57**,** 341-371.

BECK , M. E., JR., ROJAS, C. & CEMBRANO, J. 1993. On the nature of buttressing in margin-parallel strike-slip fault systems. *Geology,* 21**,** 755-758.

BÉJAR-PIZARRO, M., SOCQUET, A., ARMIJO, R., CARRIZO, D., GENRICH, J., SIMONS, M. 2013. Andean structural control on interseismic coupling in the North Chile subduction zone. *Nature Geosci*, 6, 462–467.

BENIOFF, H., PRESS, F. & SMITH, S. 1961. Excitation of the free oscillations of the Earth by earthquakes. *Journal of Geophysical Research,* 66**,** 605-619.

BENNETT, K. D. 1996. Determination of the number of zones in a biostratigraphical sequence. *New Phytologist,* 132**,** 155-170.

BERTRAND, S., HUGHEN, K. A., LAMY, F., STUUT, J. B., TORREJÓN, F. & LANGE, C. B. 2012. Precipitation as the main driver of Neoglacial fluctuations of Gualas glacier, Northern Patagonian Icefield. *Climate of the Past,* 8**,** 519-534.

BILEK, S. L. 2010. Invited review paper: Seismicity along the South American subduction zone: Review of large earthquakes, tsunamis, and subduction zone complexity. *Tectonophysics,* 495**,** 2-14.

BILEK, S., LAY, T. 2018. Subduction zone megathrust earthquakes. *Geosphere*, 1468–1500.

BIRKS, H. J. B. 1995. Statistical Modelling of Quaternary Science Data. *In:* MADDY, D., BREW, J.S. (ed.) *Statistical modelling of quaternary science data.* Cambridge: Quaternary Research Association.

BIRKS, H. J. B. 1998. Numerical tools in palaeolimnology – Progress, potentialities, and problems. *Journal of Paleolimnology,* 20**,** 307-332.

BIRKS, H. J. B. 2010. Numerical methods for the analysis of diatom assemblage data. *The diatoms: applications for the environmental and earth sciences, 2nd edn. Cambridge University Press, Cambridge***,** 23-54.

BIRKS, H. J. B., LINE, J. M., JUGGINS, S., STEVENSON, A. C. & BRAAK, C. J. F. T. 1990. Diatoms and pH Reconstruction. *Philosophical Transactions of the Royal Society of London. Series B, Biological Sciences,* 327**,** 263-278.

BLAAUW, M. & CHRISTEN, J. A. 2011. Flexible paleoclimate age-depth models using an autoregressive gamma process. *Bayesian Anal.,* 6**,** 457-474.

BLAAUW, M., CHRISTEN, J. A., BENNETT, K. D. & REIMER, P. J. 2018. Double the dates and go for Bayes — Impacts of model choice, dating density and quality on chronologies. *Quaternary Science Reviews,* 188**,** 58-66.

BLAAUW, M., CHRISTEN., J. A., MARCO A. AQUINO-LOPEZ, JUDITH ESQUIVEL-VAZQUEZ, OSCAR M. GONZALEZ V, TED BELDING, JAMES THEILER, BRIAN GOUGH & KARNEY, C. 2020. rplum: Bayesian Age-Depth Modelling of Cores Dated by Pb-210. *https://CRAN.R-project.org/package=rplum*.

BLANPIED, M. L., LOCKNER, D. A. & BYERLEE, J. D. 1991. Fault stability inferred from granite sliding experiments at hydrothermal conditions. *Geophysical Research Letters,* 18**,** 609-612.

BLANPIED, M. L., LOCKNER, D. A. & BYERLEE, J. D. 1995. Frictional slip of granite at hydrothermal conditions. *Journal of Geophysical Research: Solid Earth,* 100**,** 13045-13064.

BLETERY, Q., THOMAS, A. M., REMPEL, A. W., KARLSTROM, L., SLADEN, A. & BARROS, L. D. 2016. Mega-earthquakes rupture flat megathrusts. *Science,* 354**,** 1027-1031.

BOHM, M., LÜTH, S., ECHTLER, H., ASCH, G., BATAILLE, K., BRUHN, C., RIETBROCK, A. & WIGGER, P. 2002. The Southern Andes between 36° and 40°S latitude: seismicity and average seismic velocities. *Tectonophysics,* 356**,** 275-289.

BOOKHAGEN, B., ECHTLER, H. P., MELNICK, D., STRECKER, M. R. & SPENCER, J. Q. G. 2006. Using uplifted Holocene beach berms for paleoseismic analysis on the Santa María Island, south-central Chile. *Geophysical Research Letters,* 33**,** n/a-n/a.

BOX, G. E. 1976. Science and Statistics. *Journal of the American Statistical Association,* 71**,** 791-799.

BRADER, M., GARRETT, E., MELNICK, D. & SHENNAN, I. 2021. Sensitivity of tidal marshes as recorders of major megathrust earthquakes: constraints from the 25 December 2016 Mw 7.6 Chiloé earthquake, Chile. *Journal of Quaternary Science,* 36**,** 991-1002.

BRIGGS, R. W., ENGELHART, S. E., NELSON, A. R., DURA, T., KEMP, A. C., HAEUSSLER, P. J., CORBETT, D. R., ANGSTER, S. J. & BRADLEY, L. A. 2014. Uplift and subsidence reveal a nonpersistent megathrust rupture boundary (Sitkinak Island, Alaska). *Geophysical Research Letters,* 41**,** 2289-2296.

BRONK RAMSEY, C. 2009. Bayesian Analysis of Radiocarbon Dates. *Radiocarbon,* 51**,** 337-360.

BRUEL, R. & SABATIER, P. 2020. serac: an R package for ShortlivEd RAdionuclide chronology of recent sediment cores. *Journal of Environmental Radioactivity,* 225**,** 106449.

BRYANT, E. 2008. *Tsunami: The Underrated Hazard*, Springer-Verlag Berlin Heidelberg.

BURRIDGE, R. & KNOPOFF, L. 1967. Model and theoretical seismicity. *Bulletin of the seismological society of america,* 57**,** 341-371.

BÜRGMANN, R., KOGAN, M. G., STEBLOV, G. M., HILLEY, G., LEVIN, V. E. & APEL, E. 2005. Interseismic coupling and asperity distribution along the Kamchatka subduction zone. *Journal of Geophysical Research: Solid Earth,* 110.

BÜRGMANN, R. & DRESEN, G. 2008. Rheology of the Lower Crust and Upper Mantle: Evidence from Rock Mechanics, Geodesy, and Field Observations. *Annual Review of Earth and Planetary Sciences,* 36**,** 531-567.

CAHILL, N., KEMP, A. C., HORTON, B. P. & PARNELL, A. C. 2015. Modeling sea-level change using errors-in-variables integrated Gaussian processes. *The Annals of Applied Statistics,* 9**,** 547-571, 25.

CAHILL, N., KEMP, A. C., HORTON, B. P. & PARNELL, A. C. 2016. A Bayesian hierarchical model for reconstructing relative sea level: from raw data to rates of change. *Climate of the Past,* 12**,** 525-542.

CAHILL, T. & ISACKS, B. L. 1992. Seismicity and shape of the subducted Nazca Plate. *Journal of Geophysical Research: Solid Earth,* 97**,** 17503-17529.

CALDENIUS, C. C. Z. 1932. Las Glaciaciones Cuaternarias en la Patagonia y Tierra del Fuego: Una investigación regional, estratigráfica y geocronológica.—Una comparación con la escala geocronológica sueca. *Geografiska Annaler,* 14**,** 1-164.

CANDE, S., LESLIE, R., PARRA, J. & HOBART, M. 1987. Interaction between the Chile Ridge and Chile Trench: geophysical and geothermal evidence. *Journal of Geophysical Research: Solid Earth,* 92**,** 495-520.

CANDE, S. C. & LESLIE, R. B. 1986. Late Cenozoic tectonics of the Southern Chile Trench. *Journal of Geophysical Research: Solid Earth,* 91**,** 471-496.

CARVAJAL, M., CISTERNAS, M., GUBLER, A., CATALÁN, P. A., WINCKLER, P. & WESSON, R. L. 2017. Reexamination of the magnitudes for the 1906 and 1922 Chilean earthquakes using Japanese tsunami amplitudes: Implications for source depth constraints. *Journal of Geophysical Research: Solid Earth,* 122**,** 4-17.

CEMBRANO, J., HERVÉ, F. & LAVENU, A. 1996. The Liquiñe Ofqui fault zone: a long-lived intra-arc fault system in southern Chile. *Tectonophysics,* 259**,** 55-66.

CEMBRANO, J., SCHERMER, E., LAVENU, A. & SANHUEZA, A. 2000. Contrasting nature of deformation along an intra-arc shear zone, the Liquiñe–Ofqui fault zone, southern Chilean Andes. *Tectonophysics,* 319**,** 129-149.

CHLIEH, M., MOTHES, P. A., NOCQUET, J. M., JARRIN, P., CHARVIS, P., CISNEROS, D., FONT, Y., COLLOT, J. Y., VILLEGAS-LANZA, J. C., ROLANDONE, F., VALLÉE, M., REGNIER, M., SEGOVIA, M., MARTIN, X. & YEPES, H. 2014. Distribution of discrete seismic asperities and aseismic slip along the Ecuadorian megathrust. *Earth and Planetary Science Letters,* 400**,** 292-301.

CIFUENTES, I. L. 1989. The 1960 Chilean earthquakes. *Journal of Geophysical Research: Solid Earth,* 94**,** 665-680.

CISTERNAS, M., ATWATER, B. F., TORREJON, F., SAWAI, Y., MACHUCA, G., LAGOS, M., EIPERT, A., YOULTON, C., SALGADO, I., KAMATAKI, T., SHISHIKURA, M., RAJENDRAN, C. P., MALIK, J. K., RIZAL, Y. & HUSNI, M. 2005. Predecessors of the giant 1960 Chile earthquake. *Nature,* 437**,** 404 - 407.

CISTERNAS, M., CARVAJAL, M., WESSON, R., ELY, L. L. & GORIGOITIA, N. 2017a. Exploring the Historical Earthquakes Preceding the Giant 1960 Chile Earthquake in a Time-Dependent Seismogenic Zone. *Bulletin of the Seismological Society of America,* 107**,** 2664-2675.

CISTERNAS, M., GARRETT, E., WESSON, R., DURA, T. & ELY, L. L. 2017b. Unusual geologic evidence of coeval seismic shaking and tsunamis shows variability in earthquake size and recurrence in the area of the giant 1960 Chile earthquake. *Marine Geology,* 385**,** 101-113.

CLARK, J. A., FARRELL, W. E. & PELTIER, W. R. 1978. Global changes in postglacial sea level: A numerical calculation. *Quaternary Research,* 9**,** 265-287.

CLARK, P. U., DYKE, A. S., SHAKUN, J. D., CARLSON, A. E., CLARK, J., WOHLFARTH, B., MITROVICA, J. X., HOSTETLER, S. W. & MCCABE, A. M. 2009. The Last Glacial Maximum. *Science,* 325**,** 710.

COMBELLICK, R. 1991. *Paleoseismicity of the Cook Inlet region, Alaska: Evidence from peat stratigraphy in Turnagain and Knik Arms*, State of Alaska, Department of Natural Resources, Division of Geological ….

COMTE, D. & PARDO, M. 1991. *Reappraisal of great historical earthquakes in the Northern Chile and Southern Peru seismic gaps,* Natural Hazard.

CONTRERAS-REYES, E. 2018. Structure and Tectonics of the Chilean Convergent Margin from Wide-Angle Seismic Studies: A Review. *In:* FOLGUERA, A., CONTRERAS-REYES, E., HEREDIA, N., ENCINAS, A., B. IANNELLI, S., OLIVEROS, V., M. DÁVILA, F., COLLO, G., GIAMBIAGI, L., MAKSYMOWICZ, A., IGLESIA LLANOS, M. P., TURIENZO, M., NAIPAUER, M., ORTS, D., D. LITVAK, V., ALVAREZ, O. & ARRIAGADA, C. (eds.) *The Evolution of the Chilean-Argentinean Andes.* Cham: Springer International Publishing.

CONTRERAS-REYES, E. & CARRIZO, D. 2011. Control of high oceanic features and subduction channel on earthquake ruptures along the Chile–Peru subduction zone. *Physics of the Earth and Planetary Interiors,* 186**,** 49-58.

COOPER, S., GAISER, E.E.,WACHNICKA, A., 2010. *The Diatoms: Applications for the Environmental and Earth Sciences,* Cambridge, Cambridge University Press.

CORREA-MORA, F., DEMETS, C., CABRAL-CANO, E., MARQUEZ-AZUA, B. & DIAZ-MOLINA, O. 2008. Interplate coupling and transient slip along the subduction interface beneath Oaxaca, Mexico. *Geophysical Journal International,* 175**,** 269-290.

DAMON, P. E. & SONETT, C. P. 1991. Solar and terrestrial components of the atmospheric 14 C variation spectrum. *The sun in time***,** 360.

DARWIN, C. 1851. *Geological Observations on Coral Reefs, Volcanic Islands and on South America.*

DAVIS, S. N. & KARZULOVÍC, K. 1963. Landslides at Lago Riñihue, Chile. *Bulletin of the Seismological Society of America,* 53**,** 1403-1414.

DEMETS, C., GORDON RICHARD, G. & ARGUS DONALD, F. 2010. Geologically current plate motions. *Geophysical Journal International,* 181**,** 1-80.

DENTON, G. H., HEUSSER, C. J., LOWEL, T. V., MORENO, P. I., ANDERSEN, B. G., HEUSSER, L. E., SCHLÜHTER, C. & MARCHANT, D. R. 1999. Interhemispheric Linkage of Paleoclimate During the Last Glaciation. *Geografiska Annaler: Series A, Physical Geography,* 81**,** 107-153.

DENYS, L. 1991. *A check-list of the diatoms in the Holocene deposits of the western Belgian coastal plain with a survey of their apparent ecological requirements*, Ministerie van Economische Zaken Belgium.

DESIANTI, N., ENACHE, M. D., GRIFFITHS, M., BISKUP, K., DEGEN, A., DASILVA, M., MILLEMANN, D., LIPPINCOTT, L., WATSON, E., GRAY, A., NIKITINA, D. & POTAPOVA, M. 2019. The Potential and Limitations of Diatoms as Environmental Indicators in Mid-Atlantic Coastal Wetlands. *Estuaries and Coasts,* 42**,** 1440-1458.

DEWEY, J. F. & LAMB, S. H. 1992. Active tectonics of the Andes. *Tectonophysics,* 205**,** 79-95.

DIEDERICHS, A., NISSEN, E. K., LAJOIE, L. J., LANGRIDGE, R. M., MALIREDDI, S. R., CLARK, K. J., HAMLING, I. J. & TAGLIASACCHI, A. 2019. Unusual

kinematics of the Papatea fault (2016 Kaikōura earthquake earthquake) suggest anelastic rupture. *Science Advances,* 5**,** eaax5703.

DIGBY, P. G. N. & KEMPTON, R. A. 1987. Ordination. *In:* DIGBY, P. G. N. & KEMPTON, R. A. (eds.) *Multivariate Analysis of Ecological Communities.* Dordrecht: Springer Netherlands.

DITZEL, P. C. J. 2019. *Análisis geomorfológico y estratigráfico de la terraza del Holoceno tardío en la costa valdiviana en el marco de cambios relativos del nivel del mar asociados al ciclo sísmico.* Undergraduate Thesis, Universidad Austral de Chile.

DIXIT, S. S., CUMMING, B. F., BIRKS, H. J. B., SMOL, J. P., KINGSTON, J. C., UUTALA, A. J., CHARLES, D. F. & CAMBURN, K. E. 1993. Diatom assemblages from Adirondack lakes (New York, USA) and the development of inference models for retrospective environmental assessment. *Journal of Paleolimnology,* 8**,** 27-47.

DMOWSKA, R., ZHENG, G. & RICE, J. R. 1996. Seismicity and deformation at convergent margins due to heterogeneous coupling. *Journal of Geophysical Research: Solid Earth,* 101**,** 3015-3029.

DRAGERT, H., HYNDMAN, R. D., ROGERS, G. C. & WANG, K. 1994. Current deformation and the width of the seismogenic zone of the northern Cascadia subduction thrust. *Journal of Geophysical Research: Solid Earth,* 99**,** 653-668.

DURA, T., CISTERNAS, M., HORTON, B. P., ELY, L. L., NELSON, A. R., WESSON, R. L. & PILARCZYK, J. E. 2015. Coastal evidence for Holocene subduction-zone earthquakes and tsunamis in central Chile. *Quaternary Science Reviews,* 113**,** 93-111.

DURA, T., ENGELHART, S. E., VACCHI, M., HORTON, B. P., KOPP, R. E., PELTIER, W. R. & BRADLEY, S. 2016a. The Role of Holocene Relative Sea-Level Change in Preserving Records of Subduction Zone Earthquakes. *Current Climate Change Reports,* 2**,** 86-100.

DURA, T., HEMPHILL-HALEY, E., SAWAI, Y. & HORTON, B. P. 2016b. The application of diatoms to reconstruct the history of subduction zone earthquakes and tsunamis. *Earth-Science Reviews,* 152**,** 181-197.

DURA, T., HORTON, B. P., CISTERNAS, M., ELY, L. L., HONG, I., NELSON, A. R., WESSON, R. L., PILARCZYK, J. E., PARNELL, A. C. & NIKITINA, D. 2017. Subduction zone slip variability during the last millennium, south-central Chile. *Quaternary Science Reviews,* 175**,** 112-137.

DURA, T., RUBIN, C. M., KELSEY, H. M., HORTON, B. P., HAWKES, A., VANE, C. H., DARYONO, M., PRE, C. G., LADINSKY, T. & BRADLEY, S. 2011. Stratigraphic record of Holocene coseismic subsidence, Padang, West Sumatra. *Journal of Geophysical Research: Solid Earth,* 116.

EATON, J. P., RICHTER, D. H. & AULT, W. U. 1961. The tsunami of May 23, 1960, on the Island of Hawaii. *Bulletin of the Seismological Society of America,* 51**,** 135-157.

EGBERT, G. & EROFEEVA, S. 2010. The OSU TOPEX/Poseidon Global Inverse Solution TPXO. *Oregon State University*.

EGBERT, G. D. & EROFEEVA, S. Y. 2002. Efficient inverse modeling of barotropic ocean tides. *Journal of Atmospheric and Oceanic technology,* 19**,** 183-204.

ELY, L. L., CISTERNAS, M., WESSON, R. L. & DURA, T. 2014. Five centuries of tsunamis and land-level changes in the overlapping rupture area of the 1960 and 2010 Chilean earthquakes. *Geology,* 42**,** 995-998.

ENGDAHL, E. R. & VILLASENOR, A. 2002. Global seismicity: 1900-1999. *International handbook of earthquake and engineering seismology***,** 665-690.

ENGEL, M. & BRÜCKNER, H. 2011. *The identification of palaeo-tsunami deposits—A major challenge in coastal sedimentary research*.

ENGELHART, S. E., HORTON, B. P., NELSON, A. R., HAWKES, A. D., WITTER, R. C., WANG, K., WANG, P. L. & VANE, C. H. 2013a. Testing the use of microfossils to reconstruct great earthquakes at Cascadia. *Geology,* 41**,** 1067-1070.

ENGELHART, S. E., HORTON, B. P., VANE, C. H., NELSON, A. R., WITTER, R. C., BRODY, S. R. & HAWKES, A. D. 2013b. Modern foraminifera, δ13C, and bulk geochemistry of central Oregon tidal marshes and their application in paleoseismology. *Palaeogeography, Palaeoclimatology, Palaeoecology,* 377**,** 13-27.

FAN, J. & ZHAO, D. 2021. Subslab heterogeneity and giant megathrust earthquakes. *Nature Geoscience,* 14**,** 349-353.

FARRELL, W. E. & CLARK, J. A. 1976. On Postglacial Sea Level. *Geophysical Journal of the Royal Astronomical Society,* 46**,** 647-667.

FARÍAS, M., COMTE, D., ROECKER, S., CARRIZO, D. & PARDO, M. 2011. Crustal extensional faulting triggered by the 2010 Chilean earthquake: The Pichilemu Seismic Sequence. Tectonics, 30.

FLEMING, K., JOHNSTON, P., ZWARTZ, D., YOKOYAMA, Y., LAMBECK, K. & CHAPPELL, J. 1998. Refining the eustatic sea-level curve since the Last Glacial Maximum using far- and intermediate-field sites. *Earth and Planetary Science Letters,* 163**,** 327-342.

FREDERIKSE, T., LANDERER, F., CARON, L., ADHIKARI, S., PARKES, D., HUMPHREY, V. W., DANGENDORF, S., HOGARTH, P., ZANNA, L., CHENG, L. & WU, Y.-H. 2020. The causes of sea-level rise since 1900. *Nature,* 584**,** 393-397.

FUENZALIDA, H., V., COOKE, R., PASKOFF, R., SEGERSTROM, K., WEISCHET, W., WRIGHT, H. E., JR. & FREY, D. G. 1965. High Stands of Quaternary Sea Level Along the Chilean Coast. *International Studies on the Quaternary: Papers Prepared on the Occasion of the VII Congress of the International Association for Quaternary Research Boulder, Colorado, 1965.* Geological Society of America.

GAMERMAN, D. & LOPES, H. F. 2006. *Markov chain Monte Carlo: stochastic simulation for Bayesian inference*, CRC press.

GARCÍA, J. L. 2012. Late Pleistocene ice fluctuations and glacial geomorphology of the Archipiélago de Chiloé, southern Chile. *Geografiska Annaler: series a, physical geography,* 94**,** 459-479.

GARRETT, E., MELNICK, D., DURA, T., CISTERNAS, M., ELY, L. L., WESSON, R. L., JARA-MUÑOZ, J. & WHITEHOUSE, P. L. 2020. Holocene relative sea-level change along the tectonically active Chilean coast. *Quaternary Science Reviews,* 236**,** 106281.

GARRETT, E., SHENNAN, I., WATCHAM, E. P. & WOODROFFE, S. A. 2013. Reconstructing paleoseismic deformation, 1: modern analogues from the 1960 and 2010 Chilean great earthquakes. *Quaternary Science Reviews,* 75**,** 11-21.

GARRETT, E., SHENNAN, I., WOODROFFE, S. A., CISTERNAS, M., HOCKING, E. P. & GULLIVER, P. 2015. Reconstructing paleoseismic deformation, 2: 1000 years of great earthquakes at Chucalén, south central Chile. *Quaternary Science Reviews,* 113**,** 112-122.

GAUCH, H. G. 1982. Ordination. *In:* GAUCH, H. G. (ed.) *Multivariate Analysis in Community Ecology.* Cambridge: Cambridge University Press.

GEHRELS, W. R., ROE, H. M. & CHARMAN, D. J. 2001. Foraminifera, testate amoebae and diatoms as sea-level indicators in UK saltmarshes: a quantitative multiproxy approach. *Journal of Quaternary Science,* 16**,** 201-220.

GILKS, W. R., RICHARDSON, S. & SPIEGELHALTER, D. 1996. *Markov Chain Monte Carlo in Practice,* London, CRC press.

GLASSER, N. F., HARRISON, S., JANSSON, K. N., ANDERSON, K. & COWLEY, A. 2011. Global sea-level contribution from the Patagonian Icefields since the Little Ice Age maximum. *Nature Geoscience,* 4**,** 303-307.

GLASSER, N. F., HARRISON, S., WINCHESTER, V. & ANIYA, M. 2004. Late Pleistocene and Holocene palaeoclimate and glacier fluctuations in Patagonia. *Global and planetary change,* 43**,** 79-101.

GLASSER, N. F., JANSSON, K. N., HARRISON, S. & KLEMAN, J. 2008. The glacial geomorphology and Pleistocene history of South America between 38°S and 56°S. *Quaternary Science Reviews,* 27**,** 365-390.

GLODNY, J., ECHTLER, H., FIGUEROA, O., FRANZ, G., GRÄFE, K., KEMNITZ, H., KRAMER, W., KRAWCZYK, C., LOHRMANN, J., LUCASSEN, F., MELNICK, D., ROSENAU, M. & SEIFERT, W. 2006. Long-Term Geological Evolution and Mass-Flow Balance of the South-Central Andes. *In:* ONCKEN, O., CHONG, G., FRANZ, G., GIESE, P., GÖTZE, H.-J., RAMOS, V. A., STRECKER, M. R. & WIGGER, P. (eds.) *The Andes: Active Subduction Orogeny.* Berlin, Heidelberg: Springer Berlin Heidelberg.

GRAND PRE, C. A., HORTON, B. P., KELSEY, H. M., RUBIN, C. M., HAWKES, A. D., DARYONO, M. R., ROSENBERG, G. & CULVER, S. J. 2012. Stratigraphic evidence for an early Holocene earthquake in Aceh, Indonesia. *Quaternary Science Reviews,* 54**,** 142-151.

GRIMM, E. C. 1987. CONISS: a FORTRAN 77 program for stratigraphically constrained cluster analysis by the method of incremental sum of squares. *Computers & Geosciences,* 13**,** 13-35.

GUTSCHER, M.-A. 2002. Andean subduction styles and their effect on thermal structure and interplate coupling. *Journal of South American Earth Sciences,* 15**,** 3-10.

GUTSCHER, M.-A., SPAKMAN, W., BIJWAARD, H. & ENGDAHL, E. R. 2000. Geodynamics of flat subduction: Seismicity and tomographic constraints from the Andean margin. *Tectonics,* 19**,** 814-833.

GONZÁLEZ, G., SALAZAR, P., LOVELESS, J. P., ALLMENDINGER, R. W., ARON, F. & SHRIVASTAVA, M. 2015. Upper plate reverse fault reactivation and the unclamping of the megathrust during the 2014 northern Chile earthquake sequence. Geology, 43, 671-674.

HABERLAND, C., RIETBROCK, A., LANGE, D., BATAILLE, K. & HOFMANN, S. 2006. Interaction between forearc and oceanic plate at the south-central Chilean margin as seen in local seismic data. *Geophysical Research Letters,* 33.

HAMILTON, S. & SHENNAN, I. 2005. Late Holocene relative sea-level changes and the earthquake deformation cycle around upper Cook Inlet, Alaska. *Quaternary Science Reviews,* 24**,** 1479-1498.

HAMILTON, S., SHENNAN, I., COMBELLICK, R., MULHOLLAND, J. & NOBLE, C. 2005. Evidence for two great earthquakes at Anchorage, Alaska and implications for multiple great earthquakes through the Holocene. *Quaternary Science Reviews,* 24**,** 2050-2068.

HAMLING IAN, J., HREINSDÓTTIR, S., CLARK, K., ELLIOTT, J., LIANG, C., FIELDING, E., LITCHFIELD, N., VILLAMOR, P., WALLACE, L., WRIGHT TIM, J., D'ANASTASIO, E., BANNISTER, S., BURBIDGE, D., DENYS, P., GENTLE, P., HOWARTH, J., MUELLER, C., PALMER, N., PEARSON, C., POWER, W., BARNES, P., BARRELL DAVID, J. A., VAN DISSEN, R., LANGRIDGE, R., LITTLE, T., NICOL, A., PETTINGA, J., ROWLAND, J. & STIRLING, M. 2017. Complex multifault rupture during the 2016 Mw 7.8 Kaikōura earthquake, New Zealand. *Science,* 356**,** eaam7194.

HANKS, T. C. & KANAMORI, H. 1979. A moment magnitude scale. *Journal of Geophysical Research: Solid Earth,* 84**,** 2348-2350.

HARFF, J. 2016. Relative Sea-Level (RSL) Cycle. *In:* HARFF, J., MESCHEDE, M., PETERSEN, S. & THIEDE, J. (eds.) *Encyclopedia of Marine Geosciences.* Dordrecht: Springer Netherlands.

HASSAN, G. S., TIETZE, E. & DE FRANCESCO, C. G. 2009. Modern diatom assemblages in surface sediments from shallow lakes and streams in southern Pampas (Argentina). *Aquatic Sciences,* 71**,** 487-499.

HASTINGS, W. K. 1970. Monte Carlo sampling methods using Markov chains and their applications. *Biometrika,* 57**,** 97-109.

HAUER, M. E., FUSSELL, E., MUELLER, V., BURKETT, M., CALL, M., ABEL, K., MCLEMAN, R. & WRATHALL, D. 2020. Sea-level rise and human migration. *Nature Reviews Earth & Environment,* 1**,** 28-39.

HAWKES, A. D., HORTON, B. P., NELSON, A. R., VANE, C. H. & SAWAI, Y. 2011. Coastal subsidence in Oregon, USA, during the giant Cascadia earthquake of AD 1700. *Quaternary Science Reviews,* 30**,** 364-376.

HAYES, G. P., MEYERS, E. K., DEWEY, J. W., BRIGGS, R. W., EARLE, P. S., BENZ, H. M., SMOCZYK, G. M., FLAMME, H. E., BARNHART, W. D., GOLD, R. D. & FURLONG, K. P. 2017. Tectonic summaries of magnitude 7 and greater earthquakes from 2000 to 2015. *Open-File Report.* Reston, VA.

HAYWARD, B. W., COCHRAN, U., SOUTHALL, K., WIGGINS, E., GRENFELL, H. R., SABAA, A., SHANE, P. R. & GEHRELS, R. 2004. Micropalaeontological evidence for the Holocene earthquake history of the eastern Bay of Plenty, New Zealand, and a new index for determining the land elevation record. *Quaternary Science Reviews,* 23**,** 1651-1667.

HAYWARD, B. W., GRENFELL, H. R., SABAA, A. T., CARTER, R., COCHRAN, U., LIPPS, J. H., SHANE, P. R. & MORLEY, M. S. 2006. Micropaleontological evidence of large earthquakes in the past 7200 years in southern Hawke's Bay, New Zealand. *Quaternary Science Reviews,* 25**,** 1186-1207.

HEMPHILL-HALEY, E. 1993. *Taxonomy of recent and fossil (Holocene) diatoms (Bacillariophyta) from northern Willapa Bay, Washington [microform] / by Eileen Hemphill-Haley,* Menlo Park, CA : [Denver, Colo, U.S. Dept. of the Interior, U.S. Geological Survey ; Books and Open-File Reports Section, distributor.

HEMPHILL-HALEY, E. 1996. Diatoms as an aid in identifying late-Holocene tsunami deposits. *The Holocene,* 6**,** 439-448.

HERRENDÖRFER, R., VAN DINTHER, Y., GERYA, T. & DALGUER, L. A. 2015. Earthquake supercycle in subduction zones controlled by the width of the seismogenic zone. *Nature Geoscience,* 8**,** 471-474.

HERRON, E. M., CANDE, S. C., HALL, B. R., KULM, L. V. D., DYMOND, J., DASCH, E. J., HUSSONG, D. M. & RODERICK, R. 1981. An active spreading center collides with a subduction zone: A geophysical survey of the Chile Margin triple junction. *Nazca Plate: Crustal Formation and Andean Convergence.* Geological Society of America.

HERVÉ, F. 1994. The Southern Andes Between 39° and 44°S Latitude: The Geological Signature of a Transpressive Tectonic Regime Related to a Magmatic Arc. *In:* REUTTER, K.-J., SCHEUBER, E. & WIGGER, P. J. (eds.) *Tectonics of the Southern Central Andes: Structure and Evolution of an Active Continental Margin.* Berlin, Heidelberg: Springer Berlin Heidelberg.

HERVÉ, F., MUNIZAGA, F., PARADA, M. A., BROOK, M., PANKHURST, R. J., SNELLING, N. J. & DRAKE, R. 1988. Granitoids of the Coast Range of central Chile: geochronology and geologic setting. *Journal of South American Earth Sciences,* 1**,** 185-194.

HERVÉ, F. & OTA, Y. 1993. Fast Holocene uplift rates at the Andes of Chiloé, southern Chile. *Andean Geology,* 20**,** 15-23.

HEUSSER, C. J. & FLINT, R. F. 1977. Quaternary glaciations and environments of northern Isla Chiloé, Chile. *Geology,* 5**,** 305-308.

HEUSSER, C. J. & STREETER, S. S. 1980. A temperature and precipitation record of the past 16,000 years in southern Chile. *Science,* 210**,** 1345-1347.

HILL, M. O. & GAUCH, H. G. 1980. Detrended correspondence analysis: An improved ordination technique. *Vegetatio,* 42**,** 47-58.

HIJMA, M. P., ENGELHART, S. E., TÖRNQVIST, T. E., HORTON, B. P., HU, P. & HILL, D. F. 2015. A protocol for a geological sea-level database. Handbook of Sea-Level Research.

HO, T., C., SATAKE, K., WATADA, S. & FUJII, Y. 2019. Source Estimate for the 1960 Chile Earthquake From Joint Inversion of Geodetic and Transoceanic Tsunami Data. *Journal of Geophysical Research: Solid Earth,* 124**,** 2812-2828.

HOCKING, E., GARRETT, E., AEDO, D., D., C. & MELNICK, D. 2021. Geological evidence of an unreported historical Chilean tsunami reveals more frequent inundation. *Communications Earth & Environment,* 2.

HOCKING, E. P., GARRETT, E. & CISTERNAS, M. 2017. Modern diatom assemblages from Chilean tidal marshes and their application for quantifying deformation during past great earthquakes. *Journal of Quaternary Science,* 32**,** 396-415.

HOGG, A. G., HEATON, T. J., HUA, Q., PALMER, J. G., TURNEY, C. S. M., SOUTHON, J., BAYLISS, A., BLACKWELL, P. G., BOSWIJK, G., BRONK RAMSEY, C., PEARSON, C., PETCHEY, F., REIMER, P., REIMER, R. & WACKER, L. 2020. SHCal20 Southern Hemisphere Calibration, 0–55,000 Years cal BP. *Radiocarbon,* 62**,** 759-778.

HOLDEN, P. B., BIRKS, H. J. B., BROOKS, S. J., BUSH, M. B., HWANG, G. M., MATTHEWS-BIRD, F., VALENCIA, B. G. & VAN WOESIK, R. 2017. BUMPER v1.0: a Bayesian user-friendly model for palaeo-environmental reconstruction. *Geosci. Model Dev.,* 10**,** 483-498.

HOLLIN, J. & SCHILLING, D. 1981. Late Wisconsin-Weichselian mountain glaciers and small ice caps. *In:* HUGHES, G. H. D. A. T. J. (ed.) *The last great ice sheets.* New York: Wiley.

HOLGATE, S.J., MATTHEWS, A., WOODWORTH, P.L., RICKARDS, L.J., TAMISIEA, M.E., BRADSHAW, E., FODEN, P.R., GORDON, K.M., JEVREJEVA, S. AND PUGH, J., 2013. New data systems and products at the permanent service for mean sea level. *Journal of Coastal Research*, 29, 493-504.

HONG, I., DURA, T., ELY, L. L., HORTON, B. P., NELSON, A. R., CISTERNAS, M., NIKITINA, D. & WESSON, R. L. 2017. A 600-year-long stratigraphic record of tsunamis in south-central Chile. *The Holocene,* 27**,** 39-51.

HONG, I., HORTON, B. P., HAWKES, A. D., O'DONNELL, R. J., PADGETT, J. S., DURA, T. & ENGELHART, S. E. 2021. Diatoms of the intertidal environments of Willapa Bay, Washington, USA as a sea-level indicator. *Marine Micropaleontology*, 102033.

HORTON, B. 1999. The distribution of contemporary intertidal foraminifera at Cowpen Marsh, Tees Estuary, UK: implications for studies of Holocene sea-level changes. *Palaeogeography, Palaeoclimatology, Palaeoecology,* 149, 127-149.

HORTON, B. P., CORBETT, R., CULVER, S. J., EDWARDS, R. J. & HILLIER, C. 2006. Modern saltmarsh diatom distributions of the Outer Banks, North Carolina, and the development of a transfer function for high resolution reconstructions of sea level. *Estuarine, Coastal and Shelf Science,* 69, 381-394.

HORTON, B. P. & EDWARDS, R. J. 2005. The application of local and regional transfer functions to the reconstruction of Holocene sea levels, north Norfolk, England. *The Holocene,* 15, 216-228.

HORTON, B. P. & EDWARDS, R. J. 2006. Quantifying Holocene sea level change using intertidal foraminifera: lessons from the British Isles. *Departmental Papers (EES)*, 50.

HORTON, B. P., EDWARDS, R. J., LLOYD, J. M., SHENNAN, I. & ANDREWS, J. 2000. Implications of a microfossil-based transfer function in Holocene sea-level studies. *Holocene Land–Ocean Interaction and Environmental Change around the North Sea.* Geological Society of London.

HORTON, B. P., ENGELHART, S. E., KEMP, A. C. & SAWAI, Y. 2013. 14.25 Microfossils in Tidal Settings as Indicators of Sea-Level Change, Paleoearthquakes, Tsunamis, and Tropical Cyclones. *In:* SHRODER, J. F. (ed.) *Treatise on Geomorphology.* San Diego: Academic Press.

HORTON, B. P., SAWAI, Y., HAWKES, A. D. & WITTER, R. C. 2011. Sedimentology and paleontology of a tsunami deposit accompanying the great Chilean earthquake of February 2010. *Marine Micropaleontology,* 79, 132-138.

HU, Y., WANG, K., HE, J., KLOTZ, J. & KHAZARADZE, G. 2004. Three-dimensional viscoelastic finite element model for postseismic deformation of the great 1960 Chile earthquake. *Journal of Geophysical Research: Solid Earth,* 109.

HUA, Q. 2009. Radiocarbon: A chronological tool for the recent past. *Quaternary Geochronology,* 4, 378-390.

HUA, Q., BARBETTI, M. & RAKOWSKI, A. Z. 2013. Atmospheric radiocarbon for the period 1950–2010. *Radiocarbon,* 55, 2059-2072.

HÜBENER, T., DREßLER, M., SCHWARZ, A., LANGNER, K. & ADLER, S. 2008. Dynamic adjustment of training sets (‘moving-window’ reconstruction) by using transfer functions in paleolimnology—a new approach. *Journal of Paleolimnology,* 40, 79-95.

HUGHEN, K., LEHMAN, S., SOUTHON, J., OVERPECK, J., MARCHAL, O., HERRING, C. & TURNBULL, J. 2004. 14C activity and global carbon cycle changes over the past 50,000 years. *Science,* 303**,** 202-207.

HULTON, N. R. J., PURVES, R. S., MCCULLOCH, R. D., SUGDEN, D. E. & BENTLEY, M. J. 2002. The last glacial maximum and deglaciation in southern South America. *Quaternary Science Reviews,* 21**,** 233-241.

HYNDMAN, R. D. 2013. Downdip landward limit of Cascadia great earthquake rupture. *Journal of Geophysical Research: Solid Earth,* 118**,** 5530-5549.

HYNDMAN, R. D. & WANG, K. 1993. Thermal constraints on the zone of major thrust earthquake failure: The Cascadia Subduction Zone. *Journal of Geophysical Research: Solid Earth,* 98**,** 2039-2060.

HYNDMAN, R. D., YAMANO, M. & OLESKEVICH, D. A. 1997. The seismogenic zone of subduction thrust faults. *Island Arc,* 6**,** 244-260.

IMBRIE, J. & KIPP, N. G. 1971. A new micropaleontological method for quantitative paleoclimatology: application to a late Pleistocene Caribbean core. *The late Cenozoic glacial ages***,** 71-181.

IMBRIE, J. & WEBB, T. 1981. Transfer Functions: Calibrating Micropaleontological Data in Climatic Terms. *In:* BERGER, A. (ed.) *Climatic Variations and Variability: Facts and Theories: NATO Advanced Study Institute First Course of the International School of Climatology, Ettore Majorana Center for Scientific Culture, Erice, Italy, March 9–21, 1980.* Dordrecht: Springer Netherlands.

JACKSON, S. T. & WILLIAMS, J. W. 2004. Modern Analogs in Quaternary Paleoecology: Here Today, Gone Yesterday, Gone Tomorrow? *Annual Review of Earth and Planetary Sciences,* 32**,** 495-537.

JONGMAN, R. H. G., BRAAK, C. J. F. T. & TONGEREN, O. F. R. V. 1995. *Data Analysis in Community and Landscape Ecology,* Cambridge, Cambridge University Press.

JUGGINS, S. 1992. Diatoms in the Thames estuary, England.

JUGGINS, S. 2013. Quantitative reconstructions in palaeolimnology: new paradigm or sick science? *Quaternary Science Reviews,* 64**,** 20-32.

JUGGINS, S. 2020. rioja: Analysis of Quaternary Science Data, R package version (0.9-26). *http://cran.r-project.org/package=rioja*.

JUGGINS, S. & BIRKS, H. J. B. 2012. Quantitative Environmental Reconstructions from Biological Data. *In:* BIRKS, H. J. B., LOTTER, A. F., JUGGINS, S. & SMOL, J. P. (eds.) *Tracking Environmental Change Using Lake Sediments: Data Handling and Numerical Techniques.* Dordrecht: Springer Netherlands.

KAIZUKA, S., MATSUDA, T., NOGAMI, M. & YONEKURA, N. 1973. Quaternary tectonics and recent seismic crustal movements in the Arauco Peninsula and its environs, central Chile. *Geographical Reports Tokyo Metropolitan University,* 8**,** 1-49.

KANAMORI, H. 1977. The energy release in great earthquakes. *Journal of Geophysical Research (1896-1977),* 82**,** 2981-2987.

KANAMORI, H. 2008. Earthquake physicsand real-time seismology. *Nature*, 451, 271-273.

KELLEHER, J. & MCCANN, W. 1976. Buoyant zones, great earthquakes, and unstable boundaries of subduction. *Journal of Geophysical Research (1896-1977),* 81**,** 4885-4896.

KELLEHER, J. A. 1972. Rupture zones of large South American earthquakes and some predictions. *Journal of Geophysical Research,* 77**,** 2087-2103.

KEMP, A. C., HORTON, B. P., DONNELLY, J. P., MANN, M. E., VERMEER, M. & RAHMSTORF, S. 2011. Climate related sea-level variations over the past two millennia. *Proceedings of the National Academy of Sciences,* 108**,** 11017.

KEMP, A. C. & TELFORD, R. J. 2015. Transfer functions. *In:* I. SHENNAN, A. J. L. A. B. P. H. (ed.) *Handbook of Sea-Level Research.*

KEMP, A. C., TELFORD, R. J., HORTON, B. P., ANISFELD, S. C. & SOMMERFIELD, C. K. 2013. Reconstructing Holocene sea level using salt-marsh foraminifera and transfer functions: lessons from New Jersey, USA. *Journal of Quaternary Science,* 28**,** 617-629.

KEMP, A. C., VANE, C. H., HORTON, B. P. & CULVER, S. J. 2010. Stable carbon isotopes as potential sea-level indicators in salt marshes, North Carolina, USA. *The Holocene,* 20**,** 623-636.

KEMP, A. C., VANE, C. H., HORTON, B. P., ENGELHART, S. E. & NIKITINA, D. 2012. Application of stable carbon isotopes for reconstructing salt-marsh floral zones and relative sea level, New Jersey, USA. *Journal of Quaternary Science,* 27**,** 404-414.

KEMPF, P., MOERNAUT, J., VAN DAELE, M., VANDOORNE, W., PINO, M., URRUTIA, R. & DE BATIST, M. 2017. Coastal lake sediments reveal 5500 years of tsunami history in south central Chile. *Quaternary Science Reviews,* 161**,** 99-116.

KEMPF, P., MOERNAUT, J., VAN DAELE, M., VERMASSEN, F., VANDOORNE, W., PINO, M., URRUTÍA, R., SCHMIDT, S., GARRETT, E. & DE BATIST, M. 2015. The sedimentary record of the 1960 tsunami in two coastal lakes on Isla de Chiloé, south central Chile. *Sedimentary Geology,* 328**,** 73-86.

KHAN, N. S., ASHE, E., SHAW, T. A., VACCHI, M., WALKER, J., PELTIER, W. R., KOPP, R. E. & HORTON, B. P. 2015. Holocene Relative Sea-Level Changes from Near-, Intermediate-, and Far-Field Locations. *Current Climate Change Reports,* 1**,** 247-262.

KHAN, N. S., HORTON, B. P., ENGELHART, S., ROVERE, A., VACCHI, M., ASHE, E. L., TÖRNQVIST, T. E., DUTTON, A., HIJMA, M. P. & SHENNAN, I. 2019. Inception of a global atlas of sea levels since the Last Glacial Maximum. *Quaternary Science Reviews,* 220**,** 359-371.

KHAZARADZE, G. & KLOTZ, J. 2003. Short- and long-term effects of GPS measured crustal deformation rates along the south central Andes. *Journal of Geophysical Research: Solid Earth (1978–2012),* 108.

KLEIN, E., FLEITOUT, L., VIGNY, C. & GARAUD, J. D. 2016. Afterslip and viscoelastic relaxation model inferred from the large-scale post-seismic deformation following the 2010 Mw 8.8 Maule earthquake (Chile). Geophysical Journal International, 205, 1455-1472.

KLOTZ, J., KHAZARADZE, G., ANGERMANN, D., REIGBER, C., PERDOMO, R. & CIFUENTES, O. 2001. Earthquake cycle dominates contemporary crustal deformation in Central and Southern Andes. *Earth and Planetary Science Letters,* 193**,** 437-446.

KOPP, H. 2013. Invited review paper: The control of subduction zone structural complexity and geometry on margin segmentation and seismicity. *Tectonophysics,* 589**,** 1-16.

KOMURA, K., AIYAMA, K., NAGATA, T., SATO, H. P., YAMADA, A. & AOYAGI, Y. 2019. Surface rupture and characteristics of a fault associated with the 2011 and 2016 earthquakes in the southern Abukuma Mountains, northeastern Japan, triggered by the Tohoku-Oki earthquake. *Earth, Planets and Space*, 71, 1-23.

KRUSCHKE, J. 2014. Doing Bayesian data analysis: A tutorial with R, JAGS, and Stan.

LAMBECK, K., ESAT, T. M. & POTTER, E.-K. 2002a. Links between climate and sea levels for the past three million years. *Nature,* 419**,** 199-206.

LAMBECK, K., SMITHER, C. & JOHNSTON, P. 1998. Sea-level change, glacial rebound and mantle viscosity fornorthern Europe. *Geophysical Journal International,* 134**,** 102-144.

LAMBECK, K., YOKOYAMA, Y. & PURCELL, T. 2002b. Into and out of the Last Glacial Maximum: sea-level change during Oxygen Isotope Stages 3 and 2. *Quaternary Science Reviews,* 21**,** 343-360.

LANGE, D., RIETBROCK, A., HABERLAND, C., BATAILLE, K., DAHM, T., TILMANN, F. & FLÜH, E. R. 2007. Seismicity and geometry of the south Chilean subduction zone (41.5°S–43.5°S): Implications for controlling parameters. *Geophysical Research Letters,* 34.

LAY, T., KANAMORI, H., AMMON, C. J., KOPER, K. D., HUTKO, A. R., YE, L., YUE, H. & RUSHING, T. M. 2012. Depth-varying rupture properties of subduction zone megathrust faults. *Journal of Geophysical Research: Solid Earth,* 117.

LE PICHON, X. 1968. Sea-floor spreading and continental drift. *Journal of Geophysical Research (1896-1977),* 73**,** 3661-3697.

LEGENDRE, P. & BIRKS, H. J. B. 2012. From Classical to Canonical Ordination. *In:* BIRKS, H. J. B., LOTTER, A. F., JUGGINS, S. & SMOL, J. P. (eds.) *Tracking Environmental Change Using Lake Sediments: Data Handling and Numerical Techniques.* Dordrecht: Springer Netherlands.

LEGENDRE, P. & LEGENDRE, L. 1998. *Numerical Ecology,* Amsterdam, Elsevier.

LEGENDRE, P. & LEGENDRE, L. 2012. *Numerical Ecology,* Amsterdam, Elsevier.

LEONARD, L. J., CURRIE, C. A., MAZZOTTI, S. & HYNDMAN, R. D. 2010. Rupture area and displacement of past Cascadia great earthquakes from coastal coseismic subsidence. *GSA Bulletin,* 122**,** 2079-2096.

LEONARD, L. J., HYNDMAN, R. D. & MAZZOTTI, S. 2004. Coseismic subsidence in the 1700 great Cascadia earthquake: Coastal estimates versus elastic dislocation models. *Geological Society of America Bulletin,* 116**,** 655-670.

LEORRI, E., HORTON, B. P. & CEARRETA, A. 2008. Development of a foraminifera-based transfer function in the Basque marshes, N. Spain: Implications for sea-level studies in the Bay of Biscay. *Marine Geology,* 251**,** 60-74.

LEPŠ, J. & ŠMILAUER, P. 2003. *Multivariate Analysis of Ecological Data using CANOCO,* Cambridge, Cambridge University Press.

LIBBY, W. F. 1952. Radiocarbon Dating. *University of Chicago Press.* Chicago.

LIU, X. & ZHAO, D. 2018. Upper and lower plate controls on the great 2011 Tohoku-oki earthquake. *Science advances,* 4**,** eaat4396.

LOMNITZ, C. 1970. Major earthquakes and tsunamis in Chile during the period 1535 to 1955. *Geologische Rundschau,* 59**,** 938-960.

LOMNITZ, C. 2004. Major Earthquakes of Chile: A Historical Survey, 1535-1960. *Seismological Research Letters,* 75**,** 368-378.

LONG, A. J. & SHENNAN, I. 1994. Sea-level changes in Washington and Oregon and the "earthquake deformation cycle'. *Journal of Coastal Research,* 10**,** 825-838.

LONG, A. J., WALLER, M. P. & STUPPLES, P. 2006. Driving mechanisms of coastal change: Peat compaction and the destruction of late Holocene coastal wetlands. *Marine Geology,* 225**,** 63-84.

LOVELESS, J. P., ALLMENDINGER, R. W., PRITCHARD, M. E. & GONZÁLEZ, G. 2010. Normal and reverse faulting driven by the subduction zone earthquake cycle in the northern Chilean fore arc. *Tectonics*, 29.

LOVELESS, J. P. & PRITCHARD, M. E. 2008. Motion on upper-plate faults during subduction zone earthquakes: Case of the Atacama Fault System, northern Chile. *Geochemistry, Geophysics, Geosystems*, 9.

MALDONADO, V., CONTRERAS, M. & MELNICK, D. 2021. A comprehensive database of active and potentially-active continental faults in Chile at 1:25,000 scale. *Scientific Data*, 8, 20.

MARCHETTO, A. 1994. Rescaling species optima estimated by weighted averaging. *Journal of Paleolimnology,* 12**,** 155-162.

MARONE, C. 1998. LABORATORY-DERIVED FRICTION LAWS AND THEIR APPLICATION TO SEISMIC FAULTING. *Annual Review of Earth and Planetary Sciences,* 26**,** 643-696.

MCCAFFREY, R. 1992. Oblique plate convergence, slip vectors, and forearc deformation. *Journal of Geophysical Research: Solid Earth,* 97**,** 8905-8915.

MCCALPIN, J. 2009. *Paleoseismology,* Amsterdam: Elsevier, Academic Press.

MCCALPIN, J. P. & CARVER, G. A. 2009. Chapter 5 Paleoseismology of Compressional Tectonic Environments. *International Geophysics.* Academic Press.

MCCORMAC, F. G., HOGG, A. G., BLACKWELL, P. G., BUCK, C. E., HIGHAM, T. F. G. & REIMER, P. J. 2004. Shcal04 Southern Hemisphere Calibration, 0–11.0 Cal Kyr BP. *Radiocarbon,* 46**,** 1087-1092.

MCCULLOCH, R. D., BENTLEY, M. J., PURVES, R. S., HULTON, N. R. J., SUGDEN, D. E. & CLAPPERTON, C. M. 2000. Climatic inferences from glacial and palaeoecological evidence at the last glacial termination, southern South America. *Journal of Quaternary Science,* 15**,** 409-417.

MCELREATH, R. 2020. *Statistical rethinking: A Bayesian course with examples in R and Stan*, Chapman and Hall/CRC.

MCKENZIE, D. P. 1966. The viscosity of the lower mantle. *Journal of Geophysical Research (1896-1977),* 71**,** 3995-4010.

MCKENZIE, D. P. 1969. Speculations on the Consequences and Causes of Plate Motions*. *Geophysical Journal of the Royal Astronomical Society,* 18**,** 1-32.

MELNICK, D., BOOKHAGEN, B., STRECKER, M. R. & ECHTLER, H. P. 2009. Segmentation of megathrust rupture zones from fore-arc deformation patterns over hundreds to millions of years, Arauco peninsula, Chile. *Journal of Geophysical Research: Solid Earth,* 114.

MELNICK, D., LI, S., MORENO, M., CISTERNAS, M., JARA-MUÑOZ, J., WESSON, R., NELSON, A., BÁEZ, J. C. & DENG, Z. 2018. Back to full interseismic plate locking decades after the giant 1960 Chile earthquake. Nature Communications, 9, 3527.MERCER, J. H. 1970. Variations of some Patagonian glaciers since the Late-Glacial; II. *American Journal of Science,* 269**,** 1-25.

MERRON, E. M. & HAYES, D. E. 1969. A geophysical study of the Chile Ridge. *Earth and Planetary Science Letters,* 6**,** 77-83.

MÉTOIS, M., SOCQUET, A. & VIGNY, C. 2012. Interseismic coupling, segmentation and mechanical behavior of the central Chile subduction zone. *Journal of Geophysical Research: Solid Earth (1978–2012),* 117.

METROPOLIS, N. & ULAM, S. 1949. The Monte Carlo Method. *Journal of the American Statistical Association*, 44, 335-341.

METROPOLIS, N., ROSENBLUTH, A. W., ROSENBLUTH, M. N., TELLER, A. H. & TELLER, E. 1953. Equation of state calculations by fast computing machines. *The journal of chemical physics,* 21**,** 1087-1092.

MILKER, Y., DURA, T. & HORTON, B. P. 2022. The response of foraminifera to rapid sea-level rise from tidal restoration of Ni-les'tun marsh, Oregon, U.S.A. *Marine Geology,* 445**,** 106757.

MILNE, G. A., LONG, A. J. & BASSETT, S. E. 2005. Modelling Holocene relative sea-level observations from the Caribbean and South America. *Quaternary Science Reviews,* 24**,** 1183-1202.

MILNE, G. A., MITROVICA, J. X. & SCHRAG, D. P. 2002. Estimating past continental ice volume from sea-level data. *Quaternary Science Reviews,* 21**,** 361-376.

MITOGAWA, T. & NISHIMURA, T. 2020. Coulomb stress change on inland faults during megathrust earthquake cycle in southwest Japan. Earth, Planets and Space, 72, 66.

MITROVICA, J. X. & MILNE, G. A. 2002. On the origin of late Holocene sea-level highstands within equatorial ocean basins. *Quaternary Science Reviews,* 21**,** 2179-2190.

MITROVICA, J. X. & PELTIER, W. R. 1991a. On postglacial geoid subsidence over the equatorial oceans. *Journal of Geophysical Research: Solid Earth,* 96**,** 20053-20071.

MITROVICA, J. X. & PELTIER, W. R. 1991b. Radial Resolution in the Inference of Mantle Viscosity from Observations of Glacial Isostatic Adjustment. *In:* SABADINI, R., LAMBECK, K. & BOSCHI, E. (eds.) *Glacial Isostasy, Sea-Level and Mantle Rheology.* Dordrecht: Springer Netherlands.

MOERNAUT, J., DE BATIST, M., CHARLET, F., HEIRMAN, K., CHAPRON, E., PINO, M., BRÜMMER, R. & URRUTIA, R. 2007. Giant earthquakes in South-Central Chile revealed by Holocene mass-wasting events in Lake Puyehue. *Sedimentary Geology,* 195**,** 239-256.

MOERNAUT, J., MAARTEN VAN DAELE, KATRIEN HEIRMAN, KAREN FONTIJN, MICHAEL STRASSER, MARIO PINO, ROBERTO URRUTIA & BATIST, M. D. 2014. Lacustrine turbidites as a tool for quantitative earthquake reconstruction: New evidence for a variable rupture mode in south central Chile. *Journal of Geophysical Research: Solid Earth,* 119**,** 1607 - 1633.

MORELL, K. D., STYRON, R., STIRLING, M., GRIFFIN, J., ARCHULETA, R. & ONUR, T. 2020. Seismic Hazard Analyses From Geologic and Geomorphic Data: Current and Future Challenges. *Tectonics,* 39**,** e2018TC005365.

MORENO, M., MELNICK, D., ROSENAU, M., BAEZ, J., KLOTZ, J., ONCKEN, O., TASSARA, A., CHEN, J., BATAILLE, K., BEVIS, M., SOCQUET, A., BOLTE, J., VIGNY, C., BROOKS, B., RYDER, I., GRUND, V., SMALLEY, B., CARRIZO, D., BARTSCH, M. & HASE, H. 2012. Toward understanding tectonic control on the Mw 8.8 2010 Maule Chile earthquake. *Earth and Planetary Science Letters,* 321-322**,** 152-165.

MORENO, M., MELNICK, D., ROSENAU, M., BOLTE, J., KLOTZ, J., ECHTLER, H., BAEZ, J., BATAILLE, K., CHEN, J., BEVIS, M., HASE, H. & ONCKEN, O. 2011. Heterogeneous plate locking in the South–Central Chile subduction zone: Building up the next great earthquake. *Earth and Planetary Science Letters,* 305**,** 413-424.

MORENO, M., ROSENAU, M. & ONCKEN, O. 2010. 2010 Maule earthquake slip correlates with pre-seismic locking of Andean subduction zone. *Nature,* 467**,** 198.

MORENO, M. S., BOLTE, J., KLOTZ, J. & MELNICK, D. 2009. Impact of megathrust geometry on inversion of coseismic slip from geodetic data: Application to the 1960 Chile earthquake. *Geophysical Research Letters,* 36.

MORTON, R. A., GELFENBAUM, G. & JAFFE, B. E. 2007. Physical criteria for distinguishing sandy tsunami and storm deposits using modern examples. *Sedimentary Geology,* 200**,** 184-207.

MÜLLER, R. D., ROEST, W. R., ROYER, J.-Y., GAHAGAN, L. M. & SCLATER, J. G. 1997. Digital isochrons of the world's ocean floor. *Journal of Geophysical Research: Solid Earth,* 102**,** 3211-3214.

NAKADA, M. & LAMBECK, K. 1988. The melting history of the late Pleistocene Antarctic ice sheet. *Nature,* 333**,** 36-40.

NANAYAMA, F., FURUKAWA, R., SHIGENO, K., MAKINO, A., SOEDA, Y. & IGARASHI, Y. 2007. Nine unusually large tsunami deposits from the past 4000 years at Kiritappu marsh along the southern Kuril Trench. *Sedimentary Geology,* 200**,** 275-294.

NANAYAMA, F., SATAKE, K., FURUKAWA, R., SHIMOKAWA, K., ATWATER, B. F., SHIGENO, K. & YAMAKI, S. 2003. Unusually large earthquakes inferred from tsunami deposits along the Kuril trench. *Nature,* 424**,** 660-663.

NELSON, A. 2007. Tectonics and relative sea-level change. *In:* ELIAS, S. A. (ed.) *Encyclopedia of Quaternary Science.* Elsevier.

NELSON, A. R. 2013. SEA-LEVELS, LATE QUATERNARY | Tectonics and Relative Sea-Level Change. In: ELIAS, S. A. & MOCK, C. J. (eds.) *Encyclopedia of Quaternary Science (Second Edition)*. Amsterdam: Elsevier.

NELSON, A., SHENNAN, I. & J. LONG, A. 1996. *Identifying coseismic subsidence in tidal-wetland stratigraphic sequences at the Cascadia subduction zone of Western North America*.

NELSON, A. R., ATWATER, B. F., BOBROWSKY, P. T., BRADLEY, L.-A., CLAGUE, J. J., CARVER, G. A., DARIENZO, M. E., GRANT, W. C., KRUEGER, H. W., SPARKS, R., STAFFORD JR, T. W. & STUIVER, M. 1995. Radiocarbon evidence for extensive plate-boundary rupture about 300 years ago at the Cascadia subduction zone. *Nature,* 378**,** 371.

NELSON, A. R. & KASHIMA, K. 1993. Diatom zonation in southern Oregon tidal marshes relative to vascular plants, foraminifera, and sea level. *Journal of Coastal Research,* 9**,** 673-697.

NELSON, A. R., KASHIMA, K. & BRADLEY, L.-A. 2009. Fragmentary Evidence of Great-Earthquake Subsidence during Holocene Emergence, Valdivia Estuary, South Central Chile. *Bulletin of the Seismological Society of America,* 99**,** 71-86.

NELSON, A. R. & MANLEY, W. F. 1992. Holocene coseismic and aseismic uplift of Isla Mocha, south-central Chile. *Quaternary International,* 15**,** 61-76.

NELSON, A. R., SAWAI, Y., JENNINGS, A. E., BRADLEY, L.-A., GERSON, L., SHERROD, B. L., SABEAN, J. & HORTON, B. P. 2008. Great-earthquake

paleogeodesy and tsunamis of the past 2000 years at Alsea Bay, central Oregon coast, USA. *Quaternary Science Reviews,* 27**,** 747-768.

NEUMANN, B., VAFEIDIS, A. T., ZIMMERMANN, J. & NICHOLLS, R. J. 2015. Future coastal population growth and exposure to sea-level rise and coastal flooding-a global assessment. *PloS one,* 10**,** e0118571.

NICHOLLS, R., WONG, P. P., BURKETT, V., CODIGNOTTO, J. O., HAY, J., MCLEAN, R., RAGOONADEN, S., WOODROFFE, C., ABUODHA, P., ARBLASTER, J., BROWN, B., FORBES, D., HALL, J., KOVATS, S., LOWE, J., MCINNES, K., MOSER, S., RUPP-ARMSTRONG, S. & SAITO, Y. 2007. Coastal Systems and Low-Lying Areas. *In:* INTERGOVERNMENTAL PANEL ON CLIMATE, C. (ed.) *Climate Change 2014 – Impacts, Adaptation and Vulnerability: Part A: Global and Sectoral Aspects: Working Group II Contribution to the IPCC Fifth Assessment Report: Volume 1: Global and Sectoral Aspects.* Cambridge: Cambridge University Press.

NISHENKO, S. P. 1985. Seismic potential for large and great interplate earthquakes along the Chilean and Southern Peruvian Margins of South America: A quantitative reappraisal. *Journal of Geophysical Research: Solid Earth,* 90**,** 3589-3615.

OKSANEN, J., BLANCHET., F. G., FRIENDLY., M., KINDT., R., LEGENDRE., P., MCGLINN., D., MINCHIN., P. R., O'HARA., R. B., SIMPSON., G. L., SOLYMOS., P., STEVENS., M. H. H., SZOECS., E. & WAGNER., H. 2020. vegan: Community Ecology Package. R package version 2.5-7. *https://CRAN.R-project.org/package=vegan*.

OLESKEVICH, D. A., HYNDMAN, R. D. & WANG, K. 1999. The updip and downdip limits to great subduction earthquakes: Thermal and structural models of Cascadia, south Alaska, SW Japan, and Chile. *Journal of Geophysical Research: Solid Earth,* 104**,** 14965-14991.

OVERPECK, J. T., WEBB, T. & PRENTICE, I. C. 1985. Quantitative interpretation of fossil pollen spectra: Dissimilarity coefficients and the method of modern analogs. *Quaternary Research,* 23**,** 87-108.

PALMER, A. J. M. & ABBOTT, W. H. 1986. Diatoms as indicators of sea-level change. *In:* VAN DE PLASSCHE, O. (ed.) *Sea-Level Research: a manual for the collection and evaluation of data.* Dordrecht: Springer Netherlands.

PARDO-CASAS, F. & MOLNAR, P. 1987. Relative motion of the Nazca (Farallon) and South American Plates since Late Cretaceous time. *Tectonics,* 6**,** 233-248.

PATTERSON, R. T., DALBY, A. P., ROE, H. M., GUILBAULT, J.-P., HUTCHINSON, I. & CLAGUE, J. J. 2005. Relative utility of foraminifera, diatoms and macrophytes as high resolution indicators of paleo-sea level in coastal British Columbia, Canada. *Quaternary Science Reviews,* 24**,** 2002-2014.

PELTIER, W. 1998a. Postglacial variations in the level of the sea: Implications for climate dynamics and solid-earth geophysics. *Reviews of geophysics,* 36**,** 603-689.

PELTIER, W. 1998b. Implicit ice in the global theory of glacial isostatic adjustment. Geophysical Research Letters 25, 3957–3960. *Geophysical Research Letters* 25, 3957–3960.

PELTIER, W.R., 1999. Global sea level rise and glacial isostatic adjustment. *Global and Planetary Change* 20, 93–123.

PELTIER, W. R. 2002. On eustatic sea level history: Last Glacial Maximum to Holocene. *Quaternary Science Reviews,* 21**,** 377-396.

PELTIER, W. R. 2004. Global glacial isostasy and the surface of the ice-age earth: The ICE-5G (VM2) model and GRACE. *Annual Review of Earth and Planetary Sciences,* 32**,** 111-149.

PELTIER, W. R. & ANDREWS, J. T. 1976. Glacial-Isostatic Adjustment—I. The Forward Problem. *Geophysical Journal International,* 46**,** 605-646.

PELTIER, W. R., ARGUS, D. F. & DRUMMOND, R. 2015. Space geodesy constrains ice age terminal deglaciation: The global ICE-6G_C (VM5a) model. *Journal of Geophysical Research: Solid Earth,* 120**,** 450-487.

PELTIER, W. R. & FAIRBANKS, R. G. 2006. Global glacial ice volume and Last Glacial Maximum duration from an extended Barbados sea level record. *Quaternary Science Reviews,* 25**,** 3322-3337.

PÉREZ-GUSSINYÉ, M., LOWRY, A. R., PHIPPS MORGAN, J. & TASSARA, A. 2008. Effective elastic thickness variations along the Andean margin and their relationship to subduction geometry. *Geochemistry, Geophysics, Geosystems,* 9.

PETERS, R. & JAFFE, B. 2010. Identification of tsunami deposits in the geologic record; developing criteria using recent tsunami deposits. *US Geological Survey Open-File Report,* 1239**,** 39.

PHILIBOSIAN, B. & MELTZNER, A. J. 2020. Segmentation and supercycles: A catalog of earthquake rupture patterns from the Sumatran Sunda Megathrust and other well-studied faults worldwide. *Quaternary Science Reviews,* 241**,** 106390.

PILARCZYK, J. E., DURA, T., HORTON, B. P., ENGELHART, S. E., KEMP, A. C. & SAWAI, Y. 2014. Microfossils from coastal environments as indicators of paleo-earthquakes, tsunamis and storms. *Palaeogeography, Palaeoclimatology, Palaeoecology,* 413**,** 144-157.

PINO, M. & NAVARRO, R. X. 2005. Geoarqueología del sitio arcaico Chan-Chan 18, costa de Valdivia: discriminación de ambientes de ocupación humana y su relación con la transgresión marina del Holoceno Medio. *Revista geológica de Chile,* 32**,** 59-75.

PIRAZZOLI, P. A. 1991. World atlas of Holocene sea-level changes. *Elsevier oceanography series,* 58**,** 1-280.

PLAFKER, G. 1969. Tectonics of the March 27, 1964 Alaska Earthquake. *U.S. Geological Survey Professional Paper.*

PLAFKER, G. 1972. Alaskan earthquake of 1964 and Chilean earthquake of 1960: Implications for arc tectonics. *Journal of Geophysical Research,* 77**,** 901-925.

PLAFKER, G. & SAVAGE, J. C. 1970. Mechanism of the Chilean Earthquakes of May 21 and 22, 1960. *GSA Bulletin,* 81**,** 1001-1030.

PLESCIA, S. M. & HAYES, G. P. 2020. Geometric controls on megathrust earthquakes. *Geophysical Journal International,* 222**,** 1270-1282.

PORTER, S. C. 1981. Pleistocene glaciation in the southern Lake District of Chile. *Quaternary Research,* 16**,** 263-292.

POPPER, K. R. 1962. Conjectures and Refutations: The Growth of Scientific Knowledge, Routledge. London, England.

PRELL, W. L. 1985. Stability of low-latitude sea-surface temperatures: an evaluation of the CLIMAP reconstruction with emphasis on the positive SST anomalies. Final report. Brown Univ., Providence, RI (USA). Dept. of Geological Sciences.

QUINLAN, G. & BEAUMONT, C. 1981. A comparison of observed and theoretical postglacial relative sea level in Atlantic Canada. *Canadian Journal of Earth Sciences,* 18**,** 1146-1163.

R CORE TEAM 2021. R: A Language and Environment for Statistical Computing. R Foundation for Statistical Computing.

RABASSA, J. & CLAPPERTON, C. M. 1990. Quaternary glaciations of the southern Andes. *Quaternary Science Reviews,* 9**,** 153-174.

RACCA, J. M. J. & PRAIRIE, Y. T. 2004. Apparent and real bias in numerical transfer functions in palaeolimnology. *Journal of Paleolimnology,* 31**,** 117-124.

RAMOS, M. D., HUANG, Y., ULRICH, T., LI, D., GABRIEL, A.-A. & THOMAS, A. M. 2021. Assessing Margin-Wide Rupture Behaviors Along the Cascadia Megathrust With 3-D Dynamic Rupture Simulations. *Journal of Geophysical Research: Solid Earth,* 126**,** e2021JB022005.

REBOLLEDO, L., GONZÁLEZ, H. E., MUÑOZ, P., IRIARTE, J. L., LANGE, C. B., PANTOJA, S. & SALAMANCA, M. 2011. Siliceous productivity changes in Gulf of Ancud sediments (42°S, 72°W), southern Chile, over the last ∼150 years. *Continental Shelf Research,* 31**,** 356-365.

REBOLLEDO, L., LANGE, C. B., FIGUEROA, D., PANTOJA, S., MUÑOZ, P. & CASTRO, R. 2005. 20 th century fluctuations in the abundance of siliceous microorganisms preserved in the sediments of the Puyuhuapi Channel (44° S), Chile. *Revista Chilena de Historia Natural,* 78**,** 469-488.

REID, H. F. 1910. The mechanics of the earthquake, the California earthquake of April 18, 1906. Washington, DC: Carnegie Institution of Washington.

REIMER, P. J. 2020. Composition and consequences of the IntCal20 radiocarbon calibration curve. *Quaternary Research,* 96**,** 22-27.

RIGNOT, E., RIVERA, A. & CASASSA, G. 2003. Contribution of the Patagonia Icefields of South America to sea level rise. *Science,* 302**,** 434-437.

RIVERA, P., GEBAUER, M. & BARRALES, H. L. 1989. A guide for references and distribution for the class Bacillariophyceae in Chile between 18°28'S and 58°S. Part II. Date from 1982 to 1988. *Gayana Botánica,* 46**,** 155-198.

ROBBINS, J. A. 1978. Geochemical and geophysical applications of radioactive lead. *Biogeochemistry of Lead in the Environment***,** 285-393.

ROBINSON, D. P., DAS, S. & WATTS, A. B. 2006. Earthquake Rupture Stalled by a Subducting Fracture Zone. *Science,* 312**,** 1203.

ROE, H. M., DOHERTY, C. T., PATTERSON, R. T. & SWINDLES, G. T. 2009. Contemporary distributions of saltmarsh diatoms in the Seymour–Belize Inlet Complex, British Columbia, Canada: Implications for studies of sea-level change. *Marine Micropaleontology,* 70**,** 134-150.

ROJAS, C., BECK, M. E., BURMESTER, R. F., CEMBRANO, J. & HERVÉ, F. 1994. Paleomagnetism of the Mid-Tertiary Ayacara Formation, southern Chile: Counterclockwise rotation in a dextral shear zone. *Journal of South American Earth Sciences,* 7**,** 45-56.

ROSENAU, M., MELNICK, D. & ECHTLER, H. 2006. Kinematic constraints on intra-arc shear and strain partitioning in the southern Andes between 38°S and 42°S latitude. *Tectonics,* 25.

ROUND, F. E., CRAWFORD, R. M. & MANN, D. G. 1990. *Diatoms: Biology and Morphology of the Genera*, Cambridge University Press.

ROUND, F. E., CRAWFORD, R. M. & MANN, D. G. 2007. *Diatoms: Biology and Morphology of the Genera*, Cambridge University Press.

RUFF, L. & KANAMORI, H. 1983. Seismic coupling and uncoupling at subduction zones. *Tectonophysics,* 99**,** 99-117.

RUFF, L. J. 1989. Do trench sediments affect great earthquake occurrence in subduction zones? *pure and applied geophysics,* 129**,** 263-282.

SANDWELL, D. T. 1986. Thermal stress and the spacings of transform faults. *Journal of Geophysical Research: Solid Earth,* 91**,** 6405-6417.

SANTIBÁÑEZ, I., CEMBRANO, J., GARCÍA-PÉREZ, T., COSTA, C., YÁÑEZ, G., MARQUARDT, C., ARANCIBIA, G. & GONZÁLEZ, G. 2019. Crustal faults in the Chilean Andes: geological constraints and seismic potential. Andean Geology, 46, 32-65.

SATAKE, K. & ATWATER, B. F. 2007. Long-Term Perspectives on Giant Earthquakes and Tsunamis at Subduction Zones. *Annual Review of Earth and Planetary Sciences,* 35**,** 349-374.

SAVAGE, J. C. 1983. A dislocation model of strain accumulation and release at a subduction zone. *Journal of Geophysical Research: Solid Earth,* 88**,** 4984-4996.

SAWAI, Y., FUJII, Y., FUJIWARA, O., KAMATAKI, T., KOMATSUBARA, J., OKAMURA, Y., SATAKE, K. & SHISHIKURA, M. 2008. Marine incursions of the past 1500 years and evidence of tsunamis at Suijin-numa, a coastal lake facing the Japan Trench. *The Holocene,* 18**,** 517-528.

SAWAI, Y., HORTON, B. P., KEMP, A. C., HAWKES, A. D., NAGUMO, T. & NELSON, A. R. 2016. Relationships between diatoms and tidal environments in Oregon and Washington, USA. *Diatom research,* 31**,** 17-38.

SAWAI, Y., HORTON, B. P. & NAGUMO, T. 2004a. The development of a diatom-based transfer function along the Pacific coast of eastern Hokkaido, northern Japan—an aid in paleoseismic studies of the Kuril subduction zone. *Quaternary Science Reviews,* 23**,** 2467-2483.

SAWAI, Y., NAGUMO, T., NAMEGAYA, Y., CISTERNAS, M. V., LAGOS, M. & SHISHIKURA, M. 2017. Diatom (Bacillariophyceae) assemblages in salt marshes of south-central Chile: Relations with tidal inundation time and salinity. *Phycological Research,* 65**,** 29-37.

SAWAI, Y., NASU, H. & YASUDA, Y. 2002. Fluctuations in relative sea-level during the past 3000 yr in the Onnetoh estuary, Hokkaido, northern Japan. *Journal of Quaternary Science,* 17**,** 607-622.

SAWAI, Y., SATAKE, K., KAMATAKI, T., NASU, H., SHISHIKURA, M., ATWATER, B. F., HORTON, B. P., KELSEY, H. M., NAGUMO, T. & YAMAGUCHI, M. 2004b. Transient Uplift After a 17th-Century Earthquake Along the Kuril Subduction Zone. *Science,* 306**,** 1918.

SCHULLER, P., LØVENGREEN, C. & HANDL, J. 1993. 137Cs concentration in soil, prairie plants, and milk from sites in southern Chile. *Health physics,* 64**,** 157-161.

SCHULLER, P., VOIGT, G., HANDL, J., ELLIES, A. & OLIVA, L. 2002. Global weapons' fallout 137Cs in soils and transfer to vegetation in south–central Chile. *Journal of Environmental Radioactivity,* 62**,** 181-193.

SHAW, J., GAREAU, P. & COURTNEY, R. C. 2002. Palaeogeography of Atlantic Canada 13–0kyr. *Quaternary Science Reviews,* 21**,** 1861-1878.

SHENNAN, I. 1986. Flandrian sea-level changes in the Fenland. II: Tendencies of sea-level movement, altitudinal changes, and local and regional factors. *Journal of Quaternary Science,* 1**,** 155-179.

SHENNAN, I., BARLOW, N., CARVER, G., DAVIES, F., GARRETT, E. & HOCKING, E. 2014a. Great tsunamigenic earthquakes during the past 1000 yr on the Alaska megathrust. *Geology,* 42**,** 687-690.

SHENNAN, I., BRUHN, R., BARLOW, N., GOOD, K. & HOCKING, E. 2014b. Late Holocene great earthquakes in the eastern part of the Aleutian megathrust. *Quaternary Science Reviews,* 84**,** 86-97.

SHENNAN, I., BRUHN, R. & PLAFKER, G. 2009. Multi-segment earthquakes and tsunami potential of the Aleutian megathrust. *Quaternary Science Reviews,* 28**,** 7-13.

SHENNAN, I., GARRETT, E. & BARLOW, N. 2016. Detection limits of tidal-wetland sequences to identify variable rupture modes of megathrust earthquakes. *Quaternary Science Reviews,* 150**,** 1-30.

SHENNAN, I. & HAMILTON, S. 2006. Coseismic and pre-seismic subsidence associated with great earthquakes in Alaska. *Quaternary Science Reviews,* 25**,** 1-8.

SHENNAN, I. & HORTON, B. 2002. Holocene land- and sea-level changes in Great Britain. *Journal of Quaternary Science,* 17**,** 511-526.

SHENNAN, I., LONG, A. J. & HORTON, B. P. 2015. *Handbook of sea-level research*, John Wiley & Sons.

SHENNAN, I., LONG, A. J., RUTHERFORD, M. M., GREEN, F. M., INNES, J. B., LLOYD, J. M., ZONG, Y. & WALKER, K. J. 1996. Tidal marsh stratigraphy, sea-level change and large earthquakes, i: a 5000 year record in washington, U.S.A. *Quaternary Science Reviews,* 15**,** 1023-1059.

SHENNAN, I., MILNE, G. & BRADLEY, S. 2012. Late Holocene vertical land motion and relative sea-level changes: lessons from the British Isles. *Journal of Quaternary Science,* 27**,** 64-70.

SHENNAN, I., SCOTT, D. B., RUTHERFORD, M. & ZONG, Y. 1999. Microfossil analysis of sediments representing the 1964 earthquake, exposed at Girdwood Flats, Alaska, USA. *Quaternary International,* 60**,** 55-73.

SHERROD, B. L. 1999. Gradient analysis of diatom assemblages in a Puget Sound salt marsh: can such assemblages be used for quantitative paleoecological reconstructions? *Palaeogeography, Palaeoclimatology, Palaeoecology,* 149**,** 213-226.

SHRIVASTAVA, M. N., GONZÁLEZ, G., MORENO, M., SOTO, H., SCHURR, B., SALAZAR, P. & BÁEZ, J. C. 2019. Earthquake segmentation in northern Chile correlates with curved plate geometry. *Scientific Reports,* 9**,** 4403.

SCHOLZ, C. H. 2019. *The mechanics of earthquakes and faulting*, Cambridge university press.

SIEVERS, H. A., VILLEGAS, G. & BARROS, G. 1963. The seismic sea wave of 22 May 1960 along the Chilean coast. *Bulletin of the Seismological Society of America,* 53**,** 1125-1190.

SIMPSON, G. L. 2007. Analogue methods in palaeoecology: using the analogue package. *Journal of Statistical Software,* 22**,** 1-29.

SIMPSON, G. L. 2012. Analogue Methods in Palaeolimnology. *In:* BIRKS, H. J. B., LOTTER, A. F., JUGGINS, S. & SMOL, J. P. (eds.) *Tracking Environmental Change Using Lake Sediments: Data Handling and Numerical Techniques.* Dordrecht: Springer Netherlands.

SIMPSON, G. L. & HALL, R. I. 2012. Human impacts: Applications of numerical methods to evaluate surface-water acidification and eutrophication. *Tracking environmental change using lake sediments.* Springer.

SIMPSON, G. L. & OKSANEN, J. 2020. analogue: Analogue matching and Modern Analogue Technique transfer function models. R package version 0.17-4. *https://cran.r-project.org/package=analogue*.

SIMPSON, G. L. O. J. 2021. analogue: Analogue and weighted averaging methods for palaeoecology. R package version 0.17-6. *https://cran.r-project.org/package=analogue.*

SOMOZA, R. 1998. Updated azca (Farallon)—South America relative motions during the last 40 My: implications for mountain building in the central Andean region. *Journal of South American Earth Sciences,* 11**,** 211-215.

SONG, T.-R. A. & SIMONS, M. 2003. Large trench-parallel gravity variations predict seismogenic behavior in subduction zones. *Science,* 301**,** 630-633.

SPARKES, R., TILMANN, F., HOVIUS, N. & HILLIER, J. 2010. Subducted seafloor relief stops rupture in South American great earthquakes: Implications for rupture behaviour in the 2010 Maule, Chile earthquake. *Earth and Planetary Science Letters,* 298**,** 89-94.

SPERAZZA, M., MOORE, J. N. & HENDRIX, M. S. 2004. High-Resolution Particle Size Analysis of Naturally Occurring Very Fine-Grained Sediment Through Laser Diffractometry. *Journal of Sedimentary Research,* 74**,** 736-743.

ST-ONGE, G., CHAPRON, E., MULSOW, S., SALAS, M., VIEL, M., DEBRET, M., FOUCHER, A., MULDER, T., WINIARSKI, T., DESMET, M., COSTA, P. J. M., GHALEB, B., JAOUEN, A. & LOCAT, J. 2012. Comparison of earthquake-triggered turbidites from the Saguenay (Eastern Canada) and Reloncavi (Chilean margin) Fjords: Implications for paleoseismicity and sedimentology. *Sedimentary Geology,* 243-244**,** 89-107.

STEFER, S., MOERNAUT, J., MELNICK, D., ECHTLER, H. P., ARZ, H. W., LAMY, F., DE BATIST, M., ONCKEN, O. & HAUG, G. H. 2010. Forearc uplift rates deduced from sediment cores of two coastal lakes in south-central Chile. *Tectonophysics,* 495**,** 129-143.

STEIN, S., ENGELN, J. F., DEMETS, C., GORDON, R. G., WOODS, D., LUNDGREN, P., ARGUS, D., STEIN, C. & WIENS, D. A. 1986. The Nazca-South America convergence rate and the recurrence of the Great 1960 Chilean Earthquake. *Geophysical Research Letters,* 13**,** 713-716.

STEIN, S. & OKAL, E. A. 2011. The size of the 2011 Tohoku earthquake need not have been a surprise. *Eos, Transactions American Geophysical Union,* 92**,** 227-228.

STUIVER, M. Atmospheric 14C as a Proxy of Solar and Climatic Change. *In:* NESME-RIBES, E., ed. The Solar Engine and Its Influence on Terrestrial Atmosphere and Climate, 1994// 1994 Berlin, Heidelberg. Springer Berlin Heidelberg, 203-220.

STUIVER, M. & QUAY, P. D. 1980. Changes in atmospheric carbon-14 attributed to a variable sun. *Science,* 207**,** 11-19.

SUBARYA, C., CHLIEH, M., PRAWIRODIRDJO, L., AVOUAC, J.-P., BOCK, Y., SIEH, K., MELTZNER, A. J., NATAWIDJAJA, D. H. & MCCAFFREY, R. 2006. Plate-boundary deformation associated with the great Sumatra–Andaman earthquake. *Nature,* 440**,** 46-51.

SUESS, E. A. & TRUMBO, B. E. 2010. *Introduction to probability simulation and Gibbs sampling with R*, Springer Science & Business Media.

SUITO, H. & FREYMUELLER, J. T. 2009. A viscoelastic and afterslip postseismic deformation model for the 1964 Alaska earthquake. *Journal of Geophysical Research: Solid Earth,* 114.

SWITZER, A. D. & JONES, B. G. 2008. Large-scale washover sedimentation in a freshwater lagoon from the southeast Australian coast: sea-level change, tsunami or exceptionally large storm? *The Holocene,* 18**,** 787-803.

TASSARA, A., GÖTZE, H.-J., SCHMIDT, S. & HACKNEY, R. 2006. Three-dimensional density model of the Nazca plate and the Andean continental margin. *Journal of Geophysical Research: Solid Earth,* 111.

TAYLOR, F. W., FROHLICH, C., LECOLLE, J. & STRECKER, M. 1987. Analysis of partially emerged corals and reef terraces in the central Vanuatu Arc: Comparison of contemporary coseismic and nonseismic with quaternary vertical movements. *Journal of Geophysical Research: Solid Earth,* 92**,** 4905-4933.

TEBBENS, S. F. & CANDE, S. C. 1997. Southeast Pacific tectonic evolution from Early Oligocene to Present. *Journal of Geophysical Research: Solid Earth,* 102**,** 12061-12084.

TEBBENS, S. F., CANDE, S. C., KOVACS, L., PARRA, J. C., LABRECQUE, J. L. & VERGARA, H. 1997. The Chile ridge: A tectonic framework. *Journal of Geophysical Research: Solid Earth,* 102**,** 12035-12059.

TELFORD, R. J. & BIRKS, H. J. B. 2005. The secret assumption of transfer functions: problems with spatial autocorrelation in evaluating model performance. *Quaternary Science Reviews,* 24**,** 2173-2179.

TELFORD, R. J. & BIRKS, H. J. B. 2009. Evaluation of transfer functions in spatially structured environments. *Quaternary Science Reviews,* 28**,** 1309-1316.

TELFORD, R. J. & BIRKS, H. J. B. 2011. A novel method for assessing the statistical significance of quantitative reconstructions inferred from biotic assemblages. *Quaternary Science Reviews,* 30**,** 1272-1278.

TEN BRINK, U. & LIN, J. 2004. Stress interaction between subduction earthquakes and forearc strike-slip faults: Modeling and application to the northern Caribbean plate boundary. Journal of Geophysical Research: Solid Earth, 109.

TER BRAAK , C., J. F 1985. Correspondence Analysis of Incidence and Abundance Data: Properties in Terms of a Unimodal Response Model. *Biometrics,* 41**,** 859-873.

TER BRAAK, C. J. F. 1986. Canonical Correspondence Analysis: A New Eigenvector Technique for Multivariate Direct Gradient Analysis. *Ecology,* 67**,** 1167-1179.

TER BRAAK, C. J. F. 1988. CANOCO - a FORTRAN program for canonical community ordination by [partial] [detrended] [canonical] correspondence

analysis, principal components analysis and redundancy analysis (version 2.1). Wageningen: MLV.

TER BRAAK, C. J. F. 1995a. Non-linear methods for multivariate statistical calibration and their use in palaeoecology: a comparison of inverse (k-nearest neighbours, partial least squares and weighted averaging partial least squares) and classical approaches. *Chemometrics and Intelligent Laboratory Systems,* 28**,** 165-180.

TER BRAAK, C. J. F. 1995b. Ordination. *In:* BRAAK, C. J. F. T., TONGEREN, O. F. R. V. & JONGMAN, R. H. G. (eds.) *Data Analysis in Community and Landscape Ecology.* Cambridge: Cambridge University Press.

TER BRAAK, C. J. F. & BARENDREGT, L. G. 1986. Weighted averaging of species indicator values: Its efficiency in environmental calibration. *Mathematical Biosciences,* 78**,** 57-72.

TER BRAAK, C. J. F. & JUGGINS, S. 1993. Weighted averaging partial least squares regression (WA-PLS): an improved method for reconstructing environmental variables from species assemblages. *Hydrobiologia,* 269**,** 485-502.

TER BRAAK, C. J. F., JUGGINS, S., BIRKS, H. & VAN DER VOET, H. 1993. Weighted averaging partial least squares regression (WA-PLS): definition and comparison with other methods for species-environment calibration. *Multivariate environmental statistics.* In: PATIL, G.P., RAC, C.R. ed. Amsterdam: Elsevier Science Publishers.

TER BRAAK, C. J. F. & LOOMAN, C. W. N. 1986. Weighted averaging, logistic regression and the Gaussian response model. *Vegetatio,* 65**,** 3-11.

TER BRAAK, C. J. F. & PRENTICE, I. C. 1988. A Theory of Gradient Analysis. *In:* BEGON, M., FITTER, A. H., FORD, E. D. & MACFADYEN, A. (eds.) *Advances in Ecological Research.* Academic Press.

TER BRAAK, C. J. F. & ŠMILAUER, P. 2002. CANOCO Reference Manual and CanoDraw for Windows User's Guide: Software for Canonical Community Ordination (version 4.5). Ithaca NY, USA: www.canoco.com.

TER BRAAK, C. J. F. & VAN DAME, H. 1989. Inferring pH from diatoms: a comparison of old and new calibration methods. *Hydrobiologia,* 178**,** 209-223.

TER BRAAK, C. J. F. & VERDONSCHOT, P. F. M. 1995. Canonical correspondence analysis and related multivariate methods in aquatic ecology. *Aquatic Sciences,* 57**,** 255-289.

THORNBURG, T. M., KULM, L. D. & HUSSONG, D. M. 1990. Submarine-fan development in the southern Chile Trench: A dynamic interplay of tectonics and sedimentation. *GSA Bulletin,* 102**,** 1658-1680.

THATCHER, W. & RUNDLE, J. B. 1984. A viscoelastic coupling model for the cyclic deformation due to periodically repeated Earthquakes at subduction zones. *Journal of Geophysical Research: Solid Earth,* 89**,** 7631-7640.

TICHELAAR, B. W. & RUFF, L. J. 1991. Seismic coupling along the Chilean Subduction Zone. *Journal of Geophysical Research: Solid Earth,* 96**,** 11997-12022.

TICHELAAR, B. W. & RUFF, L. J. 1993. Depth of seismic coupling along subduction zones. *Journal of Geophysical Research: Solid Earth,* 98**,** 2017-2037.

TODA, S. & TSUTSUMI, H. 2013. Simultaneous reactivation of two, subparallel, inland normal faults during the M w 6.6 11 April 2011 Iwaki earthquake triggered by the M w 9.0 Tohoku-oki, Japan, earthquake. Bulletin of the Seismological Society of America, 103, 1584-1602.

TÖRNQVIST, T. E., WALLACE, D. J., STORMS, J. E. A., WALLINGA, J., VAN DAM, R. L., BLAAUW, M., DERKSEN, M. S., KLERKS, C. J. W., MEIJNEKEN, C. & SNIJDERS, E. M. A. 2008. Mississippi Delta subsidence primarily caused by compaction of Holocene strata. *Nature Geoscience,* 1**,** 173-176.

TÖRNQVIST, T. R. E., GONZÁLEZ, J. L., NEWSOM, L. A., VAN DER BORG, K., DE JONG, A. F. M. & KURNIK, C. W. 2004. Deciphering Holocene sea-level history on the U.S. Gulf Coast: A high-resolution record from the Mississippi Delta. *GSA Bulletin,* 116**,** 1026-1039.

TRÖELS-SMITH, J. 1955. Characterization of unconsolidated sediments. *Geological Survey of Denmark,* Series IV.

TRUMBORE, S. E., SIERRA, C. A. & HICKS PRIES, C. E. 2016. Radiocarbon Nomenclature, Theory, Models, and Interpretation: Measuring Age, Determining Cycling Rates, and Tracing Source Pools. *In:* SCHUUR, E. A. G., DRUFFEL, E. & TRUMBORE, S. E. (eds.) *Radiocarbon and Climate Change: Mechanisms, Applications and Laboratory Techniques.* Cham: Springer International Publishing.

USGS EARTHQUAKE CATALOGUE. US: United States Geological Survey Earthquake Catalogue. Available: https://www.usgs.gov/natural-hazards/earthquake-hazards/lists-maps-and-statistics [Accessed 2020].

VAN DAM, H., MERTENS, A. & SINKELDAM, J. 1994. A coded checklist and ecological indicator values of freshwater diatoms from The Netherlands. *Netherland Journal of Aquatic Ecology,* 28**,** 117-133.

VAN DE PLASSCHE, O. 1986. *Sea-level Research: a Manual for the Collection and Evaluation of Data: a Manual for the Collection and Evaluation of Data*, Springer.

VAN DEN BEUKEL, J. & WORTEL, R. 1988. Thermo-mechanical modelling of arc-trench regions. *Tectonophysics,* 154**,** 177-193.

VAN DER VOET, H. 1994. Comparing the predictive accuracy of models using a simple randomization test. *Chemometrics and Intelligent Laboratory Systems,* 25**,** 313-323.

VAN ZELST, I., WOLLHERR, S., GABRIEL, A. A., MADDEN, E. H. & VAN DINTHER, Y. 2019. Modeling Megathrust Earthquakes Across Scales: One-way Coupling From Geodynamics and Seismic Cycles to Dynamic Rupture. *Journal of Geophysical Research: Solid Earth,* 124**,** 11414-11446.

VEGA, R., MELLA, M., NIELSEN, S. & PINO, M. 2018. Stratigraphy and sedimentology of a late Pleistocene incised valley fill: “Cancagua” deposits in north-western Patagonia, Chile. *Andean Geology,* 45.

VIGNY, C., SOCQUET, A., PEYRAT, S., RUEGG, J. C., MÉTOIS, M., MADARIAGA, R., MORVAN, S., LANCIERI, M., LACASSIN, R., CAMPOS, J., CARRIZO, D., BEJAR-PIZARRO, M., BARRIENTOS, S., ARMIJO, R., ARANDA, C., VALDERAS-BERMEJO, M. C., ORTEGA, I., BONDOUX, F., BAIZE, S., LYON-CAEN, H., PAVEZ, A., VILOTTE, J. P., BEVIS, M., BROOKS, B., SMALLEY, R., PARRA, H., BAEZ, J. C., BLANCO, M., CIMBARO, S. & KENDRICK, E. 2011. The 2010 Mw 8.8 Maule Megathrust Earthquake of Central Chile, Monitored by GPS. *Science,* 332**,** 1417.

VILLALOBOS SILVA, M. P. 2005. *Evidencias de la fluctuación del nivel del mar y alzamientos tectónicos desde el Pleistoceno tardío en Isla Mancera X Región de Los Lagos-Chile: registro estratigráfico y sedimentológico.* Universidad Austral de Chile, Facultad de Ciencias, Escuela.

VINE, F. J. & MATTHEWS, D. H. 1963. Magnetic Anomalies Over Oceanic Ridges. *Nature,* 199**,** 947-949.

VLAAR, N. J. & WORTEL, M. J. R. 1976. Lithospheric aging, instability and subduction. *Tectonophysics,* 32**,** 331-351.

VÖLKER, D., GEERSEN, J., CONTRERAS-REYES, E. & REICHERT, C. 2013. Sedimentary fill of the Chile Trench (32–46°S): volumetric distribution and causal factors. *Journal of the Geological Society,* 170**,** 723-736.

VÖLKER, D., GREVEMEYER, I., STIPP, M., WANG, K. & HE, J. 2011. Thermal control of the seismogenic zone of southern central Chile. *Journal of Geophysical Research: Solid Earth,* 116.

VOS, P. C. & DE WOLF, H. 1985. Methodological aspects of paleo-ecological diatom research in coastal areas. *Geologie en mijnbouw : orgaan voor officieele mededelingen van het Geologisch-Mijnbouwkundig Genootschap voor Nederland en Kolonien,* 67**,** 31-40.

VOS, P. C. & DE WOLF, H. Diatoms as a tool for reconstructing sedimentary environments in coastal wetlands; methodological aspects. 1993 Dordrecht. Springer Netherlands, 285-296.

WALKER, M. 2005. *Quaternary Dating Methods*, Wiley.

WALTON, M. A. L., STAISCH, L. M., DURA, T., PEARL, J. K., SHERROD, B., GOMBERG, J., ENGELHART, S., TRÉHU, A., WATT, J., PERKINS, J., WITTER, R. C., BARTLOW, N., GOLDFINGER, C., KELSEY, H., MOREY, A. E., SAHAKIAN, V. J., TOBIN, H., WANG, K., WELLS, R. & WIRTH, E. 2021. Toward an Integrative Geological and Geophysical View of Cascadia Subduction Zone Earthquakes. *Annual Review of Earth and Planetary Sciences,* 49**,** 367-398.

WANG, K. & HE, J. 2008. Effects of Frictional Behavior and Geometry of Subduction Fault on Coseismic Seafloor Deformation. *Bulletin of the Seismological Society of America,* 98**,** 571-579.

WANG, K., HU, Y., BEVIS, M., KENDRICK, E., SMALLEY, R., VARGAS, R. B. & LAURÍA, E. 2007. Crustal motion in the zone of the 1960 Chile earthquake: Detangling earthquake-cycle deformation and forearc-sliver translation. *Geochemistry, Geophysics, Geosystems,* 8.

WANG, K. & TRÉHU, A. M. 2016. Invited review paper: Some outstanding issues in the study of great megathrust earthquakes—The Cascadia example. *Journal of Geodynamics,* 98**,** 1-18.

WANG, P.-L., ENGELHART, S. E., WANG, K., HAWKES, A. D., HORTON, B. P., NELSON, A. R. & WITTER, R. C. 2013. Heterogeneous rupture in the great Cascadia earthquake of 1700 inferred from coastal subsidence estimates. *Journal of Geophysical Research: Solid Earth,* 118**,** 2460-2473.

WANG, K. 1995. Coupling of tectonic loading and earthquake fault slips at subduction zones. *pure and applied geophysics,* 145**,** 537-559.

WATANABE, H. 1998. Comprehensive list of tsunamis to hit the Japanese Islands. University of Tokyo Press, Tokyo.

WATCHAM, E. P., SHENNAN, I. & BARLOW, N. L. M. 2013. Scale considerations in using diatoms as indicators of sea-level change: lessons from Alaska. *Journal of Quaternary Science,* 28**,** 165-179.

WEHRMANN, A. 2013. Tidal Depositional Systems. *In:* HARFF, J., MESCHEDE, M., PETERSEN, S. & THIEDE, J. (eds.) *Encyclopedia of Marine Geosciences.* Dordrecht: Springer Netherlands.

WELLS, D. L. & COPPERSMITH, K. J. 1994. New empirical relationships among magnitude, rupture length, rupture width, rupture area, and surface displacement. *Bulletin of the Seismological Society of America,* 84**,** 974-1002.

WELLS, R. E., BLAKELY, R. J., SUGIYAMA, Y., SCHOLL, D. W. & DINTERMAN, P. A. 2003. Basin-centered asperities in great subduction zone earthquakes: A link between slip, subsidence, and subduction erosion? *Journal of Geophysical Research: Solid Earth,* 108.

WENTWORTH, C. K. 1922. A Scale of Grade and Class Terms for Clastic Sediments. *The Journal of Geology,* 30**,** 377-392.

WESSON, R., CISTERNAS, M., ELY, L., MELNICK, D., BRIGGS, R. & GARRETT, E. Uncertainties in field estimation of mean sea level. International Geoscience Programme Project 588 Annual Meeting, Cordova, Alaska, 2014.

WHITING, M. C. & MCINTIRE, C. D. 1985. AN INVESTIGATION OF DISTRIBUTIONAL PATTERNS IN THE DIATOM FLORA OF NETARTS BAY, OREGON, BY CORRESPONDENCE ANALYSIS 1. *Journal of Phycology,* 21**,** 655-661.

WHITTAKER, R. H. 1956. Vegetation of the Great Smoky Mountains. *Ecological Monographs,* 26**,** 1-80.

WHITTAKER, R. H. 1967. GRADIENT ANALYSIS OF VEGETATION*. *Biological Reviews,* 42**,** 207-264.

WIDLANSKY, M. J., LONG, X. & SCHLOESSER, F. 2020. Increase in sea level variability with ocean warming associated with the nonlinear thermal expansion of seawater. *Communications Earth & Environment,* 1**,** 9.

WIGLEY, T. M. L. & RAPER, S. C. B. 1987. Thermal expansion of sea water associated with global warming. *Nature,* 330**,** 127-131.

WILLIAMS, A. N. 2012. The use of summed radiocarbon probability distributions in archaeology: a review of methods. *Journal of Archaeological Science,* 39**,** 578-589.

WILLIAMS, H. F. L. 2009. Stratigraphy, Sedimentology, and Microfossil Content of Hurricane Rita Storm Surge Deposits in Southwest Louisiana. *Journal of Coastal Research,* 25**,** 1041-1051.

WILLIAMS, S., GARRETT, E., MOSS, P., BARTLETT, R. & GEHRELS, W. R. 2021. Development of a Training Set of Contemporary Salt-Marsh Foraminifera for Late Holocene Sea-Level Reconstructions in southeastern Australia. *Open Quaternary*.

WILLIS, M. J., MELKONIAN, A. K., PRITCHARD, M. E. & RIVERA, A. 2012. Ice loss from the Southern Patagonian ice field, South America, between 2000 and 2012. *Geophysical research letters,* 39.

WILLNER, A. P., GLODNY, J., GERYA, T. V., GODOY, E. & MASSONNE, H. J. 2004. A counterclockwise PTt path of high-pressure/low-temperature rocks from the Coastal Cordillera accretionary complex of south-central Chile: constraints for the earliest stage of subduction mass flow. *Lithos,* 75**,** 283-310.

WILSON, G. P. & LAMB, A. L. 2012. An assessment of the utility of regional diatom-based tidal-level transfer functions. *Journal of Quaternary Science,* 27**,** 360-370.

WILSON, J. T. 1963. A possible origin of the Hawaiian Islands. *Canadian Journal of Physics,* 41**,** 863-870.

WILSON, J. T. 1965. Submarine Fracture Zones, Aseismic Ridges and the International Council of Scientific Unions Line: Proposed Western Margin of the East Pacific Ridge. *Nature,* 207**,** 907-911.

WILSON, J. T. 1965a. A New Class of Faults and their Bearing on Continental Drift. *Nature,* 207**,** 343-347.

WITTER, R., C. , KELSEY, H. M. & HEMPHILL-HALEY, E. 2001. Pacific Storms, El Niño and Tsunamis: Competing Mechanisms for Sand Deposition in a Coastal Marsh, Euchre Creek, Oregon. *Journal of Coastal Research,* 17**,** 563-583.

WITTER, R. C., KELSEY, H. M. & HEMPHILL-HALEY, E. 2003. Great Cascadia earthquakes and tsunamis of the past 6700 years, Coquille River estuary, southern coastal Oregon. *GSA Bulletin,* 115**,** 1289-1306.

WOODROFFE, S. A. & LONG, A. J. 2010. Reconstructing recent relative sea-level changes in West Greenland: Local diatom-based transfer functions are superior to regional models. *Quaternary International,* 221**,** 91-103.

WRIGHT, A. J., EDWARDS, R. J. & VAN DE PLASSCHE, O. 2011. Reassessing transfer-function performance in sea-level reconstruction based on benthic salt-marsh foraminifera from the Atlantic coast of NE North America. *Marine Micropaleontology,* 81**,** 43-62.

YÁÑEZ, G., CEMBRANO, J., PARDO, M., RANERO, C. & SELLES, D. 2002. The Challenger–Juan Fernández–Maipo major tectonic transition of the Nazca–

Andean subduction system at 33–34°S: geodynamic evidence and implications. *Journal of South American Earth Sciences,* 15**,** 23-38.

YE, L., KANAMORI, H. & LAY, T. 2018. Global variations of large megathrust earthquake rupture characteristics. *Science Advances,* 4**,** eaao4915.

YEATS, R. S., YEATS, R. S., SIEH, K., SIEH, K. E., ALLEN, C. R. & ALLEN, C. R. 1997. *The geology of earthquakes*, Oxford University Press, USA.

YOKOYAMA, Y., LAMBECK, K., DE DECKKER, P., JOHNSTON, P. & FIFIELD, L. K. 2000. Timing of the Last Glacial Maximum from observed sea-level minima. *Nature,* 406**,** 713-716.

YOMOGIDA, K., YOSHIZAWA, K., KOYAMA, J. & TSUZUKI, M. 2011. Along-dip segmentation of the 2011 off the Pacific coast of Tohoku Earthquake and comparison with other megathrust earthquakes. *Earth, Planets and Space,* 63**,** 34.

ZHAO, B., BÜRGMANN, R., WANG, D., ZHANG, J., YU, J. & LI, Q. 2022. Aseismic slip and recent ruptures of persistent asperities along the Alaska-Aleutian subduction zone. Nature Communications, 13, 3098.

ZONG, Y. & HORTON, B. P. 1998. Diatom zones across intertidal flats and coastal saltmarshes in Britain. *Diatom Research,* 13**,** 375-394.

ZONG, Y. & HORTON, B. P. 1999. Diatom-based tidal-level transfer functions as an aid in reconstructing Quaternary history of sea-level movements in the UK. *Journal of Quaternary Science,* 14**,** 153-167.

ZONG, Y., SHENNAN, I., COMBELLICK, R. A., HAMILTON, S. L. & RUTHERFORD, M. M. 2003. Microfossil evidence for land movements associated with the AD 1964 Alaska earthquake. *The Holocene,* 13**,** 7-20.